

**COMPUTATIONAL AND EXPERIMENTAL INVESTIGATION OF OIL SEPARATION  
FROM AN OIL-WATER TWO-PHASE PIPE FLOW AND ITS ACCUMULATION  
IN A SUBSEA DEAD-LEG**

by

Egemen Çağlar

A thesis submitted to the Graduate Faculty of  
Auburn University  
in partial fulfillment of the  
requirements for the Degree of  
Master of Science

Auburn, Alabama  
August 3, 2019

Keywords: CFD, flow assurance, gas hydrate, subsea pipelines, turbulence, two-phase flow

Copyright 2019 by Egemen Çağlar

Approved by

Jay M. Khodadadi, Chair, Professor of Mechanical Engineering  
Daniel Mackowski, Professor of Mechanical Engineering  
Daniel Harris, Associate Professor of Mechanical Engineering

## Abstract

Both 2- and 3-dimensional transient computational studies of two-phase turbulent flow within a horizontal channel/pipe with a vertical capped dead-leg placed downstream of an oil/water supply source simulating parts of a model subsea petroleum production system were considered. Two-phase continuity and momentum relations governing two immiscible, incompressible, Newtonian fluids were solved using the open-source software OpenFOAM. Baseline 2-D simulation results for a 90%-10% slurry of 32.8 °API crude oil-water mixture at the inlet port (Reynolds number of  $2.1 \times 10^5$ ) were studied to elucidate the extent of evolving recirculating vortices and penetration of the oil phase into the vertical dead-leg. For the 2-D channel simulations, parametric studies of the average inlet velocity, width/length of the dead-leg and oil density/viscosity on evolving recirculation zones and accumulation of oil within a vertical dead-leg were performed to determine their effects on development of the transient turbulent flow, pressure, concentrations fields and the extent of oil separation and its accumulation in the vertical dead-leg. Computationally-intensive 3-D unsteady turbulent simulations within a vertical dead-leg for a 90%-10% oil-water mixture were also performed. The general trends of oil separating from the mixture and lifting in the vertical dead-leg as time progressed was captured by both 2-D and 3-D models. However, the 3-D model exhibits greater refinement of the complex three-dimensional vortical effects at the T-junction linked to separation of the two phases leading to migration of lighter oil to the top of the vertical dead-leg.

An experimental flow loop using deionized water/olive oil mixtures treated with table salt as demulsifier was designed to test similar phenomenon. Oil accumulations tests were performed with 5% and 10% oil volume mixtures for dead-leg inclination angles of 90 (vertical), 60, 45 and 30 degrees. Following a system homogenization procedure, minimum of four oil separation/accumulation tests were performed for a minimum time period of 10 min. Videos of oil accumulation process were obtained for various inclination angles of the dead-leg. The instantaneous accumulated heights of the oil column versus time were tabulated. Through

applying the least-squares linear fit method, empirical accumulation rates were derived. Variations of the instantaneous height of the oil column within the dead-legs were observed rise linearly for the 5% oil mixture, regardless of the inclination angle. For the 10% oil mixture, the instantaneous height of the accumulated oil column was rising linearly faster than the 5% oil mixture at the early instants, however for some inclination angles the accumulation rate declined. For the 10% oil mixture, limited 3-D simulation results for a period of 1-2 min matching the operating conditions in the laboratory were compared to experimental findings for dead-leg inclination angles of 90 (vertical), 60, 45 and 30 degrees. The complex recirculating flow zone in the vicinity of the T-junction was identified to be the major source of oil separation and its rise toward the capped end of the dead-leg. Another route was also identified where oil droplets were separated at the bottom of the complex recirculating zone and while coalescing lifted toward the expanding accumulating oil column. Limited experiments were performed for the case of a horizontal dead-leg. Experimentally-obtained oil accumulation data suggest that oil accumulation was limited to the top of the horizontal dead-leg and the zone of accumulated oil reached an asymptotic value early on.

## Acknowledgments

First of all, I would like to express my sincere gratitude to my advisor Professor Jay M. Khodadadi for his guidance, encouragement and support during my graduate study at Auburn University. I am very grateful to Professors Daniel Mackowski and Daniel Harris for being members of the advising committee.

I would like to thank Prof. Jeffrey Suhling, Chairman of the Mechanical Engineering Department for his support of this project. I also highly appreciate Dr. Thomas Burch for providing insightful suggestions in relation to design/operation of the experimental set-up and his hands-on assistance on many occasions in the laboratory. Professor German Mills of the Chemistry and Biochemistry Department assisted with initial selection of oils for the experiments and was instrumental in solving the emulsion problem that was faced early in the experiments. Jason Smith, Ivey Marcell and Dr. Jordan Roberts of the Mechanical Engineering Department were very helpful in advising me to solve a number of problems at various stages of the experiments. Prof. Jose Vasconcelos Neto of the Civil and Environmental Engineering Department discussed various options for design and setting up of the flow loop at the conceptualization stage. Prof. Dan Marghitu helped unselfishly when I needed another computing platform by providing a laptop. Prof. Anwar Ahmed of the Aerospace Engineering Department provided suggestions and equipment for flowrate measurements. Mr. Yi Zeng, PhD-candidate in my research group provided great assistance during construction and operation of the experimental flow loop.

I would like to acknowledge my colleagues and friends, Wenwen Ye, Shafkat Bin Hoque, Dourna Jamshideasli, Jue Wang and Mahdi Nabil (PhD-candidate at Pennsylvania State University) for their help, support and friendship since the time I arrived in Auburn.

In the course of the computational phase of my research, I was assisted by the expert advice of capable personnel of the Network Services of the Sam Ginn College of Engineering and the high-performance Hopper System of Auburn University.

Very special expressions of gratitude go out to my parents Ali Fuat Çağlar and Aynur Çağlar, and my siblings Zeynep Çağlar and Melih Arda Çağlar. As it always has been, they constantly provided great support and love despite the long distance.

Most importantly, I would like to thank Turkish Petroleum Corporation (TPAO) for the opportunity they provided me to complete my Master of Science degree. None of this could have happened without their financial support during my graduate study at Auburn University.

## Table of Contents

Abstract.....	ii
Acknowledgments.....	iv
List of Figures .....	xi
List of Tables .....	xxv
Nomenclature .....	xxvii
1. Introduction.....	1
1.1. Gas Hydrates .....	2
1.1.1. Structure of Gas Hydrates .....	2
1.1.2. Formation of Gas Hydrates.....	3
1.2. Properties of Gas Hydrates.....	7
1.3. Gas Hydrates as an Energy Source.....	9
1.4. Techniques for Characterization of Gas Hydrates.....	9
1.5. Methods to Obtain Gas from Gas Hydrates .....	10
1.6. Potential Applications of Gas Hydrates.....	10
1.7. Gas Hydrates as an Operational Problem.....	12
1.8. Solution Techniques of Formation and Accumulation of Gas Hydrates.....	14
1.9. Closure.....	17
2. Literature Review .....	18
2.1. Descriptions of Previous Research Studies .....	18
2.2. Summary of Literature Review .....	56
2.3. Closure.....	67

3. Computational Methodology for Study of Phase Separation in Multiphase Systems and Oil Accumulation in Dead-legs .....	68
3.1. Dead-legs.....	68
3.2. Geometry of Physical Models.....	69
3.3. Multiphase Flows.....	70
3.4. Solution of Turbulent Flows Through Application of Direct Numerical Simulations (DNS), Large Eddy Simulation (LES) and Reynolds-Averaged Navier-Stokes (RANS) .....	71
3.5. Turbulence Models.....	72
3.5.1. The High-Reynolds Number $k - \varepsilon$ Turbulence Model .....	73
3.5.2. The Low-Reynolds Number $k - \varepsilon$ Turbulence Model .....	74
3.5.3. The Shear Stress Transport $k - \omega$ Turbulence Model.....	75
3.6. Wall functions and $y^+$ .....	77
3.7. OpenFOAM Computational Fluid Dynamics Package .....	79
3.8. Adopted Methodology for Solution of Two-Phase Immiscible Fluids in Channel/Pipes including Dead-legs.....	80
3.8.1. Two-Phase Mixture Relations.....	80
3.8.2. Interface-capturing equation.....	81
3.9. Closure.....	81
4. Effect of Flow Characteristics and Geometry of a Capped Dead-Leg on Separation of Phases from a Two-Phase Flow .....	82
4.1. Baseline Two-Dimensional Channel and the Dead-Leg System .....	82
4.1.1. Grid Independence Study for the 2-D Planar Geometry Simulations.....	83
4.1.2. Computational Results for the Baseline 2-D Channel with Dead-leg.....	85
4.1.3. Effect of the Dead-Leg Length.....	87
4.1.4. Effect of the Dead-Leg Width.....	92

4.1.5. Effect of the Average Inlet Velocity of the Channel .....	95
4.1.6. Effect of the Crude Oil Viscosity .....	100
4.1.7. Effect of the Hydrodynamic Development Length Upstream of the Vertical Dead-Leg .....	104
4.1.8. Effect of the Crude Oil Density.....	113
4.2. Three-Dimensional Horizontal Pipe and the Vertical Dead-Leg System .....	119
4.2.1. Grid Independence Study for the 3-D Geometry Simulations.....	120
4.2.2. Results for Three-Dimensional Pipe and the Vertical Dead-Leg System...	122
4.3. Closure.....	126
5. Experimental Study of Phase Separation and Oil Accumulation in a Deal-Leg.....	127
5.1. Details of the Experimental Investigation .....	127
5.1.1. Flow Rate Measurements.....	134
5.1.2. Density and Viscosity Measurements of Oil and Water.....	136
5.1.3. Support of the Flow Loop.....	138
5.2. Emulsification Tests .....	139
5.2.1. Distilled and Deionized Water.....	139
5.2.2. Magnetic Stirring.....	141
5.3. Degassing of the Water-Air System and Addition of Oil.....	145
5.3.1. Addition Oil.....	147
5.3.2. Breaking-up Emulsions.....	149
5.4. Procedure for Oil Accumulation Tests .....	152
5.4.1. Homogenization of the System.....	152
5.4.2. Pump Shutdown and Oil Column Initialization .....	152
5.4.3. Transient Oil Accumulation Test .....	153
5.5. Recorded System Temperature Rise.....	158
5.6. Oil Accumulation within Non-Vertically Positioned Dead-Legs.....	159



5.7. Comparison of Oil Accumulation Data for 5% and 10% Oil.....	180
5.8. Closure Inspection of the Instantaneous Behavior of Phases .....	182
5.9. Comparison of Experimental Observations and 3-D simulations.....	183
5.9.1. Inclined Dead-Leg 3-D CFD Results.....	184
5.9.2. Horizontal Dead-Leg 3-D CFD Results.....	188
5.10. Closure.....	190
6. Conclusions .....	192
References .....	194
Appendix A. BENCHMARKING/VERIFICATION OF RELATED FLOW CASES UTILIZING THE OPENFOAM SOFTWARE .....	204
Appendix A.1.1. Initially-Unstable Horizontal Three-Layer Immiscible Fluid System .	204
Appendix A.1.2. Computational Details .....	206
Appendix A.1.3. Results .....	208
Appendix A.2.1. Initially-Unstable Horizontal Three-Layer Immiscible Fluid System .	213
Appendix A.2.2. Computational Details .....	214
Appendix A.2.3. Results .....	215
Appendix A.3.1. Developing Laminar Channel Flow .....	220
Appendix A.3.2. Computational Details .....	221
Appendix A.3.3. Results .....	222
Appendix A.4.1. Developing Channel Flow Re-visited .....	228
Appendix A.4.2. Computational Details .....	229
Appendix A.4.3. Results .....	230
Appendix B. GRID INDEPENDENCE TESTS FOR 2-D CHANNEL and 3-D PIPE SIMULATIONS WITH A DEAD-LEG .....	237

Appendix C. CALCULATIONS OF FRICTIONAL PIPE LOSSES FOR EVALUATING THE PUMP POWER.....	238
Appendix D. EVALUATION OF AGITATION OF OIL (CANOLA/VEGETABLE/OLIVE) AND WATER (TAP/DISTILLED/DEIONIZED) SYSTEMS.....	239
Appendix E. RAW DATA OF THE OIL ACCUMULATION IN THE DEAD-LEG EXPERIMENTS AND THE DERIVED OIL ACCUMULATION RATES.....	248

## List of Figures

Figure 1.1. Solid hydrate plug forming within a pipe [Sloan and Koh, 2008] .....	1
Figure 1.2. Phase envelope of methane hydrate under the (a) sediment, and (b) water [Giavarini and Hester, 2011] .....	4
Figure 1.3. Schematic diagram of a unit cell with side lengths $a, b, c$ and angles $\alpha, \beta, \gamma$ [Wikipedia, “Lattice constant,” 2019].....	7
Figure 1.4. Visual proportions of the constituents of 1 m <sup>3</sup> of gas hydrate at standard conditions .....	9
Figure 2.1. Size of the vortices within dead-legs: (a) $L/D=1$ , (b) $L/D=3$ , (c) $L/D=5$ and (d) $L/D=7$ [Habib et al., 2005].....	18
Figure 2.2. Volumetric concentration of water within different size dead-legs: (a) $L/D=1$ , (b) $L/D=3$ , (c) $L/D=5$ and (d) $L/D=7$ [Habib et al., 2005].....	19
Figure 2.3. Schematic diagram of the dead-leg model [Andersen, 2007].....	20
Figure 2.4. Temperature profile along the centerline and line wall in the vertical dead-leg (1,100 W/m <sup>2</sup> K heat transfer coefficient) [Andersen, 2007] .....	21
Figure 2.5. Temperature profile along the centerline and line wall in the horizontal dead-leg (1,100 W/m <sup>2</sup> K heat transfer coefficient) [Andersen, 2007] .....	21
Figure 2.6. Contour map of the temperature field [Sean et al., 2007] .....	22
Figure 2.7. Schematic diagram of the hydrate core system [Nazridoust and Ahmadi, 2007]...	23
Figure 2.8. 3-D CAD model of the test section of the flow loop [Fatnes, 2010] .....	24
Figure 2.9. Contours of the continuous phase velocity on the midline cross section of the pipe [Fatnes, 2010].....	26
Figure 2.10. Contours of the hydrate formation fraction on the midline cross section of the pipe [Fatnes, 2010].....	26
Figure 2.11. 3-D CAD model of the flow loop section with dimensions in mm [Balakin et al., 2011] .....	27
Figure 2.12. Bed thickness as a function of the mean flow velocity for different solid stress models [Balakin et al., 2011] .....	28
Figure 2.13. Contour of water phase fraction [Naseer and Brandstätter, 2011] .....	29

Figure 2.14. Hydrate concentration and velocity vectors [Naseer and Brandstätter, 2011] .....	30
Figure 2.15. Viscosity of the mixture and the volume fraction of water [Naseer and Brandstätter, 2011].....	30
Figure 2.16. Velocity of the mixture and the volume fraction of hydrate [Naseer and Brandstätter, 2011].....	31
Figure 2.17. Selected geometry with dimensions in mm [Sallehud-Din, 2012].....	32
Figure 2.18. Temperature distribution in the cross-section of product pipe for the (a) horizontal and (b) vertical orientations [Sallehud-Din, 2012] .....	33
Figure 2.19. Temperature distribution along the product pipe wall for the (a) horizontal and (b) vertical orientations [Sallehud-Din, 2012] .....	33
Figure 2.20. Temperature distribution of the cross-section of the product pipe for (a) 10, (b) 20, (c) 30, (d) 40 and (e) 50 liter/minute flow rate [Sallehud-Din, 2012].....	34
Figure 2.21. Cross-sectional temperature distributions at the mid-plane of the bundle for various inclination angles of (a) 10°, (b) 20°, (c) 40°, (d) 60°, (e) 80° and (f) 90° [Sallehud-Din, 2012].	35
Figure 2.22. Velocity contours and velocity vectors with inlet velocity of (a) 0.75, (b) 1 and (c) 2 m/s [Ding et al., 2012] .....	36
Figure 2.23. Contours of water volumetric concentration in the dead-leg for inlet velocity of (a) 0.75, (b) 1, (c) 2, (d) 3 and (e) 5 m/s [Ding et al., 2012].....	37
Figure 2.24. Schematic diagram of combined T-junctions [Chen et al., 2012] .....	37
Figure 2.25. Static pressure distribution in the (a) upper horizontal pipe and (b) lower horizontal pipe axial centerlines [Chen et al., 2012].....	38
Figure 2.26. Volume flow rate in different branched pipes [Chen et al., 2012] .....	39
Figure 2.27. Contours of outlet flow state distribution (0.5 mm bubbles) for the (a) liquid, (b) solid, (c) gas phases and (d) the corresponding flow velocity [Li et al., 2015].....	41
Figure 2.28. Contours of axial surface flow state distribution for the (a) liquid, (b) solid, (c) gas phases and (d) the corresponding flow velocity [Li et al., 2015].....	41
Figure 2.29. Contours of axial surface flow state distribution for the (a) liquid, (b) solid, (c) gas phases and (d) the corresponding flow velocity [Li et al., 2015].....	42
Figure 2.30. Effect of inlet velocity of (a) 10, (b) 15, (c) 20, (d) 25, (e) 30 m/s on temperature distribution within the pipeline [Sule et al., 2015].....	43
Figure 2.31. Effect of viscosity of (a) 0.0112, (b) 0.0110, (c) 0.0109 and (d) 0.0107 cp on temperature distribution within the pipeline [Sule et al., 2015].....	44
Figure 2.32. Effect of pipe diameter of (a) 0.06, (b) 0.07, (c) 0.08 and (d) 0.09 m on temperature distribution within the pipeline [Sule et al., 2015].....	44

Figure 2.33. Effect of water fraction of (a) 0.1, (b) 0.15, (c) 0.2, (d) 0.25 and (e) 0.3 on temperature distribution within the pipeline [Sule et al., 2015].....	44
Figure 2.34. Four different installation orientations of a subsea Xmas tree [Hu et al., 2015]...	46
Figure 2.35. Streamlines colorized with velocity magnitude corresponding to (a) vertical and (b) horizontal cross-sections [Hu et al., 2015].....	47
Figure 2.36. Subsea Xmas tree assembly with corresponding (a) temperature and (b) convective heat transfer coefficient distributions [Hu et al., 2015] .....	47
Figure 2.37. Correlation of the convective heat transfer coefficients of various components of the system with the sea water velocity [Hu et al., 2015] .....	48
Figure 2.38. Temperature rising for individual components of the Xmas tree [Hu et al., 2015] .....	49
Figure 2.39. Correlation of convective heat transfer coefficients of various components of the system with the inner oil temperature [Hu et al., 2015].....	49
Figure 2.40. Predictions of the natural gas hydrate formation area in the wellbore for different gas production rates [Guo et al., 2016].....	51
Figure 2.41. Predictions of the natural gas hydrate formation area in the wellbore for different insulation materials [Guo et al., 2016] .....	51
Figure 2.42. Effects of throttle opening on the natural gas hydrate formation area in the wellbore [Guo et al., 2016] .....	52
Figure 2.43. Effects of shut-in time on the natural gas hydrate formation area in the wellbore [Guo et al., 2017].....	52
Figure 2.44. Melting time versus water temperature for different velocities [Liu et al., 2017] ..	55
Figure 2.45. Melting time versus flow rate for different temperatures [Liu et al., 2017] .....	56
Figure 3.1. Typical subsea pipeline systems and associated components in oil and gas fields [Oil States, 2019].....	69
Figure 3.2. Baseline two-dimensional model of the horizontal pipe and the branching vertical dead-leg (gravity point the -y direction) .....	70
Figure 3.3. Three-dimensional model of the horizontal pipe and the branching vertical dead-leg (gravity point the -y direction, however it can be at any orientation on the yz plane) .....	70
Figure 3.4. (a) Comparison of DNS, LES, RANS turbulence modeling methods and (b) the mean ( $\bar{u}$ ) and fluctuating ( $u'$ ) velocities [Scardovelli and Zaleski, 1999].....	71
Figure 3.5. Turbulent boundary layers [Çengel and Cimbala, 2006].....	78

Figure 4.1. (a) Typical mesh of the 2-D geometry for the 66,500 medium-density grid system (origin  $x=y=0$  is located at the bottom wall of channel inlet) and (b) velocity magnitude variations along the centerline within the 2-D dead-leg for different grid densities..... 84

Figure 4.2. Instantaneous streamlines within the baseline 2-D capped dead-leg system ( $Re=1.7 \times 10^5$ ) at time instants of (a) 20 s, (b) 30 s, (c) 40 s, (d) 50 s and (e) 60 s..... 86

Figure 4.3. Typical variations of the phase fraction field within the baseline 2-D capped dead-leg system ( $Re=1.7 \times 10^5$ ) at time instants of (a) 20 s, (b) 30 s, (c) 40 s, (d) 50 s and (e) 60 s..... 86

Figure 4.4. Streamline patterns overlaid with water concentration contours after 60 seconds for dead-leg lengths equal to (a)  $D$ , (b)  $2D$ , (c)  $4D$ , (d)  $6D$  and (e)  $8D$ ..... 88

Figure 4.5. Velocity contours after 60 seconds for dead-leg lengths equal to (a)  $D$ , (b)  $2D$ , (c)  $4D$ , (d)  $6D$  and (e)  $8D$ ..... 89

Figure 4.6. The x-component of the average velocity magnitude along the vertical dead-leg and the streamlines overlaid with water concentration within the dead-leg for the case of dead-leg length equal to  $8D$  at 60 seconds..... 90

Figure 4.7. The x-component of the average velocity magnitude along the vertical dead-leg at 60 seconds for different dead-leg lengths ..... 91

Figure 4.8. Pressure contours after 60 seconds for vertical dead-leg lengths equal to (a)  $D$ , (b)  $2D$ , (c)  $4D$ , (d)  $6D$  and (e)  $8D$ ..... 92

Figure 4.9. Streamline patterns superimposed on the volume fraction field after 60 seconds for vertical dead-leg widths equal to (a)  $D/2$ , (b)  $2D$  and (c)  $3D$ ..... 93

Figure 4.10. Velocity contours after 60 seconds for dead-leg widths equal to (a)  $D/2$ , (b)  $2D$  and (c)  $3D$ ..... 94

Figure 4.11. Pressure contours after 60 seconds for vertical dead-leg widths equal to (a)  $D/2$ , (b)  $2D$  and (c)  $3D$  ..... 95

Figure 4.12. Streamlines overlaid with contours of phase fraction after 60 seconds for inlet velocities equal to (a) 1 m/s ( $Re= 57,294$ ), (b) 5 m/s ( $Re= 286,473$ ), (c) 7 m/s ( $Re= 401,062$ ) and (d) 9 m/s ( $Re= 515,651$ )..... 96

Figure 4.13. Velocity contours after 60 seconds for inlet velocities equal to (a) 1, (b) 5, (c) 7 and (d) 9 m/s, corresponding to  $Re$  numbers being 57,294, 286,473, 401,062 and 515,651, respectively..... 97

Figure 4.14. Pressure contours after 60 seconds for inlet velocities equal to (a) 1, (b) 5, (c) 7 and (d) 9 m/s, corresponding to  $Re$  numbers equal to 57,294, 286,473, 401,062 and 515,651, respectively..... 98

Figure 4.15. Pressure differences between the inlet and outlet sections of horizontal channel for different inlet velocities, corresponding to $Re$ numbers equal to 57,294, 286,473, 401,062 and 515,651, respectively .....	99
Figure 4.16. Streamlines overlaid with phase concentration contours after 60 seconds for different crude oil kinematic viscosities equal to (a) $2 \times 10^{-5}$ , (b) $10^{-5}$ , (c) $2 \times 10^{-6}$ and (d) $2 \times 10^{-7}$ $m^2/s$ ....	100
Figure 4.17. Velocity contours after 60 seconds for different crude oil kinematic viscosities equal to (a) $2 \times 10^{-5}$ , (b) $10^{-5}$ , (c) $2 \times 10^{-6}$ and (d) $2 \times 10^{-7}$ $m^2/s$ .....	101
Figure 4.18. Average velocity magnitudes at the point $y=0.12$ m located at the centerline of the vertical dead-legs for Case 1 ( $2 \times 10^{-5}$ $m^2/s$ ), Case 2 ( $10^{-5}$ $m^2/s$ ), Case 3 ( $2 \times 10^{-6}$ $m^2/s$ ) and Case 4 ( $2 \times 10^{-7}$ $m^2/s$ ).....	102
Figure 4.19. Time dependence of the water fraction within the dead-leg at $x=9.66$ m and $y=1.2$ m over the time interval of 0-60 s for Case 1 ( $2 \times 10^{-5}$ $m^2/s$ ), Case 2 ( $10^{-5}$ $m^2/s$ ), Case 3 ( $2 \times 10^{-6}$ $m^2/s$ ) and Case 4 ( $2 \times 10^{-7}$ $m^2/s$ ).....	103
Figure 4.20. Time dependence of water fraction within the dead-leg at $x=9.66$ m and $y=1.2$ m over the time interval of 35-60 s for Case 1 ( $2 \times 10^{-5}$ $m^2/s$ ), Case 2 ( $10^{-5}$ $m^2/s$ ), Case 3 ( $2 \times 10^{-6}$ $m^2/s$ ) and Case 4 ( $2 \times 10^{-7}$ $m^2/s$ ) .....	103
Figure 4.21. Change in pressure drop based on different oil kinematic viscosities of (a) $2 \times 10^{-5}$ , (b) $10^{-5}$ , (c) $2 \times 10^{-6}$ and (d) $2 \times 10^{-7}$ $m^2/s$ .....	104
Figure 4.22. Instantaneous streamline patterns overlaid with phase concentration contours after (a) 10 s, (b) 20 s, (c) 30 s, (d) 40 s (e) 50 s and (f) 60 s for Case 1 (upstream hydrodynamic development length of $90D$ ) .....	105
Figure 4.23. Instantaneous streamline patterns overlaid with phase concentration contours after (a) 10 s, (b) 20 s, (c) 30 s, (d) 40 s (e) 50 s and (f) 60 s for Case 2 (upstream hydrodynamic development length of $100D$ ) .....	106
Figure 4.24. Instantaneous streamline patterns overlaid with phase concentration contours after (a) 10 s, (b) 20 s, (c) 30 s, (d) 40 s (e) 50 s and (f) 60 s for Case 3 (upstream hydrodynamic development length of $110D$ ) .....	107
Figure 4.25. Streamline patterns overlaid with phase concentration contours after 60 seconds for (a) Case 1, (b) Case 2 and (c) Case 3 corresponding to different hydrodynamic development length upstream of the dead-leg.....	108
Figure 4.26. Values of the (a) water fraction at time instant of 60 seconds and (b) the average water fraction during 60 seconds at different monitored locations for Case 1 (upstream hydrodynamic development length of $90D$ ) .....	109

Figure 4.27. Velocity contours after 60 seconds for different hydrodynamic development lengths before the dead-legs equal to (a)  $90D$ , (b)  $100D$ , (c)  $110D$  and (d) variation of the average velocity through the centerline from the bottom to the top of the dead-leg ..... 110

Figure 4.28. Instantaneous velocity magnitudes along the centerline starting from the bottom and ending at the top of the dead-legs for Case 1, Case 2 and Case 3 (upstream hydrodynamic development length of  $90D$ ,  $100D$  and  $110D$ , respectively) along with a close-up view of the inlet to the vertical dead-leg at the time instant of 60 s ..... 111

Figure 4.29. Instantaneous axial velocity magnitudes from the inlet to the end of the horizontal channel at various vertical heights of the main channel for Case 1 at the time instant of 60 s with an upstream hydrodynamic development length of  $90D$ ..... 112

Figure 4.30. Plot of (a) average velocity and (b) pressure values at the centerline of the horizontal channel corresponding the location of the dead-leg for Case 1 ..... 112

Figure 4.31. Pressure gradient for (a) Case 1, (b) Case 2 and (c) Case 3 (upstream hydrodynamic development length of  $90D$ ,  $100D$  and  $110D$ ) ..... 113

Figure 4.32. Streamlines overlaid with phase fraction contours after 60 seconds for different oil densities of (a) Case 1 ( $600 \text{ kg/m}^3$ ), (b) Case 2 ( $800 \text{ kg/m}^3$ ) and (c) Case 3 ( $900 \text{ kg/m}^3$ ) ..... 114

Figure 4.33. Velocity contours after 60 seconds for different oil densities of (a) 600, (b) 800 and (c)  $900 \text{ kg/m}^3$  ..... 115

Figure 4.34. Pressure contours after 60 seconds for different oil densities of (a) 600, (b) 800 and (c)  $900 \text{ kg/m}^3$  ..... 116

Figure 4.35. Pressure drop within (a) the horizontal main channel and (b) the vertical dead-leg ..... 117

Figure 4.36. Phase concentrations after 60 seconds for oil densities of (a) 1200 ( $^{\circ}\text{API} = 94.852$ ) and (b)  $600 \text{ kg/m}^3$  ( $^{\circ}\text{API} = -18.323$ )..... 118

Figure 4.37. Top views of the unstructured triangle mesh systems viewed along the centerline of the vertical dead-leg ( $y$ -direction) for the (a) coarse (853,000), (b) medium (1,864,000) and (c) fine (5,906,000) grid densities ..... 121

Figure 4.38. Velocity variations at the centerline ( $y$ -direction) within the vertical 3-D dead-leg for the 853,000, 1,864,000 and 5,906,000 grid densities ..... 122

Figure 4.39. Instantaneous phase fraction fields within the branching 3-D dead-leg on the vertical symmetry plane ( $z = 0$ ) at time instants of (a) 0, (b) 5, (c) 20, (d) 40 and (e) 60 s ..... 123

Figure 4.40. Isometric view of phase fraction contours on the pipe and the dead-leg surface cut-view of the double-sliced dead-leg segment at the 60 s time instant, in addition to marked striation patterns on the surface of the horizontal pipe..... 124



Figure 4.41. Phase fraction contours on 4 horizontal circular sliced cross-sections ( $y/D= 0.5, 0.83, 2.5$ and $4.17$ ) along the vertical direction at the 60 s time instant .....	125
Figure 4.42. Phase fraction contours on vertical circular sliced cross-sections ( $x=\text{constant}$ ) along the horizontal feed pipe at the 60 s time instant .....	126
Figure 5.1. Schematic view of the proposed original experimental set-up .....	127
Figure 5.2. Pump resting on rubber spacers and mounted on wood blocks.....	128
Figure 5.3. Post-pump discharge assembling of the PVC pipe sections/fittings.....	129
Figure 5.4. Bubble levels utilized to assure that the pipes/components were placed properly .....	129
Figure 5.5. Clear PVC tee connected with two flexible couplings using metal fasteners.....	130
Figure 5.6. Reinforced vinyl tubing utilized for achieving a well-mixed fluid in the system before initiating oil accumulation tests.....	130
Figure 5.7. (a) Reinforced vinyl tubing with two ball valves used to re-direct fluid from the main pipe to top of the dead-leg section, (b) valves used to control flows in vinyl tubing and horizontal main pipe and (c) valve used to control flow downstream of the vinyl tubing .....	131
Figure 5.8. Gate valve at the top of the model dead-leg shown in its vertical position .....	132
Figure 5.9. Two views of the J-shaped expansion assembly designed to accommodate expansion of oil-water into an air column .....	133
Figure 5.10. Gate valve used for drainage of the system and accurate fluid removal .....	134
Figure 5.11. (a) the location of the Flomec flow meter and (b) the flow meter .....	135
Figure 5.12. Electronic scale used to measure the mass of the liquids.....	136
Figure 5.13. Viscosity meter used to measure the dynamic viscosities of the liquids.....	137
Figure 5.14. (a) Wood supports to bear the elevated part of the system, (b) double-wide corner brace and (c) corner brace and (d) plastic hanger strap .....	138
Figure 5.15. Deionized water processing unit in the Department of Chemistry and Biochemistry at Auburn University featuring a reservoir feed water purification system.....	140
Figure 5.16. Stirring hot plate used to stir oil-water liquid systems .....	141
Figure 5.17. Appearance of the mixture of canola oil with (a) tap water, (b) deionized water and (c) distilled water near completion of stirring after 60 min; outlines of the distorted column of canola oil in the core of the system can be observed. ....	142
Figure 5.18. Comparison of the separation of canola oil from tap, deionized and distilled water upon conclusion of 60 minutes of magnetic stirring showing the oil layer sitting on top of the respective water system.....	142

Figure 5.19. Appearance of the mixture of vegetable oil with (a) tap water, (b) deionized water and (c) distilled water near completion of stirring after 60 min; outlines of the distorted column of vegetable oil in the core of the system can be observed. .... 143

Figure 5.20. Comparison of the separation of vegetable oil from tap, deionized and distilled water upon conclusion of 60 minutes of magnetic stirring showing the oil layer sitting on top of the respective water system..... 143

Figure 5.21. Appearance of the mixture of olive oil with (a) tap water, (b) deionized water and (c) distilled water at time 60 min; outline of the distorted column of olive oil in the core of the system can be observed. .... 144

Figure 5.22. Comparison of the separation of olive oil from tap, deionized and distilled water upon conclusion of 60 minutes of magnetic stirring showing the oil layer sitting on top of the respective water system..... 144

Figure 5.23. Variety of multiphase flow patterns, i.e. (a) slug, (b) slug-bubble, (c) bubble-slug and (d) bubble flow pattern ..... 145

Figure 5.24. Observed (a) slug flow followed by a wake region and (b) slug flow turning into bubble flow within the vertical dead-leg system during degassing ..... 146

Figure 5.25. Observed water levels within the vertical dead-leg (a) with air pockets during degassing and (b) without air pockets far into degassing ..... 147

Figure 5.26. Gradual emulsion formation for the 10%-90% olive oil-water system at different time instants (left to right)..... 148

Figure 5.27. System with oil-water emulsion (10%-90% olive oil-water system) ..... 148

Figure 5.28. Effectiveness of sodium chloride (NaCl), sodium sulfate (Na<sub>2</sub>SO<sub>4</sub>) on breaking oil-water emulsion with the combination of 10%-90% oil-water, respectively..... 149

Figure 5.29. Effectiveness of (a) methanol (CH<sub>3</sub>OH), (b) ethylene glycol (C<sub>2</sub>H<sub>6</sub>O<sub>2</sub>) and (c) isopropyl alcohol (CH<sub>3</sub>CHOHCH<sub>3</sub>) of breaking 10%-90% oil-water emulsion..... 150

Figure 5.30. Observation of accumulated olive oil in the vertical dead-leg separated from the 90%-10% water-oil as a result of salt addition ..... 151

Figure 5.31. Observed oil column within the dead-leg (a) before and (b) after careful drainage aimed at lowering the top column of oil to be visible in the transparent dead-leg; in this experiment, the top and bottom positions of the oil layer before start of the oil accumulation test are at 21” and 19.25” positions, respectively ..... 153

Figure 5.32. Dynamic views of oil accumulation within the 90° (vertical) dead-leg for run 1 at time instants: (a) initial time, (b) 5 min and (c) 10 min (5 vol% oil)..... 154

Figure 5.33. Dynamic views of oil accumulation within the 90° (vertical) dead-leg for run 2 at time instants: (a) initial time, (b) 5 min and (c) 10 min (5 vol% oil).....	154
Figure 5.34. Dynamic views of oil accumulation within the 90° (vertical) dead-leg for run 3 at time instants: (a) initial time, (b) 5 min and (c) 10 min (5 vol% oil).....	155
Figure 5.35. Dynamics views of oil accumulation within the 90° (vertical) dead-leg for run 4 at time instants: (a) initial time, (b) 5 min and (c) 10 min (5 vol% oil).....	155
Figure 5.36. Instantaneous height of the oil column vs. time within the 90° (vertical) dead-leg for each run (5 vol% oil) .....	157
Figure 5.37. Average instantaneous height of the oil column vs. time within the 90° (vertical) dead-leg (5 vol% oil) along with the least-squares linear curve fit.....	157
Figure 5.38. Example of segregated oil collected within the J-shaped expansion section ....	158
Figure 5.39. Observed change in volume after cooling down of the system (left column corresponds to the hot fluid at the end of oil accumulation test, whereas the right column shows the same system after cool-down for minimum of 1 hour) .....	159
Figure 5.40. Oil accumulation within the 60° dead-leg for run 1 at time instants: (a) initial time, (b) 5 min and (c) 10 min (5 vol% oil).....	160
Figure 5.41. Oil accumulation within the 60° dead-leg for run 2 at time instants: (a) initial time, (b) 5 min and (c) 10 min (5 vol% oil).....	160
Figure 5.42. Oil accumulation within the 60° dead-leg for run 3 at time instants: (a) initial time, (b) 5 min and (c) 10 min (5 vol% oil).....	161
Figure 5.43. Oil accumulation within the 60° dead-leg for run 4 at time instants: (a) initial time, (b) 5 min and (c) 10 min (5 vol% oil).....	161
Figure 5.44. Instantaneous height of the oil column vs. time within the 60° dead-leg for each run (5 vol% oil) .....	162
Figure 5.45. Average instantaneous height of the oil column vs. time within the 60° dead-leg along with the least-squares linear curve fit (5 vol% oil).....	162
Figure 5.46. Oil accumulation within the 45° dead-leg for run 1 at time instants: (a) initial time, (b) 5 min and (c) 10 min (5 vol% oil).....	163
Figure 5.47. Oil accumulation within the 45° dead-leg for run 2 at time instants: (a) initial time, (b) 5 min and (c) 10 min (5 vol% oil).....	163
Figure 5.48. Oil accumulation within the 45° dead-leg for run 3 at time instants: (a) initial time, (b) 5 min and (c) 10 min (5 vol% oil).....	164
Figure 5.49. Oil accumulation within the 45° dead-leg for run 4 at time instants: (a) initial time, (b) 5 min and (c) 10 min (5 vol% oil).....	164

Figure 5.50. Instantaneous height of the oil column vs. time within the 45° dead-leg for each run (5 vol% oil) .....	165
Figure 5.51. Average instantaneous height of the oil column vs. time within the 45° dead-leg along with the least-squares linear curve fit (5 vol% oil) .....	165
Figure 5.52. Oil accumulation within the 30° dead-leg for run 1 at time instants: (a) initial time, (b) 5 min and (c) 10 min (5 vol% oil) .....	166
Figure 5.53. Oil accumulation within the 30° dead-leg for run 2 at time instants: (a) initial time, (b) 5 min and (c) 10 min (5 vol% oil) .....	166
Figure 5.54. Oil accumulation within the 30° dead-leg for run 3 at time instants: (a) initial time, (b) 5 min and (c) 10 min (5 vol% oil) .....	166
Figure 5.55. Oil accumulation within the 30° dead-leg for run 4 at time instants: (a) initial time, (b) 5 min and (c) 10 min (5 vol% oil) .....	166
Figure 5.56. Instantaneous height of the oil column vs. time within the 30° dead-leg for each run (5 vol% oil) .....	167
Figure 5.57. Average instantaneous height of the oil column vs. time within the 30° dead-leg along with the least-squares linear curve fit (5 vol% oil) .....	167
Figure 5.58. Comparison of average instantaneous height of the oil column vs. time for each dead-leg inclination angle (5 vol% oil) .....	168
Figure 5.59. Oil accumulation within the 90° (vertical) dead-leg at initial time, 5 min and 10 min for (a) run 1, (b) run 2, (c) run 3 and (d) run 4 (10 vol% oil) .....	170
Figure 5.60. Instantaneous height of the oil column vs. time within the 90° (vertical) dead-leg for each run (10 vol% oil) .....	171
Figure 5.61. Average instantaneous height of the oil column vs. time within the 90° (vertical) dead-leg along with the least-squares linear curve fit (10 vol% oil) .....	171
Figure 5.62. Oil accumulation within the 60° dead-leg for run 1 at time instants: (a) initial time, (b) 5 min and (c) 10 min (10 vol% oil) .....	172
Figure 5.63. Oil accumulation within the 60° dead-leg for run 2 at time instants: (a) initial time, (b) 5 min and (c) 10 min (10 vol% oil) .....	172
Figure 5.64. Oil accumulation within the 60° dead-leg for run 3 at time instants: (a) initial time, (b) 5 min and (c) 10 min (10 vol% oil) .....	173
Figure 5.65. Oil accumulation within the 60° dead-leg for run 4 at time instants: (a) initial time, (b) 5 min and (c) 10 min (10 vol% oil) .....	173
Figure 5.66. Instantaneous height of the oil column vs. time within the 60° dead-leg for each run (10 vol% oil) .....	174

Figure 5.67. Average instantaneous height of the oil column vs. time within the 60° dead-leg along with the least-squares linear curve fit (10 vol% oil) .....	174
Figure 5.68. Oil accumulation within the 45° dead-leg at initial time, 5 min and 10 min for (a) run 1, (b) run 2, (c) run 3 and (d) run 4 (10 vol% oil).....	175
Figure 5.69. Instantaneous height of the oil column vs. time within the 45° dead-leg for each run (10 vol% oil) .....	176
Figure 5.70. Average instantaneous height of the oil column vs. time within the 45° dead-leg along with the least-squares linear curve fit (10 vol% oil).....	176
Figure 5.71. Oil accumulation within the 30° dead-leg for run 1 at (a) initial time, (b) 5 min and (c) 10 min (10 vol% oil) .....	177
Figure 5.72. Oil accumulation within the 30° dead-leg for run 2 at time instants (a) initial time, (b) 5 min and (c) 10 min (10 vol% oil) .....	177
Figure 5.73. Oil accumulation within the 30° dead-leg for run 3 at time instants (a) initial time, (b) 5 min and (c) 10 min (10 vol% oil) .....	177
Figure 5.74. Oil accumulation within the 30° dead-leg for run 4 at time instants (a) initial time, (b) 5 min and (c) 10 min (10 vol% oil) .....	177
Figure 5.75. Instantaneous height of the oil column vs. within the 30° dead-leg for each run (10 vol% oil) .....	178
Figure 5.76. Average instantaneous height of the oil column vs. time within the 30° dead-leg along with the least-squares linear curve fit (10 vol% oil).....	178
Figure 5.77. Comparison of average oil accumulation rates of each dead-leg position (10 vol% oil).....	179
Figure 5.78. Comparison of the heights of accumulated oil columns within the dead-leg with inclination angles of 90° (vertical), 60°, 45° and 30° for 5% and 10% oil system .....	181
Figure 5.79. Air bubbles collected at the top of the dead-leg and consecutive images (left to right) of air bubbles moving up in the 30° inclined dead-leg (5 vol% oil) .....	182
Figure 5.80. Observed foamy structure located between oil and water phases after system shutdown .....	183
Figure 5.81. Instantaneous color contours of phases on the curved sheet ( $x^2+z^2=D^2$ and $z>0$ ) of the dead-leg for the 10%-90% oil-water flow system for inclination angle of 90° (vertical) at time instants of (a) 10 s, (b) 20 s, (c) 30 s, (d) 40 s, (e) 50 s, (f) 60 s, (g) 70 s, (h) 80 s, (i) 90 s, (j) 100 s, (k) 110 s and (l) 120 s .....	185

Figure 5.82. Instantaneous color contours of phases on the downstream half-surface of the dead-leg for the 10%-90% oil-water flow system for inclination angle of 60° at time instants of (a) 5 s, (b) 10 s, (c) 20 s, (d) 40 s and (e) 60 s .....	186
Figure 5.83. Instantaneous color contours of phases on the downstream half-surface of the dead-leg for the 10%-90% oil-water flow system for inclination angle of 45° at time instants of (a) 10 s, (b) 20 s, (c) 30 s, (d) 40 s, (e) 50 s and (f) 60 s .....	187
Figure 5.84. Instantaneous color contours of phases on the downstream half-surface of the dead-leg for the 10%-90% oil-water flow system for inclination angle of 30° at time instants of (a) 10 s, (b) 20 s, (c) 30 s, (d) 40 s, (e) 50 s and (f) 60 s .....	188
Figure 5.85. Photograph of the experimental set-up with the dead-leg in its horizontal position .....	188
Figure 5.86. Instantaneous color contours of phases (top row) on the (a) downstream half-surface and (b) upstream half-surface of the dead-leg for the 10%-90% oil-water flow system compared to photographs of oil accumulation experiments (bottom row) for inclination angle of 0° (horizontal) at the 60 s time instant .....	189
Figure 5.87. Vertical cross-sectional view ( $y/D=11$ ) of accumulation of oil at the top of the horizontal dead-leg at the time instant of 60 s for the 10%-90% oil-water mixture .....	190
Figure A.1.1. Configuration of the air-water-oil (top to bottom) unstable fluid system at time $t=0$ .....	205
Figure A.1.2. The adopted grid system for the square container .....	206
Figure A.1.3. Instantaneous fields of the three-fluid system corresponding to (a) three immiscible phases, (b) fluid velocity in the x-direction, and (c) fluid pressure at time instants of 5, 8, 10, 15, 25, 35 and 60 seconds .....	209
Figure A.2.1. Configuration of the oil-water-air (left to right) unstable fluid system at time $t=0$ ....	213
Figure A.2.2. The adopted grid system for the square container .....	214
Figure A.2.3. Instantaneous fields of the three-fluid system corresponding to (a) three immiscible phases, (b) fluid velocity in the x-direction, and (c) pressure at time instants 2, 4, 6, 8, 10, 20 and 60 seconds .....	216
Figure A.3.1. The adopted grid system near the (a) inlet and (b) outlet of the channel .....	221
Figure A.3.2. Velocity field along the channel (m/s) with uniform mesh .....	222
Figure A.3.3. Velocity field at the inlet of the channel (m/s) with uniform mesh .....	223
Figure A.3.4. Velocity field at the outlet of the channel (m/s) with uniform mesh .....	223

Figure A.3.5. Velocity profiles at different locations along the length of the channel (m/s) with uniform mesh .....	225
Figure A.3.6. Pressure field along the length of the channel ( $m^2/s^2$ ) with uniform mesh .....	226
Figure A.3.7. Pressure drop divided by fluid density ( $m^2/s^2$ ) between axial positions $x=9-10$ m with uniform mesh .....	227
Figure A.4.1. The adopted grid system near the (a) inlet and (b) outlet of the channel .....	229
Figure A.4.2. Velocity field along the channel (m/s) with non-uniform grid.....	230
Figure A.4.3. The development of the axial velocity contours at (a) $x=0.0001$ m, (b) $x=0.01$ m, (c) $x=0.1$ m, (d) $x=0.2$ m, (e) $x=0.4$ m, (f) $x=0.6$ m, (g) $x=0.8$ m, (h) $x=1$ m, (i) $x=2$ m, (j) $x=7$ m, (k) $x=9$ m and (l) $x=10$ m, with non-uniform grid .....	231
Figure A.4.4. Axial velocity profiles at different locations along the channel (m/s) with non-uniform grid.....	233
Figure A.4.5. Pressure field along the length of the channel ( $m^2/s^2$ ) with non-uniform mesh	234
Figure A.4.6. Pressure drop divided by density ( $m^2/s^2$ ) along the channel between the axial distances $x=9-10$ m with non-uniform grid.....	235
Figure A.4.7. (a) Pressure drop divided by density, and (b) wall shear stress between the axial distances $x=0-10$ m with non-uniform grid.....	236
Figure D.1. Photographs of agitated 10% Canola Oil – 90% Tap Water system at various time instants (a) initial, (b) 1 min, (c) 2 min, (d) 3 min, (e) 58 min, (f) 59 min, (g) 60 min and (h) 1 min after the stirring process stops .....	239
Figure D.2. Photographs of agitated 10% Canola Oil – 90% Deionized Water system at various time instants (a) initial, (b) 1 min, (c) 2 min, (d) 3 min, (e) 58 min, (f) 59 min, (g) 60 min and (h) 1 min after the stirring process stops.....	240
Figure D.3. Photographs of agitated 10% Canola Oil – 90% Distilled Water system at various time instants (a) initial, (b) 1 min, (c) 2 min, (d) 3 min, (e) 58 min, (f) 59 min, (g) 60 min and (h) 1 min after the stirring process stops .....	241
Figure D.4. Photographs of agitated 10% Vegetable Oil – 90% Tap Water system at various time instants (a) initial, (b) 1 min, (c) 2 min, (d) 3 min, (e) 58 min, (f) 59 min, (g) 60 min and (h) 1 min after the stirring process stops .....	242
Figure D.5. Photographs of agitated 10% Vegetable Oil – 90% Deionized Water system at various time instants (a) initial, (b) 1 min, (c) 2 min, (d) 3 min, (e) 58 min, (f) 59 min, (g) 60 min and (h) 1 min after the stirring process stops.....	243

Figure D.6. Photographs of agitated 10% Vegetable Oil – 90% Distilled Water system at various time instants (a) initial, (b) 1 min, (c) 2 min, (d) 3 min, (e) 58 min, (f) 59 min, (g) 60 min and (h) 1 min after the stirring process stops.....	244
Figure D.7. Photographs of agitated 10% Olive Oil – 90% Tap Water system at various time instants (a) initial, (b) 1 min, (c) 2 min, (d) 3 min, (e) 58 min, (f) 59 min, (g) 60 min and (h) 1 min after the stirring process stops .....	245
Figure D.8. Photographs of agitated 10% Olive Oil – 90% Deionized Water system at various time instants (a) initial, (b) 1 min, (c) 2 min, (d) 3 min, (e) 58 min, (f) 59 min, (g) 60 min and (h) 1 min after the stirring process stops .....	246
Figure D.9. Photographs of agitated 10% Olive Oil – 90% Distilled Water system at various time instants (a) initial, (b) 1 min, (c) 2 min, (d) 3 min, (e) 58 min, (f) 59 min, (g) 60 min and (h) 1 min after the stirring process stops .....	247
Figure E.1. Height of accumulated oil column for the case of 5%-95% oil-water for the inclination angle of 90° (vertical dead-leg).....	255
Figure E.2. Height of accumulated oil column for the case of 5%-95% oil-water mixture for the inclination angle of 60° .....	256
Figure E.3. Height of accumulated oil column for the case of 5%-95% oil-water mixture for the inclination angle of 45° .....	257
Figure E.4. Height of accumulated oil column for the case of 5%-95% oil-water mixture for the inclination angle of 30° .....	258
Figure E.5. Height of accumulated oil column for the case of 10%-90% oil-water for the inclination angle of 90° (vertical dead-leg).....	259
Figure E.6. Height of accumulated oil column for the case of 10%-90% oil-water mixture for the inclination angle of 60° .....	260
Figure E.7. Height of accumulated oil column for the case of 10%-90% oil-water mixture for the inclination angle of 45° .....	261
Figure E.8. Height of accumulated oil column for the case of 10%-90% oil-water mixture for the inclination angle of 30° .....	262



## List of Tables

Table 1.1. Hydrocarbon gases in marine sediment [Claypool and Kvenvolden, 1983].....	6
Table 2.1. Summary of studies on hydrate formation .....	57
Table 4.1. Table 4.1. Water fraction on the horizontal line ( $x= 9.6-9.72$ m, $y=0.12$ m) within the dead-leg for Case 1 (1 m/s), Case 2 (5 m/s), Case 3 (7 m/s) and Case 4 (9 m/s) .....	98
Table 4.2. Pressure drop between inlet and outlet of the channel .....	99
Table 4.3. Correlation between pressure drop and velocity in turbulence flow .....	99
Table 5.1. Operating <i>Re</i> numbers of the flow loop based on the concentrations of the liquid components; (a) 10 vol% and (b) 5 vol% olive oil .....	136
Table 5.2. Density measurement of the liquids.....	137
Table 5.3. Dimensionless initial heights of the top and bottom positions of the oil column with the 5%-95% oil-water mixture at the start of the oil accumulation tests .....	156
Table 5.4. Oil accumulation rates (m/s) obtained using the least-squares fit method and the associated R-squared ( $R^2$ ) values (5 vol% oil) .....	168
Table 5.5. Dimensionless initial heights of the top and bottom positions of the oil column with the 10%-90% oil-water mixture at the start of the oil accumulation tests .....	169
Table 5.6. Oil accumulation rates obtained using the least-squares fit method and the coefficient of determination ( $R^2$ ) values (10 vol% oil) .....	179
Table A.3.1. The adopted domain and properties of the fluid .....	220
Table A.3.2. Boundary conditions .....	221

Table A.4.1. The adopted domain and properties of the fluid .....	228
Table A.4.2. Boundary conditions .....	229
Table B.1. Sample calculations related to grid independence tests for 2-D channel (left column) and 3-D pipe (right column) cases.....	237
Table C.1. Viscous flow calculations for a 10-90% oil- water mixture flowing inside the 2” (0.0508 m) diameter pipe flow loop .....	238
Table E.1. Change in height of oil column for the system with 5% olive oil and 90° dead-leg .....	248
Table E.2. Change in height of oil column for the system with 5% olive oil and 60° dead-leg inclination.....	249
Table E.3. Change in height of oil column for the system with 5% olive oil and 45° dead-leg inclination.....	250
Table E.4. Change in height of oil column for the system with 5% olive oil and 30° dead-leg inclination.....	251
Table E.5. Change in height of oil column for the system with 10% olive oil and 90° dead-leg inclination.....	252
Table E.6. Change in height of oil column for the system with 10% olive oil and 60° dead-leg inclination.....	252
Table E.7. Change in height of oil column for the system with 10% olive oil and 45° dead-leg inclination.....	253
Table E.8. Change in height of oil column for the system with 10% olive oil and 30° dead-leg inclination.....	253
Table E.9. Summary of the temperature and volume of oil accumulated within the J-bend expansion unit of the flow loop evaluated at the conclusion of the oil accumulation tests reported in Tables E.1-8.....	254

## Nomenclature

$C_f$	skin friction coefficient for internal pipe flow
$d_{\perp}$	distance from the nearest wall, m
$D$	channel width or pipe diameter, m
$\bar{f}_i$	external forces, N
$\bar{f}_s$	surface tension force, N
$\bar{g}$	gravitational acceleration, m/s <sup>2</sup>
$k$	turbulent kinetic energy, m <sup>2</sup> /s <sup>2</sup>
$\bar{p}$	averaged thermodynamic pressure, kg/ms <sup>2</sup>
$\tilde{P}_k$	modified production of turbulent energy term
$P_k$	production of turbulent energy term
$R^2$	coefficient of determination
$Re$	Reynolds number
$S_{ij}$	strain rate tensor
$S_t$	magnitude of the strain rate
$t$	time, s
$T$	temperature, K or °C
$\bar{u}$	mean velocity, m/s
$u_i$	local velocity, m/s
$u'$	fluctuating velocity, m/s
$U_{\infty}$	free stream velocity, m/s
$x, y, z$	Cartesian coordinates, m

## Greek Symbols

$\alpha$	phase fraction
$\delta_{ij}$	Kronecker delta

$\varepsilon$	turbulent dissipation rate, m <sup>2</sup> /s <sup>3</sup>
$\mu$	dynamic viscosity, kg/ms
$\vartheta$	kinematic viscosity, m <sup>2</sup> /s
$\rho$	density, kg/m <sup>3</sup>
$\tau_{ij}$	laminar viscous stress, kg/ms <sup>2</sup>
$\omega$	specific turbulence dissipation, s <sup>-1</sup>

### Subscripts

<i>crude oil</i>	crude oil
<i>eff</i>	effective
<i>i</i>	components
<i>t</i>	turbulent
<i>w</i>	wall
<i>water</i>	water

### Superscripts

+	dimensionless
---	---------------

### Abbreviations

°API	American Petroleum Institute gravity
CFD	Computational Fluid Dynamics
CPVC	Clear Polyvinyl Chloride
DI	Deionized
DNS	Direct Numerical Simulation
FVM	Finite Volume Method
GCI	Grid Convergence Indices
LES	Large Eddy Simulation
PVC	Polyvinyl Chloride
RANS	Reynolds Averaged Navier-Stokes
SST	Shear Stress Transport
VOF	Volume-of-Fluid

## 1. Introduction

Energy which is central to human existence is the property that is transferred to an object in order to perform work on it, or to heat the object. Broadly speaking, sources of energy are categorized in two broad groups namely renewable and non-renewable. Renewable energy (wind, solar, ocean, hydropower, geothermal, biomass) are associated with energy sources which are replenished in lifetime. Non-renewable energy (nuclear, oil sands, oil shale, fuel cells, coal, oil, natural gas, gas hydrate) is the type of energy which is produced by resources which cannot be replaced over a short time duration by natural means.

Transfer and conversion of energy is used in many areas such as heating, cooling, lighting, production, electronics, etc. In the developing world, the increasing population and consumption of energy sources is leading countries to explore alternative methods to extract conventional energy sources such as coal, crude oil and natural gas, and discover alternative energy sources [Li et al., 2015].

Greater access to energy at a lower cost in addition to development of technological advances has led to widespread exploration of oil and gas reservoirs in extreme environments, such as deep subsea environment. In relation to such operations, flow assurance that is related to uninterrupted extraction and transport of multiphase hydrocarbon-based energy source is extremely important. In such operations, many interruption sources are well-recognized in the oil and gas industry. In this thesis, attention will be focused on a deeper understanding of separation of phases and accumulation of oil within a branching pipe, known as a *dead-leg*. It is believed that a fundamental understanding of a number of physical mechanisms encountered in this problem will pave the way to an extremely hazardous problem, known as hydrate formation. A typical solid hydrate that can plug a pipeline is shown in Figure 1.1.



Figure 1.1. Solid hydrate plug forming within a pipe [Sloan and Koh, 2008]

## 1.1. Gas Hydrates

Gas hydrates are naturally-occurring ice-like crystalline solids which are formed under high pressure and low temperature conditions by the weak Van der Waals forces. Gas hydrates is a physical connection of water forming a rigid lattice of cages with gas molecules captured by the cages [Obanijesu et al., 2010, Kvenvolden, 1993]. Water crystallizes in the isometric crystallographic system in order to form gas hydrate rather than the hexagonal system of normal ice [Kvenvolden, 1993]. Even though the appearance of the hydrate is similar to snowball, it is flammable due to the hydrocarbon gases trapped within water molecules [Giavarini and Hester, 2011].

### 1.1.1. Structures of Gas Hydrates

In gas hydrate crystalline structures, hydrogen-bounded water molecules play a role as a cage by hosting guest gas molecules thanks to a gap within its center [Sloan and Koh, 2007, Giavarini and Hester, 2011, Samimi, 2012]. There is no chemical bonding which takes place between the host water molecules and the enclosed guest molecule [Englezos, 1993]. Gas hydrates occur mainly in three different crystal structure types which are body-centered cubic structure I (sI), face-centered cubic structure II (sII), and hexagonal structure H (sH) with regard to gas molecule size [Demirbas, 2010]. Methane ( $\text{CH}_4$ ), ethane ( $\text{C}_2\text{H}_6$ ), propane ( $\text{C}_3\text{H}_8$ ), isobutane ( $\text{C}_4\text{H}_{10}$ ), normal butane ( $\text{C}_4\text{H}_{10}$ ), nitrogen ( $\text{N}_2$ ), carbon dioxide ( $\text{CO}_2$ ) and hydrogen sulfide ( $\text{H}_2\text{S}$ ) are the most common gas molecules which can be located in the cavity composed of water molecules [Gas Processors Association, 1998]. Guest molecules having diameters between 4.2 and 6 Å, such as methane, ethane, carbon dioxide, and hydrogen sulfide form cubic structure I which are composed of body-center cages. Structure II of diamond-shaped packing cages can host gas molecules with the diameter between 6 and 7 Å such as propane and iso-butane besides the smaller gas molecules. The largest cavity size is seen in hexagonal structure H which can be occupied by the gas molecules with the diameter between 7 and 9 Å, such as iso-pentane and neohexene along with small size gas molecules [Demirbas, 2010, Sloan, 2003, Zarinabadi and Samimi, 2012]. In addition to these common three structure types, there are other hydrate structures, namely the Jeffrey's structures III–VII, structure T, and complex layer structures [Sloan, 2003].

### 1.1.2. Formation of Gas Hydrates

Natural gas and crude oil sources are located underground and subsea in contact with water. Due to the strong hydrogen bonds between the water molecules, the cage structures form with holes at the center of connected water molecules. Gas hydrates form when gas molecules move into these holes based on the diameters of gas and are encaged under the conditions of high pressure and low temperature which are common in oil and gas fields [Sinquin et al, 2004]. Gas hydrates can form at temperatures which is higher than the freezing temperature of water when the appropriate pressure is provided [Demirbas, 2010]. Even though the temperature and pressure conditions promoting hydrate formation show an alteration based on the kind of gas molecules, the minimum pressure and maximum temperature values are 3 MPa and 20 °C, respectively [Drive and Carroll, 2009]. A couple of methods called empirical chart, Polo Maleev, Stergaard, Hammerschmid and so on are used in order to predict gas hydrate equilibrium conditions [Guo et al., 2016]. Gas hydrates are formed below the permafrost sediments, oceans, inland seas and freshwater lakes as long as the suitable temperature and pressure conditions with the adequate gas molecules are supplied. Formation of natural gas hydrates in the permafrost areas and oceans can be predicted by means of the gas hydrate stability zone graphs which show the pressure-temperature interval suitable to form and stabilize gas hydrates. These graphs (Figure 1.1 (a) and (b)) are drawn based on the formation of gas hydrates with methane since methane gas hydrates are the most common all over the world [Kvenvolden and Lorenson, 2001]. Besides the existence of enough water and gas molecules and the suitable pressure and temperature conditions, the occurrence and stability of gas hydrates also depend on other factors which include mixing, kinetics, type of physical site, depth, surface for crystal formation, agglomeration and salinity of the system [Edmonds et al., 1998].

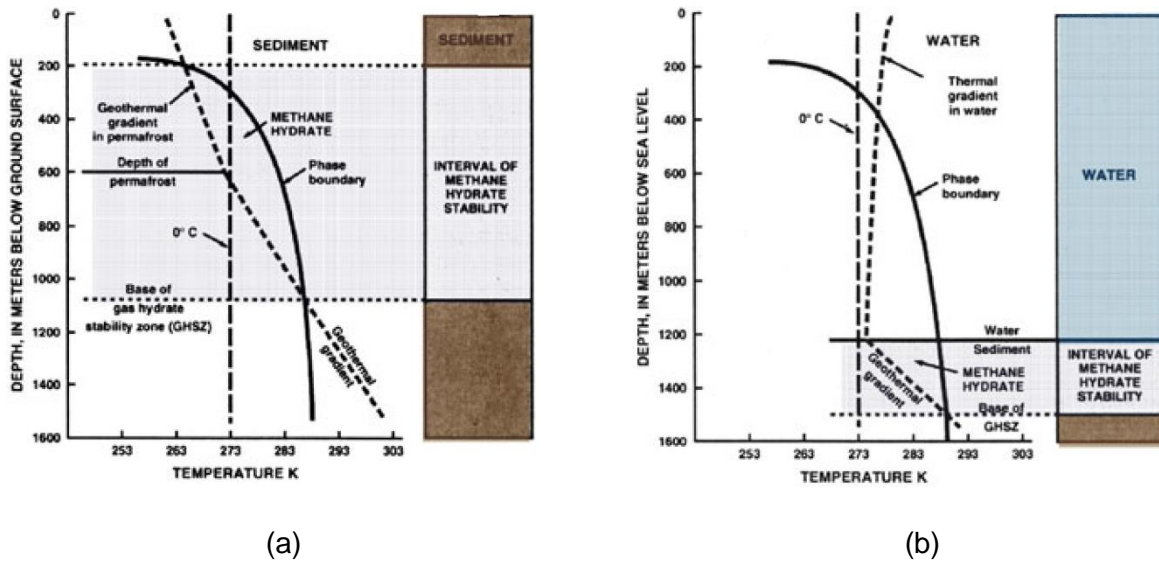


Figure 1.2. Phase envelope of methane hydrate under the (a) sediment, and (b) water [Giavarini and Hester, 2011]

The addition of salt shifts the curve to the left which means that the needed temperature for hydrate formation and stability for a given pressure decrease [Drive et al., 2009]. Higher C-number hydrocarbons (e.g.  $C_2H_6$ ,  $C_3H_8$ ) and the other gases ( $CO_2$ ,  $H_2S$ ) forming gas hydrates shift the boundary to the right which refers to an increase in the temperature for hydrate stability at the same pressure condition and the area of the hydrate stability field [Hyndman and Davis, 1992, Kvenvolden, 1993].

As shown in Figures 1.1 (a) and (b), the solid line denotes phase boundary between the free gas and hydrate. The phase boundary information suggests that the upper depth limit for methane hydrates is about 150 m in continental Polar Regions, where surface temperature is below 0 °C. In oceanic sediment on the other hand, gas hydrates appear when the water depth exceeds about 300 m, where the bottom water temperature approaches 0 °C. The dashed line represents geothermal gradient and thermal gradient for permafrost sediment and ocean, respectively. Geothermal gradient represents the rate of increasing temperature with respect to increasing depth [Donev, 2019]. Temperature gradient describes in which direction and at what rate the temperature changes most rapidly around a particular location. The lower limit of methane hydrate occurrence is determined by the geothermal and thermal gradients. The maximum lower limit is about 2000 m below the solid surface, although the lower limit is typically much less depending on local conditions. The area which is between the phase boundary and geothermal gradient



lines in Figure 1.1 (a) demonstrates where methane gas hydrate is located. This stability zone begins with the depth of about 200 m below the ground surface and ends at the depth of between 1000-1200 m, which is called “the base of gas hydrate stability zone”. Even though the pressure rises more with depth, gas hydrate does not occur after the line which the end cross point of the lines is located on since the temperature is higher than the hydrate formation temperature. Based on Figure 1.1 (b) which stands for oceanic sediments, the thermal gradient in water and phase boundary lines cross at two points at around 400 m and the other between 1400-1600 m. However, gas hydrate does not exist between the top intersection point of the lines and seafloor called water sediment due to the absence of sufficient amount of gas. Methane hydrate formation is limited by the low solubility of methane in seawater which is about 0.045 volumes of methane at standard conditions per unit volume of seawater [Yammamoto et al., 1976]. For this reason, hydrate formation is seen between water sediment which is around 1200 m below the water surface and the base of gas hydrate stability zone thanks to suitable conditions for hydrate formation. The temperature of water declines gradually from the water surface and reaches to 3-4 °C at the sea floor commonly all around the world [Giavarini and Hester, 2011]. Below the water sediment, temperature begins increasing with the average rate of 0.02 °C/m [Giavarini and Hester, 2011], and it is high enough to prevent hydrate formation for a given pressure beneath the base of gas hydrate stability zone.

The main sources of hydrocarbon gases which form gas hydrate are biogenic (microbially-derived) and thermogenic (petroleum-derived). Hydrocarbon gases generated by methanogenic archaea is known as biogenic or microbial. They form where there is no light from non-living organic matters which are buried in the seafloor sediment for many years. Biogenic gas has  $C_1/(C_2+C_3)$  ratios greater than 1000 [Waseda and Iwano, 2008]. Hydrocarbon gases generated during the thermally-activated break-down of larger organic molecules is termed thermogenic gases which are produced in regions deeper than the gas hydrate stability zone [Giavarini and Hester, 2011]. Thermogenic gas has significant quantities of low-molecular-weight hydrocarbons, with  $C_1/(C_2+C_3)$  ratios ranging from 0 to 50 [Waseda and Iwano, 2008]. Molecular weights of hydrocarbon gases is exhibited in Table 1.1.

Table 1.1. Hydrocarbon gases in marine sediment [Claypool and Kvenvolden, 1983]

Name	Symbol	Molecular Formula	Molecular Weight
<b>Methane</b>	$C_1$	$CH_4$	16
<b>Ethene</b>	$C_{2=}$	$C_2H_4$	28
<b>Ethane</b>	$C_2$	$C_2H_6$	30
<b>Propene</b>	$C_{3=}$	$C_3H_6$	42
<b>Propane</b>	$C_3$	$C_3H_8$	44
<b>Isobutane</b>	$i - C_4$	$C_4H_{10}$	58
<b>n-Butane</b>	$n - C_4$	$C_4H_{10}$	58

The solubility of hydrocarbon gases in liquid water and the solubility of water dissolved in hydrocarbon gases are low compared to their high concentrations in hydrate. That is why hydrate forms most easily at phase interfaces where there is an abundance of both hydrocarbon and water. Specifically, for gas-water two-phase systems, hydrate forms at the gas-water interface. However, for gas-water-oil three-phase systems, hydrate typically forms at the interface between the two liquids, water and oil, from small gas molecules dissolved in the oil. This interfacial phenomenon is a key concept in understanding hydrate formation and prevention [Sloan et al., 2009]. Hydrate formation on the interface between the gas and the aqueous phase adsorbed on rusty walls is also affected indirectly from the presence of solid surfaces [Kvamme et al., 2016].

The formation of gas hydrate is an exothermic process which means that heat is released to the environment and it dissociates endothermically which means that heat is absorbed [Giavarini and Hester, 2011]. The required heat for dissociation under low pressure conditions can be calculated by using the Clausius-Clapeyron equation [Sloan and Koh, 2008] which is a way of characterizing a discontinuous phase transition between two phases of matter of a single constituent [Sloan and Fleyfel, 1992]. Identify pressure and temperature as  $P$  and  $T$ , respectively, this relation is:

$$d(\ln P)/d(1/T) = -\Delta H_d/(z R) \quad (1.1)$$

where;

$\Delta H_d$  : heat of dissociation,

$z$  : gas compressibility factor,

$R$  : ideal gas constant (8.314 J/mol).

The Clausius-Clapeyron equation is suggested in order to predict the dissociation heat under high pressure conditions for better accuracy [Anderson, 2004, Gupta et al., 2006].

## 1.2. Properties of Gas Hydrates

The density of gas hydrate is calculated based on the lattice size and the gas concentration filling the cages [Giavarini and Hester, 2011]. The lattice size is calculated based on the lattice constant, or lattice parameter, consisting of the three lattice constants ( $a$ ,  $b$ ,  $c$ ) and the three angles ( $\alpha$ ,  $\beta$ ,  $\gamma$ ) between them. These regularly-repeating blocks are known as unit cells. The axial lengths are expressed in terms of Å (Ångströms) which is equal to  $10^{-10}$  m [Giavarini and Hester, 2011], and the inter axial angles are expressed in terms of degrees. Unit cell parameters of structure I, structure II and structure H are  $a = 1.2$  nm (cubic crystal structure:  $a = b = c$ ),  $a = 1.7$  nm (cubic crystal structure:  $a = b = c$ ), and  $a = 1.21$  and  $c = 1.01$  nm (hexagonal crystal structure  $a = b$ ), respectively.

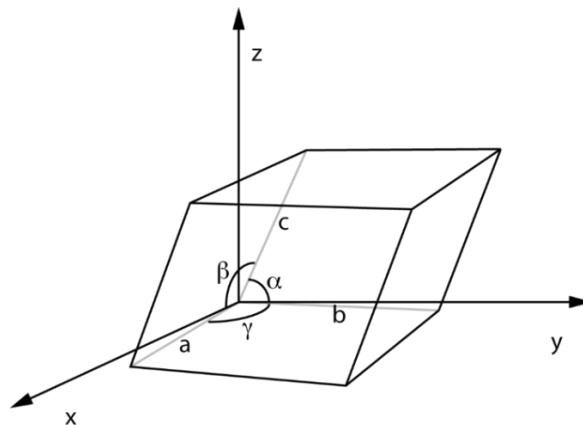


Figure 1.3. Schematic diagram of a unit cell with side lengths  $a$ ,  $b$ ,  $c$  and angles  $\alpha$ ,  $\beta$ ,  $\gamma$   
[Wikipedia, "Lattice constant," 2019]

Using unit cell volume, the density is calculated as:

$$\rho_{hydrate} = (10^{27} [MW_{water}N_{water} + MW_{gas}N_{gas}]) / (V_{unitcell}N_a) \quad (1.2)$$

where;

$\rho_{hydrate}$  : density of gas hydrate (kg/m<sup>3</sup>),

$MW_{water}$  : water molecular weight (18.02 gm/mol),

$N_{water}$  : number of water molecules per unit cell (46 for sI, 136 for sII, 34 for sH),

$MW_{gas}$  : gas molecular weight (based on the type of gas molecules inside the cavity in gm/mol),

$N_{gas}$  : number of gas molecules per unit cell,

$V_{unitcell}$  : volume of one-unit cell,

$N_a$  : Avogadro's number (6.022 x 10<sup>23</sup> mol<sup>-1</sup>).

Heat capacity, or specific heat of a material is a thermal property which is defined as the amount of heat required to change a body's temperature by a given amount. The specific heat of hydrate should be measured under expected process conditions owing to the fact that gas hydrate heat capacity grows with temperature [Giavarini and Hester, 2011].

The thermal conductivity which measures the ability of diffusion heat via molecular collisions, and the thermal expansivity which is the tendency of matter to change in shape, area, and volume in response to a change in temperature are more like a glass than ice crystal for hydrates due to the occurrence of gas molecules in the cages [Giavarini and Hester, 2011].

The strength of methane hydrate is compared with ice experimentally at temperatures just below the ice point by considering the deformation period. It is inferred that methane hydrate at a given strain rate is twenty times stronger than ice (Ih) [Durham et al., 2003].

Gas hydrates are electrical insulators which have a high resistivity against flowing electric current through it. This property allows for predicting the location where gas hydrates are occupied by reason of the increase in electrical resistivity in the gas hydrate stability zone [Giavarini and Hester, 2011].

### 1.3. Gas Hydrates as an Energy Source

Gas hydrates are considered as a valuable energy source in connection with its abundance across the world [Ruppel, 2011] and the capacity of holding a sizeable amount of gas inside its cavities. One  $\text{m}^3$  of gas hydrate contains up to  $164 \text{ m}^3$  gas and  $0.8 \text{ m}^3$  water (Figure 1.4) at standard conditions [Kvenvolden, 1993], suggesting that great amount of energy can be stored that is ideal for storage and transportation.

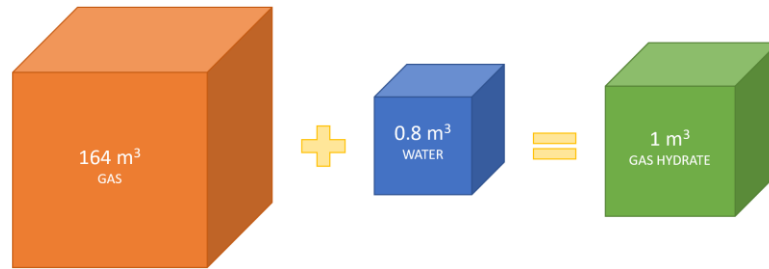


Figure 1.4. Visual proportions of the constituents of  $1 \text{ m}^3$  of gas hydrate at standard conditions

### 1.4. Techniques for Characterization of Gas Hydrates

The first method used in order to characterize gas hydrates is the X-ray (neutron) diffraction technique. In this method, X-rays are directed into a crystalline sample in order to observe the density of hydrate and ice peaks to gain information of the amount of gas hydrates [Giavarini and Hester, 2011].

Nuclear magnetic resonance spectroscopy is another technique to examine gas hydrate properties. This method is based on the observation of the absorbed radiation frequency of gas hydrate sample placed in a static magnetic field [Giavarini and Hester, 2011].

One of the direct sampling procedures for studying gas hydrates is the Raman spectroscopy technique which is used to observe the change related to absorption of laser photons by molecular vibrations by means of a laser focusing on a hydrate sample [Giavarini et al., 2011].

Bottom simulating reflection (BSR) which is a remote sensing technique is another way to explore gas hydrate presence. These seismic reflections mark the interface between the higher sonic velocity which is seen where the gas hydrate located and the lower sonic velocity [Kvenvolden, 1993].

Wire line logs can also be used for gas hydrate detection seismically [Hornbach et al., 2003]. Well logs for gas hydrate studies include caliper, gamma ray, spontaneous potential, resistivity, sonic velocity, and neutron porosity [Goodman, 1982].

The last practice for hydrate studies is modulated differential scanning calorimetry which measures variations in enthalpy as a function of temperature during controlled heating and cooling cycles [Giavarini and Hester, 2011].

### 1.5. Methods to Obtain Gas from Gas Hydrates

De-pressurization is a method based on the principle of decreasing pressure in the free-gas zone right under the gas hydrate stability zone and provide the movement of the released gas first to free-gas zone and then upward through a well bore [Max and Cruickshank, 1999]. This method is useful to be able to obtain gas from huge volume of gas hydrate rapidly [Ruppel, 2011]. The disadvantages of this technique are the requirement of high porosity hydrate deposits and the risk of hydrate reformation during the transportation toward the pipeline [Chatti et al., 2005].

Another way of attaining gas from gas hydrate is thermal stimulation which aims to raise of the gas hydrate stability zone temperature and provide gas from decomposed hydrate by injecting heated fluid as a direct method or via electric or sonic means as an indirect method [Demirbas, 2010].

Inhibitor injection is one of the approaches of obtaining gas by dissociating gas hydrate. In this process, chemical inhibitor is injected into the gas hydrate stability zone in order to shift the pressure-temperature equilibrium of hydrate formation and prevent gas hydrate stability [Desa, 2001].

The injection of gas such as carbon dioxide (CO<sub>2</sub>) into the gas hydrate stability zone via a pipe leads to a surge in pressure because of the bubbles of the inserted gas and provide an upward flow to hydrocarbon gas towards the surface which has lower pressure [Ohta, 2002].

### 1.6 Potential Applications of Gas Hydrates

A potential approach to recovering gas hydrates is through capture and sequestration of CO<sub>2</sub> and its transfer to hydrates deposit. CO<sub>2</sub> capture and storage are significant in order to reduce CO<sub>2</sub> emissions from the use of fossil fuel and its impact on global warming [Meysel et al., 2011].

Although it has negative effect on climate change, CO<sub>2</sub> is an important raw material [Gbaruko et al., 2007]. CO<sub>2</sub> is captured either from the industrial sources, concentrated into a nearly pure form, and then pumped deep underground geological formations or oceans, or from the atmosphere by enhancing natural biological processes that sequester CO<sub>2</sub> in plants, soils, and marine sediments. After the separation of the CO<sub>2</sub> from the other gases, it must be compressed in an effort to change its phase from gas to liquid and transported through pipeline or ship to the storage location where gas hydrates are located [Benson and Orr, 2008].

Gas hydrates are also preferred as a useful method for the process of separating mixed gases [Zarinabadi and Samimi, 2012]. The separation takes place by taking advantage of difference between the gas molecule diameters. Hydrate cages can contain certain diameter of gases based on the structure type of gas hydrate. Mixed gases with different molecule diameters can thus be separated.

Gas hydrates are also used so as to store and transport natural gas thanks to its capability of consisting a high gas concentration [Eslamimanesh et al., 2012]. The main advantage of using gas hydrate for storage and transportation of natural gas is that hydrates have very high gas to solid ratio. Since 1 m<sup>3</sup> gas hydrate may contain up to 180 m<sup>3</sup> of natural gas depending upon the production pressure and temperature, a higher amount of natural gas can be stored and transported by capturing it into the hydrate structures [Gudmundsson et al., 2002]. Lower investment in infrastructure and equipment provide economic advantage to the storage and transportation of natural gas in the form of gas hydrate [Javanmardi et al., 2005].

Cool reservoir is one of the most important application areas of gas hydrates. It is significant to meet the increasing demand to electric power. The cold storage technology can be applied to the air conditioning and refrigeration systems by using gas hydrate [Chatti et al., 2005, Wang et al., 2015]. CO<sub>2</sub> hydrate is one alternative way used in the refrigeration process in the form of clathrate hydrate slurries as a two-phase (solid-liquid) refrigerant. These two-phase refrigerants are phase change materials with the high latent heat of fusion and so more energy efficient than single-phase refrigerants. Instead of using mechanical methods, the heat of dissociation of CO<sub>2</sub> hydrates can be generated by direct gas injection into an aqueous solution as in the case of ice slurries. CO<sub>2</sub> hydrate slurries can also be used in air conditioning systems since the melting temperatures of some clathrate hydrates are consistent with the temperature needed in this type of applications [Akiya et al., 1997].

Gas hydrates are also good candidates as Phase Change Materials (PCM) which are effective in storing thermal energy using latent heat storage [Castellani et al., 2016]. The use of gas hydrates as PCM in buildings reduces the temperature fluctuations, particularly due to incident solar radiation loads [Ibanez et al., 2005]. Gas hydrates have a potential in terms of improving the reduction of hours in which the indoor temperature exceeds the comfort range and reducing energy consumption for cooling [Castellani et al., 2016].

### 1.7. Gas Hydrates as an Operational Problem

Gas hydrate is also called “clathrate” which is from the Greek word “khlatron” meaning barrier [Chatti et al., 2005]. Although gas hydrate is of potential benefit as a significant hydrocarbon energy source and has important application areas, it represents a severe operational problem as the hydrate crystals deposit on pipe walls and accumulate as large massive chunks resulting in blocked pipelines due to the fact that the region where pipelines are located has the suitable conditions for hydrate formation [Obanijesu et al., 2010]. The hydrate deposition within a pipeline was revealed in a natural gas pipeline by Hammerschmidt in 1934 [Chatti et al., 2005]. The potential of hydrate occurrence within a petroleum pipeline system during the production and transportation has increased as oil and gas companies have been producing in deeper and colder environments since 1970s due to the increase in the world demand for energy [Sinquin et al., 2004, Theyab, 2018].

In the normal production process, there is a steady flow of crude oil at high operating pressure which ranges from 10,000-30,000 psi and high operating temperature which reaches to 177 °C [Lu et al., 2011]. The relatively cold surrounding seawater induces a huge quantity of heat loss from high temperature fluid flowing within a long pipeline production system. The resultant high pressure and low temperature condition causes the risk of hydrate formation [Hu et al., 2015].

Hydrate problems can appear during normal production process, but transient operations are often more vulnerable [Ellison et al., 2010]. Especially restart operations have a huge risk of hydrate occurrence since the stagnant multiphase hydrocarbon fluid inside the pipe cools down to the environment temperature during shut-down. Besides, the components of the fluid separate since the gravity forces are more dominant than the viscous forces during the time of stagnation. When the extraction process restarts, separated free water meets hydrocarbon, forms hydrate under the high pressure and low temperature conditions and plugs the pipe [Sloan and Koh, 2007]. Increase in the pressure difference between upstream and downstream leads the



acceleration of the solid hydrate plug and serious damages on production facilities and personal safety [Mokhatab et al., 2007, Jassim et al., 2010]. That is why in extreme hydrate challenges, the production stoppage is needed for security.

Hydrate formation process starts with the occurrence of some hydrate particles on the colder pipe walls. These small particles come together in time and form hydrate slugs by spreading to the center of the pipe. During the whole process from hydrate particle appearance to the blockage of the pipe, the fluid velocity decreases by the effect of the resistance of solid hydrate particles [Wang et al., 2008]. While these initial plugs can be permeable to gas, they usually prevent liquid phase to flow through the pipeline. Transmission of gas phase through the hydrate deposit can lead to the Joule-Thomson cooling and further occurrence of gas hydrate. Numerous examples also exist of hydrates forming during the Joule-Thomson cooling of gas, for instance as it expands across a valve.

The removal of hydrate plugs in subsea pipeline system is dangerous, in addition to the loss of time and money [Wilkens, 2002]. It is highly important to provide flow without any interruptions for oil and gas industries in terms of a successful production [Mokhatab et al., 2007]. It is crucial to figure out which parts of a pipe system are hazardous corresponding with plugging by hydrates and take needed precautions, and when hydrate plugs can form to prevent solid formations [Sloan et al., 2009].

Flow assurance is a case which refers to the safe, efficient and economic flow of multiphase hydrocarbon stream from reservoir to the point of sale through the pipelines of oil and gas production systems. Petrobras mentioned the term of flow assurance as “portuese as garantia do escoamento” which means “guarantee of flow” for the first time in the early 1990s [Irmann-Jacobsen, 2012]. Challenging flow assurance and field development issues affect both well completion design and production operation strategies [Theyab, 2018]. Flow assurance issues include wax, asphaltene, scale, slug, naphthenate, corrosion, erosion and emulsion besides hydrate [Kutlik and Allen, 1998]. Because hydrate is promoted at a rapid formation relative to wax, scale, or asphaltene, the largest concern on the reason of a pipeline blockage is hydrate [Shuard et al., 2017]. Flow assurance is considered in every stage of production including system design, surveillance, troubleshooting operation problems, increased recovery in late life, etc. [Tarek, 2007, Bauck, 2013]. The tentative zones of solids deposition, amongst others, are near wellbore region, production tubing, subsea wellhead, subsea flow lines, and separators [Joshi et al., 2003].

## 1.8. Solution Techniques of Formation and Accumulation of Gas Hydrates

The common purpose of the prevention methods of gas hydrates is removing at least one of the factors which helps hydrate formation. The four main reasons for the occurrence of solid hydrate crystals are high pressure, low temperature, water droplets and gas molecules. Since gas molecules cannot be avoided, it is the product intended to drill, removing water and maintaining the pressure and temperature conditions outside the hydrate formation envelope [Mokhatab et al., 2007] is the logical approach. Hydrate formation (phase) envelope which is a line created based on pressure and temperature values represents the appropriate conditions for hydrate formation resulting in a closed area [Pedersen et al., 2006]. Hydrate formation prevention or removal techniques can be analyzed under four principal approaches which are hydraulic removal methods, thermal methods, chemical methods and mechanical processes [Chatti et al., 2005].

The permanent prevention method is removing of water phase from the hydrocarbon fluid by using an offshore dehydration plant or subsea separation. Nevertheless, these methods are not cost-effective [Leontaritis, 2000]. Hydraulic removal can also be provided by depressurization process. However, it is not applicable to liquid hydrocarbons due to the high possibility of vaporization [Chatti et al., 2005].

Thermal methods are based on preventing heat loss from the pipeline system to the environment or heating the production line to keep the temperature above hydrate formation temperature. One way for this objective is insulation. Insulation might be an effective way in order to avoid hydrate formation by preventing heat loss as long as the fluid within the pipe, the tie back distance, and topsides capabilities of host platform are appropriate for applying this method. Although, it generally averts hydrate formation under normal operation conditions, it is inadequate during a long-term shutdown and restart durations and also heat loss owing to the Joule-Thomson effect [Mokhatab et al., 2007]. The Joule-Thompson effect (expansion) is a reduction in expanded-gas temperature under the condition of constant enthalpy due to a decline in pressure [Marić, 2005]. There is a range of thermal insulation materials available for subsea pipeline system. It is significant to consider several application criteria, which are thermal conductivity, density, flexibility, toughness for handling and application method, for the selection of appropriate insulation material [Kroes, 2013]. For subsea equipment applications, wet thermal conductivity corresponding to operating subsea pressure and temperature must be considered in designing the required thickness and geometry. Wet insulation materials which are typically polyurethane, polypropylene, rubber, or glass reinforced plastic have the heat transfer coefficient limited to approximately  $2 \text{ W/m}^2\text{K}$ . Thermal insulation dry density impacts the overall insulated equipment

weight in air. Dry insulation, such as polyurethane foam or rockwool, can achieve lower heat transfer coefficient values of approximately  $1 \text{ W/m}^2\text{K}$  [Offshore Magazine, 2002]. Wet density combined with water absorption affects both thermal and mechanical properties [Kroes, 2013]. The presence of water degrades the performance of dry insulation, so a pipe-in-pipe system which can reduce the heat transfer coefficient up to  $0.5 \text{ W/m}^2\text{K}$  is required to ensure lower heat loss from the system [Offshore Magazine, 2002]. Pipeline burial at a certain depth or gravel dumping over the pipeline can also have an isolating effect [Lee, 2009]. For many deep-water and long-distance applications, lowering the heat transfer coefficient value by insulating the system components may not be adequate to keep the temperatures higher than the hydrate formation temperature. To overcome the limits of the passive insulation systems, active insulation systems which are hot water circulation (hot water jacket) and electrical resistance heating system can be preferred to maintain the high temperature of the system [Offshore Magazine, 2002]. The risk of corrosion can be considered one of the disadvantages of having insulation material in the system. Besides, it might be costly to insulate whole pipeline system based on the size of the system and the environmental conditions.

High pressure condition which is one of the reasons for hydrate formation can be wiped out by depressurization which refers to operating the system at a pressure less than the hydrate formation pressure. Rapid depressurization should be avoided, as it can lead to Joule-Thomson cooling, which can worsen the hydrate formation [OILFIELDWIKI, Hydrate Remediation, no date]. This approach may not be practical in long production pipelines where the high pressure is needed to extract the hydrocarbon fluid. The other prevention method with regard to pressure is adding inhibitors to the pipeline in order to keep operating pressure out of the hydrate formation suitable conditions. The objective of this method is increasing the required pressure to form hydrate for the same temperature and so prevent the hydrate formation.

Another way of the hydrate prevention is keeping the temperature out of the hydrate formation region. This goal can be achieved by adding chemical inhibitors which results in shifting the hydrate equilibrium line to the left. It means that the lower temperature is needed for hydrate formation in the same pressure condition [Esteban et al., 2000].

Thermodynamics and low dosage hydrate inhibitors are studied under chemical methods of hydrate formation prevention. Hydrate growth velocity decreases with adding such chemical inhibitors by affecting the hydrate stability pressure and temperature. This decrease is dependent on the kind and density of the inhibitor [Samimi, 2012]. These chemical inhibitors are injected to the pipeline to provide unfavorable conditions for gas hydrate formation. The essential points to

consider selection of chemical inhibitors are price, physical properties, safety, corrosion effect, gas dehydration capacity and recyclability [Mokhatab et al., 2007]. The chemicals which are methanol, ethylene glycol, diethylene glycol etc. are called thermodynamic inhibitors [Esteban et al., 2000]. Thermodynamic inhibitors can effectively prevent hydrate formation by reducing water activity and shifting the pressure-temperature hydrate equilibrium line. On the other hand, the need of large volume of thermodynamic additives leads to high cost and raises environmental and logistical concerns [Yang and Tohidi, 2011]. The working principle of low dosage hydrate inhibitors is related to interfering the formation of gas hydrate at the early stage by modifying the rheological properties of the system [Sinquin et al., 2004]. Low dosage hydrate inhibitors act at the early stages of hydrate formation by modifying the rheological properties of the system, but not changing the thermodynamic conditions of the system [Sinquin et al., 2004]. The low dosage hydrate inhibitors are divided in two types which are kinetic hydrate inhibitors and anti-agglomerants. Kinetic hydrate inhibitors may prevent crystal nucleation or growth during the extraction and transformation of the hydrocarbon fluid. How long the kinetic inhibitor can delay hydrate formation depends on the depth where the pipeline is located corresponding with the environment temperature. Contrary to kinetic hydrate inhibitors, anti-agglomerants, which are surface active chemicals do not prevent the formation of hydrate crystals but keep the particles small and well-dispersed. Thus, the hydrates to be transported along with the produced fluid. Unlike kinetic hydrate inhibitors, anti-agglomerants performance is relatively independent of time, and they are more effective at extreme operating conditions [Frostman, 2000]. On the other hand, they are only applicable at lower water cut which means the water fraction in a multiphase mixture between 40 and 50 %. This limitation is caused by the rheological properties of suspensions with high solid fraction and may depend on flow regime conditions. Deployment of low dosage hydrate inhibitors is a complex operation that must be carefully prepared in order to prevent any side effects that could compromise normal production operations or the efficiency of additional chemical treatments [Frostman and Crosby, 2003].

Cold flow is another practice whose idea is to form “dry” hydrates in a controlled way. These types of hydrates move with the fluid through the flow direction and so do not cause blockages at any part of the pipeline [Irmann-Jacobsen, 2012]. The treatment of this method is cooling the fluid temperature around the seawater temperature in a mechanical device. Generally, the hydrate appearance temperature of is greater than the seawater temperature. As a result, certain amount of hydrate precipitates and transports as a slurry along with the associated liquid.

If hydrate forms despite of prevention strategies, “mechanical pigging” can be used not to prevent hydrate formation but clean the pipeline by removing the hydrate accumulation in order to provide continuous flow within the pipe. The method involves a moving large disk, or a spherical or cylindrical device made of a flexible material having an outside diameter nearly equal to the inside diameter of the pipe [Sørheim and Gudmundsson, 2005]. Since shutting down the system is needed to be able to apply this method, it is not the best way to avoid hydrate formation due to the fact that it is time and money consuming [Sami et al., 2013].

## 1.9. Closure

It light of the above background on gas hydrates and its associated operational problems in pipelines, the present investigation aims at specifically studying the topic of oil separation and its accumulation within a dead-leg segment of a subsea pipeline carrying a two-phase fluid of oil and water. A combination of computational and experimental techniques will be utilized.

Chapter 2 will be devoted to a survey of literature on the topic. Two- and three-dimensional versions of the model problem will be identified in Chapter 3. The multiphase governing equations will be presented along with an overview of the open source computational fluid dynamics (CFD) code called OpenFOAM that will be utilized to solve these transport equations. Benchmarking of relevant simpler problems using OpenFOAM will be briefly discussed.

Chapter 4 will present results of CFD analysis of both transient 2-D and 3-D computations of a baseline 90%-10% oil-water mixture as an ideal model for oil originating from a subsea reservoir. For the 2-D case, a parametric study of geometric and fluid properties will be presented. Limited 3-D results of similar phenomenon in realistic pipelines will be discussed.

Chapter 5 is devoted to conceptualization, design, construction and testing of a lab-scale two-phase flow loop in order to provide visual observations of oil separation and its accumulation in a dead-leg with varying inclination angle that can then be compared to computational findings.

Conclusions of the present investigation will be outlined in Chapter 6, followed by the References and Appendices.

## 2. Literature Review

In this Chapter, highlights of prior computational and experimental studies of multi-phase flows including dead-legs and sealed T-branches are reviewed in a chronological order. Emphasis is placed on surveying the range of computational analyses and/or experimental approaches that have been adopted to date. It will be noticed that the survey of literature is exclusively based on model studies and no reports based on actual field data measurements are available.

### 2.1. Descriptions of Previous Research Studies

The impact of the length of a dead-leg on the velocity vectors and flow separation of crude oil-water two-phase flow was studied by Habib et al. (2005). With the purpose of observing how the dead-leg's length affects the flow behavior, four different length/diameter ratios of 1, 3, 5 and 7 were considered. The diameter of the dead-leg was 0.1 m, while the diameter of the horizontal pipe was 0.3 m. The homogenous mixture consisted 90% oil and 10% water flowing with 1 m/s average velocity in all cases. The continuity and momentum equations were solved for the mixture under the steady-state condition. The fluid properties of immiscible components were calculated based on the algebraic slip mixture model. The velocity was set to be zero at the pipe walls with regard to no-slip condition. Turbulence variables were calculated based on the standard  $k-\varepsilon$  model. The simulations performed to investigate the influence of the dead-leg length on the velocity vectors showed that as the length to diameter of the dead-leg grew, the size of the stagnant zone(s) where the fluid is motionless increased (Figure 2.1).

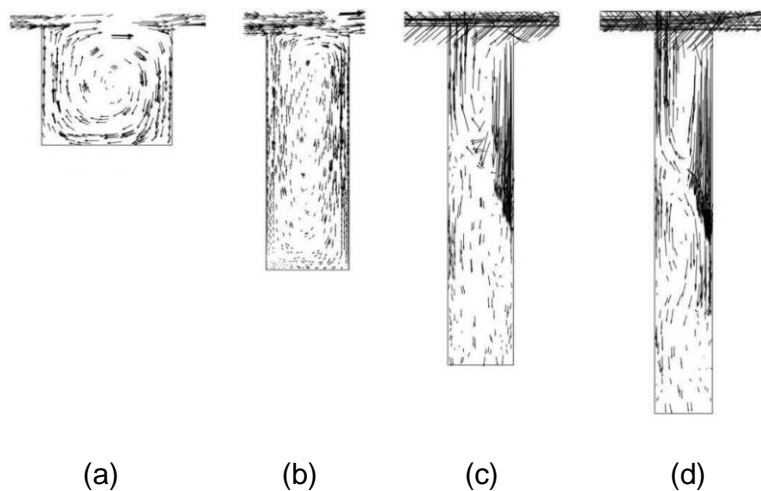


Figure 2.1. Size of the vortices within dead-legs: (a)  $L/D=1$ , (b)  $L/D=3$ , (c)  $L/D=5$  and (d)  $L/D=7$   
[Habib et al., 2005]

While the velocity vectors were maximum around the center of the dead-leg whose length was equal its diameter, lower velocity was observed at the center of the dead-leg due to the presence of a vortex. As the ratio of the length to diameter surged, the velocity became lower and lower toward the upper part of the dead-leg. The drop-in velocity caused a rise in the size of the stagnant region. The other significant outcome was that the water concentration accumulated at the bottom of the dead-leg increased with the increase of the ratio of the length to the diameter of the dead-leg (Figure 2.2).

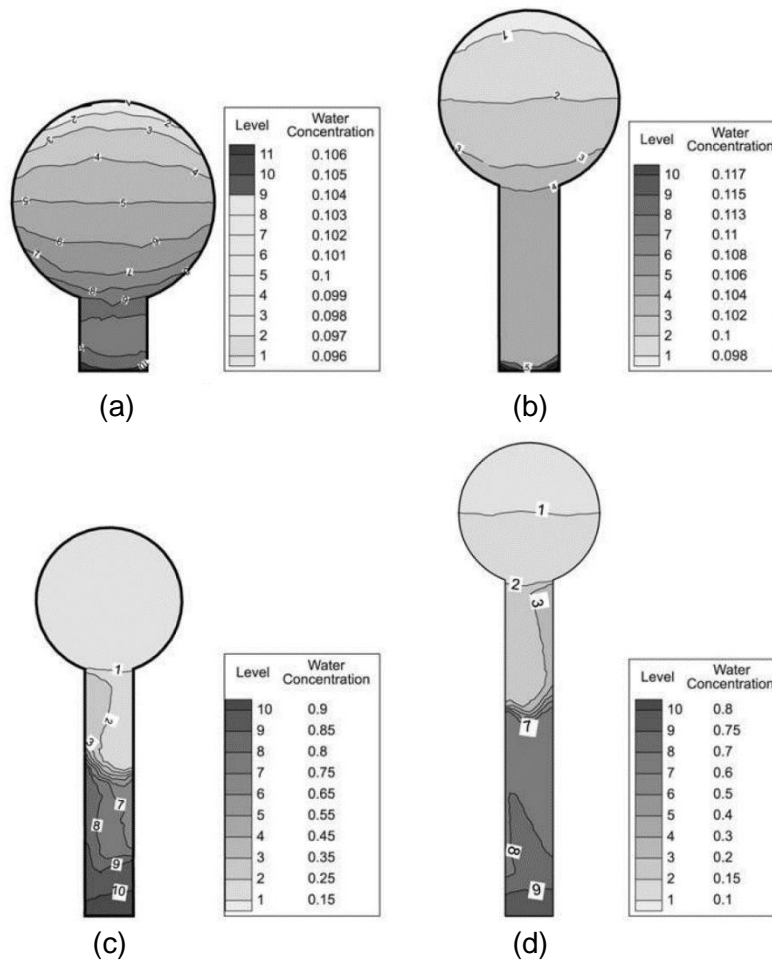


Figure 2.2. Volumetric concentration of water within different size dead-legs: (a)  $L/D=1$ , (b)  $L/D=3$ , (c)  $L/D=5$  and (d)  $L/D=7$  [Habib et al., 2005]

This segregation of crude oil and water phases was not obvious for the case for which the ratio of the length to the diameter is 1, since the strong vorticity prevented water to go down even though the gravity force was present.

Andersen (2007) conducted a 3-D computational a study to observe temperature and velocity profiles for a non-compressible ideal gas in an uninsulated submerged dead-leg. Single-phase forced, and natural convection simulations were conducted in this study aimed at correlating the length of the recirculating vortices driven by the flow in the main horizontal pipe with possible hydrate formation in the system. The generally inactive part of a pipeline system called a “dead-leg” was chosen as the geometry of interest because of its vulnerability to hydrate formation. The base geometry was developed as a straight horizontal pipe with a 90° branch pipe with the same diameter attached to it (Figure 2.3).



Figure 2.3. Schematic diagram of the dead-leg model [Andersen, 2007]

The length of the straight horizontal pipe before the dead-leg was chosen to be 20 times that of the pipe diameter in order to provide a fully-developed flow before the branch. A steel plate was located at the end of the branch to simulate the access port of the dead-leg section. The reason for using a steel plate instead of a valve which is used in practice was to enable easier modelling. Eight separate CFD simulations were performed utilizing the Fluent 6.2.16 CFD package with pipe inlet conditions of the natural gas corresponding to the pressure at 10 MPa abs and the temperature of 338 K. The simulations were performed for different cases: mass flow rates at 6 and 26 kg/s, average fluid velocities at 2.2 and 9 m/s, and pipeline to sea water heat transfer coefficients of 580 and 1100 W/m<sup>2</sup>K for both vertical and horizontal orientations of the dead-leg segment. Free convection was assumed not to have an important influence on the flow pattern for the case of the horizontal dead-leg. A high-*Re* number form of the *k-ε* turbulent model was used in all flow simulations. Besides, a re-normalization *k-ε* turbulent model was



applied to simulate the buoyancy effects for cases with the vertical closed top cylindrical geometry of the branch dead-leg. Regarding the results of the simulations, it was inferred that the vertical dead-legs were more susceptible to reaching the hydrate equilibrium temperature because of higher heat loss stemming from formation of the recirculating vortices within the branch and the velocity fluctuations throughout the dead-leg (Figures 2.4 and 2.5).

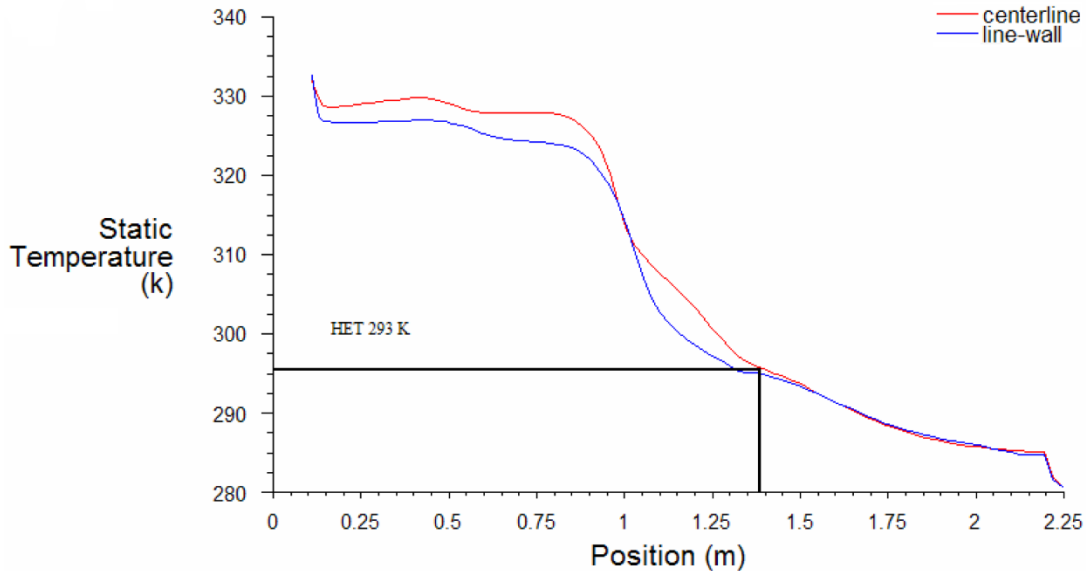


Figure 2.4. Temperature profile along the centerline and line wall in the vertical dead-leg (1,100  $W/m^2K$  heat transfer coefficient) [Andersen, 2007]

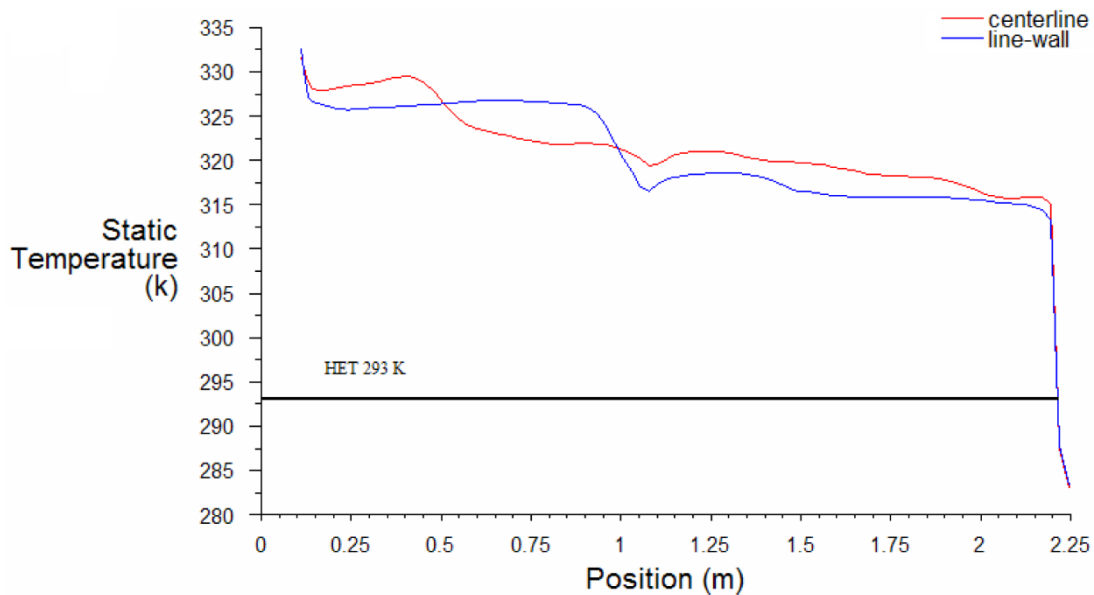


Figure 2.5. Temperature profile along the centerline and line wall in the horizontal dead-leg (1,100  $W/m^2K$  heat transfer coefficient) [Andersen, 2007]

For the case of the vertical dead-leg configuration, warm gas from the main pipe was prevented from replacing the cold gas in the branch. Consequently, the higher possibility of hydrate formation was observed in this colder region of the pipeline system. Thus, it was concluded that horizontal dead-leg configuration was preferable in order to avoid gas hydrate formation.

Dissociation process of methane hydrate under pure freshwater flow was investigated by Sean et al. (2007) by carrying out a 3-D computational and experimental study on an incompressible three-phase system which were hydrate, liquid water and vapor fluid flow in a cylindrical tube. The inlet boundary condition was defined as a fully-developed laminar cylindrical Poiseuille flow, and the zero-gradient Neumann boundary condition was imposed for the outlet boundaries. The pipeline walls and the surfaces of the methane hydrate were assigned the no-slip condition. The convection terms and the diffusion terms were discretized by a third-order upwind scheme, and a second-order central differencing scheme, respectively. A second-order explicit scheme was preferred to approximate the unsteady terms. Pressure and velocity were coupled based on the marker and cell (MAC) fractional step method. With respect to the simulations which were conducted under the conditions of the water pressure of 7 MPa and the water temperature of 280.15 K, and the initial hydrate temperature of 253.15 K, the temperature gradient inside the methane hydrate was getting higher from the center towards the wall of the methane hydrate (Figure 2.6).

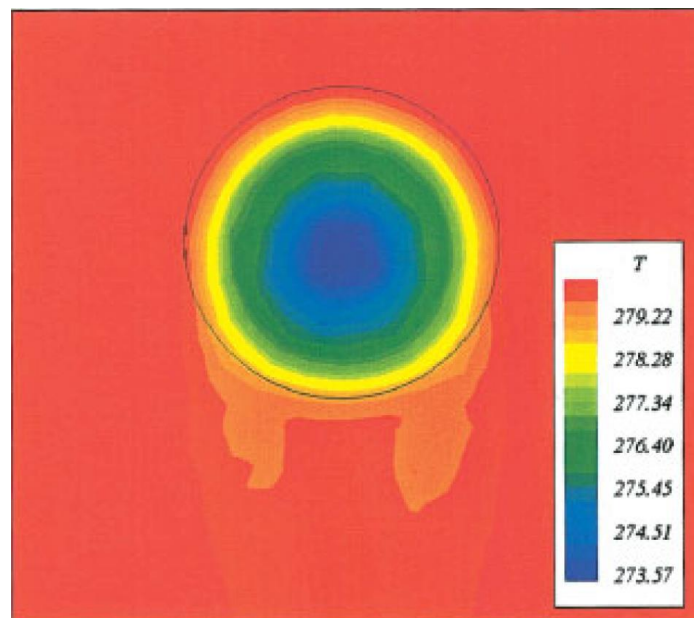


Figure 2.6. Contour map of the temperature field [Sean et al., 2007]

Since the surface temperature of the hydrate was almost identical with the surroundings, the dissolution process was assumed to be isothermal and heat transfer was ignored. The other important consequence was that whereas the hydrate dissociation rate was found to be dependent on the temperature, the pressure and the flow rate had limited effect on it. Besides, the distribution of the methane gas inside hydrate formation was not homogeneous.

Nazridoust and Ahmadi (2007) performed a 3-D computational study on methane hydrate dissociation in a sandstone core by using the volume-of-the-fluid method. They focused on the dissociation process of hydrate including the rate of dissociation, the amount of absorbed heat, the generated gas and water, the effects of relative permeabilities of water and gas and effective porosity of the core, and time evolutions of temperature and pressure profiles, as well as the cumulative amount of natural gas production for different core initial temperatures and various outlet valve pressures. An axisymmetric core model with the length of 30 cm and the diameter of 5.1 cm was studied with multiphase flows composed of methane hydrate, methane gas (ideal gas) and liquid water inside it (Figure 2.7).

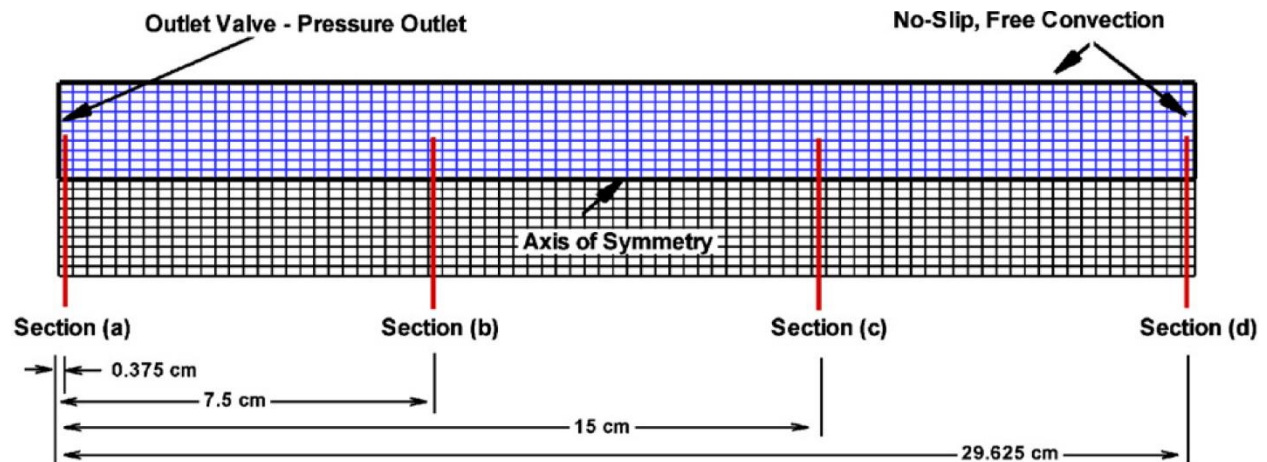


Figure 2.7. Schematic diagram of the hydrate core system [Nazridoust and Ahmadi, 2007]

The dissociation was an endothermic process. The convection heat transfer coefficient was 16.6 W/m<sup>2</sup>K between the core and the surrounding. The initial core temperature and the initial pressure were assigned to be 275.45 K and 3.75 MPa, respectively. The simulations were made for four different cases with the diverse ambient temperature and the outlet valve pressure. Case 2 (275.15 K, 2.84 MPa) was considered as the reference case in order to be able to

compare the outcomes of case 2 to the results obtained from the other cases and the experimental data. The influences of the change in the ambient temperature on the gas hydrate dissociation was shown with case 1 (274.15 K, 2.84 MPa) and case 3 (276.15 K, 2.84 MPa), whereas case 4 (275.15 K, 2.99 MPa) and case 5 (275.15 K, 3.28 MPa) served investigating how the outlet valve pressure impacts hydrate dispersal. When the initial pressure decreased below the hydrate equilibrium pressure after the outlet valve opened, hydrate started to dissociate by absorbing of heat with convection. During the entire process, while hydrate saturation was becoming lower, gas and water saturation became higher. Since the dissociation process was endothermic, the surrounding temperature of hydrate formation reduced. When gas hydrate dissociation was completed, the core temperature started to increase until reaching the surrounding temperature. The other important observation was that as hydrate dissociated, the permeability and the porosity of the core increased. When case 1 and case 3 were considered with the reference case 2, it was seen that the increase in surrounding temperature led to growth in the heat transfer and the dissociation speed of gas hydrate. From this information, in the event that the surrounding temperature rose, the drop in the core pressure would be faster. The case 4 and case 5 with the reference case 2 were simulated to gain insight about how the outlet valve pressure impacted to the rate of hydrate dissociation. The simulation results showed that the increase in the outlet valve pressure gave rise to decrease in the hydrate dissociation rate. The general conclusion was the finding that higher surrounding temperature and lower outlet valve pressure accelerated the gas hydrate dissociation.

Fatnes (2010) reported a 3-D Euler-Euler computational study with the purpose of observing hydrate particles accumulation and bed formation during a water-hydrate multiphase flow within a 90-degree bend with 45.2 mm diameter, 450 mm horizontal length, 200 mm vertical length and 105 mm radii (Figure 2.8).



Figure 2.8. 3-D CAD model of the test section of the flow loop [Fatnes, 2010]

The bend dimensions were chosen the same with a part of an experimental set-up of Balakin et al. (2008) to be able to compare the outcomes obtained from the ANSYS code with the experimental data for validation. One of the components of the fluid was water as a continuous phase with the density of  $1000 \text{ kg/m}^3$ , the molar mass of  $18.02 \text{ g/mole}$  and the dynamic viscosity of  $0.001 \text{ Pa s}$ . The other component was hydrate as a dispersed phase with the density of  $1140 \text{ kg/m}^3$ , the molar mass of  $137 \text{ g/mole}$  and two different viscosities which were defined based on the Roscoe-Brinkmann correlation and the expression derived by Krieger-Dougherty (1959). The viscosity of solid hydrate particles had a significance effect on the fluid velocity. The higher solid hydrate viscosity led to the lower fluid velocity. The results achieved from both expressions for the viscosity of solid hydrate were almost the same. The turbulent, isothermal flow was chosen to be inhomogeneous which means that the velocities and turbulence models of the dependent phases are supposed to be defined separately. Hence the zero-equation algebraic turbulence model and the  $k-\varepsilon$  turbulence model were used for the dispersed and continuous phases, respectively. The inlet boundary conditions were set up based on the velocities and fractions of both phases, while the atmospheric pressure was defined at the outlet boundary condition. The velocities of both phases were specified as zero at the walls by setting the no-slip condition. The wall-function approach was applied for the accuracy of turbulent flow near the walls. The Second Order Backward Euler numerical scheme was adopted as the transient scheme, which is a first order scheme for turbulence equation, while a bounded second order scheme for volume fraction was adopted. A coupled solver in the ANSYS CFX package was used for the solution of the hydrodynamic equations as a single system. The Gidaspow drag model [Gidaspow, 1994] was used to consider the interphase drag force between the solid hydrate and liquid water phases. Two separate particle collision models which were the kinetic theory model and the Gidaspow solid pressure model were simulated to gain insight about the bed formation with respect to the mean flow velocity ranging between  $0.1\text{-}1 \text{ m/s}$ . As a common result of both methods, it was shown that the hydrate bed thickness was conversely proportional to the fluid mean velocity. In addition, an apparent concentration gradient between the top of the bed and the homogeneous suspension was seen at very low flow velocities. Although there was not an enormous difference between the results of both models, the solid pressure model was preferred for the other simulations due to improved convergence. According to Mühle (1993), the particle size changes in connection with flow parameters and cohesive properties. The particle size has a key role on the hydrate agglomeration and bed thickness. The dispersed hydrate particles sank to the bottom of the pipe when the gravity force is higher than the combination of the drag force and buoyancy. Koroos et al. (2013) stated that since the gravity

force has more impact on bigger particles, the rate of falling particles will increase. Consequently, the larger the particle size, the more particles were located at the bottom, and the higher deposition and bed thickness was observed. This finding was improved with the simulations conducted based on the solid pressure particle collision model, the Roscoe-Brinkmann correlation for the solid viscosity and 0.2 m/s mean flow velocity. It was also determined that the hydrate particles were exhibiting a tendency to accumulate at the outer section of the bend due to centrifugal effect of the fastest fluid which was observed at the inner part of the bend (Figures 2.9 and 2.10).

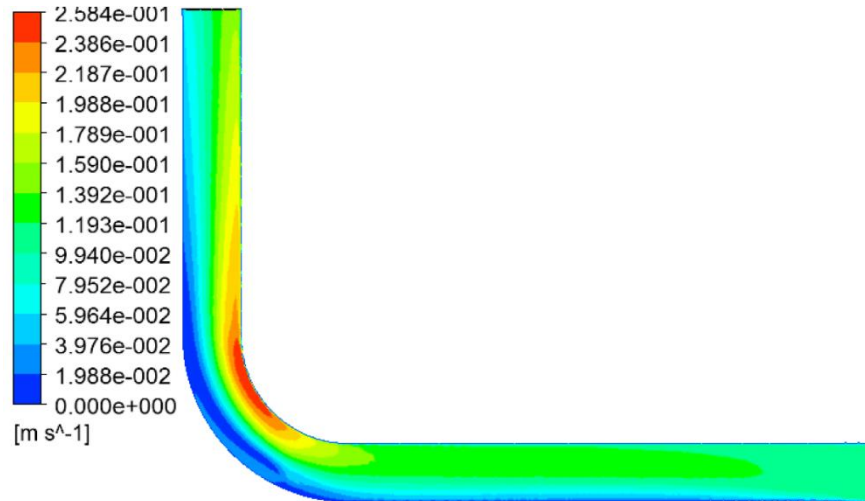


Figure 2.9. Contours of the continuous phase velocity on the midline cross section of the pipe [Fatnes, 2010]

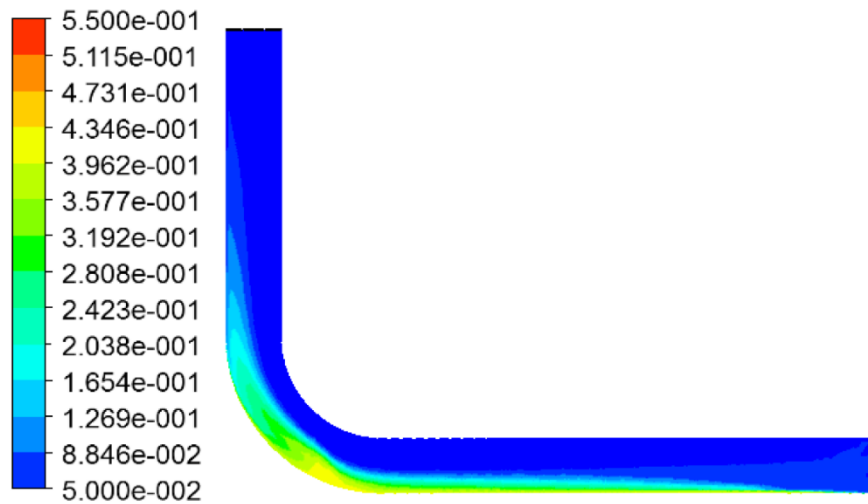


Figure 2.10. Contours of the hydrate formation fraction on the midline cross section of the pipe [Fatnes, 2010]

Balakin et al. (2011) carried out an experimental and 3-D computational study by using the transient Eulerian-Eulerian model to analyze gas hydrate deposition in turbulent and isothermal flow in a pipeline loop which had a diameter of 45.2 mm and three 90° bends (Figure 2.11).

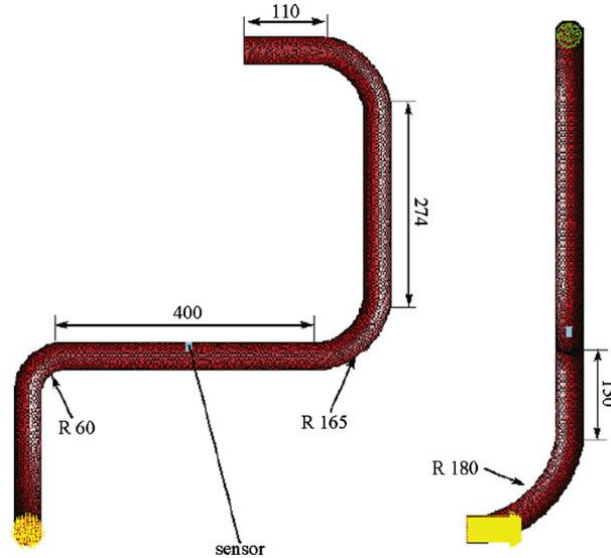


Figure 2.11. 3-D CAD model of the flow loop section with dimensions in mm [Balakin et al., 2011]

Trichlorofluoromethane (Freon R11) hydrate which is stable up to 8.35 °C at atmospheric pressure combined with water was specified as a homogeneous fluid. Since the fully-developed flow was not obtained in the experimental study due to the lack of the adequate length after the pump, the velocity profile was not uniform. The standard  $k$ - $\epsilon$  turbulent model was employed. The inlet boundary conditions involved specifying values of  $k$  and  $\epsilon$ , whereas the outlet boundary condition was chosen to be a standard outlet. The initial velocity was zero under the atmospheric pressure, and it was increased during the experiments up to a maximum of 3.9 m/s and then brought back to zero velocity. The no-slip boundary conditions were defined at the inner surfaces of the pipeline. In consequence of the experimental and computational studies, it was deduced that the hydrate accumulation occurred especially at the lower bend section of the pipeline where the mean flow velocity was lower. In a similar manner, increasing the inlet flow velocity provided a basis for the decrease in the bed thickness. Since the mean particle size was inversely proportional to the mean flow velocity, the smaller particles were observed in the vicinity of the pipeline's inner wall where the velocity was higher. In addition, increase in the particle size led to growth in the thickness of the hydrate formation bed. Another simulation was

completed to compare how the bed thickness changed with regard to the diverse types of the solid stress model which were viscous solid stress, solid pressure, viscous and solid pressure combined and granular temperature theory. As a result of the simulation, the bed thickness obtained using the viscous and solid pressure combined model showed the best similarity with experiment (Figure 2.12).

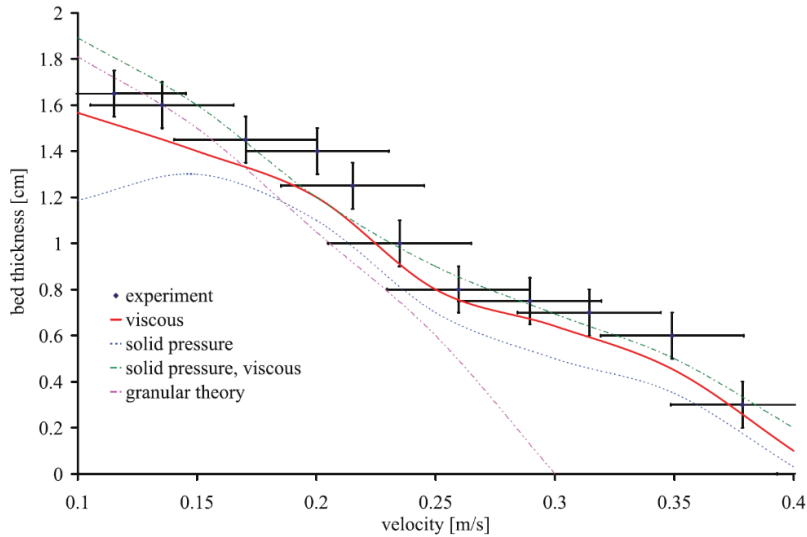


Figure 2.12. Bed thickness as a function of the mean flow velocity for different solid stress models [Balakin et al., 2011]

Lo (2011) described a mathematical model for simulation of hydrate formation in oil-dominated flows by conducting a computational analysis which is based on the Eulerian multiphase flow modelling approach. The flow model consisted of four phases which were the oil phase as a continuous fluid, gas phase as dispersed bubbles and water and hydrate phases as dispersed droplets. It was assumed that gas and water phases formed hydrate coming together under proper circumstances. The process was modeled in three steps which were mass transfer of methane from gas bubbles into oil, mass transfer of methane from oil into water, and reaction process from water to hydrate. The simulation was conducted using the pro-STAR 4.12 CFD package for a horizontal channel with the length of 1 m and the depth of 0.01 m. The model was built in a three-dimensional reference frame but projected in two dimensions by imposing symmetry boundary conditions to limit computational costs. The constant temperature of 7 °C was defined at the top and bottom part of the channel. The uniform inlet velocity and the inlet temperature of the 3 phases were 1 m/s and 16 °C. As inferred from the simulation results, the



maximum velocity was observed at the center of the channel, and it was zero at the channel surfaces as a result of the no-slip condition. Whereas the higher gas volume fraction was seen at the top of the channel due to buoyancy, the water fraction was observed to be higher near the bottom of the channel. As it was expected, the inner fluid temperature dropped towards the exit of the channel due to heat transfer to cooler surfaces and the environment. That is why the formation of the gas hydrate was observed in the vicinity of the exit region.

Naseer and Brandstätter (2011) carried out a 3-D unsteady computational study to observe which parts of typical natural gas pipelines are more vulnerable to hydrate formation. The computational fluid dynamics software Fluent that accounted for a high- $Re$  number  $k-\epsilon$  turbulence model along with the continuity, momentum and energy equations were solved. A mixture model for the phases was adopted. The specific geometry selected for analysis consisted of a segment of a pipeline with both uphill and downhill sections. Subject to the pipeline inlet conditions (temperature at 315 K, gage pressure at 6.3 MPa and water vapor volume fraction of 0.2), the lower part of the pipeline before the uphill section was found to be more susceptible to formation of condense water (Figure 2.13).

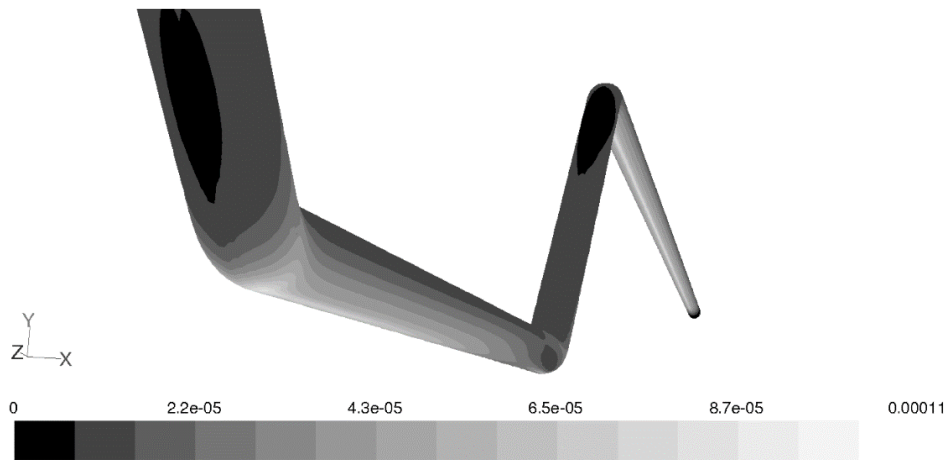


Figure 2.13. Contour of water phase fraction [Naseer and Brandstätter, 2011]

This can be related to dropping of the temperature under the condensation temperature of water, leading to accumulation of condensed water vapors at the lower part of the pipeline. This specific region of accumulated water had high potential for hydrate formation due to presence of water vapor under favorable temperature and pressure conditions, in addition to presence of

stagnation points. Contours of hydrate volume fraction coincident with the observed position of condensed water are presented in Figure 2.14.

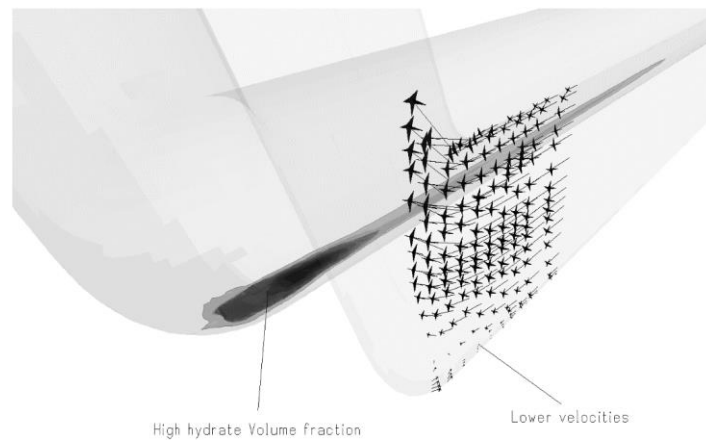


Figure 2.14. Hydrate concentration and velocity vectors [Naseer and Brandstätter, 2011]

In Figure 2.14, the velocity vectors are also presented on an offset vertical plane. The low-velocity regions are clearly observed to accommodate hydrate formation, imposing extra resistance to flow. Variations of the mixture viscosity, volume fraction of water, mixture velocity and volume fraction of hydrate along a horizontal line within the lower part of the pipeline before the uphill section are presented in Figures 2.15 and 2.16.

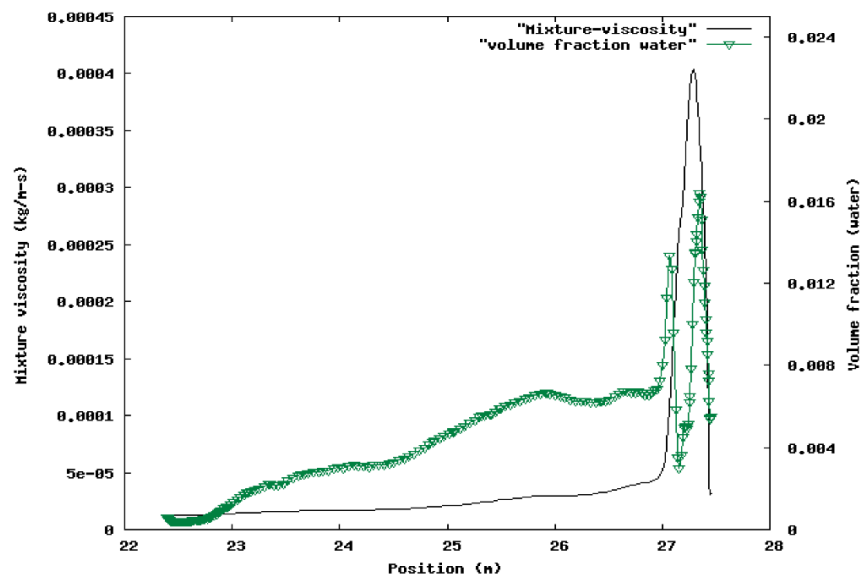


Figure 2.15. Viscosity of the mixture and the volume fraction of water [Naseer and Brandstätter, 2011]

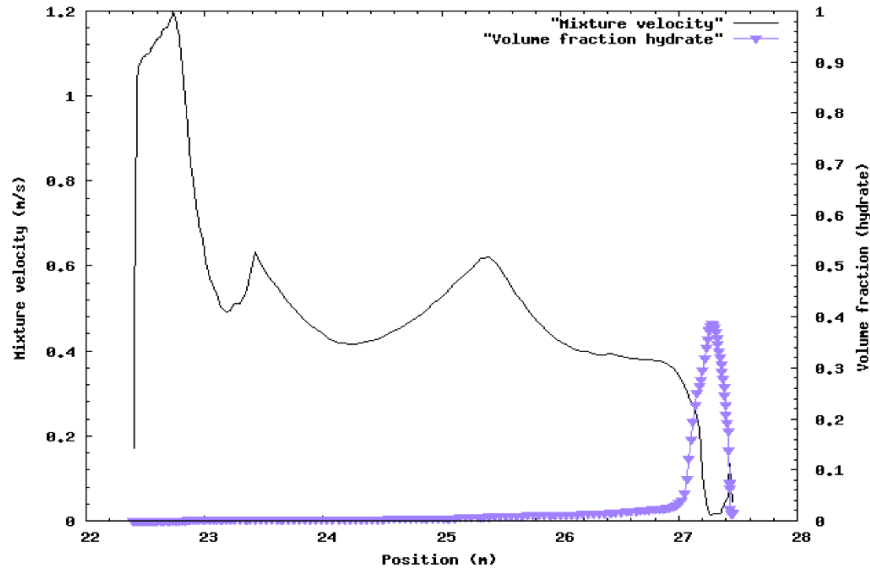


Figure 2.16. Velocity of the mixture and the volume fraction of hydrate [Naseer and Brandstätter, 2011]

The dramatic decline in water volume fraction was observed in the region coinciding with site of hydrate formation, where water molecules turned into hydrate structures by bonding with gas molecules. Another significant effect of the hydrate deposition detected was growth in the value of the static pressure and decline of the dynamic pressure.

Sallehud-Din (2012) accomplished a steady-state computational study using the commercial code CFX (ANSYS, Pittsburgh, PA) to gain insight into heat transfer in or/and out of a bundle pipeline system which was actively heated to prevent temperature drops under the critical temperature for the hydrate or wax formation temperature. This study was carried out in parallel with an experimental study on heat transfer in a similar tube bundle which was conducted by Thant (2012) in order to validate the results obtained from the CFD model. The internal pipelines called the product, test, heat flow, and heat return which were enclosed by the sleeve pipeline (3 m long and 0.3556 m outer diameter) was considered in this study as the geometry (Figure 2.17).

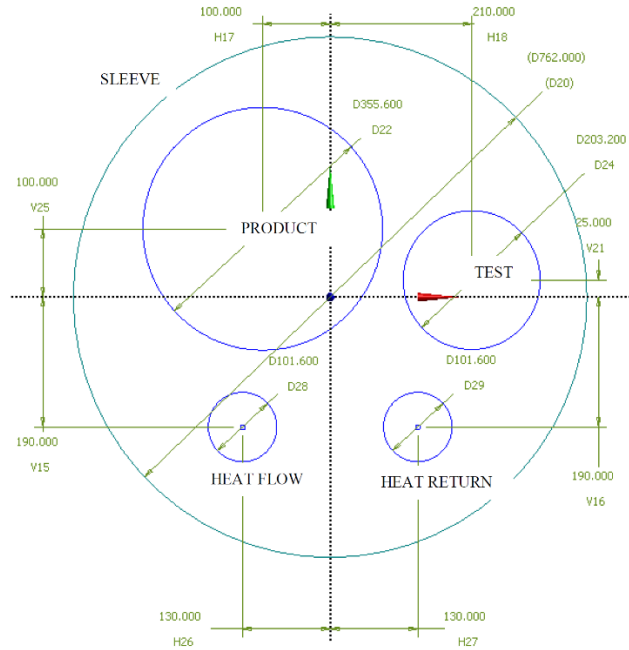


Figure 2.17. Selected geometry with dimensions in mm [Sallehud-Din, 2012]

Air/Nitrogen and water with constant properties were modeled in order to fill the space within the internal pipeline and the product pipeline, respectively. The computational study was conducted as 2-D for the horizontal position of the bundle to reduce the computational time. The results showed that the 2-D heat transfer analysis was sufficiently accurate since the air flow in the bundle is likely to be nearly two-dimensional. However, a 3-D model was used for the inclined and vertical tube bundle positions. Heat transfer was analyzed taking account of conduction in the pipeline walls, natural convection within the gas medium and the fluids within the internal pipelines, and radiative heat transfer inside the gas medium. The Shear Stress Transport turbulence model corresponding to a low- $Re$  number flow regime was specified for the gas region. The Boussinesq buoyancy model was chosen for both gas and water regions. The Monte Carlo radiation model was utilized with an emissivity at 0.9 for all smooth surfaces by assuming that the gas between the interior pipes was transparent to radiation. Even though different ranges of the temperature were set for the pipeline for 2-D and 3-D CFD models, the temperature of the surfaces was assumed to be constant for both models. The highest temperature belonged to the heat flow pipe, and the sleeve pipe had the lowest temperature for all sets of temperatures. The type of the fluid flow within the passageway was determined to be laminar depending on the value of the  $Re$  number, and natural convection was decided to be more dominant by calculating the  $Ri$  number (i.e.  $Ri > 10$ ). First of all, simulations were made to

investigate thermal stratification phenomena at different positions of the bundle for different mass flow rates. According to the results of the simulations, it was concluded that the effect of thermal stratification surged with increasing of natural convection effects connected with rise of the inclination angle and gravitational force (Figures 2.18 and 2.19).

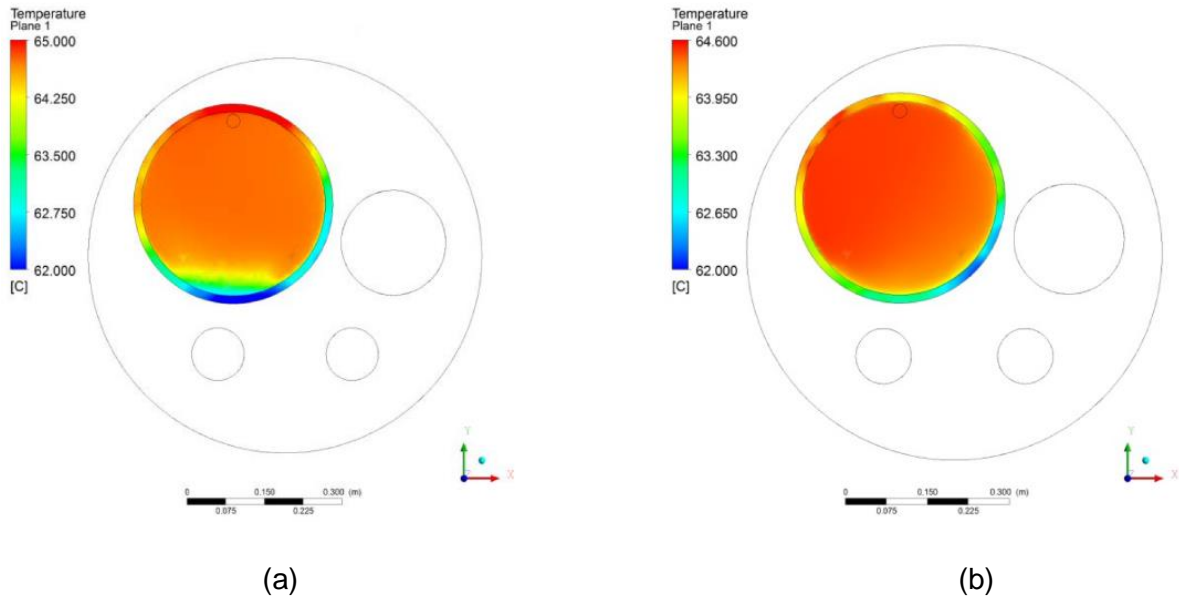


Figure 2.18. Temperature distribution in the cross-section of product pipe for the (a) horizontal and (b) vertical orientations [Sallehud-Din, 2012]

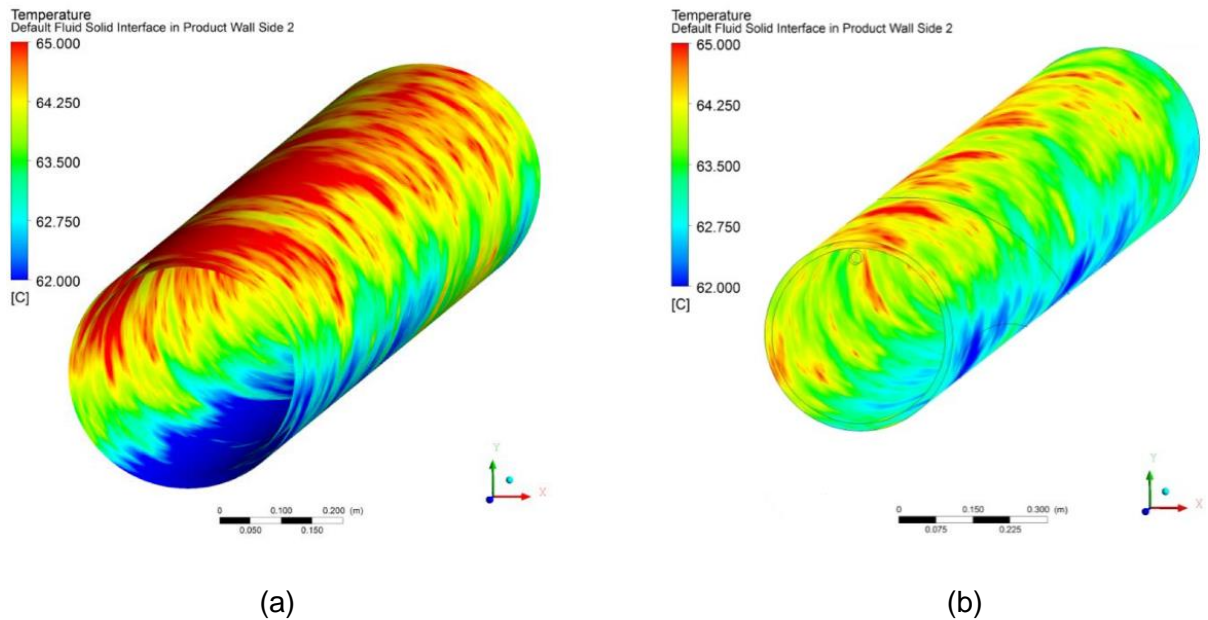


Figure 2.19. Temperature distribution along the product pipe wall for the (a) horizontal and (b) vertical orientations [Sallehud-Din, 2012]

The ratio of the relevant  $Ra$  numbers for these extreme cases was  $2.7 \times 10^4$ . The other significant result obtained was that decreasing the mass flow rate gave rise to increasing the influence of thermal stratification in consequence of laminar flow regime (Figure 2.20).

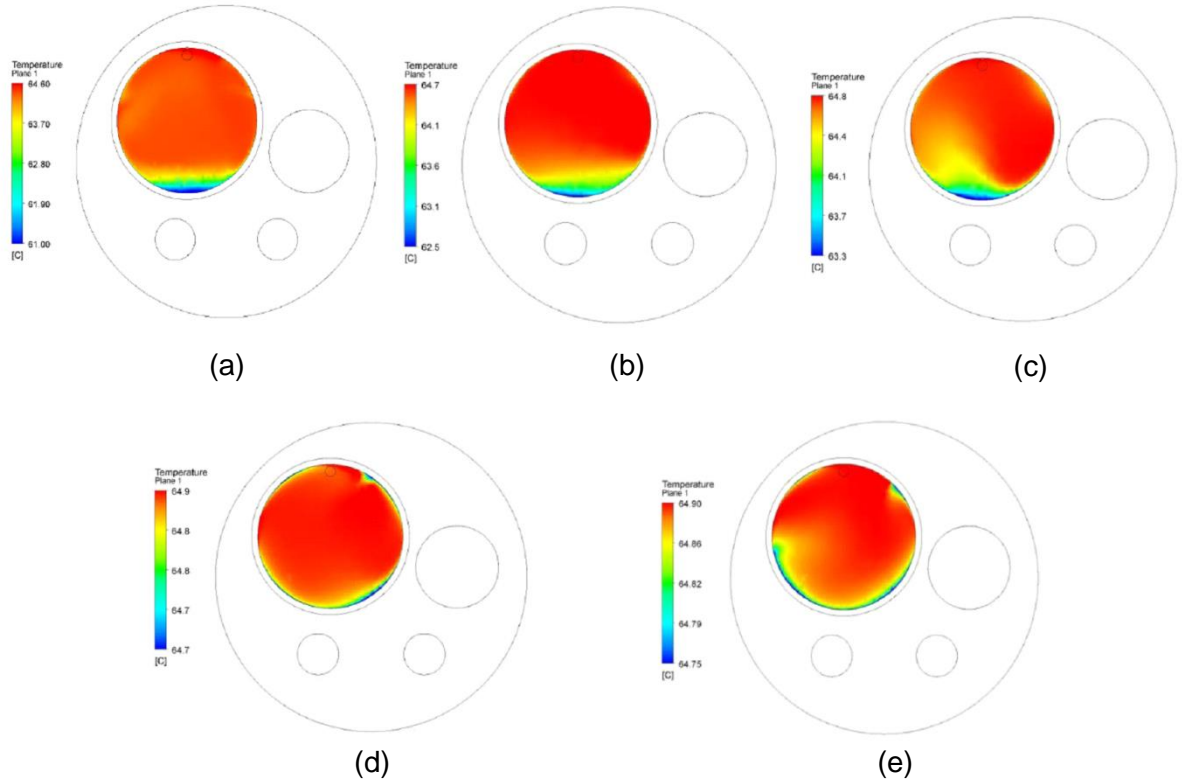


Figure 2.20. Temperature distribution of the cross-section of the product pipe for (a) 10, (b) 20, (c) 30, (d) 40 and (e) 50 liter/minute flow rate [Sallehud-Din, 2012]

Another study was reported on the Joule-Thompson cooling effect in the pipeline system and the impact of various thicknesses of the insulation layer on it. It was a favorable outcome that the insulation with any thicknesses was not effective in preventing the temperature drop because the decline in pressure due to the riser sections causes lowering of the temperature. As a consequence of the thermal distribution studies of the horizontal, inclined and vertical pipelines, it was observed that the highest temperature areas corresponded to the greatest average gas velocities. Another common result for all orientations was that the hotter gas rose toward the top part of the bundle, while the colder gas occupied the bottom section of the bundle due to the fact that the cold gas is denser than the hot gas. While this movement of the gas led to thermal interaction between the pipelines located within the sleeve pipe for the

horizontal position, heat started to accumulate around the circumferences of each internal pipeline as the inclination angle of the pipeline increased (Figure 2.21).

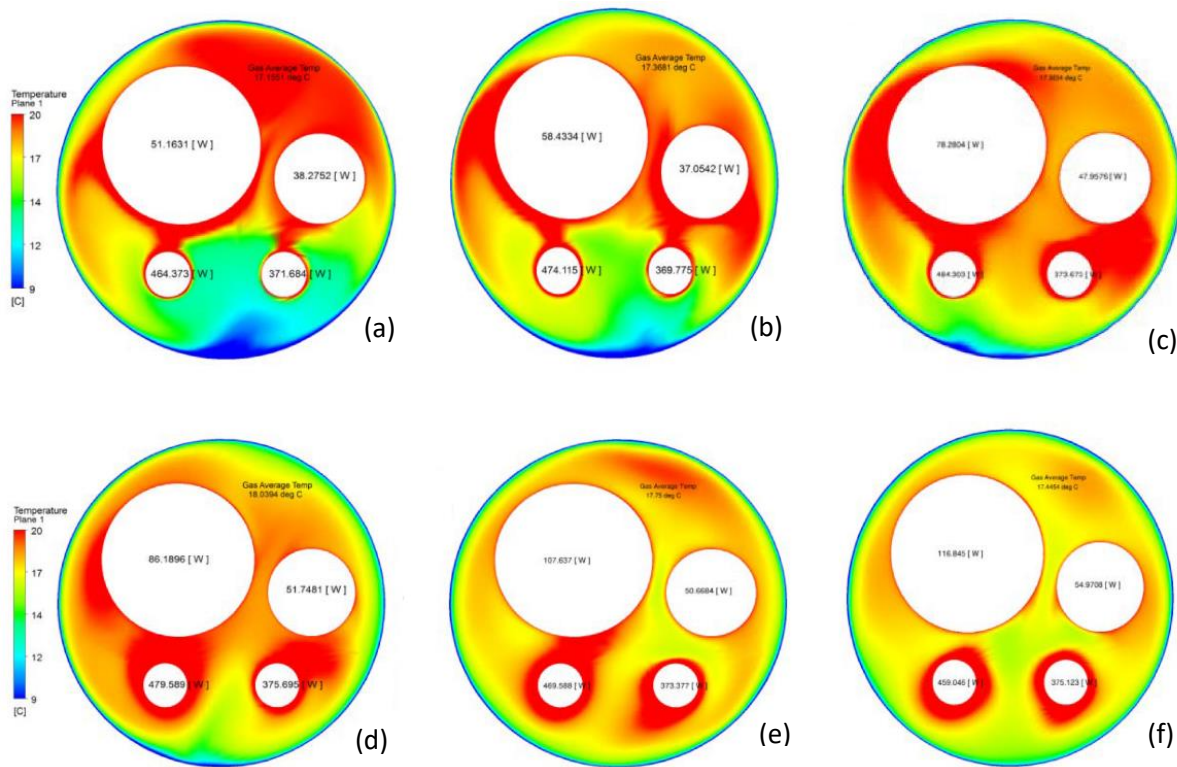


Figure 2.21. Cross-sectional temperature distributions at the mid-plane of the bundle for various inclination angles of (a) 10°, (b) 20°, (c) 40°, (d) 60°, (e) 80° and (f) 90° [Sallehud-Din, 2012]

As a significant outcome of changing the orientation of the bundle tube from horizontal to vertical, the product pipe lost more heat since the heat flow pipe became less effective. Naturally, the sleeve pipe gained more heat which means the total system lost greater heat to the surrounding. Consequently, it was concluded that increase in the inclination angle of the bundle tube resulted in the formation of hydrates or waxes due to decrease in the temperature of the product pipe.

Ding et al. (2012) carried out a steady-state computational study in an effort to obtain results on the structure of the complex flow, the separation of oil and water, and how the characteristics of the fluid flow affects water concentration in a vertical dead-leg. The chosen geometry had a horizontal main pipe and a vertical dead-leg which had the same diameter as the main pipe. The location of the dead-leg was decided in view of the fact that the fluid flow became fully-

developed upstream of the dead-leg. The average inlet flow velocity of the mixture fluid which consisted of 90% oil and 10% water was between 0.75 and 5 m/s. The continuity and momentum equations were solved for the mixture of oil and water. The mixture properties were calculated based on the algebraic mixture model, and the volume fraction equation was solved for the water which is the secondary phase. The effects of the inlet velocity on the length of the mixing zone in the dead-leg was shown in Figure 2.22.

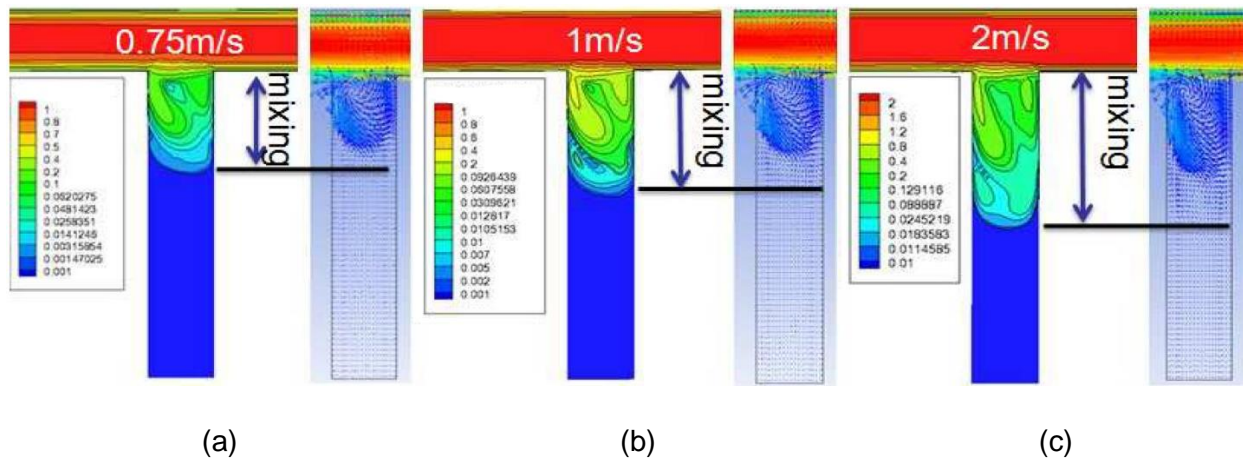


Figure 2.22. Velocity contours and velocity vectors with inlet velocity of (a) 0.75, (b) 1 and (c) 2 m/s [Ding et al., 2012]

Two different regions occurred (the upper mixing zone and the lower stagnant zone) with the critical cut-off velocity assigned to a value of 0.01 m/s. The length of the mixing zone was observed to be proportional to the average inlet velocity magnitude. Another significant inference from Figure 3 is that there were two recirculation flows occurring in the dead-leg. While the length of the upper circulation flow remained in the same level with increasing the average inlet velocity, the intensity of the recirculating flow increased, and caused the formation of the lower recirculating flow. The water volumetric concentration within the dead-leg as a function of the average inlet flow velocity was shown in Figure 2.23.



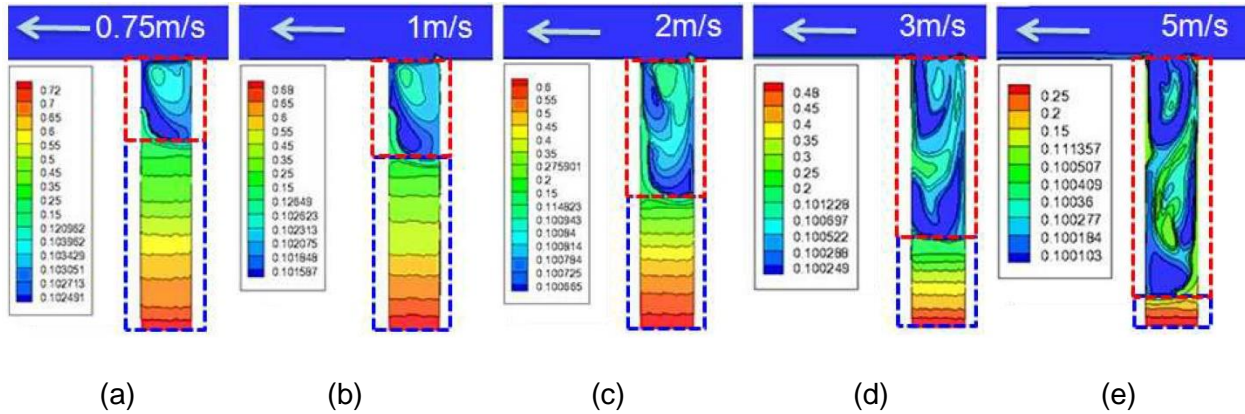


Figure 2.23. Contours of water volumetric concentration in the dead-leg for inlet velocity of (a) 0.75, (b) 1, (c) 2, (d) 3 and (e) 5 m/s [Ding et al., 2012]

The length of the dead zone pipe dominated by significant layering of the concentration of water was inversely proportional to the average inlet flow speed. Accordingly, the lower values of the water concentration were seen in the regions where faster fluid velocity was present. Similarly, the higher values of the water concentration were located at the center of the recirculation flow due to the slower fluid velocity. The stagnation part which is the bottom of the dead-leg pipe had the fluid with the maximum percentage of water because of the lowest fluid velocity and the gravity force.

The separation behavior of an immiscible two-phase flow within two horizontal pipes connected with vertical branches (Figure 2.24) was investigated computationally based on the Eulerian multi-fluid model by Chen et al. (2012) by adopting a stratified flow pattern with mixing at interfaces.

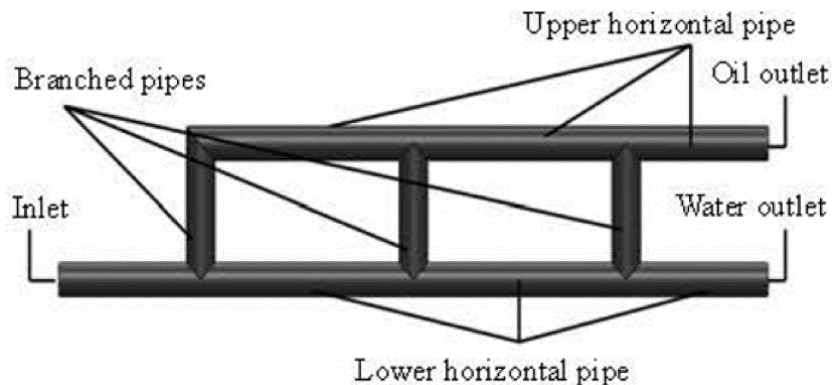


Figure 2.24. Schematic diagram of combined T-junctions [Chen et al., 2012]

Turbulent flow characteristics were acquired by means of the  $k-\varepsilon$  turbulence model. The inlet boundary condition was defined subject to the velocity. The volumetric flow rate was adopted at the outlets as the boundary condition. The zero velocity was defined at the walls by choosing the no-slip boundary condition. It was aimed to gain insight into how the separation behavior of oil and water mixture was affected by the number and the height of the vertical branches. First of all, the general separation profile of the mixture was obtained under the specified conditions which were the inlet mixture velocity of 0.5 m/s, and the oil volume fraction of 0.4. The dimensions of the geometry were 0.04 m in diameter, 6 times of the diameter in height, and 20 times of the diameter in the distance between two branches. The main reason for the mixture fluid separation was the density difference. As expected, the oil phase was tending to go toward the upper horizontal pipe through the vertical T-junctions due to its lower density. Based on the simulations, it was measured that the static pressure was reducing along both horizontal pipelines as a result of the frictional forces. Besides, the decline in the static pressure was observed at each junction point on the upper horizontal pipe with respect to the growth in the kinetic energy in connection with the increase in flow rate (Figure 2.25-a). The opposite situation was seen at the lower horizontal pipe (Figure 2.25-b).

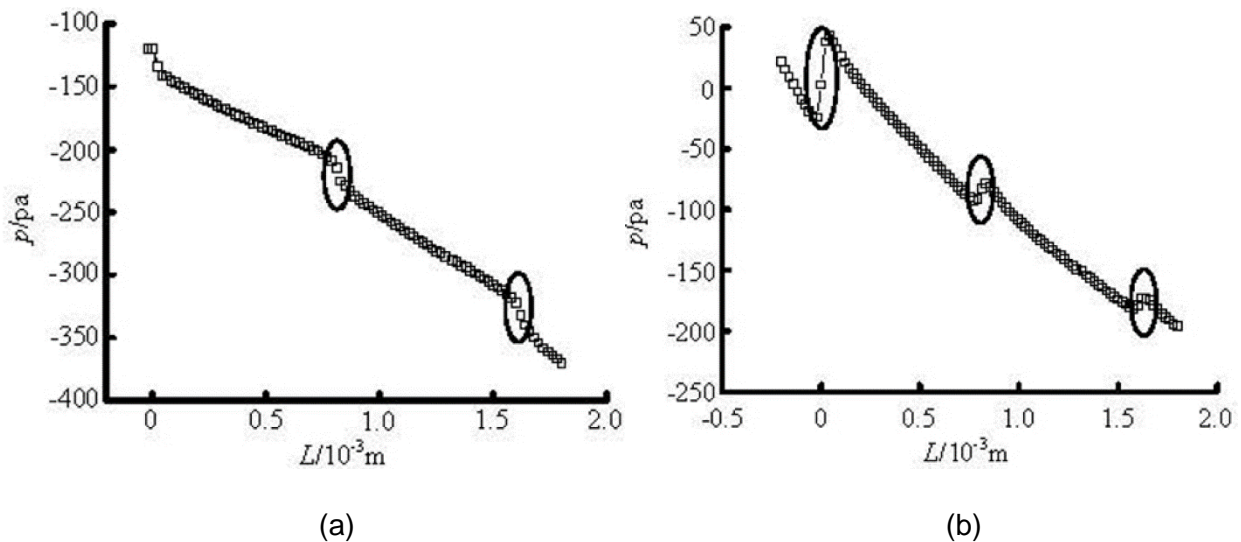


Figure 2.25. Static pressure distribution in the (a) upper horizontal pipe and (b) lower horizontal pipe axial centerlines [Chen et al., 2012]

The other significant finding obtained from these two figures was that the static pressure variation was becoming smaller since the flow rate was gradually decreasing towards the outlet (Figure 2.26).

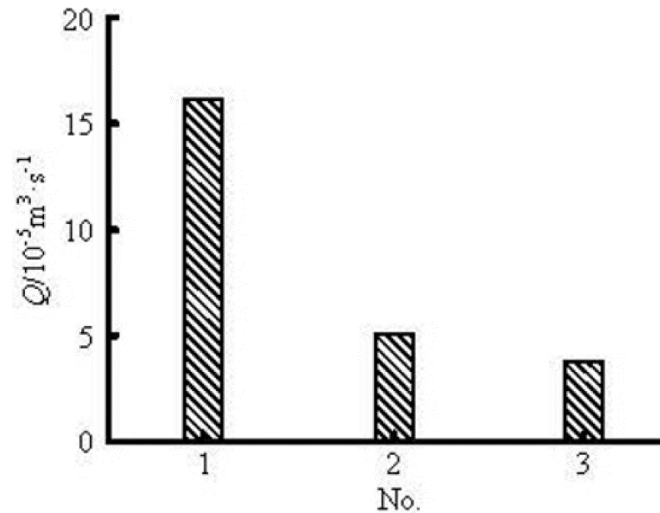


Figure 2.26. Volume flow rate in different branched pipes [Chen et al., 2012]

The influence of the distance between the vertical junctions on the flow separation was investigated by varying the respective distance as 4, 8, 12, 16, 20, 24 and 28 times of the diameter. The vertical pipes were equal in height and 4 times larger than the pipe diameter. Since the longer length interval between branches provide improved separation and more stable flow, the amount of oil gathering at the upper horizontal pipe was higher. However, it was important to choose the best length interval in order to achieve the most efficient separation without economic loss since the impact of the interval was less effective after some value. The impact of the vertical junction height on separation was studied with heights equal to 4, 6, 8, 10, 12, and 14 times of the diameter. In a similar manner with the interval test results, the increase in the branch height until some value was found to be more convenient for better flow separation.

Li et al. (2013) observed the effects of the pressure and initial flow rate on particle size and hydrate formation by considering a three-phase flow consisting of diesel oil, water and natural gas within a high-pressure flow loop which was 2.51 cm in internal diameter and 30 m in length. The experimental study was started with the injection of the liquid mixture composed of 10% water. After the pressure and temperature of the flow loop were stabilized, the fluid mixture was

saturated with natural gas. In order to reach hydrate formation conditions, the temperature was decreased from 18 °C to 1 °C without any changes in the pressure and flow rate values. Since hydrate formation is an exothermic process, the fluid started to lose heat to the environment. The temperature drop caused a surge in the viscosity and volume expansion, while the flow rate and density declined. The impact of the pressure on hydrate formation was investigated by comparing the temperature, density and flow rate at two different pressure values, i.e. 3.2 and 4.1 MPa. According to the results of comparison, it was concluded that the higher pressure led to the faster hydrate formation. Since the occurrence of hydrate is an exothermic process, the temperature decreased during the formation. The growth in the hydrate agglomeration caused decrease of the flow rate and the fluid density with respect to increase in the fluid volume expansion. The hydrate formation and blockage temperatures raised with the higher pressure. When hydrate accumulation ended up the blockage of the pipe, the relationship between the flow rate and transportability of the hydrate blockage was observed by rising of the flow rate gradually. A longer time period was observed to be needed for hydrate formation when the initial flow rate was higher. Moreover, blockage resulted by the accumulation of the hydrate particles was prevented under favor of the strong carrying capability and sheer stress of higher flow rate.

Li et al. (2015) studied a three-phase flow consisting of solid (hydrate), liquid (water) and gas (methane) numerically in 3-D by using the Euler Model and Computational Fluid Dynamics (CFD)-Population Balance Model (PBM) in order to observe flow patterns within a 10 m long pipe with the 0.3 m inner diameter. The RNG  $k$ - $\epsilon$  turbulent model was used as the turbulent flow solving model. The SIMPLE algorithm was adopted for coupling of the velocity and pressure fields. The first-order upwind differencing scheme was used to solve the governing equations. The inlet boundary condition was defined with the velocity, while the pressure was identified as the outlet boundary condition. The velocity of the fluid at the wall was determined to be zero by choosing the no-slip boundary condition. The simulations of the distribution of the multiphase flow were conducted for three different bubble sizes which are 0.5, 5, and 10 mm based on the Euler Model. According to the results, it was established that the gas and solid phases were prone to be found at the center of the pipe while the liquid phase fraction was higher near the wall (Figure 2.27).

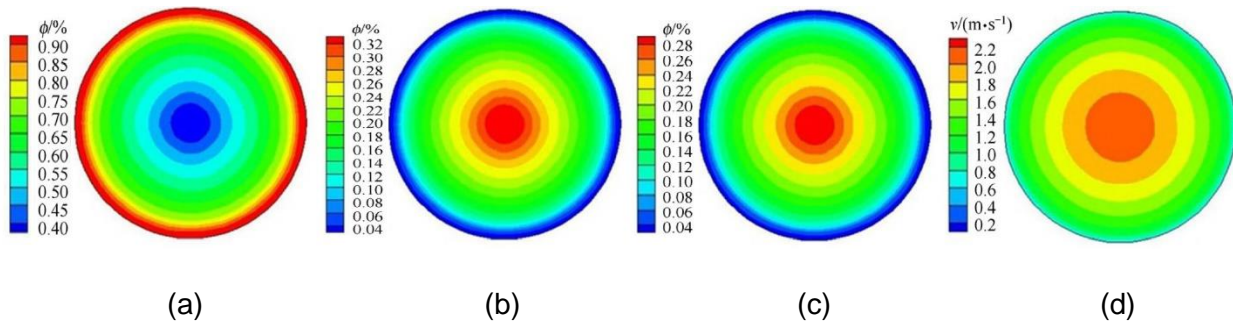


Figure 2.27. Contours of outlet flow state distribution (0.5 mm bubbles) for the (a) liquid, (b) solid, (c) gas phases and (d) the corresponding flow velocity [Li et al., 2015]

The reason for this distribution is that the velocity gradient causes a radial force, and gas and solid particles are thrust in the direction of the pipeline's center. By comparing the flow velocities with regard to the bubble sizes, it was deduced that increase in the bubble size brought on more uniform flow velocity. The other result of larger bubble size was found to be growths in the accumulation rate of denser phase. The same simulations were made for five different bubble sizes ranging from 0.5 to 10 mm by applying the CFD-PBM Model, and the similar consequences were obtained with the Euler Model with a slight difference. While the gas and solid particles were mostly located at the center of the pipeline, it was not as noticeable as that in the Euler Model (Figure 2.28).

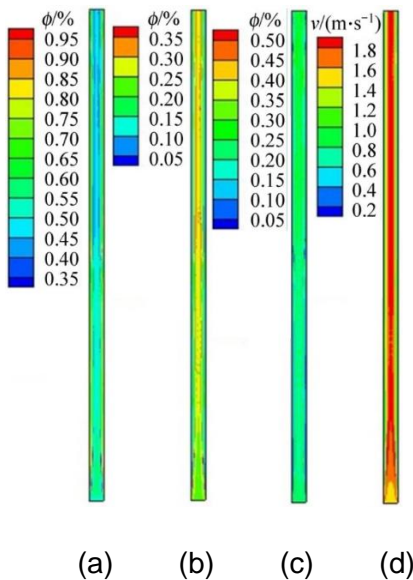


Figure 2.28. Contours of axial surface flow state distribution for the (a) liquid, (b) solid, (c) gas phases and (d) the corresponding flow velocity [Li et al., 2015]

Another crucial point was that the gas fraction became higher at the outlet in both models; however, this ratio was increasing from the inlet to the outlet of the pipeline according to the Euler Model, although it was oscillating through the pipeline based on the CFD-PBM Model. The outcomes which were obtained from the computational studies were compared with the experimental study conducted at the State Key Laboratory of Deep-Sea Mineral Resources Development and Utilization (College of Mechanical and Electrical Engineering of Central South University) to verify the accuracy of the numerical models. Based on this comparison, performance of the Euler Model was evaluated to be acceptable, whereas the CFD-PBM Model was found more realistic.

Sule et al. (2015) performed a 3-D steady-state computational study to explore hydrate formation behavior in subsea pipelines. A geometry was generated as a pipeline with two 90° elbows, one 60° elbow, and one constriction section by using the ANSYS design modeler (Figure 2.29).

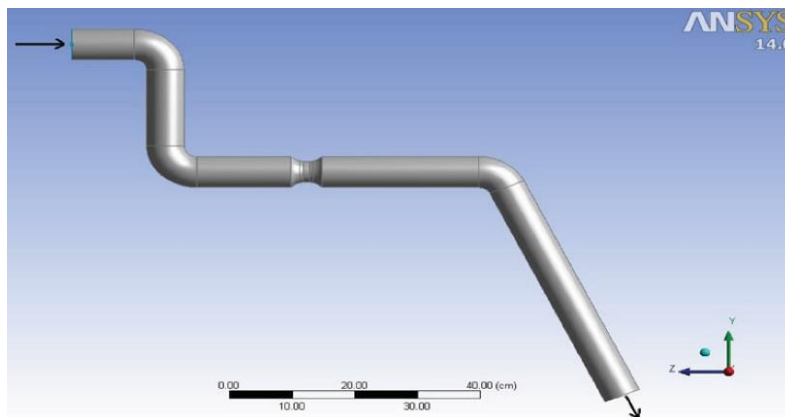


Figure 2.29. 3-D CAD model of the pipeline [Sule et al., 2015]

The pipeline was 1.37 m in length, whereas the diameters of the pipeline and the constriction part were 6 and 4 cm, respectively. The properties of a homogeneous fluid mixture with 90% gas and 10% water fraction was obtained from the PVTsim flash test in order to create a gas phase in the ANSYS CFX software package. The boundary conditions identified were the inlet temperature of 18 °C, the average pressure in the pipeline of 3.2 MPa gage pressure, the inlet velocity of 10 m/s, and the wall temperature of 1 °C. The k- $\epsilon$  turbulence model was preferred for prediction of the effects of turbulence, and the total energy heat transfer model was chosen to predict the temperature field throughout the flow. CFX-based simulations were executed in two

parts: the baseline simulation and sensitivity simulations. The results of the baseline simulation provided a basis for subsequent sensitivity simulations. The sensitivity analysis was carried out to examine how the changes of velocities (10, 15, 20, 25, and 30 m/s), pipe diameters (6, 7, 8, and 9 cm), viscosities (0.0112, 0.011, 0.0109, and 0.0107 cp), and water fractions (10%, 15%, 20%, 25%, and 30%) affect the flow line temperature. Baseline simulation results demonstrated that temperature at the center of the pipe reduced to 2-4 °C which is appropriate for hydrate formation at 3.2 MPa gage pressure according to Wenqing et al. (2013). The influence of variations of velocity, viscosity, water fraction, and pipeline diameter on temperature alteration along the pipeline were evaluated under the sensitivity analysis part of the study. Temperature contours as a function of the inlet fluid velocity are shown in Figure 2.30.

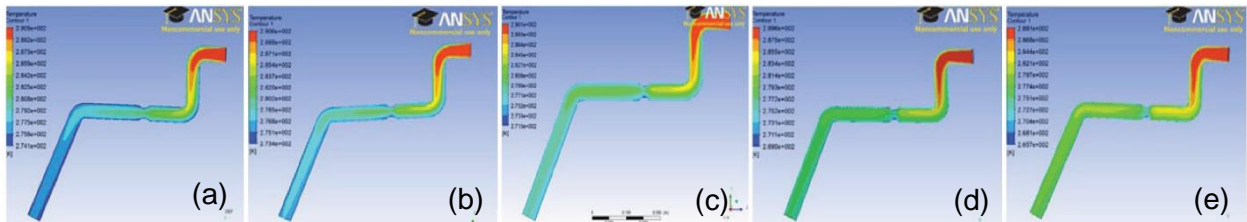


Figure 2.30. Effect of inlet velocity of (a) 10, (b) 15, (c) 20, (d) 25, (e) 30 m/s on temperature distribution within the pipeline [Sule et al., 2015]

It is observed that the possibility of hydrate formation based on various inlet velocities differed depending on which segment of the pipeline reached a temperature below the hydrate equilibrium temperature. Throughout the pipeline, the magnitude of the decrease in the average temperature reduced with rise of the average flow velocity except in the regions near the elbows and the constriction section. The most favorable temperature field to prevent hydrate formation among all cases studied was reached with the average velocity of 25 m/s. As the velocity was increased further, temperature along the flow lines started to decline. Regarding elbows and constriction regions in the pipeline, the increase in the average velocity led to a rise in fluid temperature drop. Similarly, small reduction in fluid viscosity while keeping all parameters unchanged led to somehow noticeable fall in the temperature drop of the fluid along the pipeline (Figure 2.31).

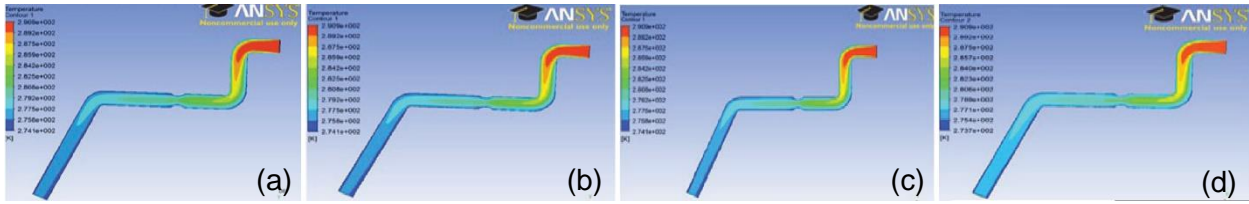


Figure 2.31. Effect of viscosity of (a) 0.0112, (b) 0.0110, (c) 0.0109 and (d) 0.0107 cp on temperature distribution within the pipeline [Sule et al., 2015]

These effects are clearly linked to the governing Reynolds number in the problem and similar trends were manifested once the value of the pipe diameter was raised (Figure 2.32).

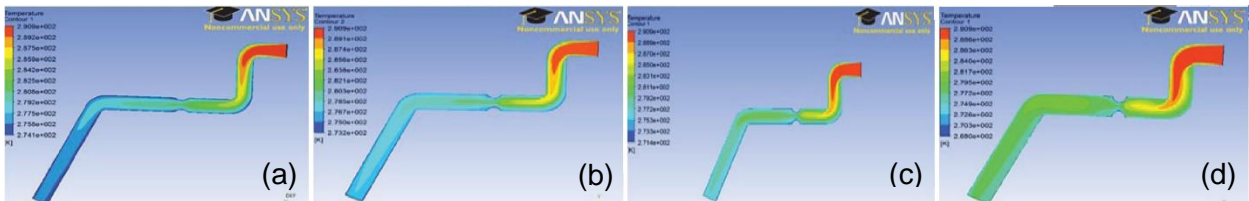


Figure 2.32. Effect of pipe diameter of (a) 0.06, (b) 0.07, (c) 0.08 and (d) 0.09 m on temperature distribution within the pipeline [Sule et al, 2015]

On the other hand, the observed temperature drops of the fluid was inversely proportional to increasing the value of water fraction (Figure 2.33).

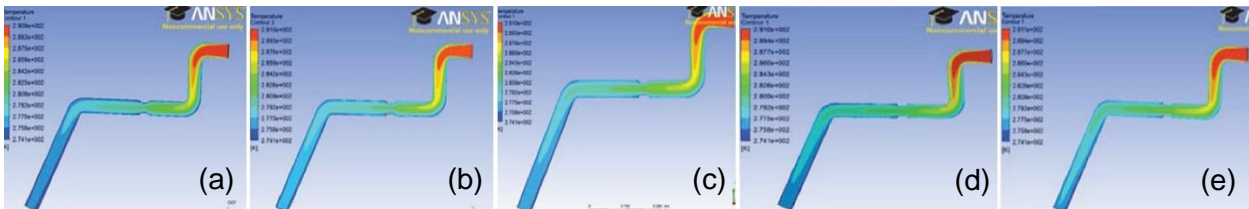


Figure 2.33. Effect of water fraction of (a) 0.1, (b) 0.15, (c) 0.2, (d) 0.25 and (e) 0.3 on temperature distribution within the pipeline [Sule et al., 2015]



As a general outcome, the outer segment of the bends and the pipe constriction were observed as more vulnerable for hydrate formation because of higher temperature drops.

Hu et al. (2015) performed a 3-D, steady-state computational study using the Fluent CFD package in order to investigate how convection heat transfer of the subsea Xmas tree assembly is affected by the installation orientation, the sea water velocity and the inner oil (incompressible hydrocarbon fluid) temperature. Besides, the effects of the installation orientation on the flow characteristics around the subsea Xmas tree were observed. The computational work was supplied with the results obtained from an experimental set-up which was focused on the heat transfer aspects of an underwater gate valve which had similar complex features common with the Xmas tree unit under investigation. In addition, the experimental results were used to verify the computational findings. The SIMPLE (Semi-Implicit Method for Pressure Linked Equations) algorithm was practiced for coupling the pressure and velocity terms. While the second-order central differencing scheme was applied for the diffusion terms, the second-order upwind differencing scheme was adopted for the convective terms, energy equation and turbulent quantities. The  $y^+$  values which are the wall coordinates were below 3 for all cases since a low- $Re$  number form of the  $k-\varepsilon$  turbulent model was adopted in all flow simulations. The computational model was carried out for the subsea Xmas tree which was designed to be located in a sea water environment with the depth of 1500 m, the sea water temperature of 4 °C, and the sea water velocity of 0.05-0.45 m/s. The sea water velocity and the oil temperature were set as 0.3 m/s and 60 °C in an attempt to detect the effects of the installation orientation on heat transfer. The temperature of the hydrocarbon within the Xmas tree ranged from 30 °C to 120 °C during the production process. Based on the results of the simulations conducted for four different orientations (Figure 2.34), it was discovered that although installation orientation had a limited impact on the temperature distribution, it was highly influential on the convection heat transfer coefficient.

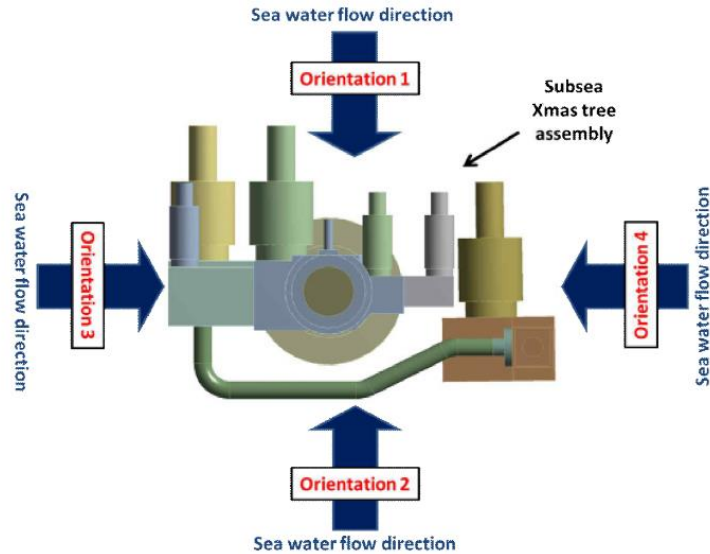


Figure 2.34. Four different installation orientations of a subsea Xmas tree [Hu et al., 2015]

Higher convection heat transfer was provided with assignment of a greater convective heat transfer coefficient of  $958.15 \text{ W/m}^2\text{K}$ . In effect, the temperature difference between the subsea Xmas tree and surrounding sea water became smaller, and thermal stress on the subsea tree decreased. Even though the higher heat transfer from the system leads to gas hydrate formation and causes the system to have more risk for blockage, orientation 2 was selected as the design condition among the four options. The reason for this selection is to be able to choose an improved thermal insulation design. The flow and heat transfer analysis were conducted taking account of orientation 2 under the condition of the constant inner surface temperature of the production channel of  $60 \text{ }^\circ\text{C}$  and the average sea water velocity of  $0.3 \text{ m/s}$ . According to streamlines observed on a vertical cross section (Figure 2.35-a) and a horizontal cross section (Figure 2.35-b), the stagnation point, flow separation zones, recirculation, reattachments, wake and high velocity regions were observed.

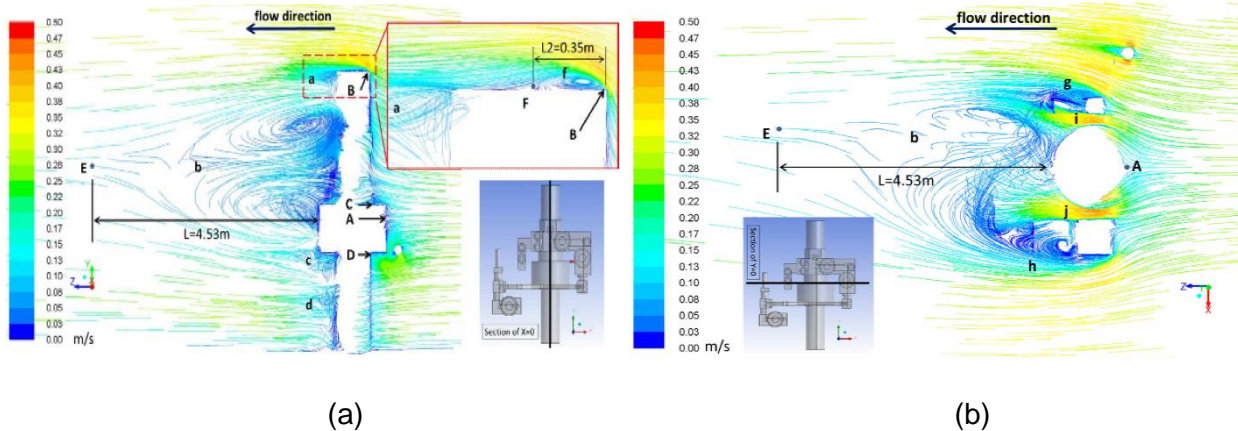


Figure 2.35. Streamlines colored with velocity magnitude corresponding to (a) vertical and (b) horizontal cross-sections [Hu et al., 2015]

The temperature (Figure 2.36-a) and convection heat transfer coefficient (Figure 2.36-b) distributions were also evaluated by means of CFD simulations under the same temperature (60 °C) and velocity (0.3 m/s) conditions for orientation 2.

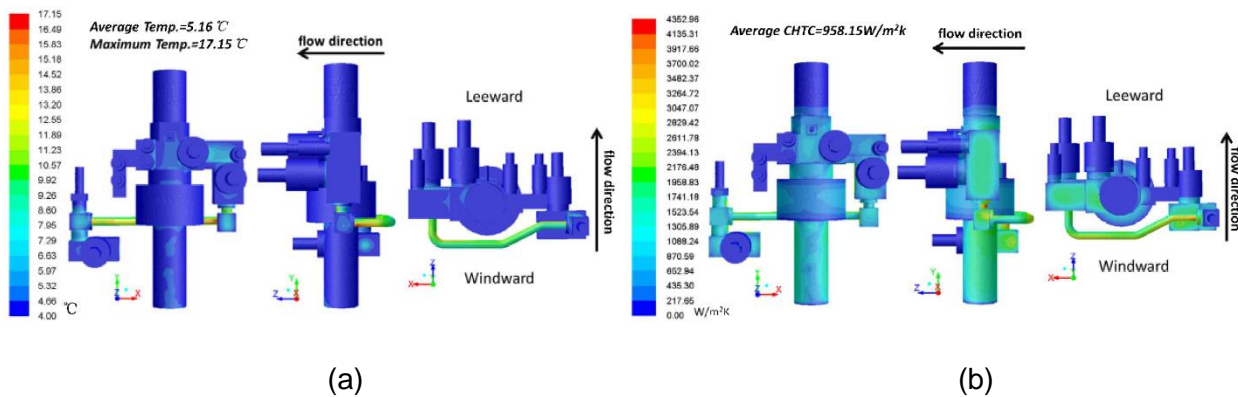


Figure 2.36. Subsea Xmas tree assembly with corresponding (a) temperature and (b) convective heat transfer coefficient distributions [Hu et al., 2015]

In accordance with the simulation results, the production pipeline, the wellhead, the choke model, the production model, and the short connector were defined as “hot spots” which means that these components of the Xmas tree were exposed to high convection heat transfer coefficient and heat loss accordingly. In order to gain insight about how the sea water velocity affects the heat transfer of the subsea Xmas tree, the simulation was obtained by keeping the

oil temperature and orientation direction the same and changing the sea water velocity from 0.1 m/s to 0.4 m/s. It was discovered that the level of the influence of the sea water velocity changed with respect to the convection heat transfer coefficients of the components proportionally (Figure 2.37).

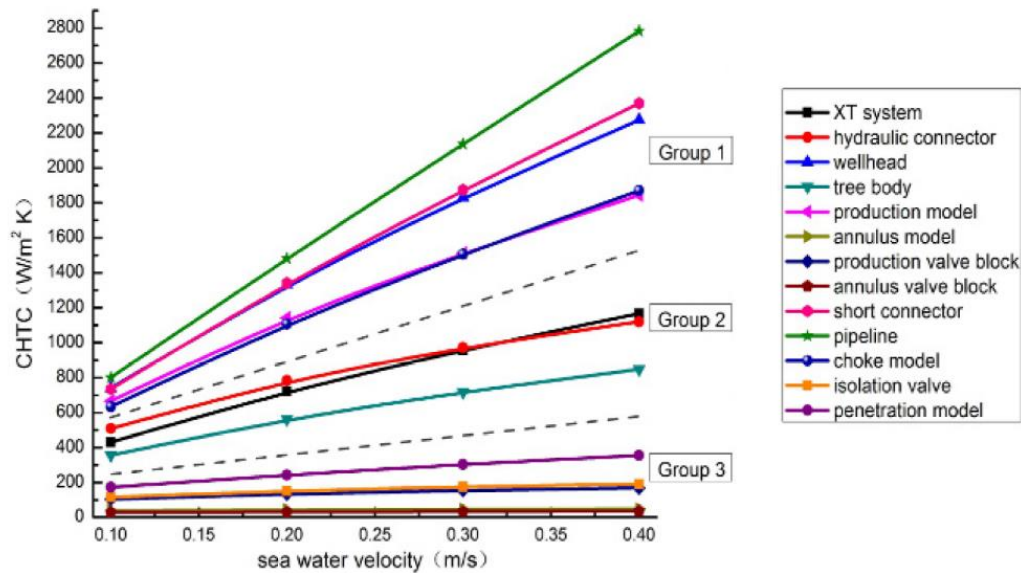


Figure 2.37. Correlation of the convective heat transfer coefficients of various components of the system with the sea water velocity [Hu et al., 2015]

The increase of the heat transfer coefficient with rise in the sea water velocity was obvious for the components in group 1 since these components had hot oil inside them. Although the components in group 2 interacted with hot oil directly, their heat transfer coefficients were smaller due to their greater wall thickness. The reason for the negligible change in the heat transfer coefficient of the components in group 3 was their disconnection with hot oil. The influence of the inner oil temperature on the wall temperature was discovered to be related to the wall thickness and the thermal resistance. Since the production pipeline was the thinnest component, it had the highest surface temperature and the temperature growth rate (Figure 2.38).

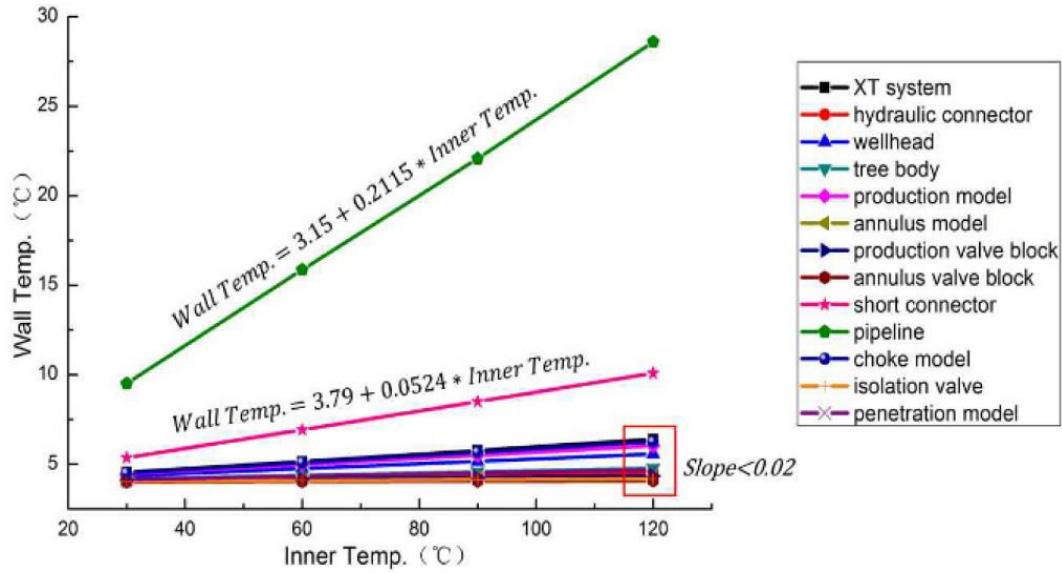


Figure 2.38. Temperature rising for individual components of the Xmas tree [Hu et al., 2015]

The relationship between the increase of the inner oil temperature and its effect on the convection heat transfer coefficient was related to the correlation of the heat flux and the temperature difference between the wall and surrounding (Figure 2.39).

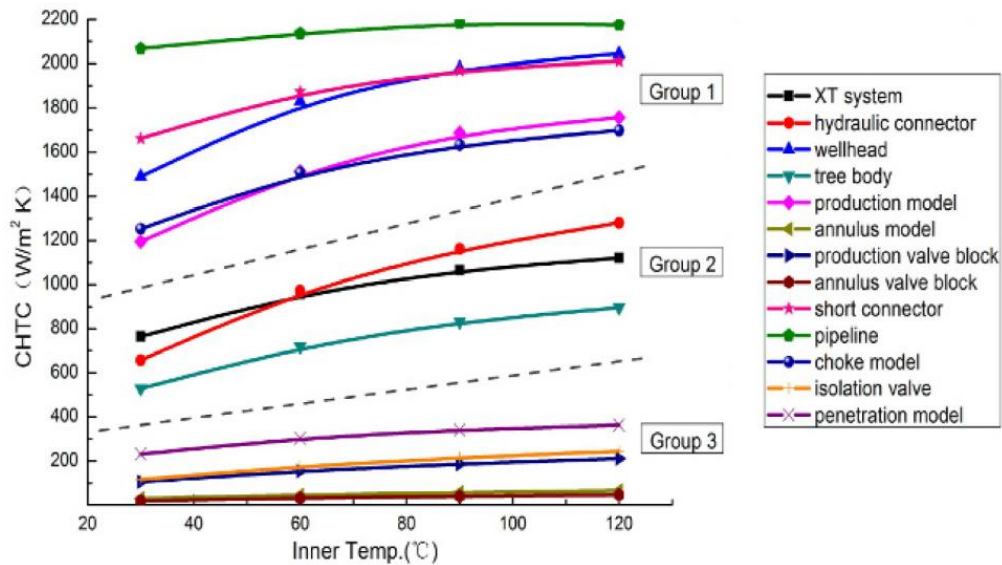


Figure 2.39. Correlation of convective heat transfer coefficients of various components of the system with the inner oil temperature [Hu et al., 2015]

It was concluded that there was not remarkable change in the convection heat transfer coefficient of the pipeline with the increase in the inner oil temperature due to the fact that the magnitude of the heat flux and the temperature difference rose almost at the same rate. The reason for why the heat transfer coefficient of the components in group 3 did not change significantly when the inner oil temperature grew was that they did not have a direct connection with the hot oil. On the contrary, the heat transfer coefficients of the other components except the pipeline in group 1 and group 2 investigated rose with increase in the inner oil temperature since the growth in the heat flux was higher than the temperature difference term.

Guo et al. (2016) conducted a computational study on the effects of gas production, hydrate inhibitors, insulation materials, downhole throttling and well shut-in after choosing the best prediction model of temperature and hydrate formation. The fluid physical property parameters were calculated using PVTsim for OLGA which is a package of PVTsim modules for exporting reliable fluid properties to dynamic multiphase flow simulators, OLGA. OLGA is an oil, water and gas transport modelling tool in the same pipeline. The fluid had two phases which were gas bubbles with liquid droplets and liquid which formed gas hydrate when the proper conditions were met. As a result of the comparison of the methods, the approach which was explained in the paper was figured out the most efficient one due to its lowest relative error. Based on this method and under the conditions of the bottom hole pressure of 41.8 MPa, the bottom hole temperature of 80.3 °C, the sea surface temperature of 25 °C, the subsea temperature of 2.5 °C, the influence of gas production, insulation materials, downhole throttling, and well shut-in on hydrate formation was investigated. The growing gas production rate led to surge in the flow rate and the Reynolds number of the flow. Increase in the Reynolds number caused higher heat transfer between the wellbore and its environment. However, a rise in gas production brought on an increase in wellbore temperature. From the simulation results, it was obtained that the hydrate formation possibility diminished with increasing wellbore temperature which was caused by increasing gas production (Figure 2.40).

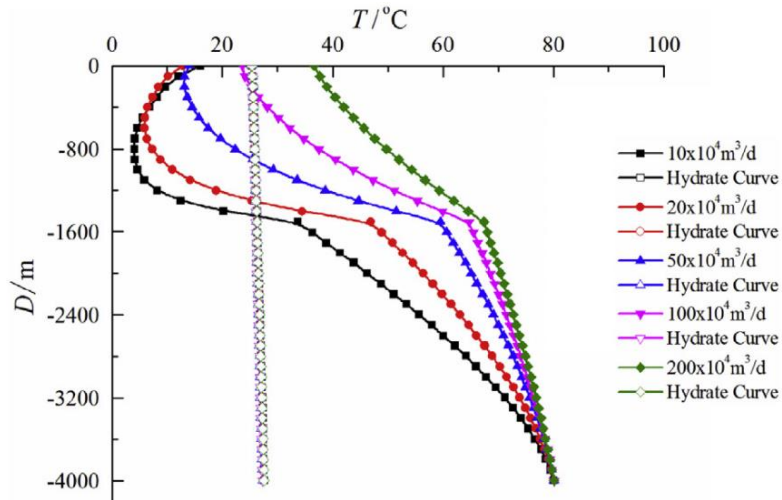


Figure 2.40. Predictions of the natural gas hydrate formation area in the wellbore for different gas production rates [Guo et al., 2016]

The thermal conductivity and the thickness of insulation material were observed to play significant role to avoid hydrate formation. By analyzing the simulation results, it was found that the insulation material with smaller thermal conductivity and higher thickness caused preventing hydrate formation by decreasing heat loss from the wellbore to surrounding due to the rise in thermal resistance of conduction (Figure 2.41).

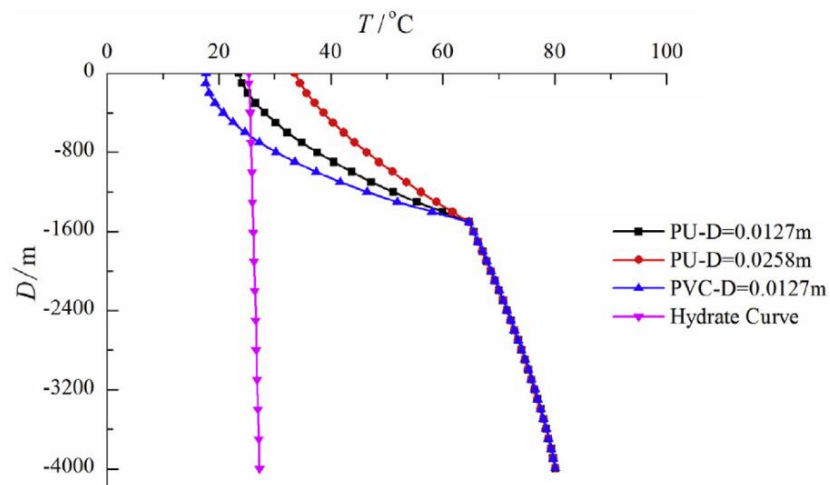


Figure 2.41. Predictions of the natural gas hydrate formation area in the wellbore for different insulation materials [Guo et al., 2016]

Downhole throttling was discovered to not be an effective way to prevent gas hydrate formation for gas wells due to the fact that the wellbore temperature dropped under the hydrate formation temperature decrease after the throttle (Figure 2.42).

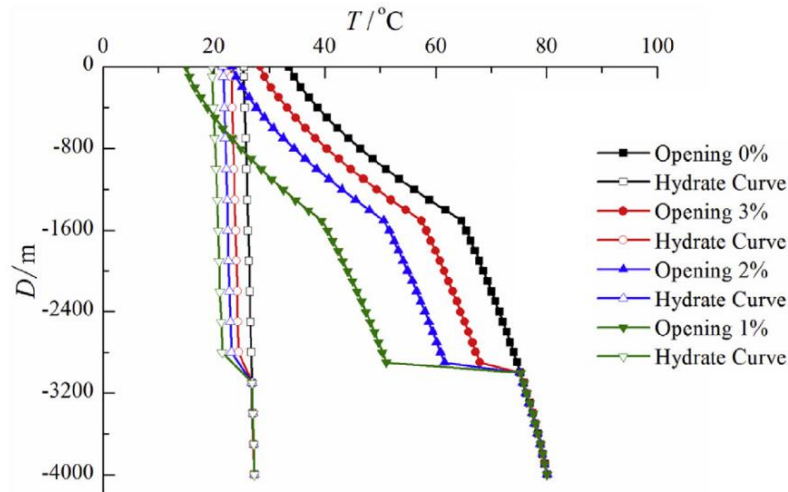


Figure 2.42. Effects of throttle opening on the natural gas hydrate formation area in the wellbore [Guo et al., 2016]

During gas production process, the wellbore temperature was higher than the surrounding water temperature. This situation helped to avoid gas hydrate formation along the wellbore. In case of shut-in, since the process of gas production stopped, the wellbore temperature decreased until it became equal to the lower surrounding temperature. As soon as the wellbore temperature dropped the hydrate equilibrium temperature, hydrate formation began to appear (Figure 2.43).

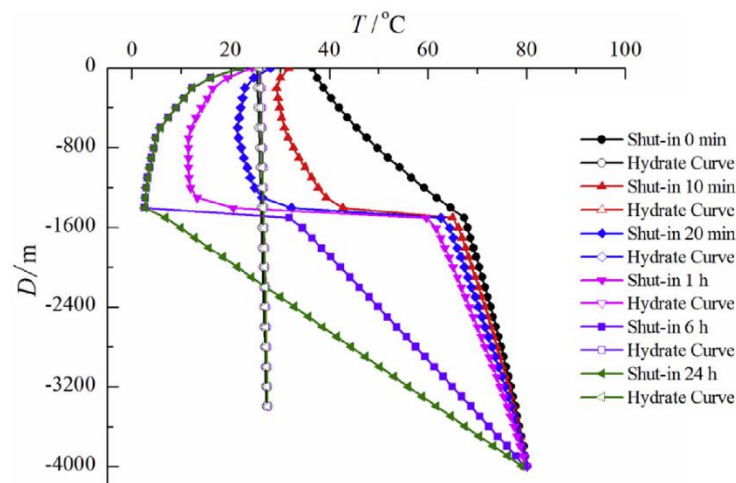


Figure 2.43. Effects of shut-in time on the natural gas hydrate formation area in the wellbore [Guo et al., 2017]



That is why discovering safety shut-in time was important to prevent hydrate formation inside the wellbore.

Rukthong et al. (2016) developed a computational fluid dynamics model using computer language code so as to figure out how the density, viscosity, heat capacity and thermal conductivity properties of the crude oil affect the transport profile. Having an insight into this phenomenon is significant in order to prevent the system from the appearance of gas hydrate, wax and so on. This developed numerical model was verified with the commercial software ANSYS-FLUENT. The viscous flow of crude oil inside the pipeline with 1500 m in length and 0.15 m in diameter was simulated under transient conditions. The flow regime was fully-developed laminar flow with the  $Re$  number ranging from 35.63 to 261.16. No-slip condition was applied for the pipeline wall. The inlet temperature was specified as 50 °C with the constant ambient temperature of 35 °C. The atmospheric pressure was defined as the outlet pressure. The SIMPLE algorithm was applied to couple the pressure and velocity fields. The cell face problem was solved by adopting the first-order upwind numerical scheme. The linear algebraic equations were solved by means of the Tri-Diagonal Matrix Algorithm. As a result of the numerical solutions, the hottest crude oil was located at the pipe's center and the temperature was decreasing through the pipe wall and reached the same temperature with the surrounding at the wall. Since the temperature drop caused an increase in the viscosity, the crude oil was slower near the wall. During the flow within the pipeline, the fluid temperature falls due to heat loss driven by the temperature difference between the fluid and the environment. This temperature drop caused wax formation after some distance from the pipe inlet when the crude oil temperature decreased below the wax appearance temperature. Based on the obtained mathematical model, the location of wax appearance was found to be directly proportional with the crude oil density and heat capacity. The other observation was that the heat capacity of the crude oil had more impact on the wax appearance distance than the density of crude oil.

A computational study with the population balance technique was conducted by Balakin et al. (2016) with the purpose of modelling gas hydrate formation, agglomeration and deposition in industrial pipelines. The CFD-PBM simulations were applied on a 2-D rectangular channel model 1 m long and 0.102 m high which contained oil and gas as continuous phase and water as dispersed phase. The continuity, momentum and energy equations were identified separately for each phase in consequence of the Eulerian-Eulerian computational model. The SIMPLE algorithm for pressure-velocity coupling and the second-order Euler model for time discretization were applied. The periodic inlet boundary condition and the pressure outlet condition were

selected with the no-slip wall boundary condition. The constant temperature was defined 4 °C at the inlet, and 3 °C at the outlet and the walls. The hydrate kinetic model from the Colorado School of Mines (CSMHyK) was verified with some literature experimental data, and then the CFD-PBM-based results were compared with the CSMHyK model. Hydrate formation started with the smallest primary hydrate particles and enlarged through the process in the CFD-PBM model, while the opposite behavior was observed in the CSMHyK model which was non-physical. The reason why the particle diameter reduced with time in the CSMHyK model was interpreted to be the rise in the apparent viscosity. The computational domain was assigned the uniform phase fraction initially for both methods. The water phase was observed at the bottom part of the domain after a while from the initial moment due to its higher density as a result of the gravity effect in the CFD-PBM model. Therefore, the bottom section of the domain was specified where the maximum particle sizes were located. However, this agglomeration was not seen in the CSMHyK model results since the CSMHyK model does not take into account convective particle size transfer. Conversely, the particles with the maximum sizes were perceived at the center of the domain by reason of the minimum shear stress at the center and the maximum turbulent energy dissipation near the walls. As a common consequence for both models, it was inferred that the viscosity was higher near the bottom wall due to the presence of hydrate accumulation. At the end of the study, the CFD-PBM model was decided more realistic based on all comparisons.

Liu et al. (2017) conducted a transient computational study to explore how the temperature and the flow rate affects to melting process of the waxy crude oil. The geometry was created to be a cylinder which had the inner diameter of 53 mm, the wall thickness of 2 mm, and the length of 1000 mm with mixing oil and water fluid in. Besides the fluid phase, there was a solid phase, crude oil, which was located at the inner top wall of the pipeline. The crude oil was 50 mm in length and 10 mm in maximum radial height. The melting process took place by means of hot water flowing through the pipeline. The situation was considered to be an unsteady phase change heat transfer problem with some assumptions which were using temperature-independent thermophysical properties of oil, ignoring the natural convection effects inside the oil block, and assuming the arched crude oil block to be stationary. The high Reynolds number  $k-\varepsilon$  turbulence model was preferred for calculation of turbulent properties. The water, oil, pipeline, and air temperatures were defined constant as the initial boundary conditions. The inlet boundary condition was chosen to be the velocity inlet. Fully-developed flow was aimed to reach by specifying the outlet boundary condition as the outflow boundary which means the gradients of all parameters were zero. The SIMPLE numerical method was adopted to couple the

pressure and velocity fields. The second-order upwind differencing scheme was chosen to solve the momentum and energy equations. The standard scheme was considered for the pressure correction equation. Based on the information from the national standard which suggests the safe temperature of a long-distance crude oil transportation should be 3 °C higher than its solidification point, the solidification temperature was defined as 41 °C which was 3 °C higher than 38 °C which was the solidification point of the simulated crude oil. The impact of the temperature variance between the fluids on the melting period of the crude oil block was obtained by changing the water temperature from 50 to 70 °C for three different flow velocities (0.1, 0.2, and 0.3 m/s). As the temperature difference between the oil and water increased, reduction in the melting time was observed for all velocity values due to growth the convection heat transfer coefficient and the heat transfer interrelatedly. Since the crude oil was already melting faster for the higher flow velocities, the remarkable decrease was seen at the velocity of 0.1 m/s (Figure 2.44).

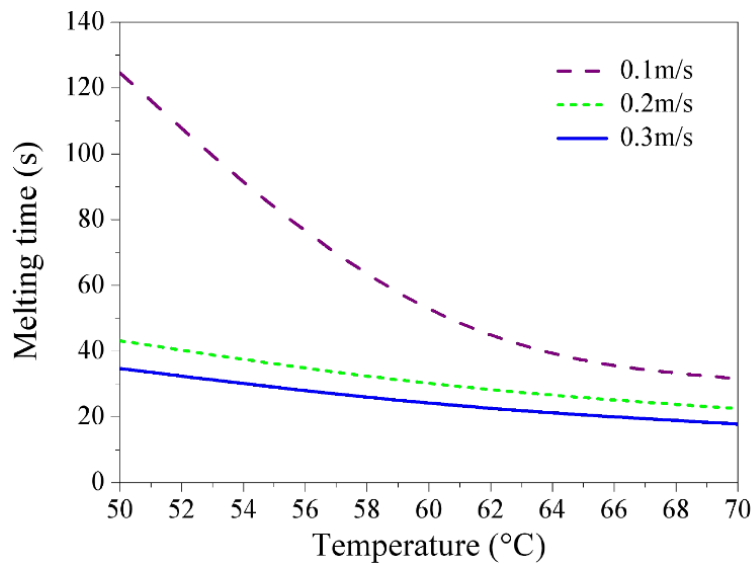


Figure 2.44. Melting time versus water temperature for different velocities [Liu et al., 2017]

Based on the simulation conducted under the constant water temperatures of 50, 60 and 70 °C, and the range of flow rate between 0.05 and 0.3 m<sup>3</sup>/s, the impact of the flow rate on the crude oil melting was explored. According to the simulation results, it was proved that the crude oil melted faster with higher flow rate which caused higher heat transfer coefficient and turbulence effect (Figure 2.45).

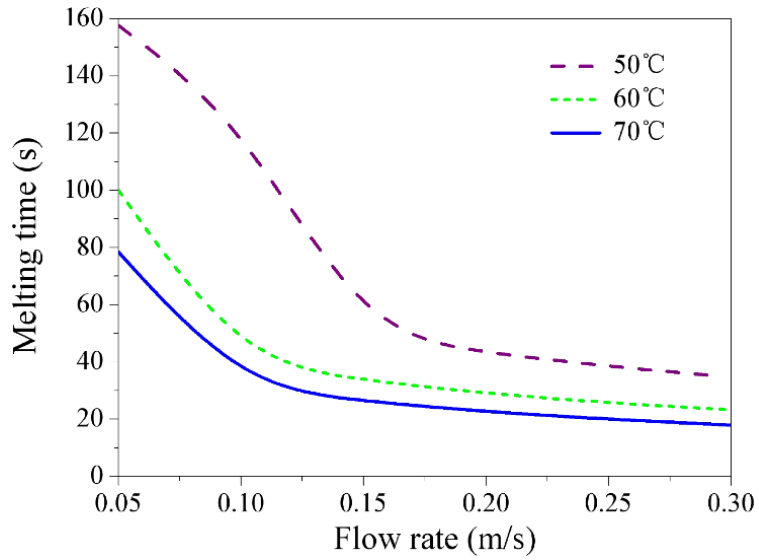
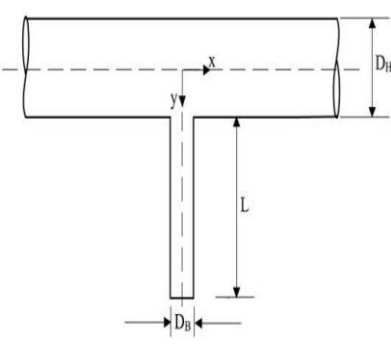
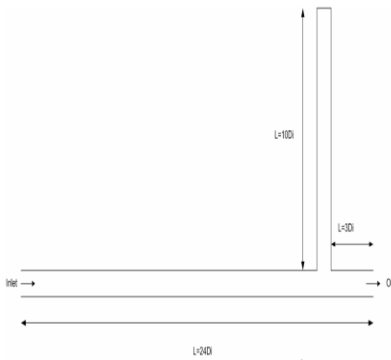


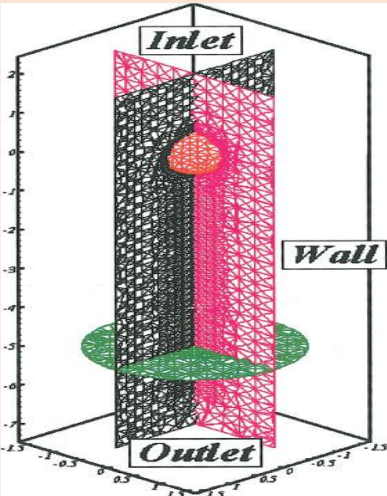
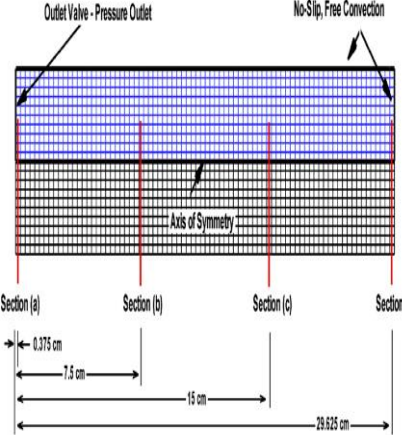
Figure 2.45. Melting time versus flow rate for different temperatures [Liu et al., 2017]

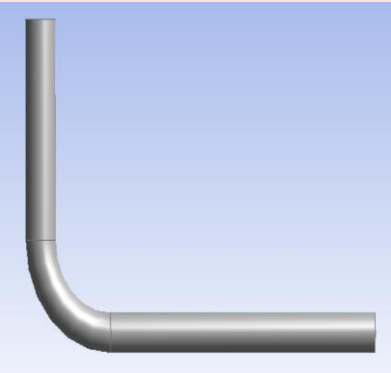
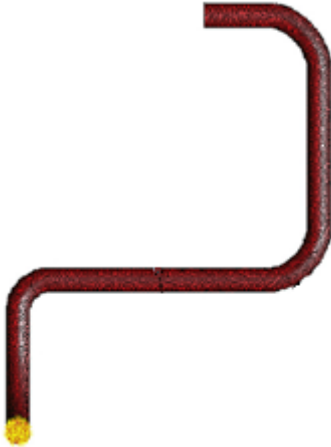
## 2.2. Summary of Literature Review

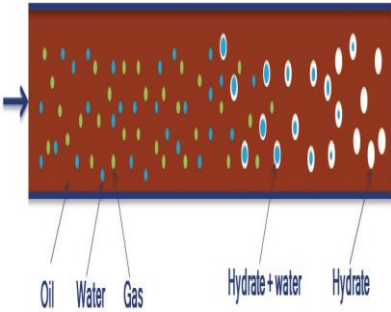
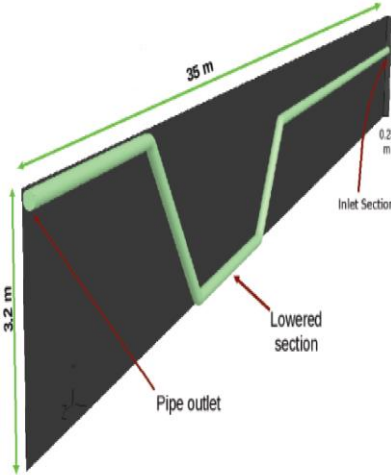
A number of research papers were summarized in this Chapter. Table 2.1 highlights the major findings of prior research in order to provide a quick reference for interested readers

Table 2.1. Summary of studies on hydrate formation

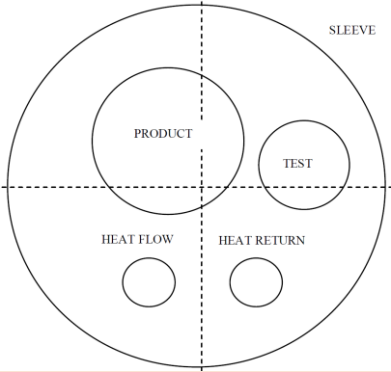
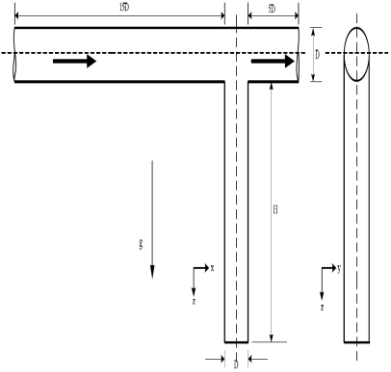
Author (year)	Geometry	Techniques of Analysis	Fluid Properties	General Observations	Results
<p><b>Habib et al. (2005)</b></p>	<p>Horizontal pipe with 90° dead-leg with changeable length</p>  <p><math>L/D_B = 1, 3, 5, 7</math>  <math>D_H = 0.3 \text{ m}</math>  <math>D_B = 0.1 \text{ m}</math></p>	<p>CFD (ANSYS-FLUENT), 3-D, Steady-State, Standard <math>k-\epsilon</math> Model, Algebraic Slip Mixture Model.</p>	<p>Immiscible 90% crude oil and 10% water</p> <p><math>U_{inlet} = 1 \text{ m/s}</math></p>	<p>Influence of various dead-leg lengths with a constant diameter, average velocity and crude oil-water proportion at the inlet on the flow velocity and water concentration within the dead-leg was investigated.</p>	<p>Upsurge of the length to the diameter ratio led to increase in the stagnation zone size and the amount of water gathered at the bottom of the dead-leg.</p>
<p><b>Andersen (2007)</b></p>	<p>Straight horizontal pipe with a 90° branch</p> 	<p>CFD (ANSYS-FLUENT), 3-D Steady-State, High-<math>Re</math> Number <math>k-\epsilon</math> Model, RNG <math>k-\epsilon</math> Turbulence Model.</p>	<p>Incompressible ideal gas</p> <p><math>U_{gas} = 2.2, 9 \text{ m/s}</math>  <math>\dot{m} = 6, 26 \text{ kg/s}</math>  <math>h_1 = 580 \text{ W/m}^2\text{K}</math>  <math>h_2 = 1100 \text{ W/m}^2\text{K}</math>  <math>P_{gas} = 10^7 \text{ Pa}</math>  <math>T_{gas} = 338 \text{ K}</math>  <math>U_{seawater} = 0.1 - 2 \text{ m/s}</math>  <math>T_{seawater} = 280 \text{ K}</math></p>	<p>Possibility of hydrate formation in vertically- and horizontally-orientated dead-legs with different mass flow rate, average velocity and heat transfer coefficient values was studied.</p>	<p>Vertical dead-legs were found more vulnerable to hydrate formation.</p>

<p><b>Sean et al. (2007)</b></p>	<p>Cylindrical tube</p> 	<p>Experimental and CFD, 3-D Unsteady, Third-Order Upwind Scheme, Second-Order Central Differencing Scheme, Second-Order Explicit Scheme, The MAC Type Fractional Step Method.</p>	<p>Hydrate, liquid water, and vapor</p> <p><math>T_{initial,hydrate} = 253.15 \text{ K}</math></p> <p><math>T_{water} = 280.15 \text{ K}</math></p> <p><math>P = 7 \text{ MPa}</math></p>	<p>Methane hydrate dissociation under various conditions of pressure, temperature, volumetric flow rate of water was observed in order to gain insight into the flow fields, the temperature distribution, and the rate of dissociation experimentally and numerically.</p>	<p>Occurrence of a laminar ring-type vortex in the wake, inhomogeneous methane distribution inside hydrate, and increased temperature from center to wall of the hydrate ball were observed. Moreover, the flow rate and the pressure were discovered to have limited impact on the dissociation rate while it was affected by the temperature changes.</p>
<p><b>Nazridoust et al. (2007)</b></p>	<p>Axisymmetric porous core sample with the length of 300 mm</p> <p>Surrounding, <math>h = 16.6 \text{ W/m}^2 \cdot \text{K}</math></p> 	<p>CFD (ANSYS-FLUENT), 3-D, The VOF Method, The Corey's Model.</p>	<p>Methane hydrate, ideal methane gas, liquid water</p> <p><math>T_{initial,core} = 275.45 \text{ K}</math></p> <p><math>P_{initial} = 3.75 \text{ MPa}</math></p> <p><math>P_{outlet} = 2.84 - 3.28 \text{ MPa}</math></p> <p><math>h = 16.6 \text{ W/(m}^2\text{K)}</math></p>	<p>Relating gas hydrate dissociation to core temperatures, pressures, and permeability, a 3-D computational study was conducted by observing the axisymmetric core sample with hydrate, gas and water phases.</p>	<p>Increase in temperature and decrease in pressure led to growth in hydrate dissociation rate since low temperature and high-pressure conditions are required to form gas hydrate.</p>

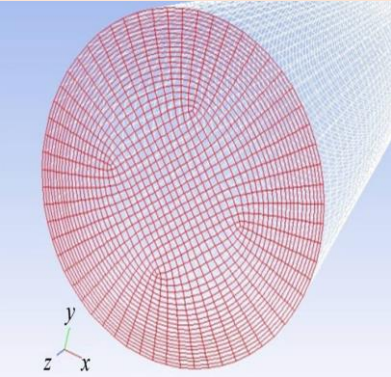
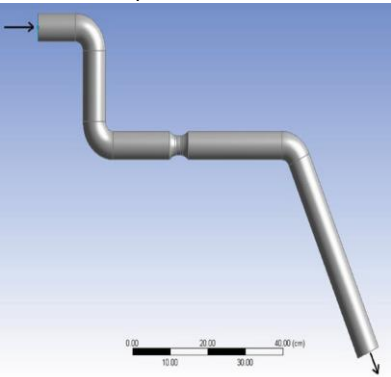
<p><b>Fatnes (2010)</b></p>	<p>90-degree bend with 45.2 mm diameter, 450 mm horizontal length, 200 mm vertical length and 105 mm radii</p> 	<p>CFD (OpenFOAM), 3-D, Roscoe-Brinkmann Correlation, Expression Derived by Krieger-Dougherty, <math>k-\epsilon</math> Model, Second Order Backward Euler Numerical Scheme, A Bounded Second Order Scheme, Gidaspow Drag Model, Kinetic Theory Particle Collision Model, Gidaspow Solid Pressure Particle Collision Model.</p>	<p>Two-phase flow with water as a continuous phase and hydrate as a dispersed phase.</p> <p><math>\rho_{water} = 1000 \text{ kg/m}^3</math></p> <p><math>\rho_{hydrate} = 1140 \text{ kg/m}^3</math></p> <p><math>U = 0.1 - 1 \text{ m/s}</math></p>	<p>The computational study was performed based on Eulerian-Eulerian approach with the purpose of investigating hydrate deposition and bed formation behaviors. CFD study was set up based upon an experimental study to allow comparison of the associated results.</p>	<p>Results of numerical simulations were similar to the experimental findings, i.e. the particle size had substantial effect on the deposition and bed thickness of hydrate formation. As the particle size increased, the impact of gravity force on the particle was bigger, and consequently, the deposition rate and the bed thickness were higher.</p>
<p><b>Balakin et al. (2011)</b></p>	<p>Experimental flow loop with three 90-degree bends</p> 	<p>Experimental and CFD (STAR-CD), 3-D, Unsteady, Eulerian-Eulerian Model, Standard <math>k-\epsilon</math> Model, Upwind-Differencing Scheme, Euler Implicit Technique, SIMPLE Algorithm, PBM Model.</p>	<p>Homogenous flow regime of trichlorofluoromethane (Freon R11) hydrate and water</p> <p><math>U_{initial} = 0 \text{ m/s}</math></p> <p><math>P_{initial} = P_{atm}</math></p> <p><math>U_{mean} = 0.4 - 4 \text{ m/s}</math></p>	<p>Mean particle size, frictional pressure drop, deposited bed thickness, and effect of the velocity and solid stress model on the bed thickness were evaluated by conducting an experimental and numerical study.</p>	<p>The important parameter which was effective on the hydrate formation, particle size and the deposited bed thickness was discovered to be the flow velocity. The lower velocity caused accumulation of the gas hydrate with the bigger particle size and thicker bed formation.</p>

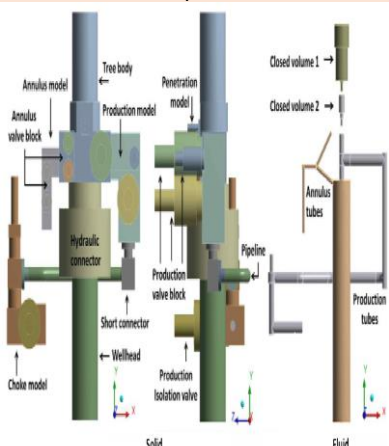
<p><b>Lo (2011)</b></p>	<p>Horizontal channel with the length of 1 m and the depth of 0.01 m</p>  <p><math>T_{wall} = 7\text{ }^{\circ}\text{C}</math></p>	<p>CFD (pro-STAR), 2-D, Unsteady, Eulerian Multiphase Flow Modelling Approach.</p>	<p>Oil, gas and water</p> <p><math>T_{hydrate\ formation} = 15.6\text{ }^{\circ}\text{C}</math></p> <p><math>T_{inlet} = 16\text{ }^{\circ}\text{C}</math></p> <p><math>U_{inlet} = 1\text{ m/s}</math></p> <p><math>D_{gas\ bubble} = 0.05\text{ mm}</math></p> <p><math>D_{water\ hydrate} = 0.04\text{ mm}</math></p>	<p>A computational study was conducted to investigate the hydrate formation in oil-dominated multiphase flows.</p>	<p>It was observed that there was no hazard to form hydrate in the entrance region thanks to the elevated temperature conditions.</p>
<p><b>Naseer and Brandstätter (2011)</b></p>	<p>Straight horizontal with downhill and uphill sections in flow direction</p> 	<p>CFD (ANSYS-FLUENT), 3-D, Unsteady, Multiphase, Mixture Model Theory, <math>k-\epsilon</math> Model, PISO Algorithm.</p>	<p>Water and vapor</p> <p>Water vapor volume fraction = 0.2</p> <p>Water vapor mass fraction = 0.866</p> <p><math>T_{inlet} = 315\text{ K}</math></p> <p><math>P_{inlet} = 6.3\text{ MPa}</math></p> <p><math>U_{inlet} = 2\text{ m/s}</math></p>	<p>The study was conducted to specify which parts of the pipeline were receptive to hydrate formation and determine the effects of presence of hydrate on mixture viscosity, mixture velocity, static pressure and dynamic pressure.</p>	<p>Hydrate formation tended to occur at the lower section of the pipeline before the uphill segment. Hydrate formation led to decrease in mixture viscosity, mixture velocity and dynamic pressure while increase in static pressure.</p>

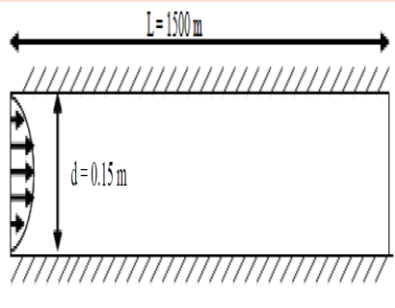
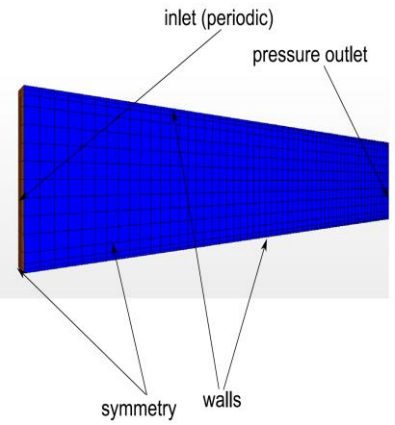


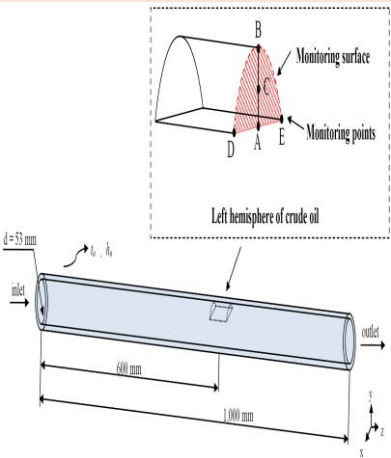
<p><b>Sallehud-din (2012)</b></p>	<p>Four internal pipelines surrounded by an outer pipeline</p>  <p><math>T_{wall} = \text{fixed}</math>  <math>L_{pipe} = 3 \text{ m}</math>  <math>t_{wall} = 15 \text{ mm}</math></p>	<p>CFD (ANSYS-CFX &amp; STAR-CCM+), Steady State, 2-D (horizontal) and 3-D (inclined &amp; vertical), SST Turbulence Model, Boussinesq Buoyancy Model, Monte Carlo Radiation Model, Navier-Stokes Equations, Total Energy Heat Transfer Model.</p>	<p>Water was inside the “product” pipe</p> <p>Air-Nitrogen was within the internal pipes</p>	<p>Heat transfer into or from the bundle pipeline system which was actively heated by using hot fluid circulation calculated to predict the possibility of the hydrate formation.</p>	<p>Increase in possibility of hydrate formation with the increase of the inclination angle of the pipeline system due to growth in heat transfer from the product pipe to the ocean was concluded.</p>
<p><b>Ding et al. (2012)</b></p>	<p>Straight horizontal pipe with 90° branch</p>  <p><math>D = 23 \text{ mm}</math></p>	<p>CFD (ANSYS-FLUENT), Steady-State, Algebraic Slip Mixture Model, SIMPLE Algorithm, High-Re Number <math>k-\epsilon</math> Model.</p>	<p>Fluid mixture with 0.9 oil and 0.1 water</p> <p><math>U_{inlet} = 0.75 - 5 \text{ m/s}</math></p>	<p>The main aim of the study was to investigate how the average inlet fluid velocity influences stratification of the fluid mixture and water concentration in the dead-leg.</p>	<p>Rise in the length of the mixing zone was linked with the increase in the average inlet velocity. Besides, the higher water fraction regions were observed as to be sections which the fluid with lower velocities were located.</p>



<p><b>Li et al. (2015)</b></p>	<p>Vertical pipe with length of 10 m</p> 	<p>CFD-PBM Model, 3-D, Euler Model, RNG <math>k-\epsilon</math> Model, SIMPLE Algorithm, First-Order Upwind Differencing Scheme.</p>	<p>Methane, hydrate and water</p>	<p>Distribution of phases within the pipeline and the change in the mean flow velocity were investigated with respect to the bubble size using two different models (Euler and CFD-PBM). Experimental results were used to validate the accuracy of the computational outcomes.</p>	<p>Based on the common consequences, gas and solid phases were observed mostly at the center of the pipe, and the more uniform flow distribution was sighted when the bubble size was larger.</p>
<p><b>Sule et al. (2015)</b></p>	<p>Two 90° and one 60° bends, and constriction part</p>  <p><math>D_{pipe} = 6 - 7 - 8 - 9 \text{ cm}</math>  <math>D_{constriction} = 4 \text{ cm}</math>  <math>L_{pipe} = 1.37 \text{ m}</math>  <math>T_{wall} = 1 \text{ }^\circ\text{C}</math></p>	<p>CFD (ANSYS-CFX), 3-D, Steady State, <math>k-\epsilon</math> Model, Total Energy Heat Transfer Model, Mixture Model Theory.</p>	<p>Compressible homogenous fluid (10% water, 90% gas)</p> <p><math>\rho = 0.7905 \text{ kg/m}^3</math></p> <p><math>h = 945.5 \text{ J/mol}</math></p> <p><math>T_{inlet} = 18 \text{ }^\circ\text{C}</math></p> <p><math>U_{inlet} = 10 \text{ m/s}</math></p> <p><math>P_{average} = 3.2 \text{ MPa}</math></p>	<p>Parametric study of hydrate formation scenarios was conducted by observing dependence of temperature drop on average velocity, diameter, viscosity, and water fraction.</p>	<p>Average temperature drop declined with increasing velocity until some certain value, water fraction, diameter, and decreasing viscosity. The outer segment of the bends and the pipe constriction were observed as more vulnerable for hydrate formation because of higher temperature drops.</p>

<p><b>Hu et al. (2015)</b></p>	<p>Subsea Christmas tree assembly with several components</p> 	<p>CFD (ANSYS-FLUENT), 3-D, Steady-State, Low-<i>Re</i> Number <i>k-ε</i> Model, SIMPLE Algorithm, Second-Order Central, Differencing Scheme, Second-Order Upwind Differencing Scheme.</p>	<p>Incompressible hydrocarbon fluid</p> <p><math>H_{location} = 1500 \text{ m}</math></p> <p><math>T_{ambient} = 4^\circ\text{C}</math></p> <p><math>U_{sea} = 0.05 - 0.45 \text{ m/s}</math></p> <p><math>T_{oil} = 30 - 120^\circ\text{C}</math></p>	<p>Effects of installation orientation, the sea water velocity and the inner oil temperature on the convection heat transfer was figured out. Also, installation orientation affecting the flow characteristics were evaluated.</p>	<p>Installation orientation was figured out as a significant factor which affected the convection heat transfer coefficient, whereas it did not play an important role on the temperature distribution. Rising sea water velocity and the inner oil temperature brought on the increase in the heat transfer rate from the Xmas tree but not at the same level for all components.</p>
<p><b>Guo et al. (2016)</b></p>	<p><math>H_{water} = 1504 \text{ m}</math>  <math>H_{well} = 4094 \text{ m}</math>  <math>D_{wellboreinner} = 0.12 \text{ m}</math></p>	<p>CFD (OLGA), Unsteady, Temperature and Pressure Model, Natural Gas Hydrate, Equilibrium Model, Prediction Method of Natural Gas Hydrate Formation Area in Wellbore.</p>	<p>Gas with liquid droplets and film</p> <p><math>P_{bottomhole} = 41.8 \text{ MPa}</math></p> <p><math>T_{bottomhole} = 80.3^\circ\text{C}</math></p> <p><math>T_{subsea} = 2.5^\circ\text{C}</math></p> <p><math>C_{formation} = 1900 \text{ J/kg}^\circ\text{C}</math></p> <p><math>k_{formation} = 1.745 \text{ W/m}^\circ\text{C}</math></p> <p><math>C_{wellbore} = 500 \text{ J/kg}^\circ\text{C}</math></p> <p><math>k_{wellbore} = 50 \text{ W/m}^\circ\text{C}</math></p> <p><math>\rho = 7850 \text{ kg/m}^3</math></p>	<p>Natural gas production wellbore was observed with the variable amount of flow rate, the insulation materials with different thicknesses and thermal conductivities, downhole throttling, the duration of the well shut-in, and the addition of hydrate inhibitors.</p>	<p>It was shown that the gas hydrate formation decreased with increased flow rate with regard to gas production, insulation thickness, and hydrate inhibitors addition. Otherwise, drop insulation thermal conductivity and the well shut-in time decreased the hydrate formation inside the wellbore.</p>

<p><b>Rukthong et al. (2016)</b></p>	<p>Horizontal pipeline</p> 	<p>CFD (ANSYS-FLUENT), 2-D, SIMPLE Algorithm, First-Order Upwind Scheme, Tri-Diagonal Matrix Algorithm, Laminar Flow.</p>	<p>Crude oil</p> $T_{inlet} = 50\text{ }^{\circ}\text{C}$ $T_{surrounding} = 35\text{ }^{\circ}\text{C}$ $P_{outlet} = 101.325\text{ Pa}$ $\dot{m}_{inlet} = 133\text{ barrel/day}$	<p>Crude oil flow profile during transportation and wax appearance were examined related to the dynamic viscosity, density, heat capacity and thermal conductivity properties of the crude oil.</p>	<p>Crude oil lost heat during its transportation due to the temperature difference between the fluid and the environment. The temperature drop led to wax occurrence at some location of the pipeline. Position of wax formation was connected to the fluid density and heat capacity proportionally.</p>
<p><b>Balakin et al. (2016)</b></p>	<p>Rectangular domain (which is 1 m long and 10.2 cm high)</p> 	<p>CFD-PBM Model (STAR-CCM+), 3-D, Eulerian-Eulerian Model, <math>k-\epsilon</math> Model, SIMPLE Algorithm, Upwind Differencing Schemes.</p>	<p>Three-phase flow of oil, water and gas</p> $T_{inlet} = 4\text{ }^{\circ}\text{C}$ $T_{outlet} = 3\text{ }^{\circ}\text{C}$ $T_{walls} = 3\text{ }^{\circ}\text{C}$ $\rho_{hydrate} = 807.77\text{ kg/m}^3$ $\rho_{water} = 1000\text{ kg/m}^3$ $\rho_{oil} = 768\text{ kg/m}^3$	<p>The process from hydrate formation through deposition was studied using the CSMHyK model. The particle size distribution and the change in the viscosity were focused in order to gain insight on the hydrate settling profile.</p>	<p>Although some differences between two models on the particle size distribution and phase separation were found, the common result was that hydrate showed a tendency to locate at the bottom section of the domain, and accordingly, the viscosity was found higher where hydrate formation occurred.</p>

<p><b>Liu et al. (2017)</b></p>	<p>Pipe</p> 	<p>CFD (ANSYS-FLUENT), Unsteady, High-<i>Re</i> Number <i>k-ε</i> Model, SIMPLE Numerical Method, Second-Order Upwind Differencing Scheme, The Standard Scheme.</p>	<p>Oil and water as a fluid phase and crude oil as a solid phase</p> <p><math>\rho_{crudeoil} = 889.9 \text{ kg/m}^3</math>  <math>Cp_{crudeoil} = 2000 \text{ J/kg K}</math>  <math>k_{crudeoil} = 0.2 \text{ W/mK}</math>  <math>\mu_{crudeoil} = 0.05 \text{ Pa s}</math>  <math>T_{water} = 50 - 60 - 70 \text{ }^\circ\text{C}</math>  <math>U_{water} = 0.1 - 0.2 - 0.3 \text{ m/s}</math>  <math>\dot{m} = 0.05 - 0.3 \text{ m}^3/\text{s}</math></p>	<p>The melting process of solid crude oil located in a pipeline containing oil and water liquid phases was studied with regard to various temperatures, flow rates and velocities.</p>	<p>It was inferred that all the higher temperature, flow rate and flow velocity provide the faster melting of crude oil block inside the oil-water two-phase flow.</p>
---------------------------------	---	---	--	--	--

CFD=Computational Fluid Dynamics; PBM=Population Balance Model; PISO=Pressure-Implicit with Splitting of Operators; SIMPLE=Semi-Implicit Method for Pressure-Linked Equations; SST=Shear Stress Transport; VOF=Volume-of-Fluid

### 2.3. Closure

Having reviewed a number of relevant experimental and computational studies focusing on multi-phase flows including dead-legs, there appears to be a need for a more detailed analysis of oil separation from an oil/water stream and accumulation of oil within a dead-leg. The remaining Chapters are devoted to reporting of the results of the present computational and experimental investigation devoted to this subject.

### 3. Computational Methodology for Study of Phase Separation in Multiphase Systems and Oil Accumulation in Dead-Legs

In this Chapter, an outline of the practices for utilizing dead-legs in subsea oil and gas exploration/processing systems are provided. Two- and three-dimensional models of typical dead-leg systems at various inclination angles will be presented. The governing transport relations for multiphase flow inside pipelines will be summarized along with an outline of the OpenFOAM computational fluid dynamics (CFD) platform used for solutions of these equations. Simple benchmark cases of developing laminar channel/pipe flows and behavior of immiscible fluid systems which are relevant to the present study will be discussed.

#### 3.1. Dead-Legs

One important practice in the oil and gas industry is utilization of a branching finite-length pipeline called a dead-leg which can take form of a line closed by a fitting, stagnant control valve, bypass piping, chemical injection lines, etc. Dead-leg is a critical pipeline element in relation to hydrate formation since water accumulates by separating from oil due to low or zero fluid velocity at some part of the dead-leg. When enough amount of water meets hydrocarbon gases at the hydrate formation temperature and pressure conditions, gas hydrate starts forming and eventually blocks the pipeline. It is suggested to remove it when possible, or shorten the length of the deadleg as much as possible to avoid stagnant or low velocity flow. The present study reports the computational findings related to investigation of water/oil flow in typical deadleg configurations and accumulation of oil within the dead-leg.





Figure 3.1. Typical subsea pipeline systems and associated components in oil and gas fields  
[Oil States, 2019]

### 3.2. Geometry of Physical Models

Oil and gas processing equipment and sub-components are extremely complex and demand resolution of the geometric details. Whereas 3-D modeling is widely adopted in industrial scenarios in order to save computational resources and obtain insights into effects of various parameters (average inlet velocity, length of the dead-leg, width of the dead-leg, position of the dead-leg relative to the inlet of the feed channel, viscosity of crude oil and density of crude oil) on oil separation within deadlegs and their stagnant zones, a baseline 2-D model was first developed and a grid independence study was conducted in the present study. The baseline model was created as a horizontal channel with a vertical capped T-branch located at a downstream position, assuring fully-developed flow before the T-branch. The width of the horizontal and vertical channels was equal with  $D = 0.12$  m. The channel length before the dead-leg was  $80D$ , while the length of the downstream channel section was  $10D$ . The length of the branching dead-leg was taken as  $10D$ . The adopted 2-D channel geometry for a vertical dead-leg is shown in Figure 3.2 along with the adopted  $xyz$  coordinates. It must be noted that for the 2-D model only vertical dead-legs pointing in the  $+y$  or  $-y$  (direction of gravitational acceleration) directions can be considered. The 3-D pipe system in the vicinity of the branching pipe is shown in Figure 3.3. It should be noted for 3-D model, the inclination angle of the dead-leg can be varied.



Figure 3.2. Baseline two-dimensional model of the horizontal channel and the branching vertical dead-leg (gravity points the -y direction)



Figure 3.3. Three-dimensional model of the horizontal pipe and the branching vertical dead-leg (gravity points in the -y direction, however it can be at any orientation on the yz plane)

### 3.3. Multiphase Flows

Multiphase flows, i.e. the simultaneous flows of more than one phase of matter, are found in a wide range of naturally-observed situations and industrial applications, e.g. particulate flows in the atmosphere, chemical and petroleum industries, etc. For example, gas-liquid two-phase flows occur in distillation, absorption, and evaporation; liquid-liquid two-phase flows in extraction; and various two-phase and three-phase flows in heterogeneous chemical reactions in the petrochemical industry. Among these multiphase flows, there is particular interest in the flows encountered in the oil production industry, where crude oil, mixed with natural gas, water, and (occasionally) sand, emerges from wells [Yang et al., 2006].

Pipelines with multiphase flow of gas, oil, and water flowing through them are commonly used in the oil and gas industry [Peeters, 2016]. This type of flow is frequently found in oil-producing wells and associated pipelines. Most well fluids are composed of oil and gas; however, water fraction increases during the production life of a well [Xu, 2007]. From the point of gas hydrate formation, plugging tendency increases as the *water cut* (a term used in the petroleum industry to define the ratio of the water compared to the volume of the total liquids produced) grows since there is a higher likelihood that sufficient hydrate particles will contact each other and stick together.

Multiphase flow describes multi-component systems in which the interaction among the different components have major influence on the overall flow structure. In oil and gas industry, the multiphase flow is the combined flow of gas, oil and water in a pipe [Irmann-Jacobsen, 2012].

### 3.4. Solution of Turbulent Flows Through Application of Direct Numerical Simulations (DNS), Large Eddy Simulation (LES) and Reynolds-Averaged Navier-Stokes (RANS)

Classically, three methods for numerically simulating the Navier-Stokes equations are available [Murakami, 1998] when turbulence fluctuations are present (Figure 3.4). The first method to model turbulence is by using the Direct Numerical Simulations approach. This method resolves all scales up to the scale of the smallest eddies (the Kolmogorov scales) and can therefore be regarded as an exact solution. Unfortunately, the DNS has a computational cost of the order of  $Re^3$  [Pope, 2010] and is therefore deemed to be not yet feasible for high Reynolds number flows [Scardovelli and Zaleski, 1999]. Another method of turbulence simulation is by using the Large Eddy Simulation approach. CFD calculations utilizing LES only resolve the large energy-containing structures in the flow and use a sub-grid scale to model the small dissipative scales. One of the common methods for simulating turbulence is by using the Reynolds-Averaged Navier-Stokes equations with the addition of a closure model for the Reynolds stress terms. In adopting the RANS approach, the flow-related variables are decomposed into an average part and a fluctuating component, i.e.  $u(t) = \bar{u}(t) + u'(t)$  (Figure 3.4).

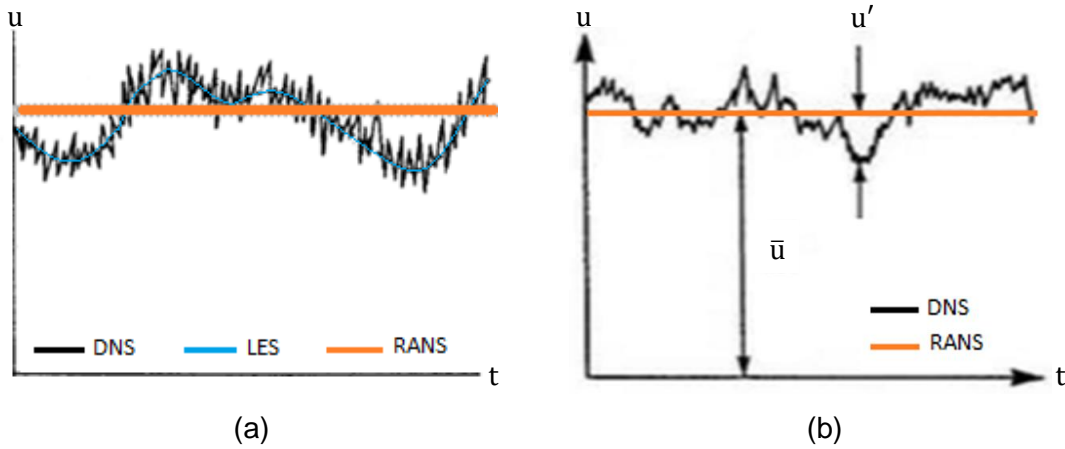


Figure 3.4. (a) Comparison of the DNS, LES, RANS turbulence modeling methods and (b) the mean ( $\bar{u}$ ) and fluctuating ( $u'$ ) velocities [Scardovelli and Zaleski, 1999]

Dropping the averaging symbol for the velocity components ( $u_i$ ) from this point forward, the continuity and RANS equations for an incompressible ( $\rho=\text{constant}$ ) Newtonian fluid using the index notation are:

$$\frac{\partial u_i}{\partial x_i} = 0 \quad (3.1)$$

$$\rho \frac{\partial u_i}{\partial t} + \rho u_j \frac{\partial u_i}{\partial x_j} = -\frac{\partial \bar{p}}{\partial x_i} + \frac{\partial (\tau_{ij} + \tau_{tj})}{\partial x_j} + \bar{f}_i \quad (3.2)$$

with  $\bar{f}_i$  and  $\bar{p}$  being a vector representing external forces and the averaged thermodynamic pressure, respectively.

The mean laminar viscous stress,  $\tau_{ij}$  is:

$$\tau_{ij} = \mu \left[ \left( \frac{\partial u_i}{\partial x_j} + \frac{\partial u_j}{\partial x_i} \right) \right] \quad (3.3)$$

with  $\mu$  and  $\delta_{ij}$  standing for dynamic viscosity of the fluid and the Kronecker delta, respectively.

The Reynolds stress tensor (i.e. turbulent stress),  $\tau_{tij}$  is given by:

$$\tau_{tij} = 2\mu_t S_{ij} - \frac{2}{3} \rho k \delta_{ij} \quad (3.4)$$

with  $\mu_t$  standing for the turbulent (eddy) viscosity of the fluid, the mean strain rate tensor,  $S_{ij}$  expressed as:

$$S_{ij} = \frac{1}{2} \left( \frac{\partial u_i}{\partial x_j} + \frac{\partial u_j}{\partial x_i} \right) \quad (3.5)$$

and turbulent kinetic energy,  $k = 1/2(\overline{u'^2} + \overline{v'^2} + \overline{w'^2})$  ( $\text{m}^2/\text{s}^2$ ) characterizing the intensity of velocity fluctuations in three directions.

Combining relations 3.3 and 3.4;

$$\begin{aligned} \tau_{ij} + \tau_{tij} &= \mu \left[ \left( \frac{\partial u_i}{\partial x_j} + \frac{\partial u_j}{\partial x_i} \right) \right] + 2\mu_t S_{ij} - \frac{2}{3} \rho k \delta_{ij} \\ \tau_{ij} + \tau_{tij} &= \mu \left[ \left( \frac{\partial u_i}{\partial x_j} + \frac{\partial u_j}{\partial x_i} \right) \right] + 2\mu_t \left[ \frac{1}{2} \left( \frac{\partial u_i}{\partial x_j} + \frac{\partial u_j}{\partial x_i} \right) \right] - \frac{2}{3} \rho k \delta_{ij} \\ \tau_{ij} + \tau_{tij} &= \mu \left[ \left( \frac{\partial u_i}{\partial x_j} + \frac{\partial u_j}{\partial x_i} \right) \right] + \mu_t \left( \frac{\partial u_i}{\partial x_j} + \frac{\partial u_j}{\partial x_i} \right) - \frac{2}{3} \rho k \delta_{ij} \\ \tau_{ij} + \tau_{tij} &= (\mu + \mu_t) \left( \frac{\partial u_i}{\partial x_j} + \frac{\partial u_j}{\partial x_i} \right) - \frac{2}{3} \rho k \delta_{ij}. \end{aligned} \quad (3.6)$$

Defining the effective dynamic viscosity  $\mu_{eff} = \mu_t + \mu$ , one gets:

$$\tau_{ij} + \tau_{tij} = \mu_{eff} \left( \frac{\partial u_i}{\partial x_j} + \frac{\partial u_j}{\partial x_i} \right) - \frac{2}{3} \rho k \delta_{ij} \quad (3.7)$$

Substitution of relation 3.7 into the momentum relation 3.2 leads to;

$$\rho \frac{\partial u_i}{\partial t} + \rho u_j \frac{\partial u_i}{\partial x_j} = -\frac{\partial \bar{p}}{\partial x_i} + \frac{\partial}{\partial x_j} \left( \mu_{eff} \left( \frac{\partial u_i}{\partial x_j} + \frac{\partial u_j}{\partial x_i} \right) - \frac{2}{3} \rho k \delta_{ij} \right) + \bar{f}_i. \quad (3.8)$$

### 3.5. Turbulence Closure Models

The Reynolds number which is the ratio of the inertia force to the viscous force is an important dimensionless quantity that characterizes the dominant flow regime. The dominant flow regime is predicted based on the critical  $Re$  number which differs for every geometry, imposed boundary and initial conditions. The  $Re$  number above the critical value leads to a radical change in the flow

character. This regime is referred to as turbulent flow, which is chaotic, highly diffusive causing rapid mixing, time-dependent, and involves 3-D fluctuations in vorticity with a broad range of time and length scales [Tennekes and Lumley, 1972].

There are four main types of turbulence models in order to calculate turbulence properties. The “zero-equation” (algebraic) models use an algebraic equation to compute a turbulent viscosity without the need to solve any differential equation for turbulence properties. The “one-equation” models require solving only one differential equation for a turbulence quantity to compute the turbulent eddy viscosity. The “two-equation” turbulence models necessitate the solution of two equations for turbulence properties in order to calculate the turbulent eddy viscosity. Turbulence closure models, e.g. the algebraic stress models and the Reynolds stress models are the most computationally expensive as separate differential equations for turbulence quantities are solved for the individual turbulent fluxes.

### 3.5.1. The High-Reynolds Number $k - \varepsilon$ Turbulence Model

The high- $Re$  number  $k - \varepsilon$  model of Launder and Spalding (1973) which is also known as the standard  $k - \varepsilon$  turbulence model or the  $k - \varepsilon$  model is an example of the two-equation group of turbulence models. The variable  $\varepsilon$  is known as the rate of dissipation of turbulence kinetic energy per unit mass due to viscous stress. The flow is assumed to be fully turbulent in the derivation of the standard  $k - \varepsilon$  model and the effect of molecular viscosity is negligible. The standard  $k - \varepsilon$  model is therefore a high- $Re$  number turbulence model valid only for fully turbulent free shear flows that cannot be integrated all the way to the solid wall. The turbulent viscosity formulated as:

$$\mu_t = C_\mu \rho k^2 / \varepsilon \quad (3.9)$$

with:

$C_\mu$  : model constant (0.09).

The transport equation for the turbulent kinetic energy is:

$$\frac{\partial}{\partial t}(\rho k) + \nabla \cdot (\rho \bar{u} k) = \nabla \cdot [\mu_{eff,k} \nabla k] + P_k - \rho \varepsilon \quad (3.11)$$

with:

$$\mu_{eff,k} = \mu + \mu_t / \sigma_k$$

$$P_k = \mu_t \nabla \bar{u} \cdot (\nabla \bar{u} + \nabla \bar{u}^T) .$$

The transport equation for the turbulent energy dissipation rate is:

$$\frac{\partial}{\partial t}(\rho \varepsilon) + \nabla \cdot (\rho \bar{u} \varepsilon) = \nabla \cdot [\mu_{eff,\varepsilon} \nabla \varepsilon] + C_{\varepsilon 1} P_k \varepsilon / k - C_{\varepsilon 2} \rho \varepsilon^2 / k \quad (3.12)$$

with:

$$\mu_{eff,\varepsilon} = \mu + \mu_t / \sigma_\varepsilon$$

$\frac{\partial}{\partial t}(\rho k)$	: rate of change of $k$ at a fixed position
$\nabla \cdot (\rho \bar{u} k)$	: transport of $k$ by convection
$\nabla \cdot [\mu_{eff,k} \nabla k]$	: transport of $k$ by diffusion
$\frac{\partial}{\partial t}(\rho \varepsilon)$	: rate of change of $\varepsilon$ at a fixed position
$\nabla \cdot (\rho \bar{u} \varepsilon)$	: transport of $\varepsilon$ by convection
$\nabla \cdot [\mu_{eff,\varepsilon} \nabla \varepsilon]$	: transport of $\varepsilon$ by diffusion
$\rho \varepsilon$ and $C_{\varepsilon 2} \rho \varepsilon^2 / k$	: rate of destruction
$\mu_{eff,k}$	: effective viscosity for $k$
$\mu_{eff,\varepsilon}$	: effective viscosity for $\varepsilon$
$P_k$	: production of turbulent energy term
$\sigma_k$	: model constant (1.0)
$\sigma_\varepsilon$	: model constant (1.3)
$C_{\varepsilon 1}$	: model constant (1.44)
$C_{\varepsilon 2}$	: model constant (1.92)
$C_{\varepsilon 3}$	: model constant (-0.33).

### 3.5.2. The Low-Reynolds Number $k - \varepsilon$ Turbulence Model

Modeling flows near solid walls require integration of the two equations for turbulence quantities over a finely-resolved grid system to accurately capture the turbulent quantities within the shearing layer. A turbulence model that can be integrated all the way to the wall is called a low- $Re$  number turbulence model (e.g., Launder and Sharma, 1974). The idea behind their development is to dampen the turbulent viscosity near the wall through the use of a damping function that tends towards zero as the distance to the wall decreases, i.e.:

$$\mu_t = C_\mu f_\mu \rho k^2 / \varepsilon$$

$$f_\mu = \exp[-3.4 / (1 + R_t / 50)^2]$$

with:

$f_\mu$  : damping function

$\vartheta$  : kinematic viscosity ( $m^2/s$ ).

Quantity  $R_t$  being the local turbulence Reynolds number,  $R_t = k^2/(\vartheta\varepsilon)$ , the damping function becomes:

$$f_\mu = \exp[-3.4/(1 + k^2/(50\vartheta\varepsilon))^2].$$

For the low- $Re$  number model, the modified turbulent kinetic energy and dissipation rate are

$$\frac{\partial}{\partial t}(\rho k) + \nabla \cdot (\rho \bar{u}k) = \nabla \cdot [\mu_{eff,k} \nabla k] + P_k - \rho(\varepsilon + D) \quad (3.13)$$

$$\frac{\partial}{\partial t}(\rho \varepsilon) + \nabla \cdot (\rho \bar{u}\varepsilon) = \nabla \cdot [\mu_{eff,\varepsilon} \nabla \varepsilon] + C_{\varepsilon 1} f_{\varepsilon 1} \rho P_k \varepsilon / k - C_{\varepsilon 2} f_{\varepsilon 2} \rho \varepsilon^2 / k + \rho E \quad (3.14)$$

with:

$$D = 2\vartheta \left( \frac{\partial \sqrt{k}}{\partial y} \right)^2$$

$$E = 2\vartheta \vartheta_t \left( \frac{\partial^2 u}{\partial y^2} \right)^2$$

$$\vartheta_t = C_\mu f_\mu k^2 / \varepsilon$$

$$f_{\varepsilon 1} = 1$$

$$f_{\varepsilon 2} = 1 - 0.3 \exp[-(k^2/(\vartheta\varepsilon))^2]$$

$D$  : a parameter for the Launder-Sharma low- $Re$  number turbulence model

$f_{\varepsilon 1}$  : damping function

$f_{\varepsilon 2}$  : damping function.

### 3.5.3. The Shear Stress Transport $k - \omega$ Turbulence Model

Denoting the specific turbulence dissipation,  $\omega$ , the Shear Stress Transport (SST)  $k - \omega$  turbulence model combines the  $k - \omega$  model which is robust near a wall surface and the  $k - \varepsilon$  model which gives improved solution near the boundary layer edge and away from walls due to its insensitivity to the freestream values. The SST  $k - \omega$  turbulence model of Menter (2003) is adopted by the OpenFOAM CFD code.

The turbulent viscosity in the SST  $k - \omega$  model is:

$$\mu_t = \rho \alpha_1 k / \max(\alpha_1 \omega, b_1 S_t F_2) \quad (3.15)$$

with:

$$S_t = \sqrt{2S_{ij}S_{ij}}$$

$$F_2 = \tanh(\phi_2^2)$$

$$\phi_2 = \max[(2\sqrt{k}/\beta^* \omega(d_\perp), 500\vartheta/(d_\perp)^2 \omega]$$

- $Pr_t$  : turbulent Prandtl number (1)  
 $\alpha_1$  : model coefficient (0.31)  
 $b_1$  : model coefficient (1)  
 $S_t$  : magnitude of the strain rate  
 $F_2$  : blending function (the weight function)  
 $d_{\perp}$  : distance from the nearest wall (m)  
 $max$  : higher value between two quantities.

To maintain the original formulation of the eddy-viscosity for free shear layers, a blending function approach is adopted in the SST  $k - \omega$  turbulence model. The blending function has a value of unity in the freestream and zero in the boundary layer. This is how the  $k - \omega$  model is activated in the boundary layer and turned off in the freestream.

For the shear stress transport  $k - \omega$  turbulence model, the turbulent kinetic energy equation is:

$$\frac{\partial}{\partial t}(\rho k) + \nabla \cdot (\rho \bar{u} k) = \nabla \cdot [\mu_{eff,k} \nabla k] + S^k \quad (3.16)$$

with:

$$\mu_{eff,k} = \mu + \mu_t \sigma_{k3}$$

$$\sigma_{k3} = F_1 \sigma_{k1} + (1 - F_1) \sigma_{k2}$$

$$\sigma_{k1} = 0.85$$

$$\sigma_{k2} = 1$$

$$S^k = \tilde{P}_k - \beta^* \rho k \omega$$

$$\tilde{P}_k = \min(P_k, c_1 \beta^* \rho k \omega)$$

$$P_k = \tau_{ij} \frac{\partial u_i}{\partial x_j}$$

$$\tau_{ij} = \mu_t \left( 2S_{ij} - \frac{2}{3} \frac{\partial u_k}{\partial x_k} \delta_{ij} \right) - \frac{2}{3} \rho k \delta_{ij}$$

$$c_1 = 10$$

$min$  : lower value between two quantities.

The specific turbulence dissipation,  $\omega$ :

$$\frac{\partial}{\partial t}(\rho \omega) + \nabla \cdot (\rho \bar{u} \omega) = \nabla \cdot [\mu_{eff,\omega} \nabla \omega] + S^\omega \quad (3.17)$$

with:

$$\mu_{eff,\omega} = \mu + \mu_t \sigma_{w3}$$

$$\sigma_{w3} = F_1 \sigma_{w1} + (1 - F_1) \sigma_{w2}$$

$$S^\omega = \gamma \omega \tilde{P}_k / k - \beta \rho \omega^2 - \rho (F_1 - 1) CD_{k\omega}$$



$$\gamma = F_1\gamma_1 + (1 - F_1)\gamma_2$$

$$\beta = F_1\beta_1 + (1 - F_1)\beta_2$$

$$F_1 = \tanh(\phi_1^4)$$

$$\phi_1 = \min[\max[\sqrt{k}/\beta^* \omega(d_\perp), 500\vartheta/(d_\perp)^2 \omega], 4\rho\sigma_{\omega 2}k/CD_{k\omega}^+(d_\perp)^2]$$

$$CD_{k\omega}^+ = \max[CD_{k\omega}, 10^{-10}] = \max[2\sigma_{\omega 2}\nabla k \cdot \nabla \omega/\omega, 10^{-10}]$$

$$CD_{k\omega} = 2\sigma_{\omega 2}\nabla k \cdot \nabla \omega/\omega$$

$\mu_{eff,\omega}$  : effective turbulent viscosity for  $\omega$

$\tilde{P}_k$  : modified production of turbulence kinetic energy

$\gamma$  : model coefficient, relation given above

$\gamma_1$  : model coefficient (5/9)

$\gamma_2$  : model coefficient (0.44)

$\beta^*$  : model coefficient (0.09)

$\beta$  : model coefficient, relation given above

$\beta_1$  : model coefficient (0.075)

$\beta_2$  : model coefficient (0.0828)

$F_1$  : blending function (the weight function)

$CD_{k\omega}^+$  : positive portion of the cross-diffusion term

$\sigma_{k1}$  : model coefficient (0.85)

$\sigma_{k2}$  : model coefficient (1)

$\sigma_{\omega 1}$  : model coefficient (0.5)

$\sigma_{\omega 2}$  : model coefficient (0.856)

$c_1$  : model coefficient (10).

### 3.6. Wall functions and wall coordinate $y^+$

Consider the generic case of viscous flow over a horizontal flat plate (Figure 3.5). The fluid is stationary on the non-moving solid wall due to the no-slip condition. The fluid close to the wall is retarded, and eventually a turbulent boundary layer forms. The turbulent boundary layer can be divided into three regions (Figure 3.5) based on dimensionless wall coordinates,  $y^+$ , namely:

$y^+ < 5$	the viscous sublayer
$5 < y^+ < 30$	the buffer sublayer
$30 < y^+ < 300$	the logarithmic or log-law region or inertial sublayer

with:

$$y^+ = u_\tau \cdot y / \nu$$

$$u_\tau = \sqrt{\tau_w / \rho}$$

$$\tau_w = 0.5 C_f \rho U_\infty^2$$

$$C_f = 0.079 Re^{-0.25}$$

$$u^+ = u_i / u_\tau$$

- $u_\tau$  : shear (friction) velocity (m/s)
- $y$  : distance from the wall to the cell center of the first cell in the mesh (m)
- $\tau_w$  : wall shear stress (kg/ms<sup>2</sup>)
- $C_f$  : skin friction coefficient for internal pipe flow
- $U_\infty$  : free stream velocity (m/s)
- $Re$  : Reynolds number based on distance from the leading edge
- $u^+$  : dimensionless velocity
- $u_i$  : local velocity (m/s).

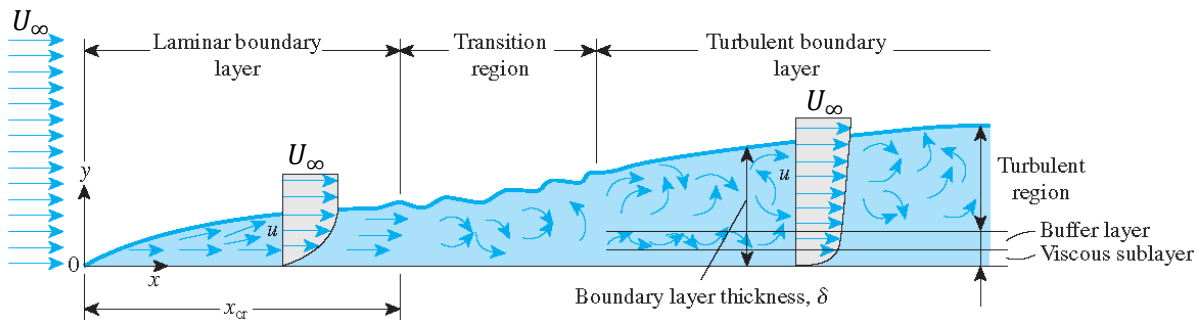


Figure 3.5. Turbulent boundary layers [Çengel and Cimbala, 2006]

Turbulence is negligible, and viscous forces dominate in the viscous sublayer. The mean flow velocity in this region is a linear function of the distance from the wall and  $u^+ = y^+$ . The low- $Re$  number turbulence models are capable of simulating the dampening effects of the wall. However, fully resolving the viscous sublayer is computationally expensive since the thickness of the layer is so small and a very fine mesh is needed.

Outside the viscous sublayer, the buffer layer occurs in which both turbulence and viscous effects are important. In this region, the transition to turbulent flow begins. There is no analytical solution for the velocity in this region. Since it is very difficult to model the flow in the buffer region,

turbulence models avoid the buffer layer near a wall by placing the first internal grid point either in the viscous or the inertial sublayer.

The high computational cost of solving flow parameters in viscous sublayer can be avoided by the use of so-called the wall functions. The center of the first cell is placed in the log-law region and it is adopted with the high- $Re$  number turbulence models. The flow in the logarithmic region is fully turbulent, and viscous effects are small in this sublayer. The average flow velocity in this region is related to the logarithm of the distance to the wall, i.e.  $u^+ = \ln(Ey^+)/\kappa$ ,  $\kappa$  is the von Karman's constant (0.41) and  $E$  is a model constant (9.8 for the smooth walls).

### 3.7. OpenFOAM Computational Fluid Dynamics Package

Computational Fluid Dynamics (CFD) is a collective term for analysis of fluid flow, heat transfer and other transport phenomena using computer simulations. Open Source Field Operations and Manipulation (OpenFOAM) which is an open-source CFD package is used in the present study for multiphase flow calculations. The OpenFOAM computer code is a C++ library of source codes for solvers and utilities. Three directories are located in the root of the case folder which are identified as "0", "constant" and "system". The initial conditions and the boundary conditions are specified with sub-directories in folder "0". The "constant" folder contains the properties of fluid(s), flow characteristics, and the grid distribution. The "system" folder is associated with the solution procedure.

OpenFOAM solvers that handle multiphase systems are dependent upon the Volume-of-Fluid (VOF) method which is based on the numerical method called the Finite Volume Method (FVM) which discretizes a volume of interest (computational domain) to solve the relevant partial differential equations for calculation of the temporally- and spatially-resolved variables. The VOF method can be used for modeling multiphase flow of immiscible fluids by solving a single set of momentum equations and tracking the volume fraction of each of the fluids throughout the domain.

In order to gain experience and become familiar with the inner working of OpenFOAM, including pre-processing, post-processing using ParaView, preliminary benchmarking studies involving;

- a. Steady-state, single-phase laminar flows in straight channel/pipes,
- b. Unsteady, multiphase flow of immiscible fluids,

were conducted. These simple studies are deemed pertinent to the topic of this study and the relevant details are summarized in Appendix A.

### 3.8. Adopted Methodology for Solution of Two-Phase Immiscible Fluids in Channel/Pipes Including Dead-Legs

Unsteady, turbulent behavior of the multiphase flows is a challenging problem in science and engineering. Utilizing the continuum approach, consider a mixture composed of a number of components ( $i$ ), each with their density ( $\rho_i$ , also called phase density, kg/m<sup>3</sup>). The fraction of volume occupied by constituent  $i$  is identified as  $\alpha_i$ , also called the phase fraction. Therefore,  $\sum \alpha_i = 1$ . The pertinent two-phase continuity and momentum relations were solved using the open-source computational software OpenFOAM. The solver for incompressible, isothermal immiscible fluid flow called interFoam was used to solve the Navier-Stokes equations.

Considering the fluid velocity  $\bar{u}$  (m/s), the continuity relation is [Currie, 2016]:

$$\frac{\partial(\alpha_i \rho_i)}{\partial t} + \nabla \cdot (\alpha_i \rho_i \bar{u}) = 0 \quad (3.18)$$

Applying vector operations and introducing the Lagrangian derivative will lead to;

$$\alpha_i \frac{\partial(\rho_i)}{\partial t} + \rho_i \frac{\partial(\alpha_i)}{\partial t} + \rho_i \nabla \cdot (\alpha_i \bar{u}) + \alpha_i \bar{u} \cdot \nabla(\rho_i) = 0. \quad (3.19)$$

Denoting terms forming the Lagrangian derivative:  $\alpha_i \frac{\partial(\rho_i)}{\partial t} + \alpha_i \bar{u} \cdot \nabla(\rho_i) = \alpha_i \frac{D\rho_i}{Dt}$ , one gets:

$$\begin{aligned} \rho_i \frac{\partial(\alpha_i)}{\partial t} + \rho_i \nabla \cdot (\alpha_i \bar{u}) + \alpha_i \frac{D\rho_i}{Dt} &= 0 \\ \frac{\partial(\alpha_i)}{\partial t} + \nabla \cdot (\alpha_i \bar{u}) + \frac{\alpha_i D\rho_i}{\rho_i Dt} &= 0 \\ \frac{\partial(\alpha_i)}{\partial t} + \alpha_i \nabla \cdot (\bar{u}) + \bar{u} \cdot \nabla(\alpha_i) + \frac{\alpha_i D\rho_i}{\rho_i Dt} &= 0. \end{aligned} \quad (3.20)$$

For a divergence-free fluid, i.e.  $\nabla \cdot (\bar{u}) = 0$  and  $\frac{D\rho_i}{Dt} = 0$ , equation 3.20 becomes;

$$\frac{\partial(\alpha_i)}{\partial t} + \bar{u} \cdot \nabla(\alpha_i) = 0. \quad (3.21)$$

The momentum equation is:

$$\rho \frac{\partial \bar{u}}{\partial t} + \nabla \cdot (\rho \bar{u} \bar{u}) = -\nabla \bar{p} + \nabla \cdot (\mu_{eff} (\nabla \bar{u} + \nabla \bar{u}^T)) + \rho \bar{g} + \bar{f}_s \quad (3.22)$$

with:

$\bar{g}$  : gravitational acceleration (m/s<sup>2</sup>)

$\bar{f}_s$  : surface tension force (N)

with the values of density and dynamic viscosity evaluated from the mixture rule.

#### 3.8.1. Two-Phase Mixture Relations

The flow-related quantities are calculated based on the properties of the fluids and their fractions in the mixture. For the two-phase oil-water fluid system considered in this investigation,  $i$  stands for crude oil and water phases. Recalling  $\alpha_{crude\ oil} + \alpha_{water} = 1$ , the mixture density is:

$$\rho = \sum \alpha_i \rho_i$$

$$\rho = \alpha_{crude\ oil} \rho_{crude\ oil} + \alpha_{water} \rho_{water} \quad (3.23)$$

where  $\rho_{crude\ oil}$ ,  $\rho_{water}$ ,  $\alpha_{crude\ oil}$  and  $\alpha_{water}$  are the densities and volumetric fractions of crude oil and water, respectively.

The mixture dynamic viscosity is evaluated using:

$$\mu = \sum \alpha_i \mu_i$$

$$\mu = \alpha_{crude\ oil} \mu_{crude\ oil} + \alpha_{water} \mu_{water} \quad (3.24)$$

where  $\mu_{crude\ oil}$  and  $\mu_{water}$  are the dynamic viscosities of crude oil and water, respectively.

### 3.8.2. Interface-capturing equation

In the present study, we utilized interFoam that is a solver for handling two incompressible, isothermal immiscible fluids using a VOF phase-fraction based interface capturing approach. The algebraic slip mixture model [Manninen et al., 1996] which emphasizes that the relative velocity is calculated from an algebraic relation rather than solving the pertinent phase velocities was utilized for modeling of the two immiscible fluids (water and crude oil).

### 3.9. Closure

Upon introducing the rationale behind utilization of dead-legs in subsea oil and gas exploration systems, details of 2-D and 3-D channel/pipe models with dead-legs were discussed. Transport relations governing multiphase flows within these systems were discussed in addition to coverage of turbulence closure models used for simulating turbulent flows. A broad outline of the open source CFD code (OpenFOAM) was provided. The two-phase flow relations utilized for the present oil-water system along with utilization of the interFoam solver were given. The specific computational results for 2-D and 3-D channel/pipe models including a vertical dead-leg will be discussed in the next Chapter.

#### 4. Effects of Flow Characteristics and Geometry of a Capped Dead-Leg on Separation of Phases from a Two-Phase Flow

In this Chapter, a parametric study of the unsteady turbulent two-phase flow behavior of crude oil in model subsea 2-D channel and 3-D pipe systems are investigated. This parametric study of the 2-D model is preferred in comparison to realistic 3-D subsea systems that are generally composed of pipes with circular cross-sections, in light of its low cost of computational resources while maintaining the general features of the governing physical mechanisms. In effect, the influence of the relative importance of various parameters can be determined at a lower cost. Consequently, the effects of the important parameters can then be studied in greater detail for 3-D two-phase flow systems.

##### 4.1. Baseline Two-Dimensional Channel and the Dead-Leg System

A dead-leg which is an inactive part of a subsea petroleum production system can be a line closed by a fitting, by-pass piping, chemical injection line and so on in a typical drilling pipeline system. Even though existence of this kind of section in the pipeline system causes many serious problems, dead-legs are still needed for the purpose of being able to reach the main pipe and perform required processes where necessary. Since the fluid velocity is very low or even zero within a dead-leg, lighter oil separates from the mixture and can rise up in a dead-leg with inclined orientations, while water sinks in consequence of its higher density and gravity effect, accumulating at the intersection part of the vertical dead-leg and horizontal main channel/pipe.

Pertinent two-phase continuity and momentum relations were solved using the open-source computational software OpenFOAM. The solver called interFoam which is suitable for incompressible, isothermal immiscible fluids was used to solve the Navier-Stokes equations using the volume-of-fluid (VOF) method. The baseline 2-D channel model was presented in section 3.1 along with a schematic diagram (Figure 3.2). A model vertical capped dead-leg branch is positioned at a downstream position. The widths of the horizontal and vertical channels were equal to  $D = 0.12$  m. The channel length before the dead-leg was  $80D$ , while the length of the downstream channel section was  $10D$ . The length of the branching dead-leg was taken as  $10D$ . The model fluid consists of 90%-10% slurry of 32.8 °API crude oil-water at the inlet port of the horizontal channel. The initial condition of the computational domain was set to

be that of motionless homogenous 90%-10% oil-water slurry, and the same proportions of oil/water (90/10) were maintained at the upstream inlet port throughout the simulations. In light of utilization of the standard  $k - \varepsilon$  model, the wall coordinates of the next-to-the-wall grids were monitored for consistency with the adopted model.

The velocity distribution was considered uniform at the inlet port of the two-dimensional channel and a constant pressure was defined at the outlet of the horizontal channel/pipe. At the wall boundaries, velocity components were set to zero in accordance with the no-slip condition.

#### 4.1.1. Grid Independence Study for the 2-D Planar Geometry Simulations

Grid independence tests were conducted for 2-D and 3-D geometries based on the Grid Convergence Method [Celik et al., 2008] that is based on the Richardson extrapolation method [Richardson, 1911; Richardson and Gaunt, 1927]. Details on the grid independence tests can be found in Appendix B.

As a first step, the grid size,  $h$  (m<sup>2</sup>), was calculated based on the total cell number,  $N$ , and the area of the  $i$ th cell,  $\Delta A_i$  (m<sup>2</sup>), for a 2-D case, i.e.

$$h = \left[ \frac{1}{N} \sum_{i=1}^N (\Delta A_i) \right]^{1/2}. \quad (4.1)$$

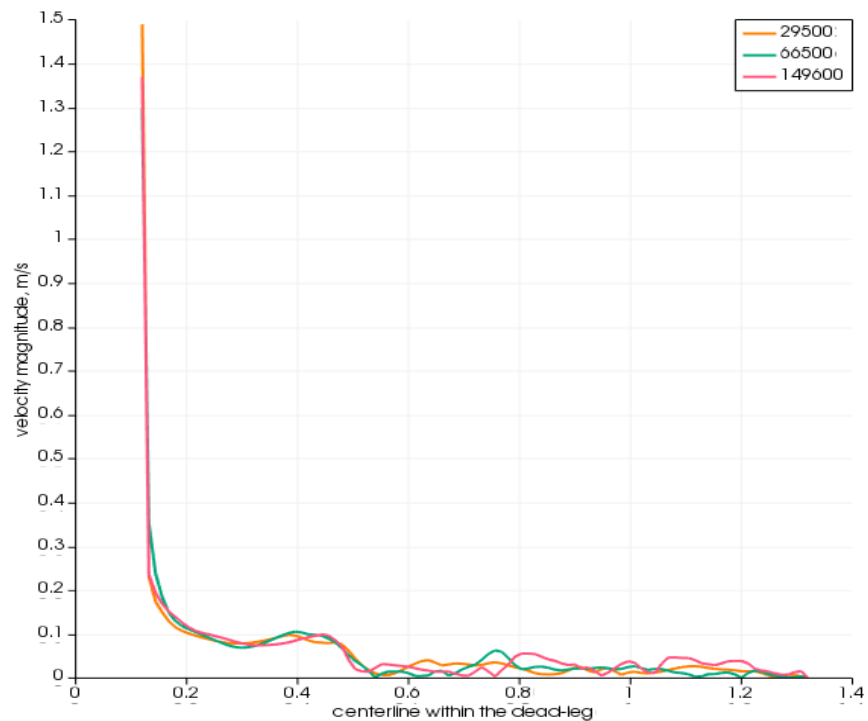
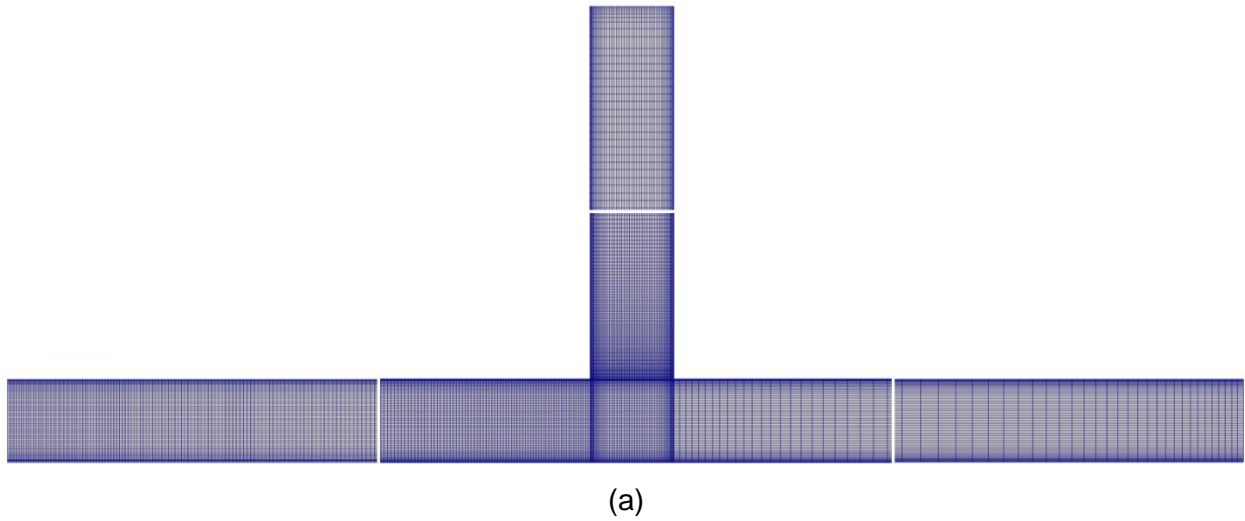
The grid refinement factor,  $r$ , was chosen equal to 2 based on the suggestion that it should be greater than 1.3 in order to allow the discretization error to be differentiated from other error sources such as the iterative convergence error and computer round-off error. Three different sets of grids (29,500, 66,500 and 149,600) were selected (Figure 4.1-a) and simulation results were obtained for the case which is two-phase 90%-10% oil-water mixture flow with the average inlet velocity of 3 m/s. Variations of the y-component of the velocity along the centerline of the dead-leg for these three grid cases are shown in Figure 4.1-b. The velocity field at  $x/D=100.5$  and  $y/D=0.15$  was chosen in order to calculate discretization error. The apparent order of the method was calculated to be 3.744 based on the simulated velocities for different grid numbers and refinement factors. The theoretical apparent order of the method is 2. The difference might be due to many reasons such as grid stretching, non-linearities in the solution, turbulence modeling, etc.

The grid convergence indices (GCI) were calculated for the coarse and medium grid systems to be around 0.0455% and for the medium and fine grid systems to be around 0.0034%. The GCI is a measure of the percentage of the computed value away from the value of the asymptotic numerical value. It indicates an error band as to how far the solution is from the asymptotic value and how much the solution would change with a further refinement. A small value of the GCI reveals that the calculation is within the asymptotic range [Slater, 2008].

Whether the solutions are within the asymptotic range of convergence was checked with;

$$GCI^{21}/r^p GCI^{32} = 0.0455/(2^{3.744}0.0034) \cong 0.99 \quad (4.2)$$

which indicates that the solutions are within the asymptotic range of convergence since the computed ratio is approximately equal to 1.



(b)

Figure 4.1. (a) Typical mesh of the 2-D geometry for the 66,500 medium-density grid system (origin  $x=y=0$  is located at the bottom wall of channel inlet) and (b) velocity magnitude variations along the centerline within the 2-D dead-leg for different grid densities



#### 4.1.2. Computational Results for the Baseline 2-D Channel with Dead-leg

Based on unsteady solution of the governing equations, the extent of the stagnant flow zone(s) and formation of vortices were investigated depending on the following baseline operating conditions (origin  $x=y=0$  is located at the bottom wall of channel inlet):

- (a) average inlet velocity (baseline value of  $V_i=3$  m/s),
- (b) length of the dead-leg (baseline value of  $10D=1.2$  m, extending from  $y/D=1$  to  $y/D=11$ ),
- (c) width of the dead-leg (baseline value of  $D=0.12$  m),
- (d) upstream position of the dead-leg relative to channel inlet (baseline value of  $x/D=80$ ),
- (e) viscosity of crude oil (baseline value of  $2 \times 10^{-6}$  m<sup>2</sup>/s corresponding to temperature of 100 °C) and
- (f) density of crude oil (baseline value of 830 kg/m<sup>3</sup> corresponding to temperature of 100 °C).

Using water density equal to 959.8 kg/m<sup>3</sup>, for a 90%-10% oil-water mixture the inlet  $Re=\rho D V_i/\mu=1.7 \times 10^5$ , with mixture density and viscosity evaluated from equations 3.23 and 3.24, respectively. The interfacial surface tension between oil and water was 0.03 N/m.

Turbulent properties of the flow were solved by using the standard  $k - \varepsilon$  model [Launder and Spalding, 1974]. The turbulent kinetic energy field was initialized at time  $t=0$  to:

$$k = \frac{3}{2} (I |u_{ref}|)^2 \quad (4.1)$$

where  $I$  and  $u_{ref}$  are the intensity ( $3.55 \times 10^{-2}$ ) and reference velocity (3 m/s), respectively. This level of turbulent kinetic energy was maintained through the simulations at the inlet plane of the channel (inlet boundary condition).

The dissipation of turbulent kinetic energy field was initialized at  $t=0$  to:

$$\varepsilon = \frac{C_\mu^{0.75} k^{1.5}}{L} \quad (4.2)$$

where  $L$  is a reference length scale (0.12 m) which is the inlet channel width. This level of dissipation of turbulent kinetic energy was maintained through the simulations at the inlet plane of the channel (inlet boundary condition).

Instantaneous streamline patterns corresponding to the baseline 2-D channel flow with a vertical dead-leg are presented in Figure 4.2. The streamline patterns are shown at time instants on 20

s, 30 s, 40 s, 50 s and 60 s. Starting with a motionless velocity field at time  $t=0$ , the turbulent flow within the main channel drives the formation of a slow-moving separated counter-clockwise rotating (CCW) vortex at early time instants. Later on, this vortex will itself lead to formation of many CW and CCW weaker vortices above it in the dead-leg as observed in Figure 4.2-a. Marching in time, the number, relative positions and strengths of these CW and CCW-rotating vortices changes markedly (Figs. 4.2b-e). The corresponding phase fractions at various time instants are shown in Figure 4.3. The noticeable variations of the phase field at the monitored time instants clearly points to the effect of the recirculating flow patterns in combination with the lower density of the oil phase that promote oil accumulation within the vertical dead-leg.

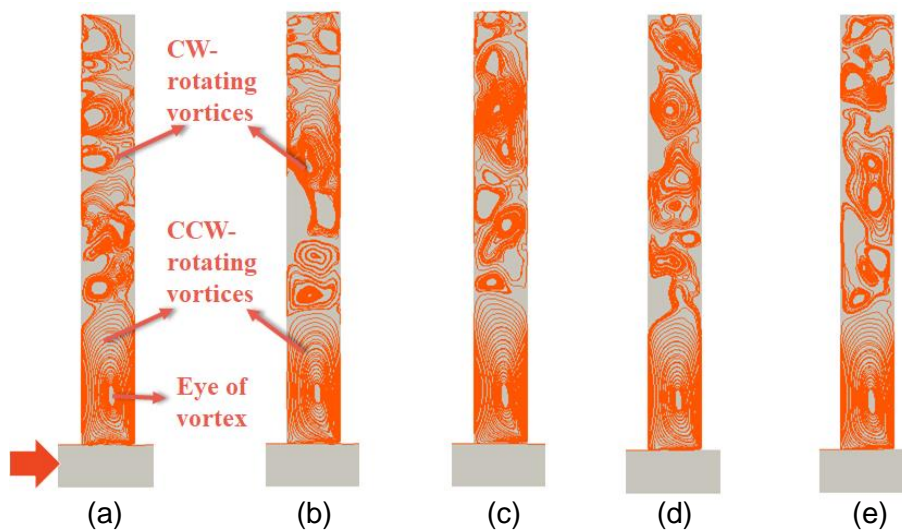


Figure 4.2 Instantaneous streamlines within the baseline 2-D capped dead-leg system ( $Re=1.7 \times 10^5$ ) at time instants of (a) 20 s, (b) 30 s, (c) 40 s, (d) 50 s and (e) 60 s

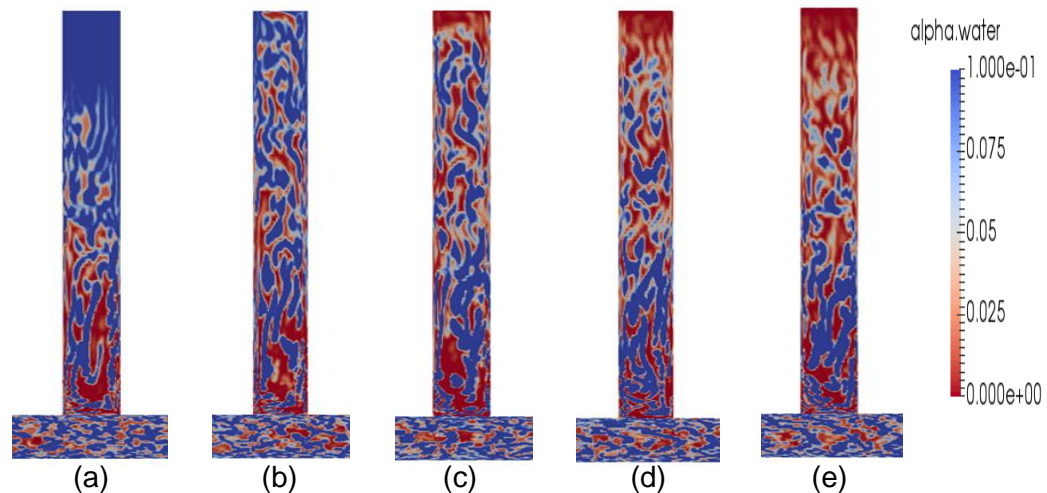


Figure 4.3. Typical variations of the phase fraction field within the baseline 2-D capped dead-leg system ( $Re=1.7 \times 10^5$ ) at time instants of (a) 20 s, (b) 30 s, (c) 40 s, (d) 50 s and (e) 60 s

Having discussed the general features of the flow and phase fraction fields within the channel with a vertical dead-leg, we now focus on a parametric study of the effects of a number of important geometric, flow and properties on oil accumulation.

#### 4.1.3. Effect of the Dead-Leg Length

The effect of the dead-leg length on unsteady phase separation and the stagnant flow zone(s) within the dead-leg was investigated based on the lengths of  $D$  (Case 1),  $2D$  (Case 2),  $4D$  (Case 3),  $6D$  (Case 4) and  $8D$  (Case 5). The width of the horizontal channel and vertical dead-leg was defined equal to  $0.12$  m corresponding to  $D$ . The length of the main channel before the dead-leg was kept equal to  $80D$  ( $9.6$  m) so as to achieve hydrodynamic fully-developed flow upstream of the dead-leg. The average inlet velocity for all cases were  $3$  m/s ( $Re = 171,884$ , corresponding to turbulent flow). The densities of crude oil and water were  $830$  and  $959.8$  kg/m<sup>3</sup>, respectively. Values of crude oil and water viscosities at the temperature of  $100$  °C were  $2 \times 10^{-6}$  and  $3 \times 10^{-7}$  m<sup>2</sup>/s, respectively.

The streamline patterns overlaid with the water concentration contours and velocity contours within the branching vertical dead-leg after  $60$  seconds for different dead-leg lengths are presented in Figures 4.4, 4.5 and 4.6, respectively. Due to the strong vortical motion of a dominant single counter-clockwise (CCW) rotating vortex, fluid velocity was high at the top, bottom and side regions of the dead-leg, while low velocity was observed in the middle of the dead-legs with shorter lengths equal to  $D$  and  $2D$  (see Figures 4.4 a-b exhibiting these streamlines). Such recirculating flow patterns tend to eliminate the stagnant fluid zone in the vertical dead-leg. As it is expected, the higher water fraction was observed at the bottom region of the dead-leg in consequence of its higher density and the influence of gravity. Besides, the relatively strong recirculating vortex led separated water to move higher into the dead-leg and almost the same amount of water located at the bottom was observed at the top of the dead-leg. When the length of the dead-leg was increased, the strength of the dominant vortex became weaker at the top by its decomposition into many smaller recirculating vortices in both CW- and CCW-rotating directions (Figure 4.4 c-d-e).

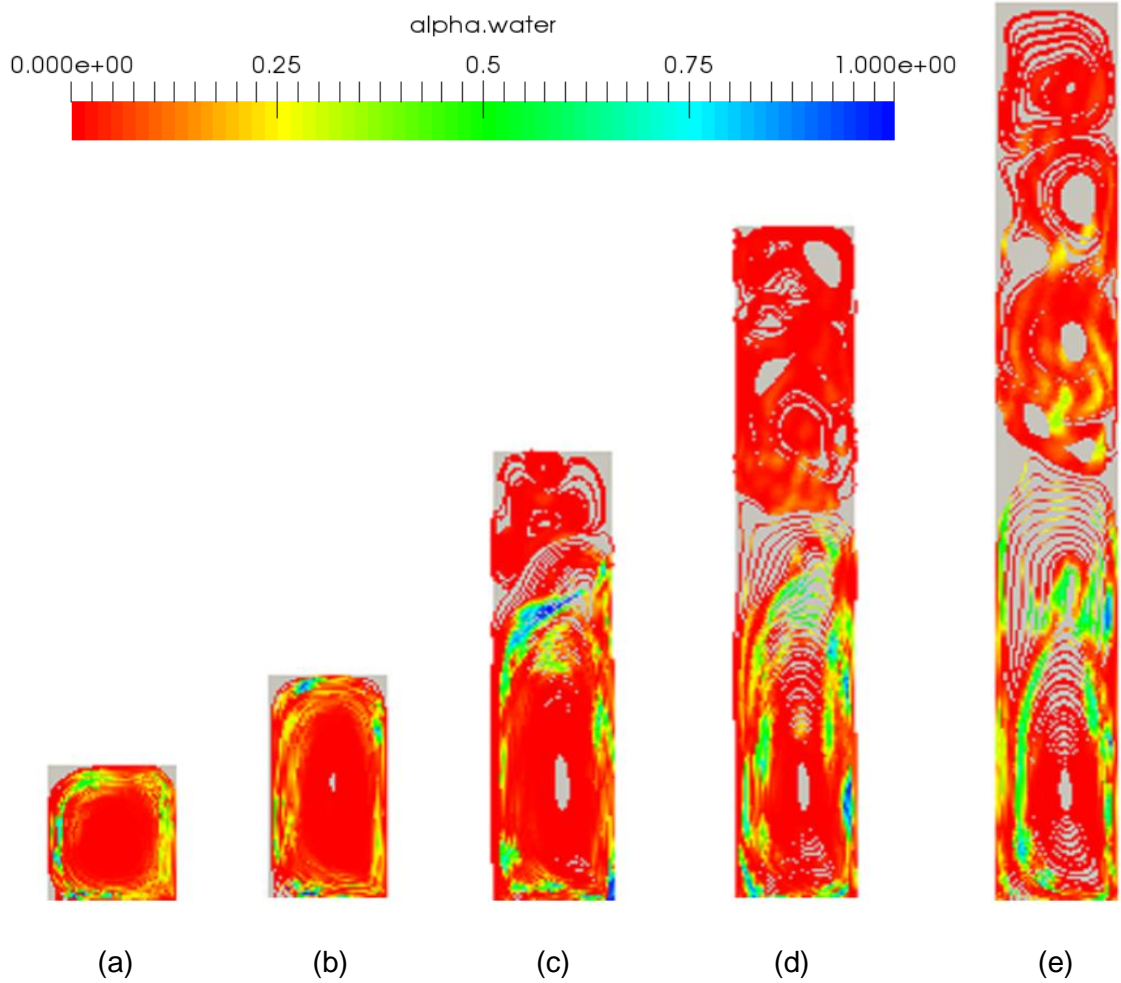


Figure 4.4 Streamline patterns overlaid with phase concentration contours after 60 seconds for dead-leg lengths equal to (a)  $D$ , (b)  $2D$ , (c)  $4D$ , (d)  $6D$  and (e)  $8D$

Since the size of the stagnant zone where the fluid was motionless or had a very low velocity was expanding with a longer dead-leg (Figure 4.5), the separated water zone moved downward and started accumulating at the intersection region.

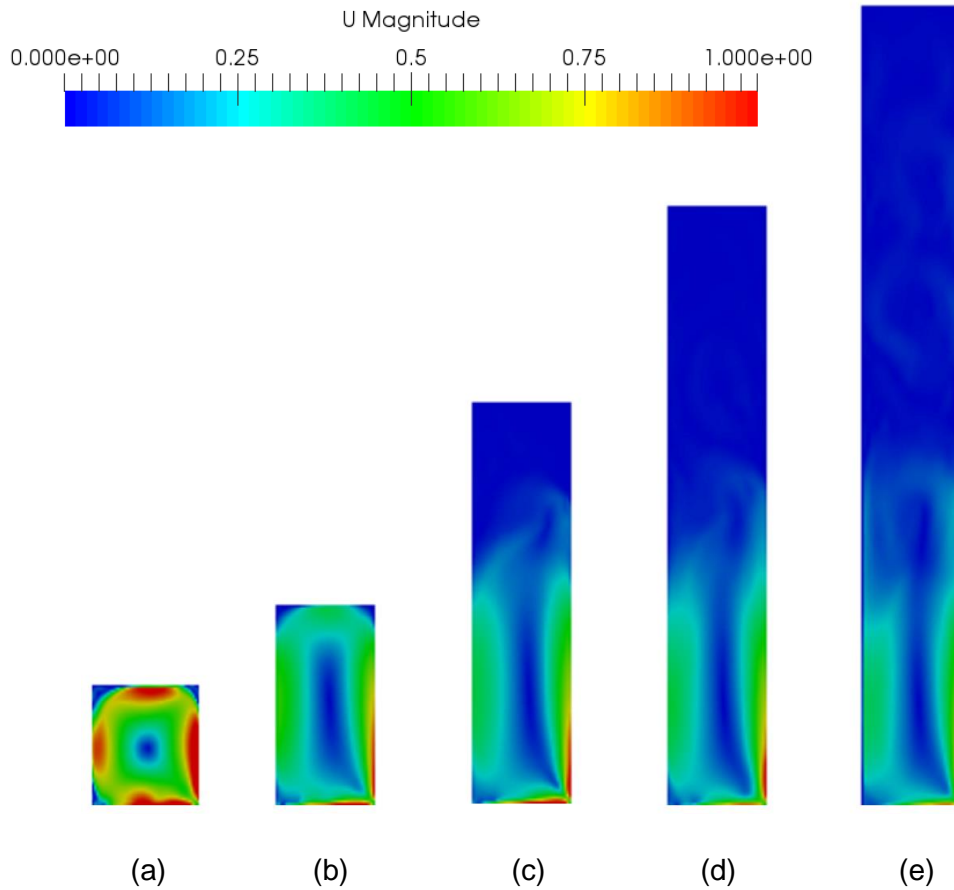


Figure 4.5 Velocity contours after 60 seconds for dead-leg lengths equal to (a)  $D$ , (b)  $2D$ , (c)  $4D$ , (d)  $6D$  and (e)  $8D$

As it can be seen clearly from Figure 4.6, the longest channel exhibited bigger and multiple near-stagnant recirculating zones. It is also obvious that the stacking of recirculating vortices induce velocity fluctuations in both positive and negative directions through the whole length of the dead-leg, indicative of existence of alternating CW- and CCW-rotating vortices.

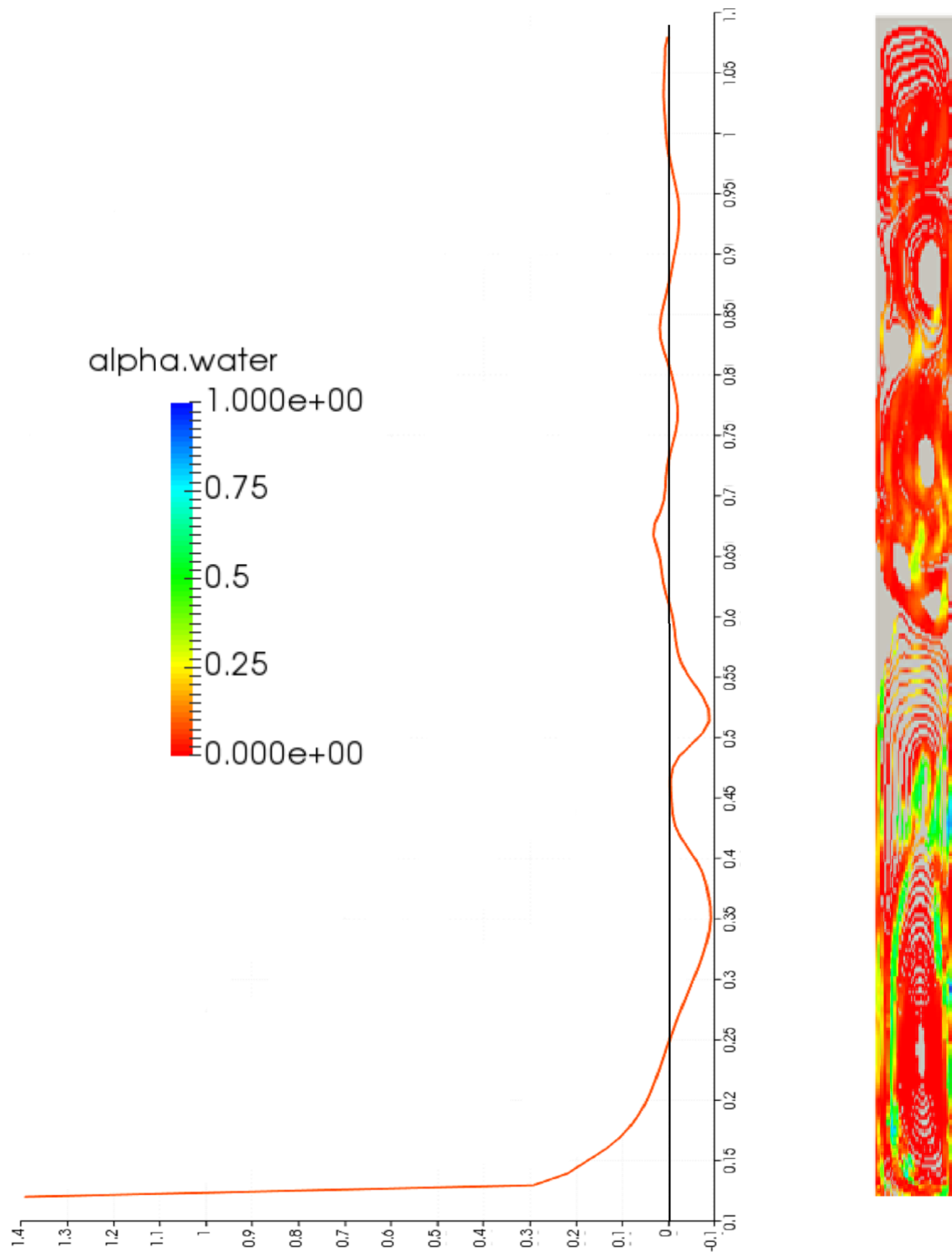


Figure 4.6 The x-component of the average velocity magnitude along the vertical dead-leg and the streamlines overlaid with phase concentration within the vertical dead-leg for the case of dead-leg length equal to  $8D$  at 60 seconds

It is obvious in Figure 4.7 that the dead-legs with lengths of  $D$  and  $2D$  had only two points with the zero velocity which were at the center of the recirculating region and the top wall of the dead-leg. On the other hand, the fluid had very low velocity or was stagnant at heights greater than  $0.2\text{ m}$  ( $D=0.12\text{ m}$ ) from the bottom of the dead-leg for the remaining of the dead-legs.

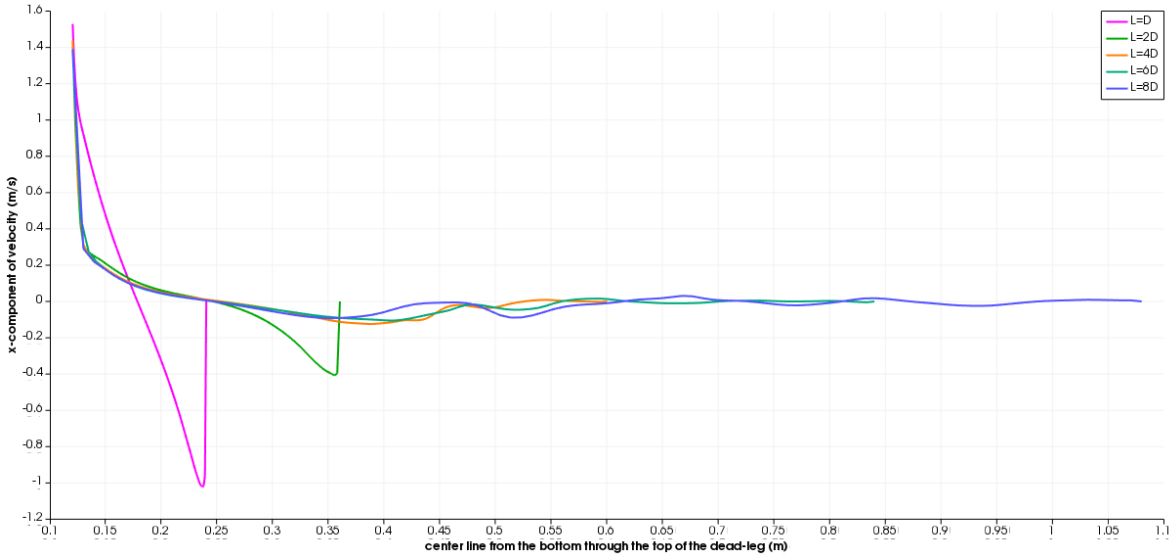


Figure 4.7 The x-component of the average velocity magnitude along the vertical dead-leg at 60 seconds for different dead-leg lengths

Figure 4.8 clearly illustrates that the longer dead-leg length also caused higher pressure difference between the top and bottom of the dead-leg due to the higher value of the vertical elevation. All figures represent the situations at the time instant of 60 seconds.

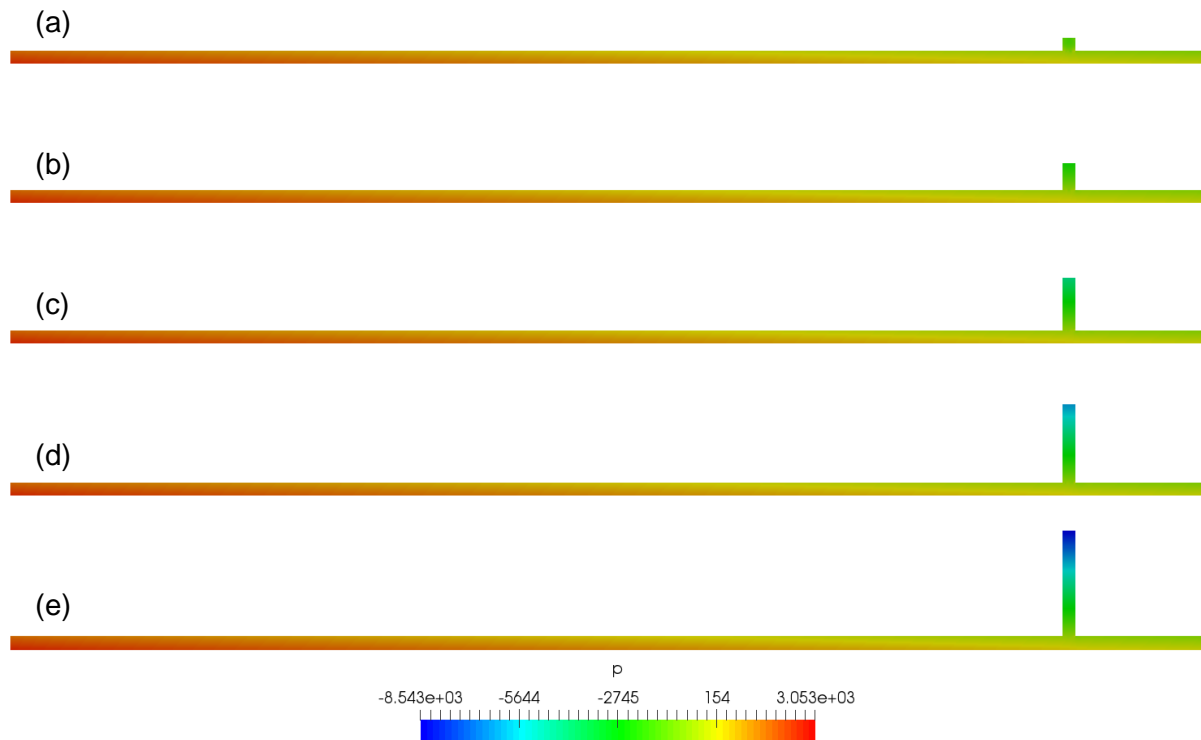


Figure 4.8 Pressure contours after 60 seconds for vertical dead-leg lengths equal to (a)  $D$ , (b)  $2D$ , (c)  $4D$ , (d)  $6D$  and (e)  $8D$

#### 4.1.4. Effect of the Dead-Leg Width

While keeping the width of the horizontal feed channel constant, the influence of the vertical dead-leg's width on the flow characteristics within the dead-leg was studied by changing the width of the dead-leg to  $D/2$  (Case1),  $2D$  (Case 2) and  $3D$  (Case 3). The width of the horizontal channel was defined to be equal to  $0.12$  m which is corresponding to  $D$ . The length of the main channel before the dead-leg was kept equal to  $80D$  ( $9.6$  m) so as to achieve hydrodynamically fully-developed flow upstream of the dead-leg. The average inlet velocity for all cases were  $3$  m/s ( $Re = 171,884$ , corresponding to turbulent flow). The densities of crude oil and water were  $830$  and  $959.8$  kg/m<sup>3</sup>, respectively. Crude oil and water viscosities at the temperature of  $100$  °C were set to  $2 \times 10^{-6}$  and  $3 \times 10^{-7}$  m<sup>2</sup>/s, respectively.

The streamline patterns superimposed with the water fraction contours and velocity contours within the branching dead-leg after 60 seconds for different vertical dead-leg widths are presented in Figures 4.9 and 4.10. Based on the computational findings, it was observed that the extent of the recirculating flow zone covered most of the entire length of the dead-leg when the dead-leg width was increased, and high-concentration water moved from the bottom of the



dead-leg to the middle and upper parts of the dead-leg. As might be expected, the low velocity flow field became smaller with the increase in the dead-leg width (Figure 4.10). As a result of longest stagnant zone, more oil separation was obtained in Case 1; however, oil separation was slower in that case due to existence of a large number of small recirculating vortices and frictional forces.

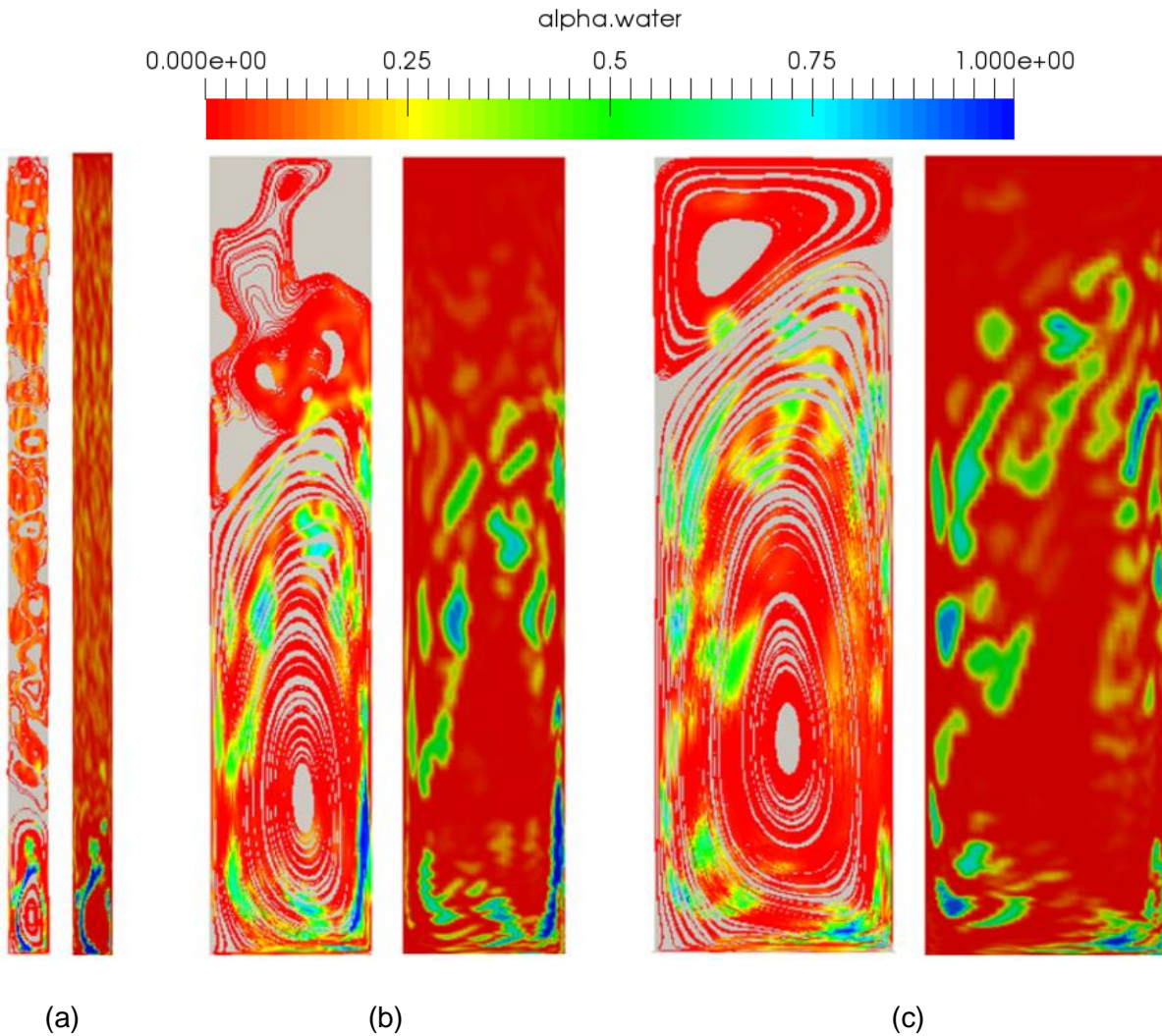


Figure 4.9 Streamline patterns superimposed on the phase fraction field after 60 seconds for vertical dead-leg widths equal to (a)  $D/2$ , (b)  $2D$  and (c)  $3D$

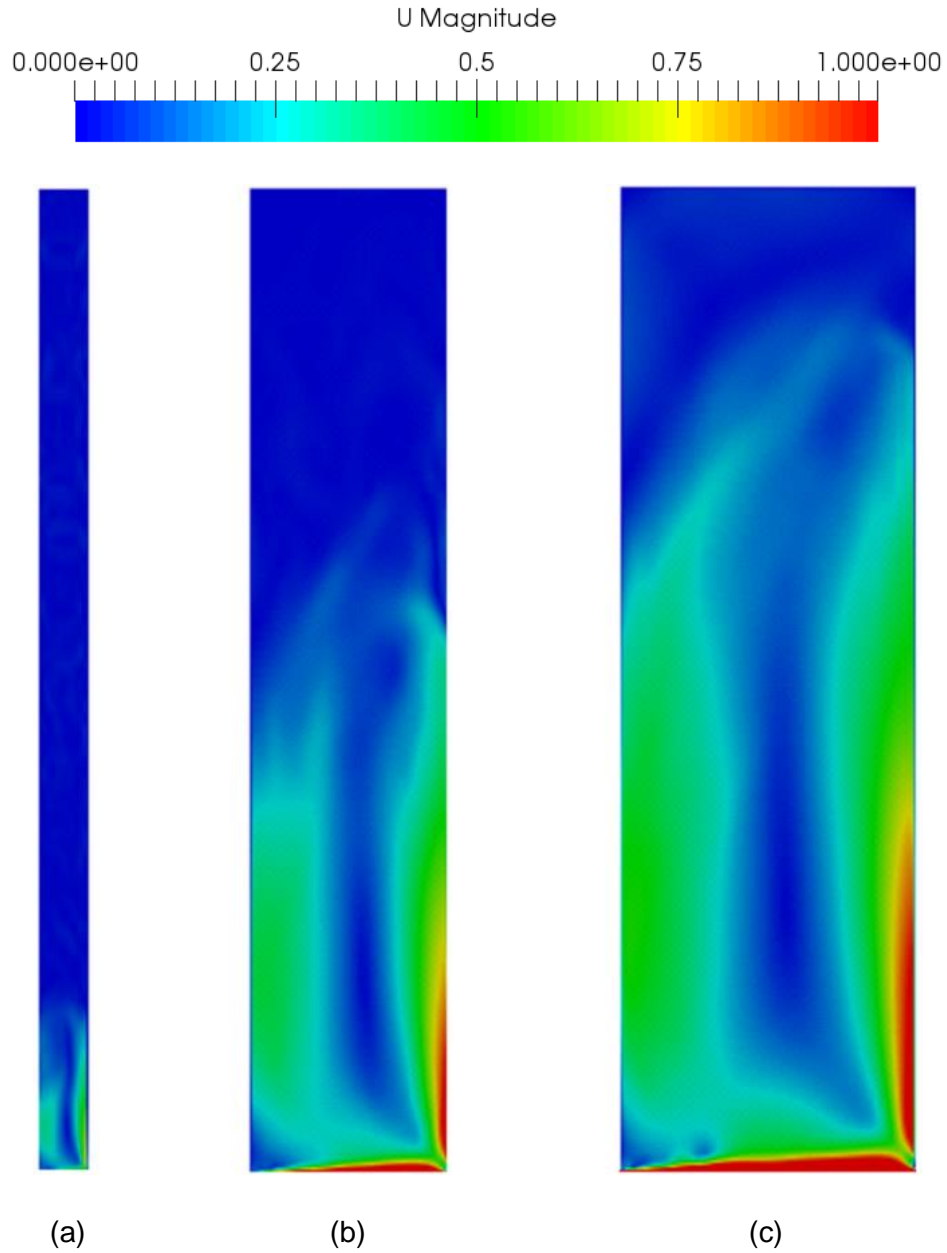


Figure 4.10 Velocity contours after 60 seconds for vertical dead-leg widths equal to (a)  $D/2$ , (b)  $2D$  and (c)  $3D$

Since the vertical dead-leg was not the channel which accommodated continuous fluid flow with a certain velocity, a change in the channel width did not affect the pressure drop as it is demonstrated in Figure 4.11.

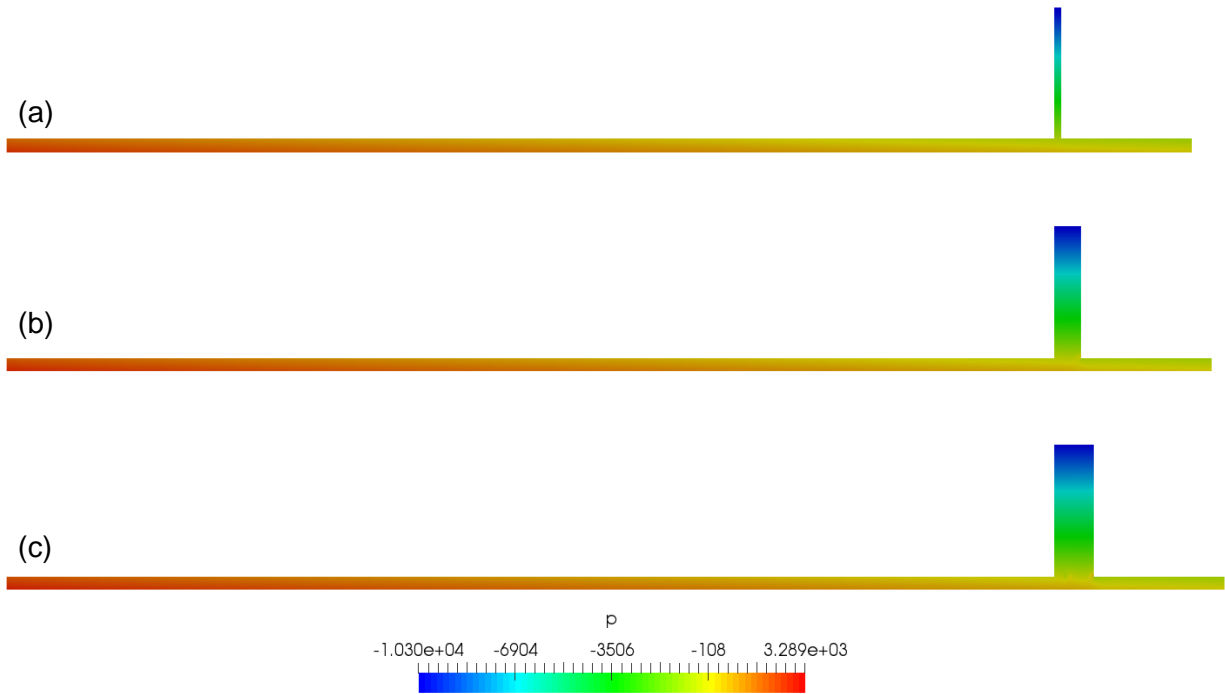


Figure 4.11 Pressure contours after 60 seconds for vertical dead-leg widths equal to (a)  $D/2$ , (b)  $2D$  and (c)  $3D$

#### 4.1.5. Effect of the Average Inlet Velocity of the Channel

The impact of the average inlet velocity on unsteady phase separation, the stagnant fluid regions, the recirculating vortices and pressure gradients within the dead-leg was investigated with the inlet velocities being 1 (Case 1), 5 (Case 2), 7 (Case 3) and 9 (Case 4) m/s corresponding to the Reynolds numbers being 57,294, 286,473, 401,062 and 515,651, respectively. The width of the horizontal channel and vertical dead-leg was defined equal to 0.12 m which is corresponding to  $D$ . The length of the main channel before the dead-leg was kept equal to  $80D$  (9.6 m) so as to achieve hydrodynamics fully-developed flow upstream of the dead-leg. The densities of crude oil and water were 830 and 959.8 kg/m<sup>3</sup>, respectively. Values of crude oil and water viscosities at the temperature of 100 °C were set to  $2 \times 10^{-6}$  and  $3 \times 10^{-7}$  m<sup>2</sup>/s, respectively.

The streamline patterns overlaid with water concentration contours and velocity contours within the branching vertical dead-leg after 60 seconds for different values of the average inlet velocities are presented in Figures 4.12 and 4.13, respectively. It was observed that the stronger recirculating vortices at the bottom of the dead-leg occurred with the higher inlet

velocities. In connection with this, the stagnant zone above the vortex occurring at the bottom of the dead-leg was becoming smaller (Figure 4.13).

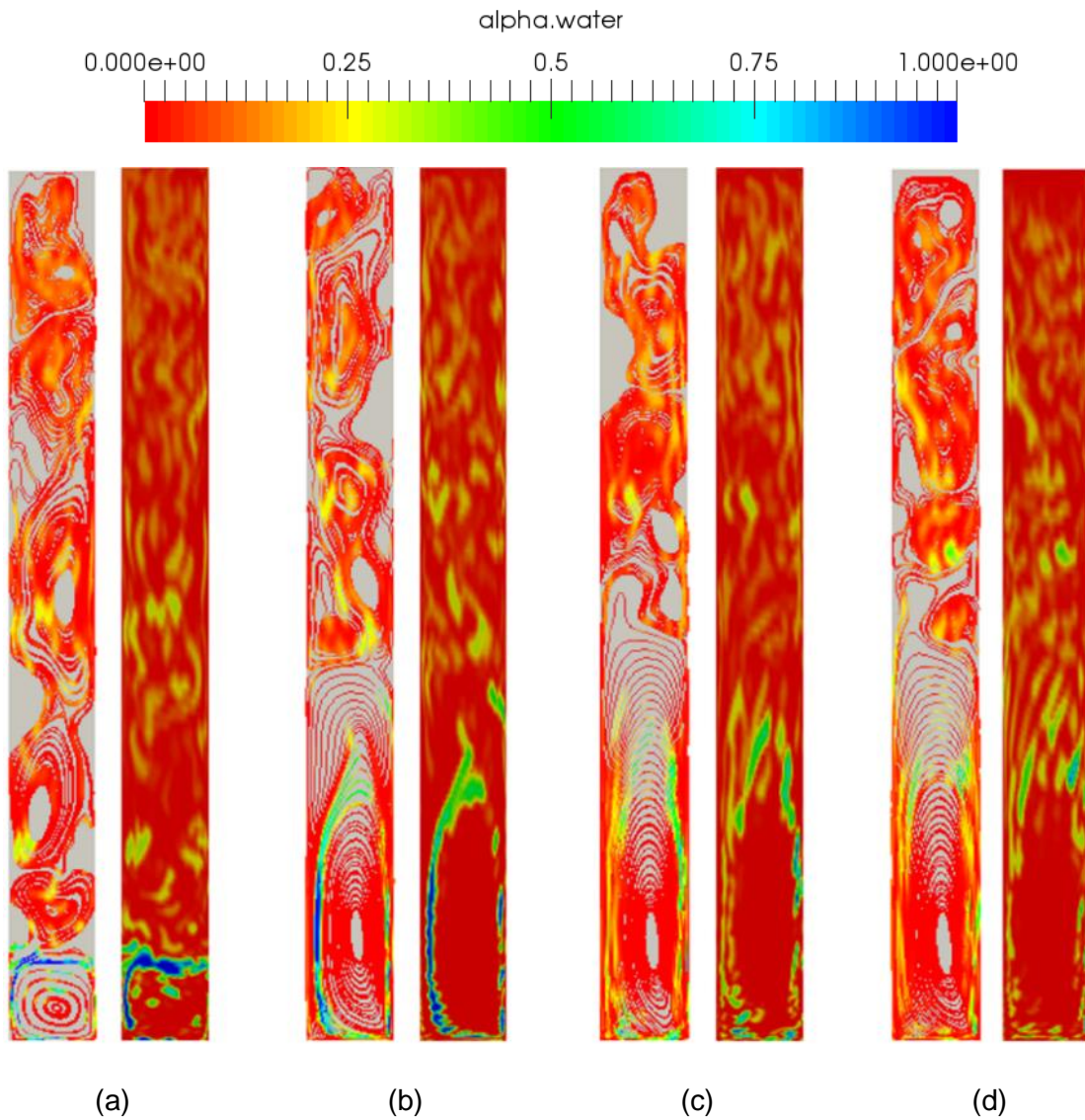


Figure 4.12. Streamlines overlaid with contours of phase fraction after 60 seconds for inlet velocities equal to (a) 1 m/s ( $Re= 57,294$ ), (b) 5 m/s ( $Re= 286,473$ ), (c) 7 m/s ( $Re= 401,062$ ) and (d) 9 m/s ( $Re= 515,651$ )

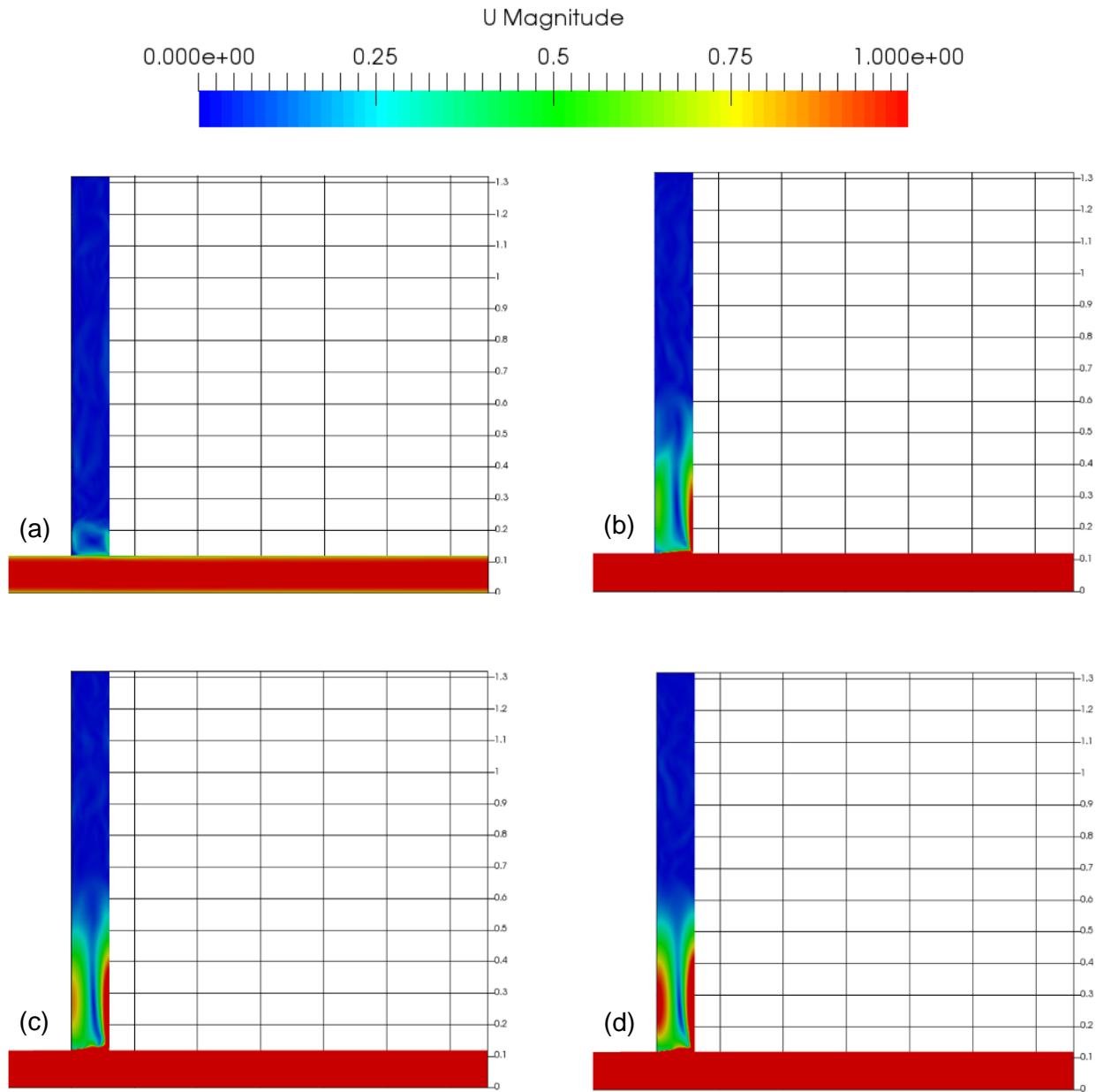


Figure 4.13. Velocity contours after 60 seconds for inlet velocities equal to (a) 1, (b) 5, (c) 7 and (d) 9 m/s, corresponding to  $Re$  numbers being 57,294, 286,473, 401,062 and 515,651, respectively

The decrease in the size of the near-stagnant zone affected oil separation efficiency negatively. Water fraction at the intersection was decreasing with the increase in the average inlet velocity and so was the size of the vortex (Table 4.1). Due to the strong vortex formation at higher velocities, water phase with higher concentration was recirculating due to the motion of the vortex within the zone where the vortex formed.

Table 4.1. Water fraction on the horizontal line (x= 9.6-9.72 m, y=0.12 m) within the dead-leg for Case 1 (1 m/s), Case 2 (5 m/s), Case 3 (7 m/s) and Case 4 (9 m/s)

Total water concentration				
Coordinates	Case 1	Case 2	Case 3	Case 4
x=9.6-9.72 m, y=0.12 m	0.15	0.09	0.08	0.07

Higher flow velocities resulted in larger pressure drop within the channel due to more frictional forces (Figures 4.14 and 4.15). For internal flows, the pressure drop is directly proportional to the inlet velocity for both laminar and turbulent flows. This proportion is  $\Delta P \propto U$  for laminar flow while it is  $\Delta P \propto U^{1.75}$  for turbulent flow [White, 2003]. This phenomenon matched up with the computational results as can be seen Tables 4.2 and 4.3.

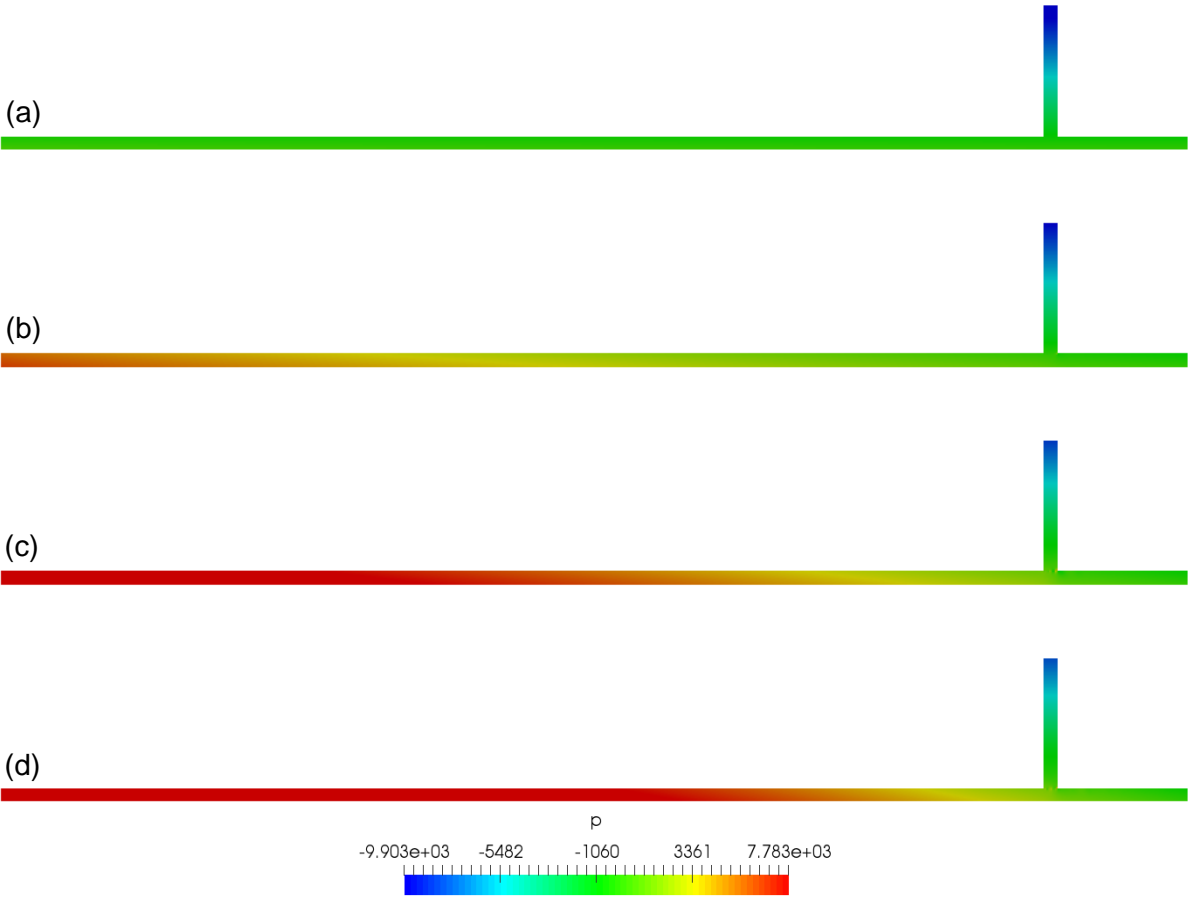


Figure 4.14. Pressure contours after 60 seconds for inlet velocities equal to (a) 1, (b) 5, (c) 7 and (d) 9 m/s, corresponding to *Re* numbers equal to 57,294, 286,473, 401,062 and 515,651, respectively

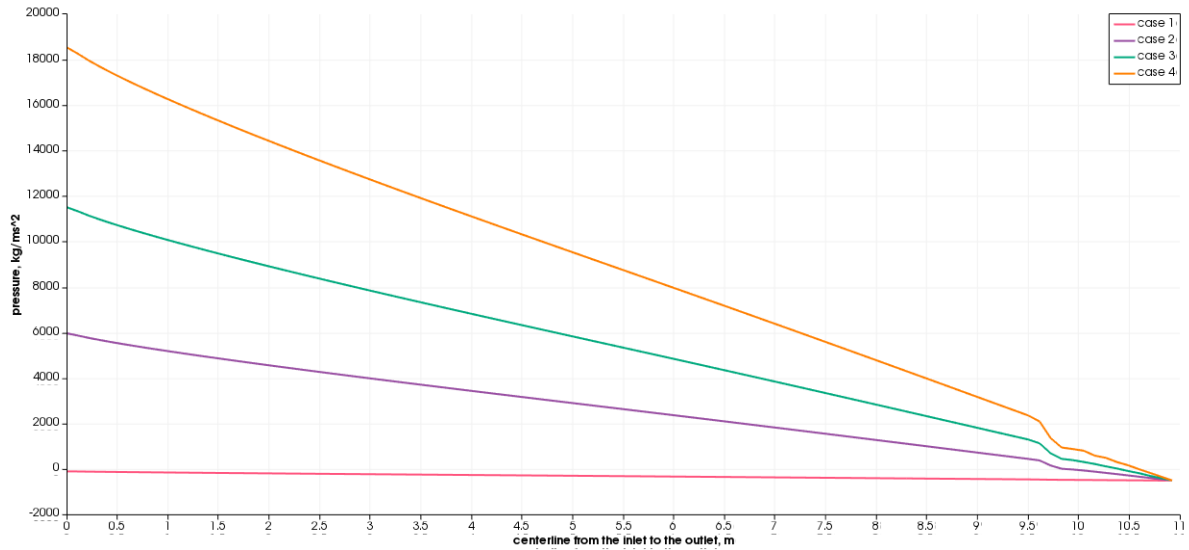


Figure 4.15. Pressure differences between the inlet and outlet sections of the horizontal channel for different inlet velocities, corresponding to  $Re$  numbers equal to 57,294, 286,473, 401,062 and 515,651, respectively

Table 4.2. Pressure drop between inlet and outlet of the horizontal channel  
**Pressure drop (kg/ms<sup>2</sup>)**

Coordinates	Case 1	Case 2	Case 3	Case 4
$x=0-10.92$ m, $y=0.06$ m	405.636	6,436.031	12,265.32	18,606.69

Table 4.3. Correlation between pressure drop and velocity in turbulent flow

$\Delta P_i$	405.636	6436.031	12265.32	18606.69
$U_i$ (m/s)	1	5	7	9
$U_i^{1.75}$ (m/s)	1	16.71851	30.12462	46.76537
$\Delta P_i / U_i^{1.75}$	405.636	384.9644	407.1527	397.8732
$\Delta P_1 * U_i^{1.75} = \Delta P_i$	405.636	6781.629	12219.63	18969.72

#### 4.1.6. Effect of the Crude Oil Viscosity

Influence of the crude oil viscosity on the magnitude of the vortices, the stagnant zone and pressure drop was studied with four different values of the kinematic viscosity of crude oil which were  $2 \times 10^{-5}$  (Case 1),  $10^{-5}$  (Case 2),  $2 \times 10^{-6}$  (Case 3) and  $2 \times 10^{-7}$  (Case 4)  $\text{m}^2/\text{s}$ . Even though the oil/water viscosity ratio can vary over a wide range from more than a million to less than one due to quite diverse oil properties [Xu, 2007], oil viscosity differences was kept small for this study (order of magnitude of 2). The widths of the horizontal channel and vertical dead-leg were equal to  $0.12 \text{ m}$  corresponding to  $D$ . The length of the main channel before the dead-leg was kept equal to  $80D$  ( $9.6 \text{ m}$ ) so as to achieve hydrodynamic fully-developed flow upstream of the dead-leg. The average inlet velocity for all cases were  $3 \text{ m/s}$  ( $Re = 59,034$  for the lowest viscosity case, corresponding to turbulent flow). The densities of crude oil and water were  $830$  and  $959.8 \text{ kg/m}^3$ , respectively. The streamline patterns overlaid with water concentration contours and velocity contours within the branching vertical dead-leg after 60 seconds for different values of the crude oil viscosity are presented in Figures 4.16 and 4.17, respectively. As can be seen in Figure 4.16, the stronger vortex occurred at the bottom of the dead-leg with decrease in oil viscosity.

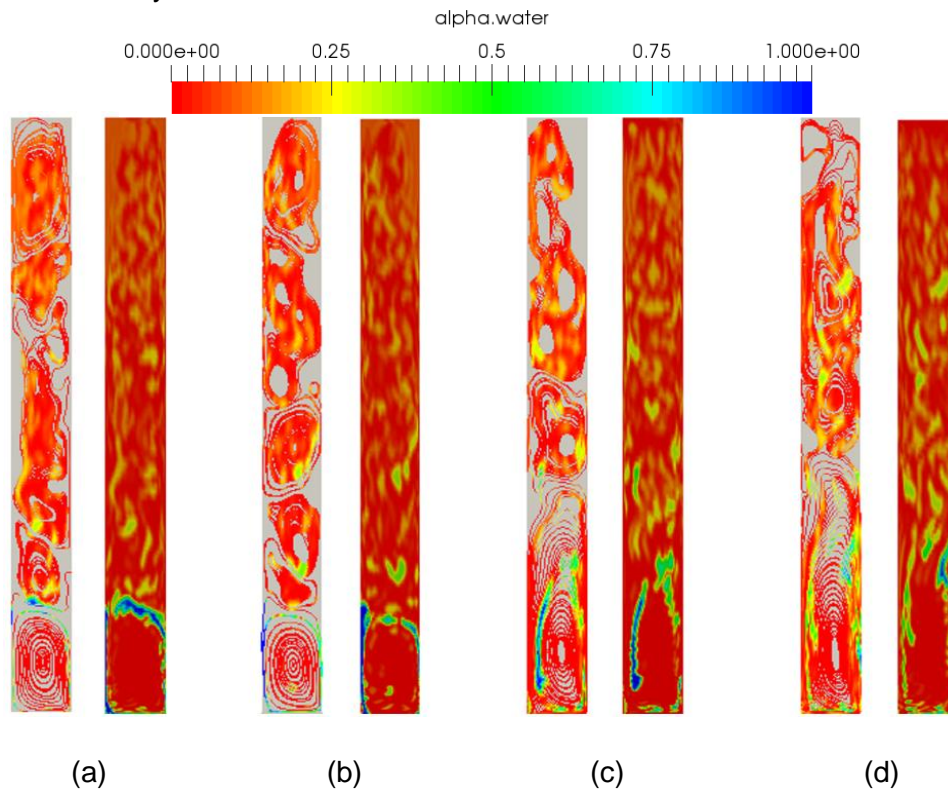


Figure 4.16. Streamlines overlaid with phase concentration contours after 60 seconds for different crude oil kinematic viscosities equal to (a)  $2 \times 10^{-5}$ , (b)  $10^{-5}$ , (c)  $2 \times 10^{-6}$  and (d)  $2 \times 10^{-7} \text{ m}^2/\text{s}$



The stronger vortex had bigger magnitude and so it helped water to move higher within the dead-leg. The bigger vortex caused the smaller low velocity fluid region above it (Figure 4.17).

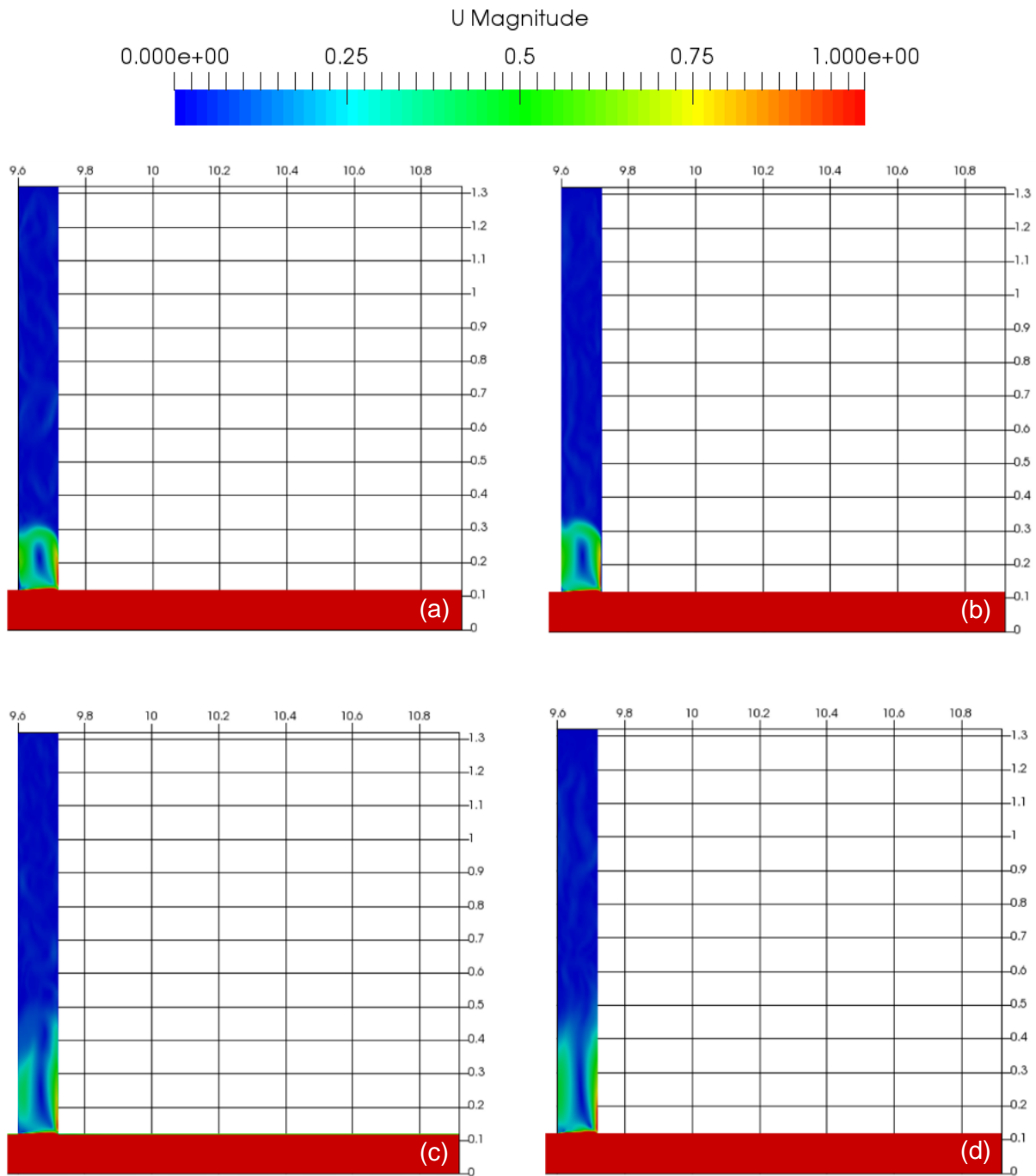


Figure 4.17. Velocity contours after 60 seconds for different crude oil kinematic viscosities equal to (a)  $2 \times 10^{-5}$ , (b)  $10^{-5}$ , (c)  $2 \times 10^{-6}$  and (d)  $2 \times 10^{-7}$   $\text{m}^2/\text{s}$

In addition, the less viscous fluid led to higher velocity within the vertical dead-leg since it was influenced relatively less by the frictional forces which resist relative motion of the fluid particles (Figure 4.18). Slower fluid flow or stagnation states resulted in improved oil separation of crude oil and water phases. While crude oil tended to stay within the upper part of the dead-leg, water phase separated and moved downward due to its higher density (Figure 4.16). Besides, the viscosity influenced the settling speed of the denser phase which was water and the phase separation time of the mixture.

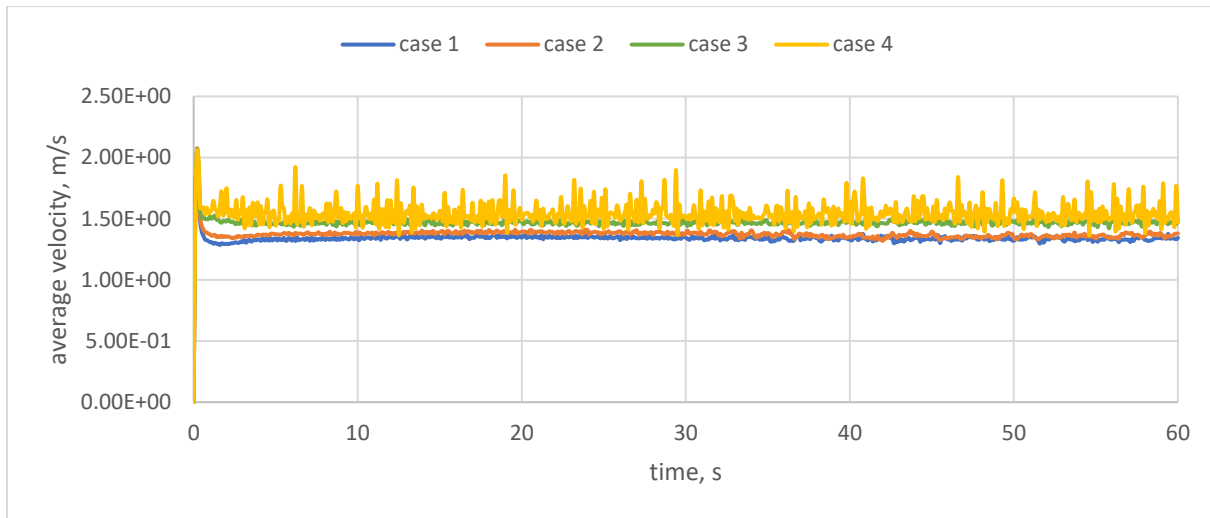


Figure 4.18. Average velocity magnitudes at the point  $y=0.12$  m located at the centerline of the vertical dead-legs for Case 1 ( $2 \times 10^{-5} \text{ m}^2/\text{s}$ ), Case 2 ( $10^{-5} \text{ m}^2/\text{s}$ ), Case 3 ( $2 \times 10^{-6} \text{ m}^2/\text{s}$ ) and Case 4 ( $2 \times 10^{-7} \text{ m}^2/\text{s}$ )

Water concentration as a function of time at point  $x=9.66$  m and  $y=1.2$  m ( $x=80.5D$ ,  $y=10D$ ) within the vertical dead-leg over the time intervals of 0-60 s and 35-60 s are shown in Figures 4.19 and 4.20, respectively. For nearly 38 seconds, the concentration of water at this point remained unaltered (Figure 4.19), therefore a more detailed graph is plotted in Figure 4.20. In the cases with the lower viscosity oil, separation of oil started earlier since weaker viscous forces bring about oil separation and the movement of the fluid becomes easier. In brief, a lower oil viscosity leads to higher interfacial tension, larger drop size, higher gravitational force on larger droplets and so more oil separation. Besides, turbulent dispersive forces are less prominent in the case of lower oil viscosity and therefore more oil separation and lower values of wall shear stress are expected.

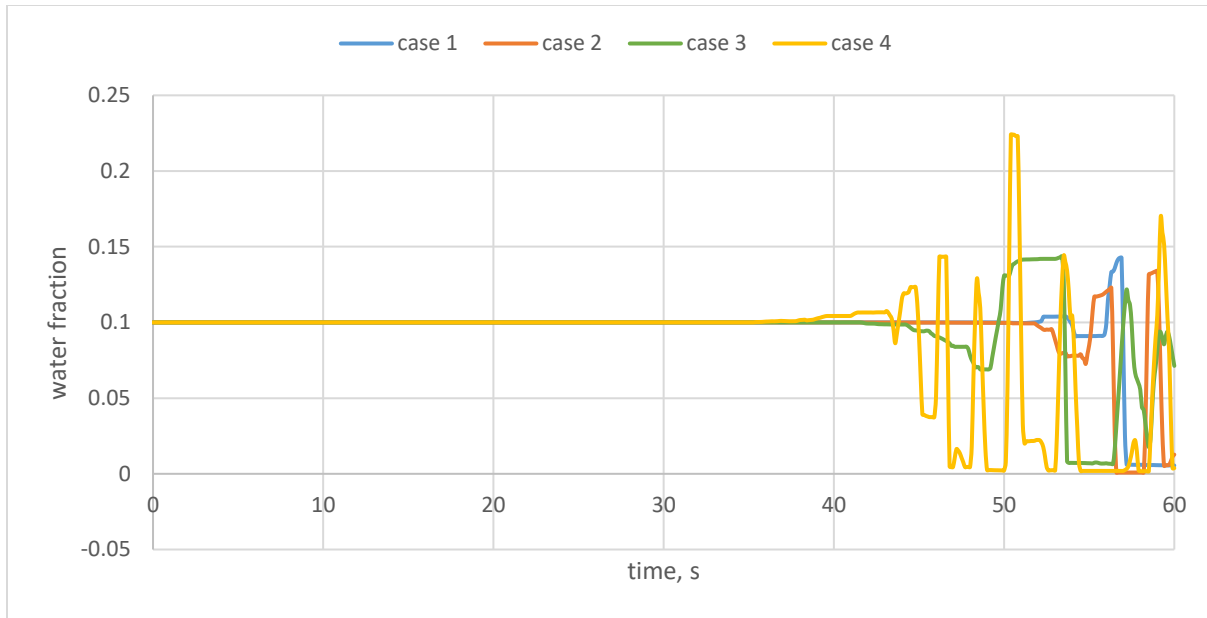


Figure 4.19. Time dependence of the water fraction within the vertical dead-leg at  $x=9.66$  m and  $y=1.2$  m during the time interval of 0-60 s for Case 1 ( $2 \times 10^{-5}$  m<sup>2</sup>/s), Case 2 ( $10^{-5}$  m<sup>2</sup>/s), Case 3 ( $2 \times 10^{-6}$  m<sup>2</sup>/s) and Case 4 ( $2 \times 10^{-7}$  m<sup>2</sup>/s)

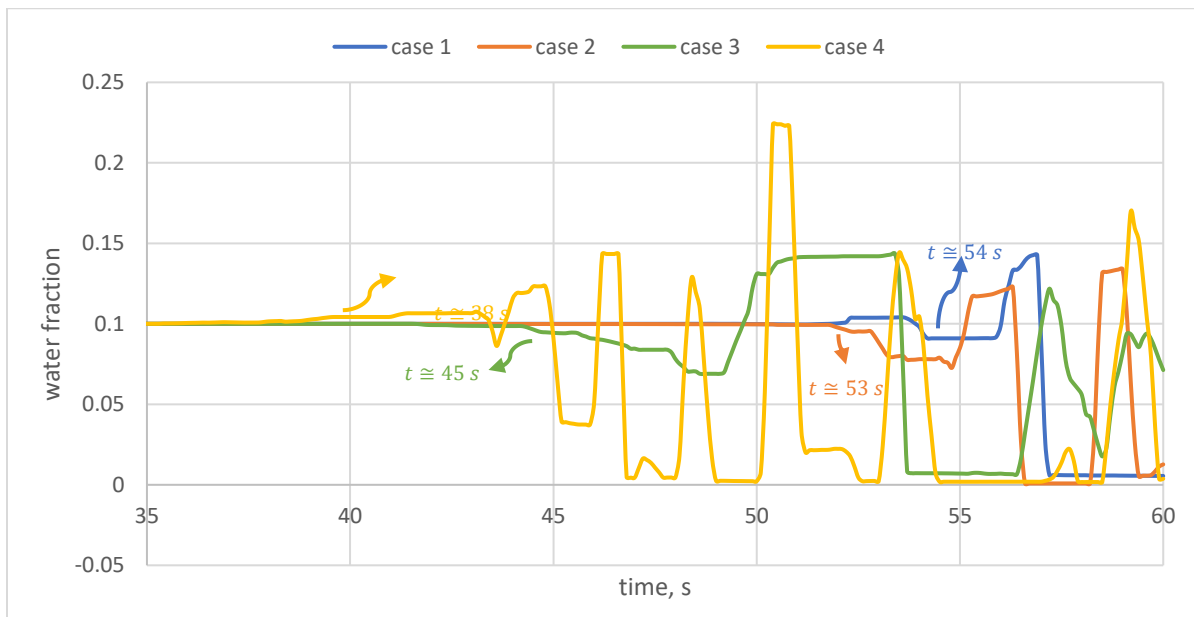


Figure 4.20. Time dependence of water fraction within the vertical dead-leg at  $x=9.66$  m and  $y=1.2$  m during the time interval of 35-60 s for Case 1 ( $2 \times 10^{-5}$  m<sup>2</sup>/s), Case 2 ( $10^{-5}$  m<sup>2</sup>/s), Case 3 ( $2 \times 10^{-6}$  m<sup>2</sup>/s) and Case 4 ( $2 \times 10^{-7}$  m<sup>2</sup>/s)

Viscosity is a fluid property which represents the resistance to flow and leads to frictional forces. Frictional forces which act on a fluid as it flows through a channel result in a pressure drop. The significant effect of fluid viscosity is that a narrow pressure gradient occurs under the condition of lower fluid viscosity (Figure 4.21).

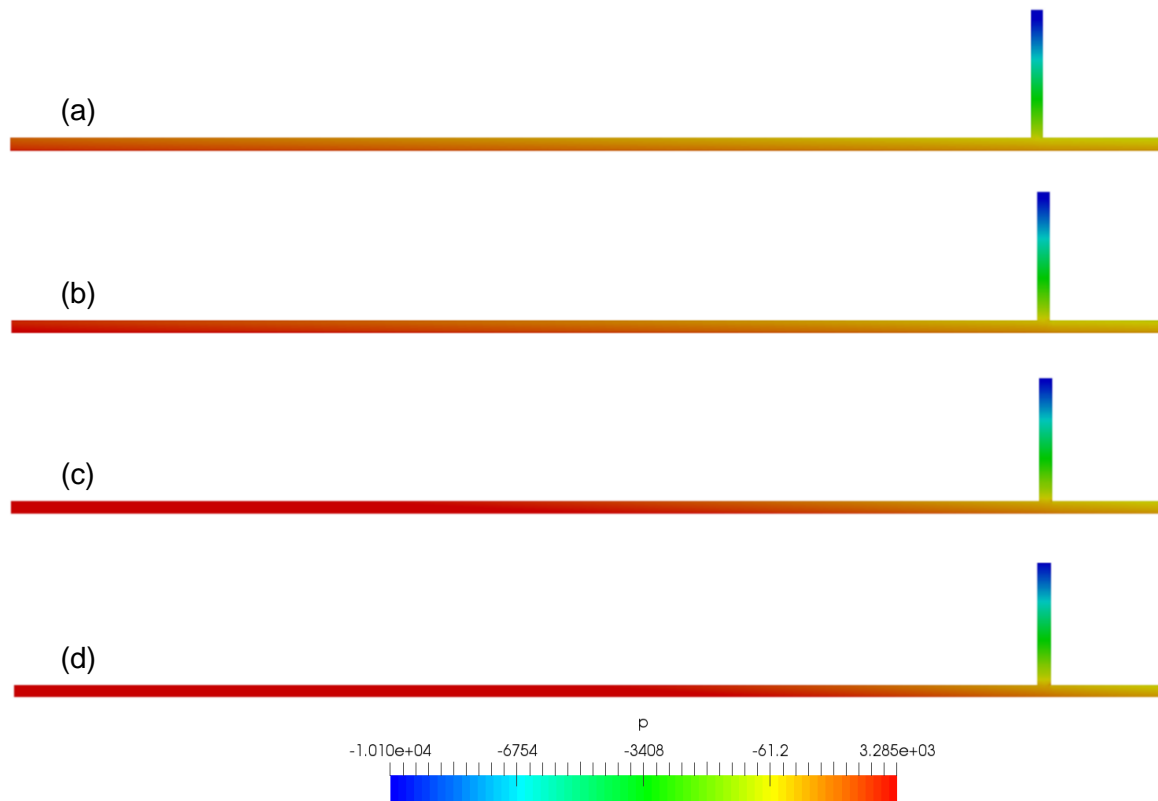


Figure 4.21. Change in pressure drop based on different oil kinematic viscosities of (a)  $2 \times 10^{-5}$ , (b)  $10^{-5}$ , (c)  $2 \times 10^{-6}$  and (d)  $2 \times 10^{-7}$   $\text{m}^2/\text{s}$

#### 4.1.7. Effect of the Hydrodynamic Development Length Upstream of the Vertical Dead-Leg

The effect of the length interval between the vertical dead-leg and the inlet of the horizontal channel was studied by changing the distance to be  $90D$  (Case 1),  $100D$  (Case 2) and  $110D$  (Case 3). The system contained a mixture of 90%-10% oil-water at every point of the computational domain as a starting initial condition. The average inlet velocity was 3 m/s ( $Re = 171,883$ , corresponding to turbulent flow) in all cases, in effect keeping the Reynolds number constant. The widths of the horizontal channel and vertical dead-leg were equal to 0.12 m corresponding to  $D$ . The densities of crude oil and water were 830 and 959.8  $\text{kg}/\text{m}^3$ , respectively. Values of crude oil and water viscosities at the temperature of 100 °C were  $2 \times 10^{-6}$  and  $3 \times 10^{-7}$   $\text{m}^2/\text{s}$ , respectively.

Marching in time, the phase fraction was becoming lower at the top of the dead-leg as it is the denser liquid compared to crude oil and the vortex magnitude increased (Figures 4.22, 4.23 and 4.24).



Figure 4.22. Instantaneous streamline patterns overlaid with phase concentration contours after (a) 10 s, (b) 20 s, (c) 30 s, (d) 40 s (e) 50 s and (f) 60 s for Case 1 (upstream hydrodynamic development length of  $90D$ )

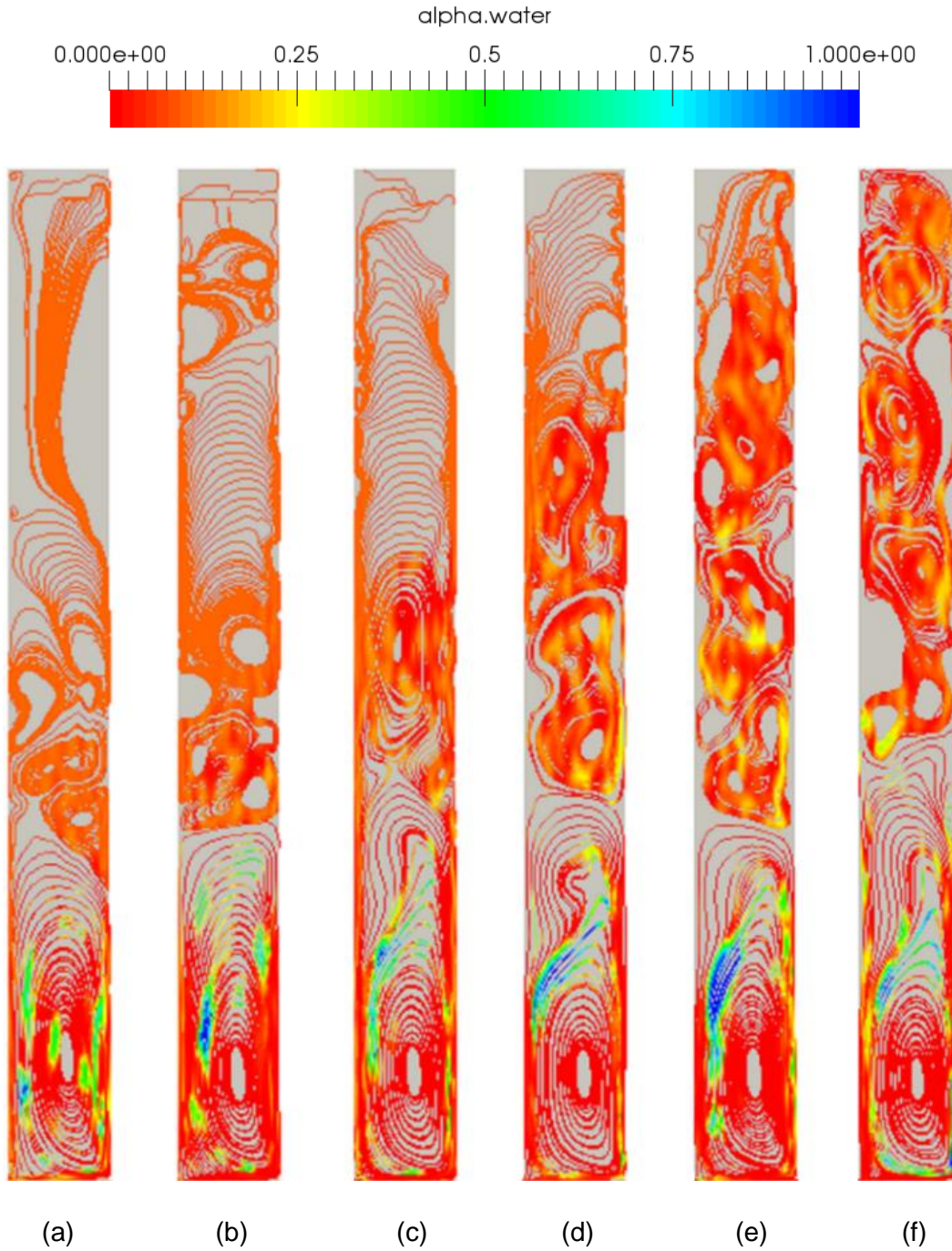


Figure 4.23. Instantaneous streamline patterns overlaid with phase concentration contours after (a) 10 s, (b) 20 s, (c) 30 s, (d) 40 s (e) 50 s and (f) 60 s for Case 2 (upstream hydrodynamic development length of  $100D$ )

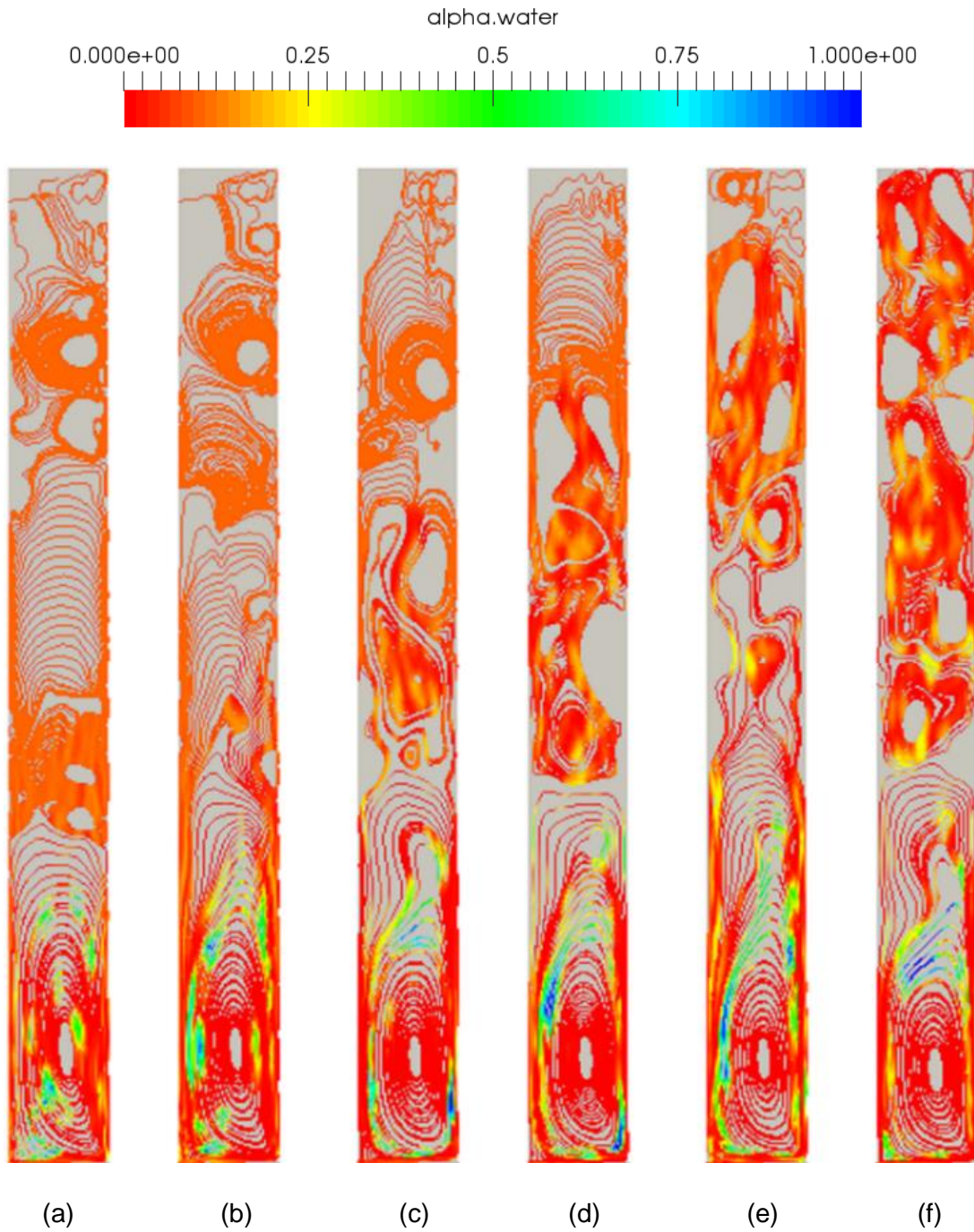


Figure 4.24. Instantaneous streamline patterns overlaid with phase concentration contours after (a) 10 s, (b) 20 s, (c) 30 s, (d) 40 s (e) 50 s and (f) 60 s for Case 3 (upstream hydrodynamic development length of  $110D$ )

While the separated water phase tended to accumulate at the bottom zone of the vertical dead-leg owing to its higher density and the effect of gravitational force, recirculated strong vortex moved water between 0.12 m (the bottom of the dead-leg) and around 0.6 m in the  $y$ -direction (Figure 4.25).

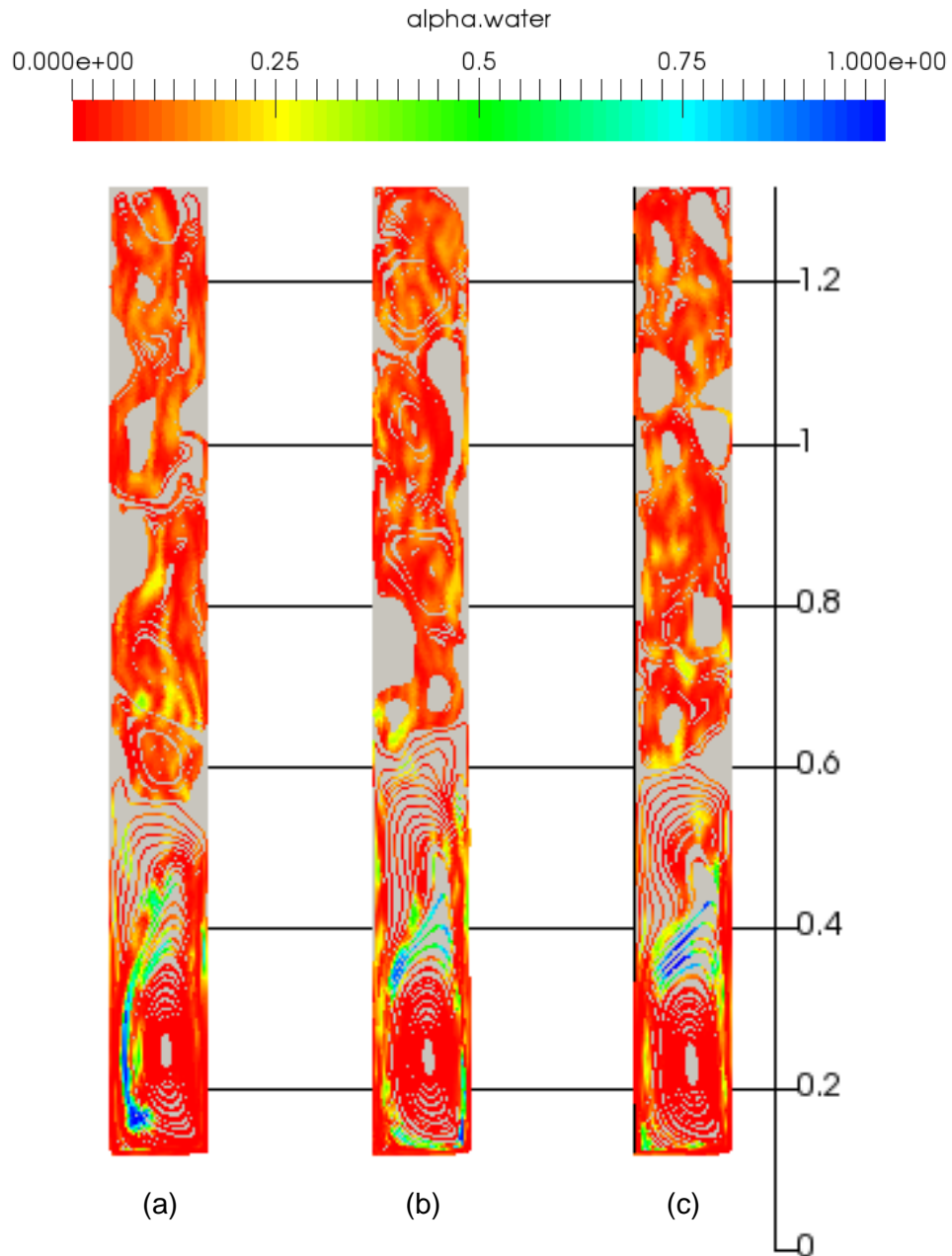


Figure 4.25. Streamline patterns overlaid with phase concentration contours after 60 seconds for (a) Case 1, (b) Case 2 and (c) Case 3 corresponding to different hydrodynamic development length upstream of the dead-leg



Due to the strong recirculating motion of the vortices, greater amount of water was observed around 0.4 m in the  $y$ -direction at the 60 second time instant (Figure 4.26-a) and the average water fraction was the highest again at the same location during the simulation time (Figure 4.26-b). The lowest water fraction was observed around the stagnant point of the vortex which is the center of the rotating vortex. As an impact of centrifugal force, the denser component (water) moved to the outside toward to the walls by displacing the lower-density liquid (oil) to the center of the rotating vortex (Figure 4.26-a-b).

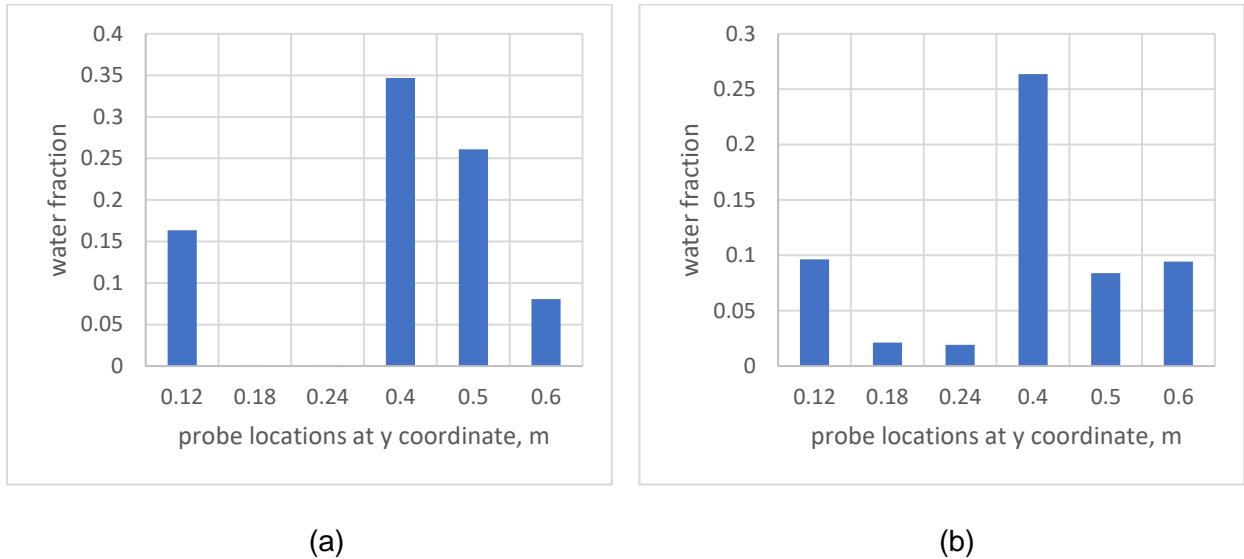


Figure 4.26. Values of the (a) water fraction at time instant of 60 seconds and (b) the average water fraction during 60 seconds at different monitored locations for Case 1 (upstream hydrodynamic development length of  $90D$ )

The highest velocity magnitude was investigated at the intersection region of the dead-leg and the horizontal channel where the strong vortex was located for all cases (Figure 4.27-a-b-c). The average velocity was becoming slower through the upper part of the vertical dead-leg regardless of the dead-leg's axial location (Figure 4.27-d). However, a closer inspection of the graph proved that the velocity magnitude at a height of 0.132 m in the  $y$ -direction was smallest for the Case 3 which had the longest hydrodynamics developing distance from the channel inlet (Figure 4.28). The reason for this might be the viscous forces which lowered the fluid velocity during the channel flow. There was not huge difference between the magnitude of the vortices and velocity fields of each case. The reason for these similar patterns could be the inadequate length difference between the cases.

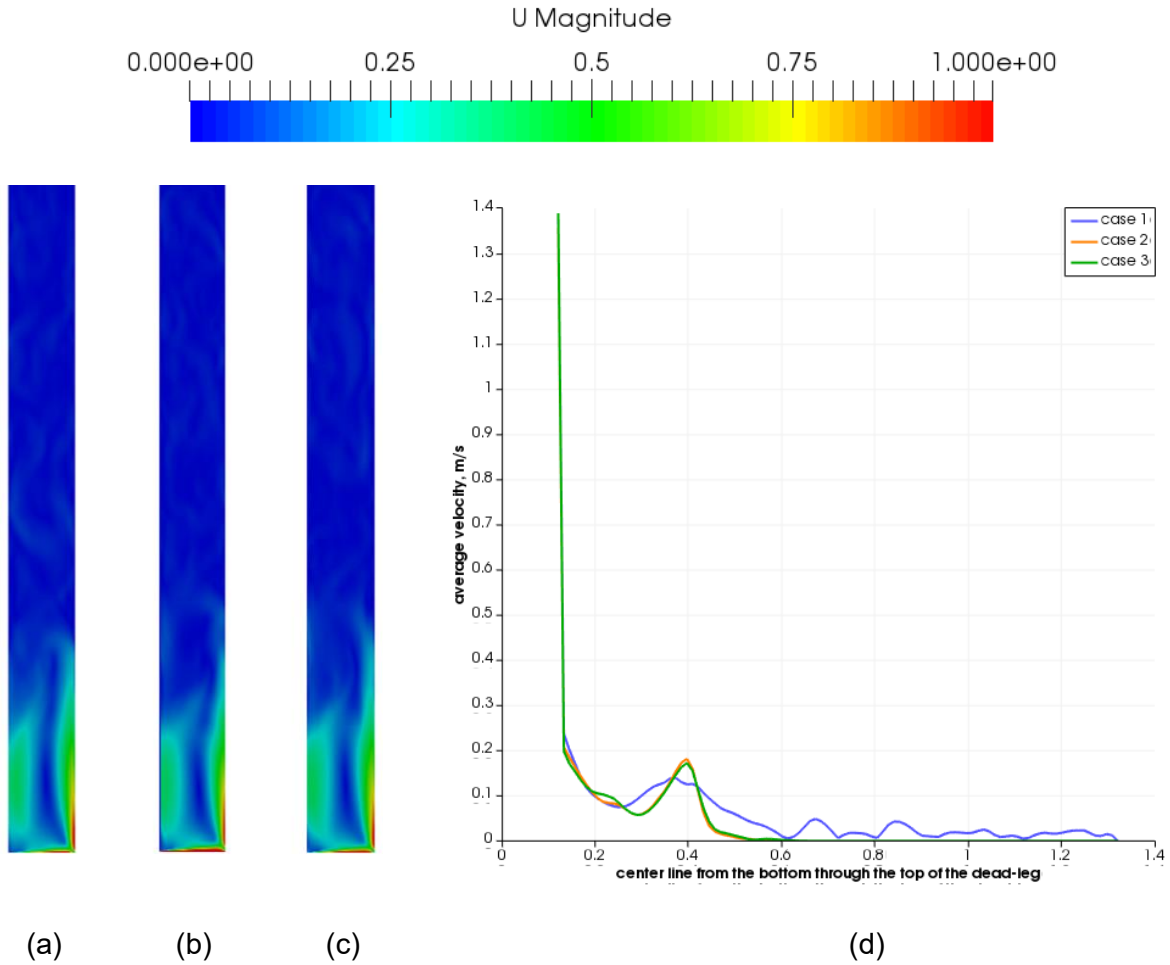


Figure 4.27. Velocity contours after 60 seconds for different hydrodynamic development lengths before the vertical dead-legs equal to (a)  $90D$ , (b)  $100D$ , (c)  $110D$  and (d) variation of the average velocity through the centerline from the bottom to the top of the dead-leg

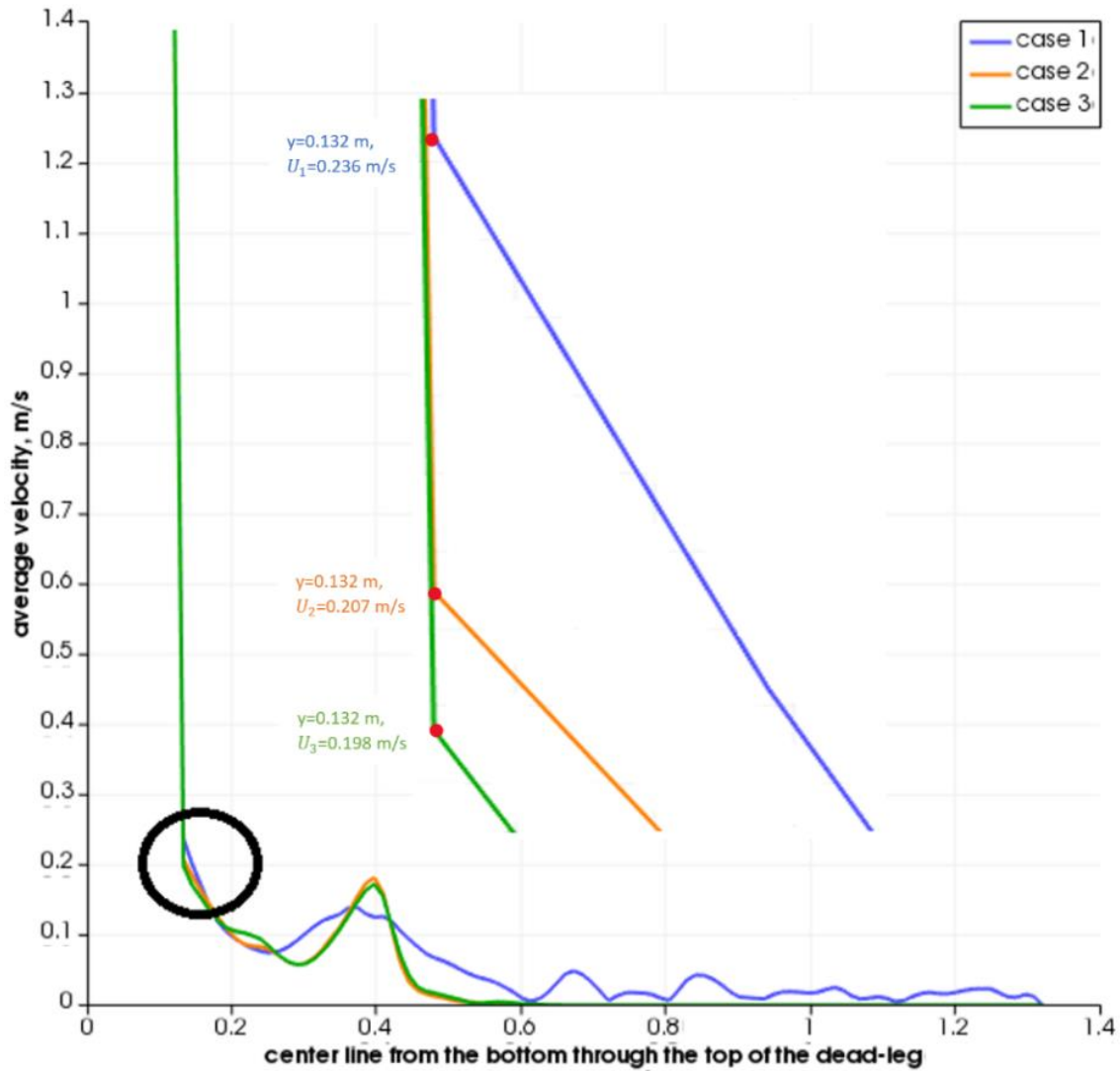


Figure 4.28. Instantaneous velocity magnitudes along the centerline starting from the bottom and ending at the top of the dead-legs for Case 1, Case 2 and Case 3 (upstream hydrodynamic development length of  $90D$ ,  $100D$  and  $110D$ , respectively) along with a close-up view of the inlet to the vertical dead-leg at the time instant of 60 s

As can be seen in Figure 4.29, the average inlet velocity was 3 m/s and the velocity profile developed as the fluid moved across in x-direction. After the fluid velocity reached the maximum value, it started decreasing with the effect of frictional forces.

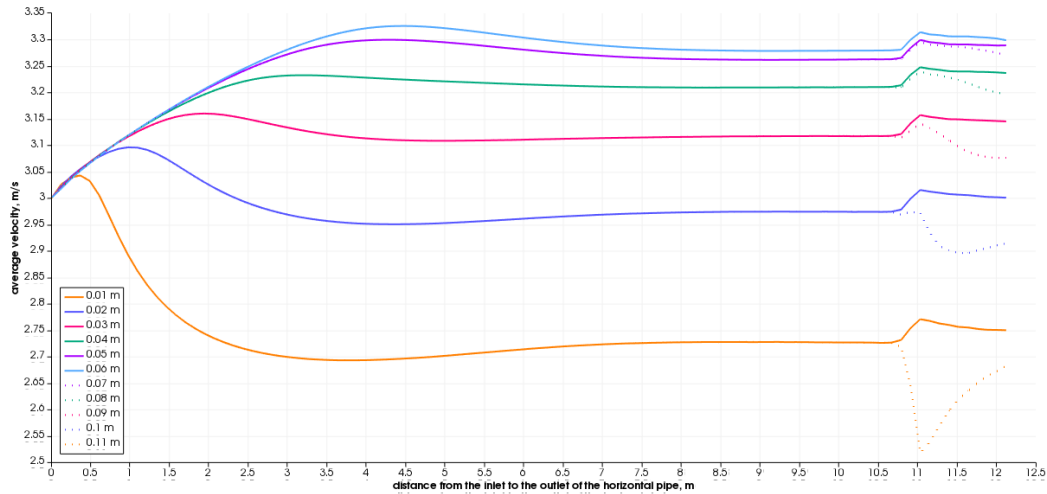


Figure 4.29. Instantaneous axial velocity magnitudes from the inlet to the end of the horizontal channel at various vertical heights of the main channel for Case 1 at the time instant of 60 s with an upstream hydrodynamic development length of  $90D$

With the vertical positions closer to the channel walls, the reduction in velocities was more sudden due to the rise in frictional forces. When the fluid reached the dead-leg, the fluid velocity increased suddenly due to a decrease in pressure (Figure 4.30 a-b). However, this pattern became reversed as approaching to the upper wall of the horizontal channel (Figure 4.29).

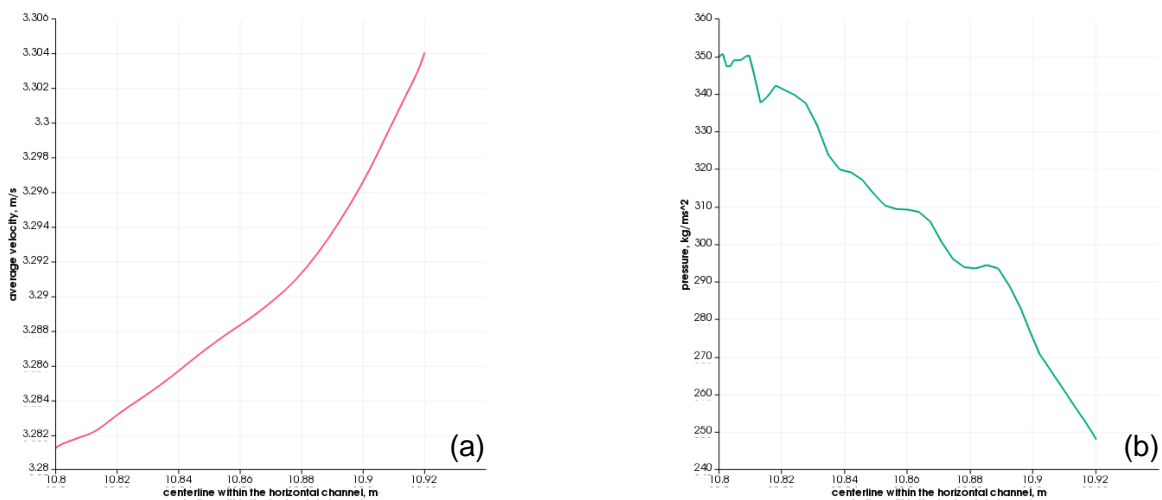


Figure 4.30. Plots of the instantaneous (a) axial velocity and (b) pressure values at the centerline of the horizontal channel corresponding the location of the dead-leg for Case 1 at the time instant of 60s

Similarly, larger pressure gradient between the inlet and the outlet of the horizontal channel was observed with the increase in the length which the fluid flows through (Figure 4.31).

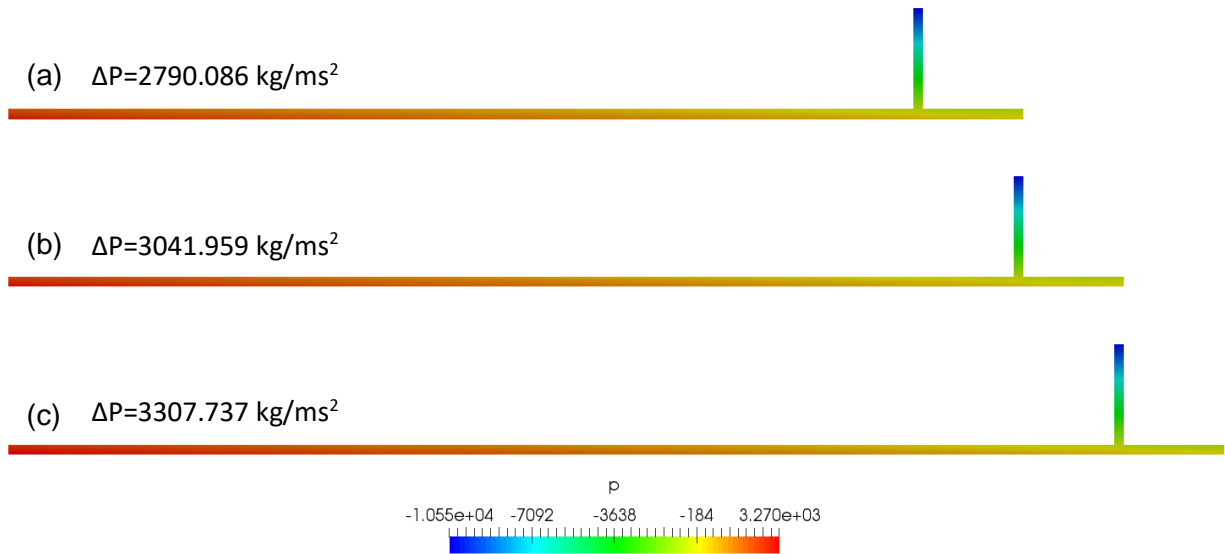


Figure 4.31. Pressure gradient for (a) Case 1, (b) Case 2 and (c) Case 3 (upstream hydrodynamic development length of  $90D$ ,  $100D$  and  $110D$ ) at the time instant of  $60 \text{ s}$

#### 4.1.8. Effect of the Crude Oil Density

Crude oil can be denser or less dense than water based on the American Petroleum Institute (API) gravity which is a measure of how heavy or light a petroleum liquid is compared to water. API gravity ( $^\circ\text{API}$ ) is calculated based on the specific gravity of oil,  $SG_{oil}$ , which is the oil density,  $\rho_{oil}$ , relative to water density,  $\rho_{H_2O}$ :

$$^\circ\text{API} = 141.5/SG_{oil} - 131.5 \quad (4.3)$$

$$SG_{oil} = \rho_{oil}/\rho_{H_2O} \quad (4.4)$$

In the present study, the  $^\circ\text{API}$  of the baseline 90%-10% oil-water mixture was 32.084 corresponding to  $SG_{oil}=0.865$ .

The effect of the oil density on phase separation, the stagnant zone(s) and pressure drop within the dead-leg was investigated based on oil densities of 600 (Case 1), 800 (Case 2), 900 (Case 3) and 1200 (Case 4)  $\text{kg/m}^3$ , corresponding to the  $^\circ\text{API}$  values of 94.852, 38.264, 19.401 and -18.323, respectively. The density of water was not changed for any of the cases and it was set to  $959.8 \text{ kg/m}^3$ . Values of crude oil and water viscosities at the temperature of  $100 \text{ }^\circ\text{C}$  were

$2 \times 10^{-6}$  and  $3 \times 10^{-7}$   $\text{m}^2/\text{s}$ , respectively. The width of the horizontal channel was equal to  $0.12 \text{ m}$  corresponding to  $D$ . The width of the dead-leg was equal to the width of the horizontal feeding channel. The length of the main channel before the dead-leg was kept equal to  $80D$  ( $9.6 \text{ m}$ ) so as to achieve hydrodynamics fully-developed flow upstream of the dead-leg. The average inlet velocity for all cases were  $3 \text{ m/s}$ , however the prevailing  $Re$  number will change as the density of the mixture is varied (e.g.,  $Re = 171,883$ , for oil density of  $830 \text{ kg/m}^3$  corresponding to turbulent flow).

The streamline patterns colored according to water concentration and velocity contours within the vertical dead-leg after 60 seconds for different oil densities are presented in Figure 4.32. As it can be observed from Figure 4.32, oil separation efficiency increased from Case 3 to Case 1 since the larger density difference between two fluids led to improved separation of phases. The magnitude of the vortex which was formed at the intersection of the main channel and the dead-leg became larger with increase in the oil density and so decrease in the density difference.

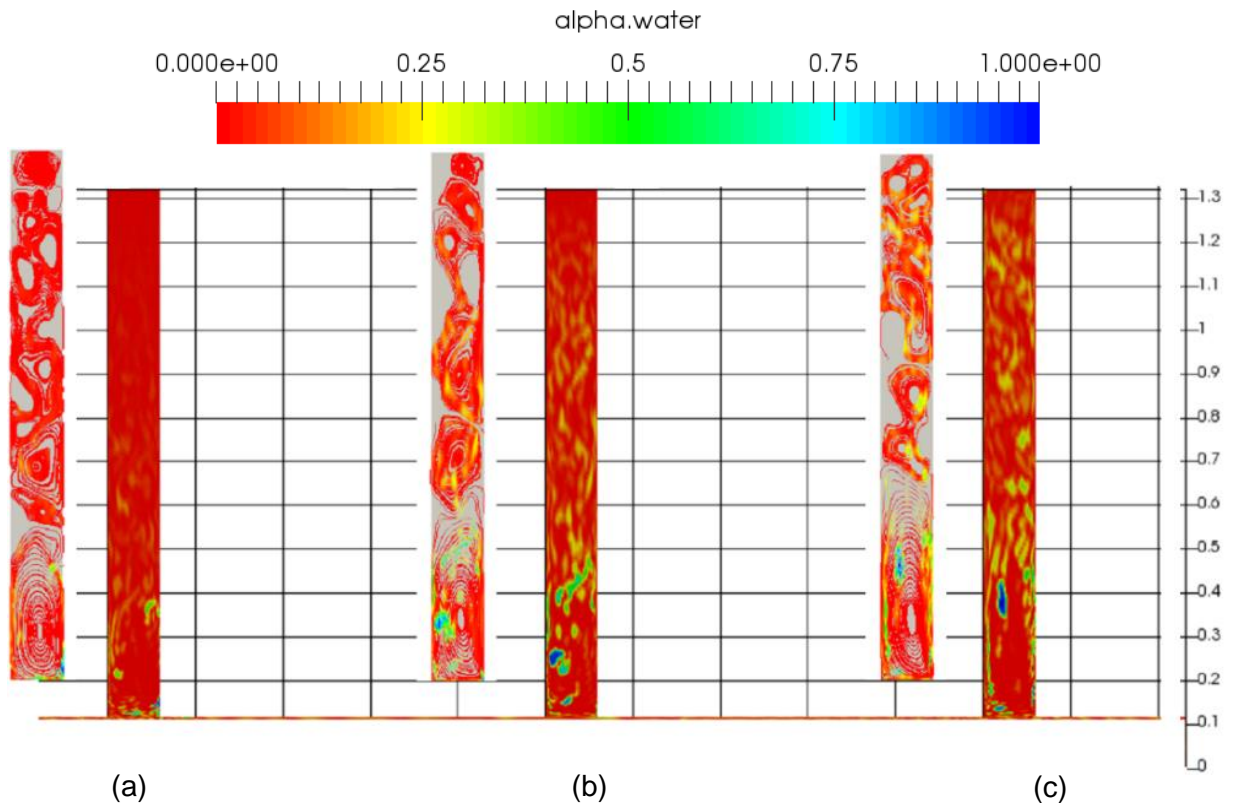


Figure 4.32 Streamlines overlaid with phase fraction contours after 60 seconds for different oil densities of (a) Case 1 ( $600 \text{ kg/m}^3$ ), (b) Case 2 ( $800 \text{ kg/m}^3$ ) and (c) Case 3 ( $900 \text{ kg/m}^3$ )

The existence of larger recirculation region at the intersection led to decrease in lower velocity zone above it (Figure 4.33). Decrement in the stagnation zone which was caused by the larger vortex movement had a negative effect on oil separation effectiveness.

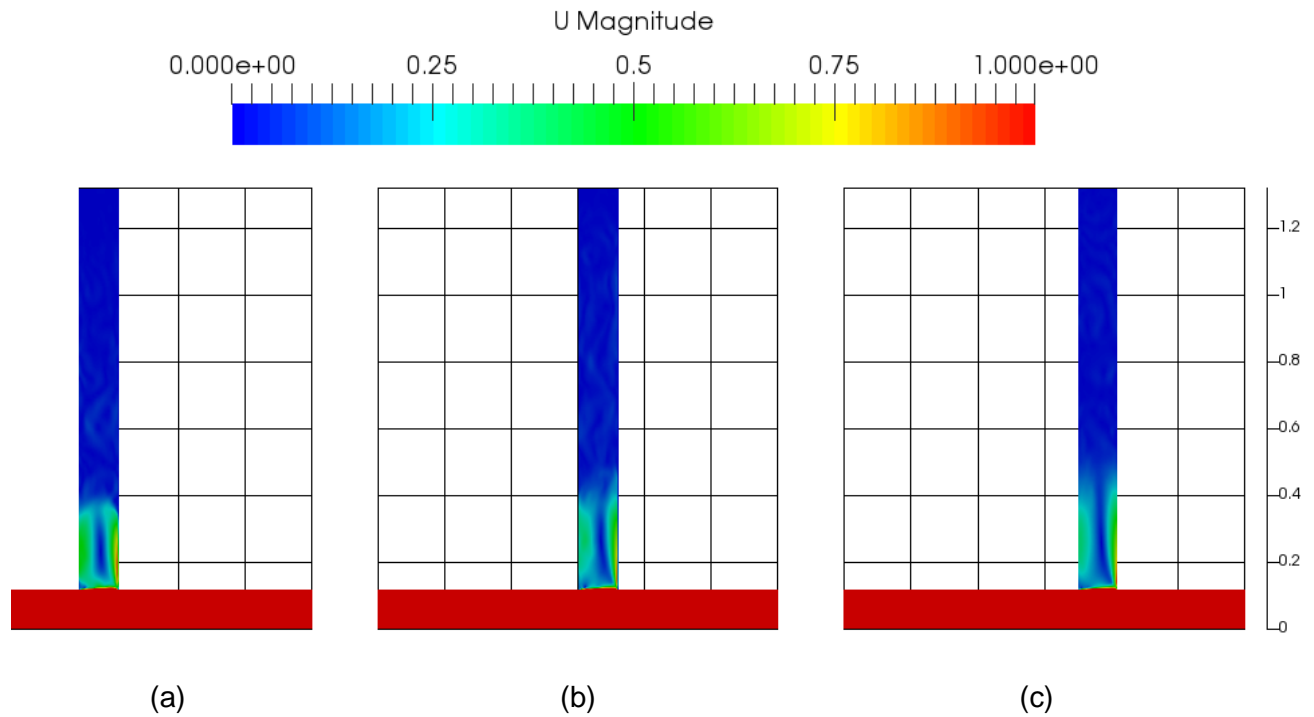


Figure 4.33 Velocity contours after 60 seconds for different oil densities of (a) 600, (b) 800 and (c) 900 kg/m<sup>3</sup>

The magnitude of pressure drop within the channel system was connected with the incompressible fluid density (Figure 4.34). The higher fluid density resulted in the higher pressure drop (Figure 4.35 a). In respect of the dead-leg, the highest-pressure drop due to the vertical elevation was observed in Case 3 due to having the densest fluid (Figure 4.35 b).

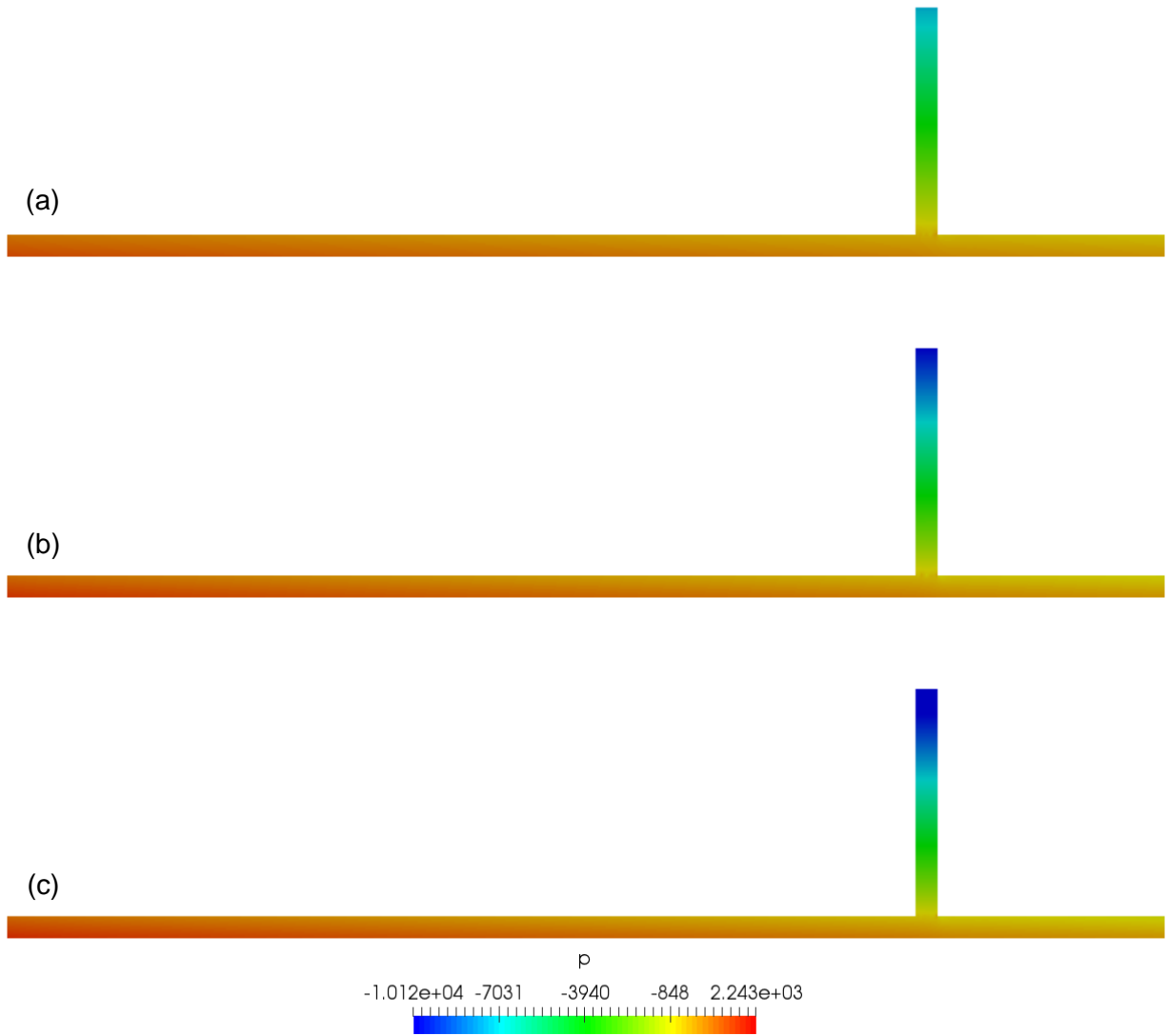


Figure 4.34. Pressure contours after 60 seconds for different oil densities of (a) 600, (b) 800 and (c) 900 kg/m<sup>3</sup>



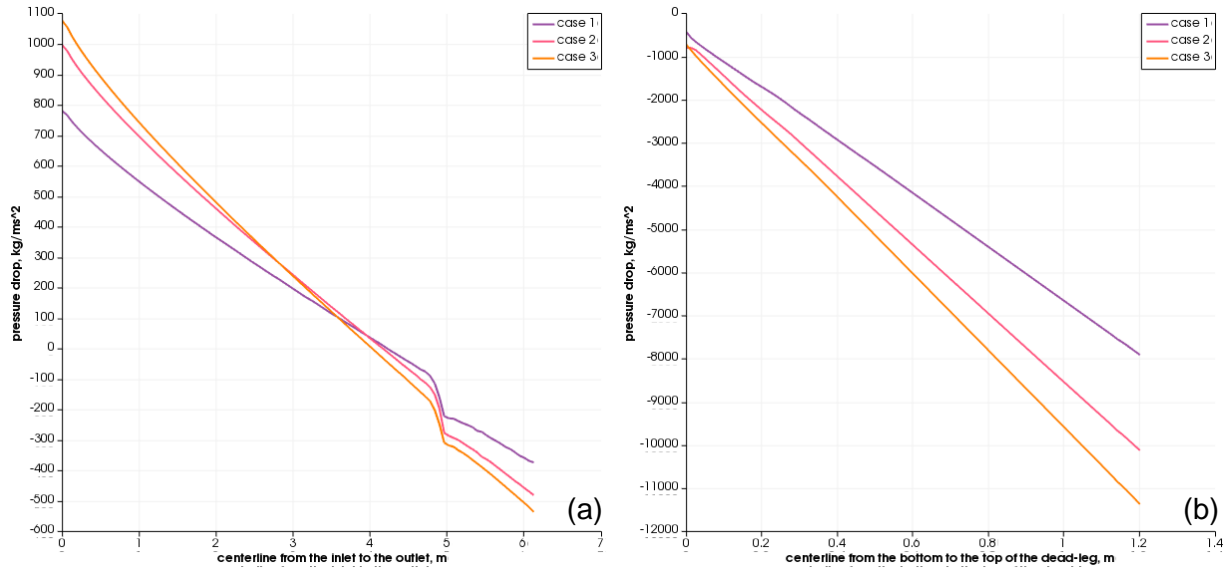


Figure 4.35. Pressure drop within (a) the horizontal main channel and (b) the vertical dead-leg

In order to gain a better understanding of oil-water separation in our system, the value of API gravity (American Petroleum Institute gravity) of oil must be also considered.

The crude oil whose °API is less than 10 is heavier than water and sinks (Figure 4.36). In other words, it is not always the case that oil is less dense than water and separated oil rises up while water sinks. This fact must be considered for the oil-water separation studies in order to predict correctly which part of the geometry is vulnerable for water accumulation.

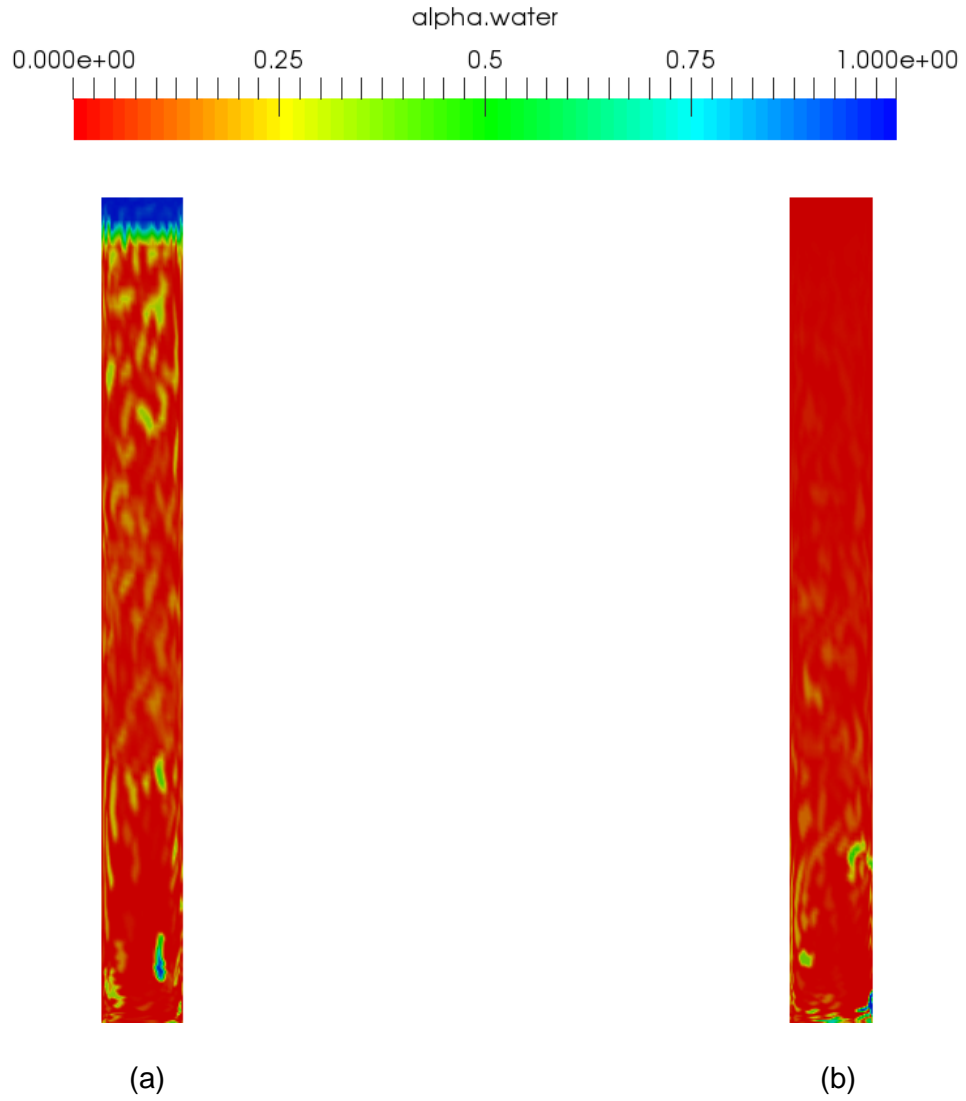


Figure 4.36. Phase concentrations after 60 seconds for oil densities of (a) 1200 ( $^{\circ}\text{API} = 94.852$ ) and (b) 600  $\text{kg/m}^3$  ( $^{\circ}\text{API} = -18.323$ )

#### 4.2. Three-Dimensional Horizontal Pipe and the Vertical Dead-Leg System

Having discussed the general behavior of transient 2-D turbulent two-phase 90%-10% oil-water channel flows along with a parametric study of a number of variables, unsteady 3-D turbulent simulations of 90-10% oil-water pipe flow with a capped vertical dead-leg was also attempted. Based on unsteady solution of the governing equations, the extent of the stagnant recirculating flow zone(s) were investigated depending on the following operating conditions (origin  $x=y=z=0$  is located on the centerline of the main pipe at the inlet station, with the centerline of the dead-leg pointing in the +y direction):

- (a) average inlet velocity ( $V_i=3$  m/s),
- (b) diameter of the dead-leg pipe ( $D=0.12$  m),
- (c) length of the dead-leg ( $10D=1.2$  m, extending from  $y/D=0.5$  to  $y/D=10.5$ ),
- (d) distance from upstream edge of the dead-leg to the pipe inlet ( $79.5D$ ),
- (e) viscosity of crude oil ( $2 \times 10^{-6}$  m<sup>2</sup>/s evaluated at temperature of 100 °C) and
- (f) density of crude oil (830 kg/m<sup>3</sup> evaluated at temperature of 100 °C).

Using water density equal to 959.8 kg/m<sup>3</sup>, for a 90%-10% oil-water mixture, the inlet  $Re=\rho DV_i/\mu=1.7 \times 10^5$ , with mixture density and viscosity evaluated from equations 3.23 and 3.24, respectively. Oil/water surface tension was 0.03 N/m.

The velocity distribution was considered uniform at the inlet port of the pipe and a constant pressure was defined at the pipe's outlet. At the wall boundaries, velocity components were set to zero in accordance with the no-slip condition.

Turbulent properties of the flow were solved by using the standard  $k - \varepsilon$  model [Lauder and Spalding, 1974]. The turbulent kinetic energy field was initialized at time  $t=0$  to:

$$k = \frac{3}{2} (I |u_{ref}|)^2 \quad (4.5)$$

where  $I$  and  $u_{ref}$  are the intensity ( $3.55 \times 10^{-2}$ ) and reference velocity (3 m/s), respectively. This level of turbulent kinetic energy was maintained through the simulations at the inlet plane of the pipe (inlet boundary condition).

The dissipation of turbulent kinetic energy field was initialized at  $t=0$  to:

$$\varepsilon = \frac{C_{\mu}^{0.75} k^{1.5}}{L} \quad (4.6)$$

where  $L$  is a reference length scale (0.12 m) which is the inlet pipe diameter. This level of dissipation of turbulent kinetic energy was maintained through the simulations at the inlet plane of the pipe (inlet boundary condition). Similar to the 2-D simulations, a grid independent study was performed, and relevant findings are discussed in Appendix B.

#### 4.2.1. Grid Independence Study for the 3-D Geometry Simulations

Similar to the 2-D counterpart, the grid size,  $h$  ( $m^3$ ), was calculated based on the total cell number,  $N$ , and the volume of the  $i$ th cell,  $\Delta V_i$  ( $m^3$ ), for the 3-D model, i.e.

$$h = \left[ \frac{1}{N} \sum_{i=1}^N (\Delta V_i) \right]^{1/3} \quad (4.7)$$

Three different sets of grids which are 853,000, 1,864,000 and 5,906,000 were created with the ANSYS Fluent R19.2 software (Figure 4.37) and corresponding simulation results were obtained for the case which is that of a two-phase 90%-10% oil-water mixture flow with the average inlet velocity of 4 m/s. The variations of the vertical (y-component) velocity along the centerline of the vertical dead-leg corresponding to the three grid densities are shown in Figure 4.38. The velocity field at specific point ( $x=1$  m,  $y=0$  m,  $z=0$  m, with the origin  $x=y=z=0$  is located at the center of the inlet) at time instant 30 s was chosen in order to calculate the discretization error by following the same procedure which was used in the 2-D grid independence test (Appendix B).

Whether the solutions are within the asymptotic range of convergence was checked with;

$$GCI^{21}/r^p GCI^{32} = 0.0455/(2^{3.744} 0.0034) \cong 1 \quad (4.8)$$

which indicates that the solutions are within the asymptotic range of convergence since the computed ratio is very close to 1.

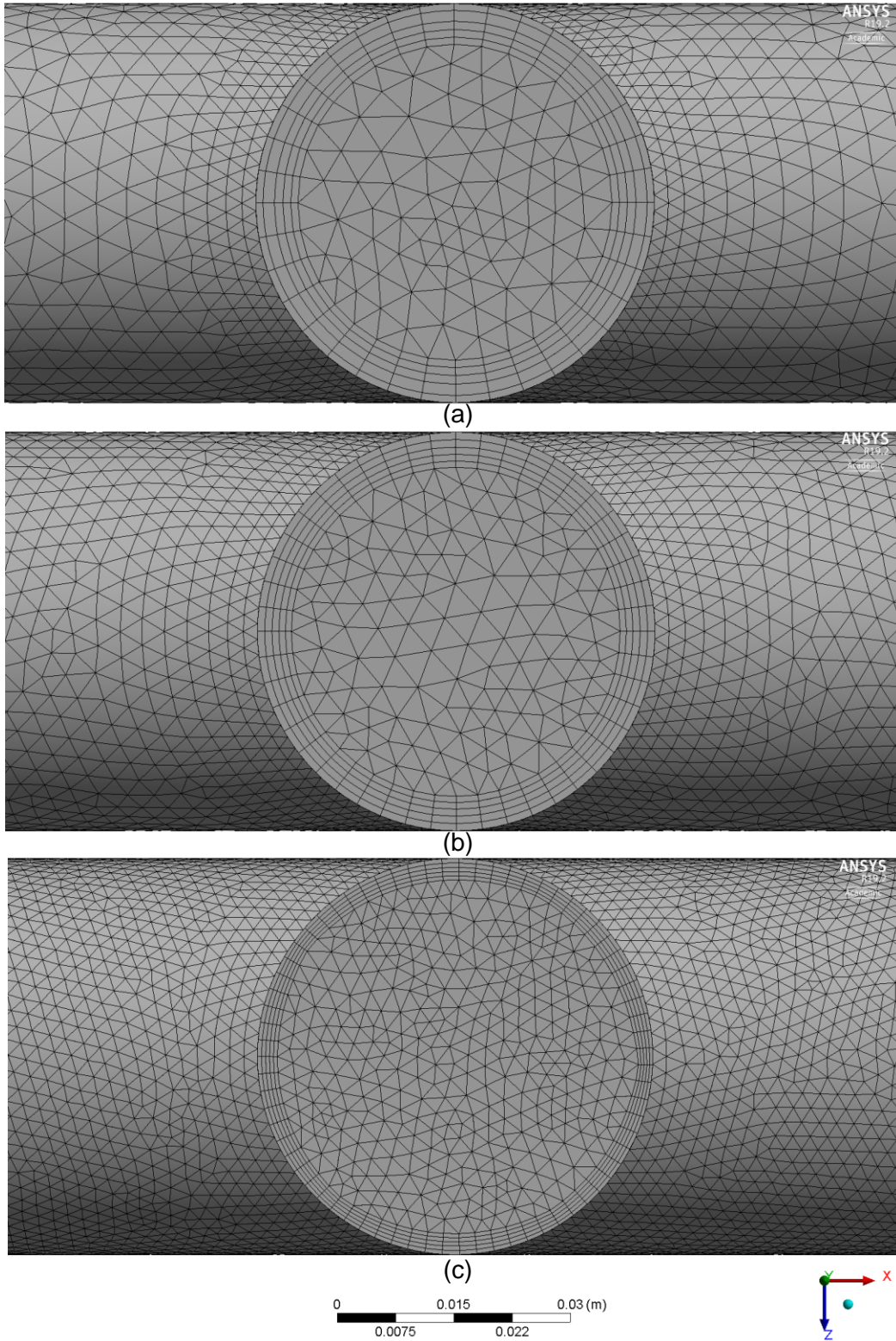


Figure 4.37. Top views of the unstructured triangle mesh systems viewed along the centerline of the vertical dead-leg ( $y$ -direction) for the (a) coarse (853,000), (b) medium (1,864,000) and (c) fine (5,906,000) grid densities

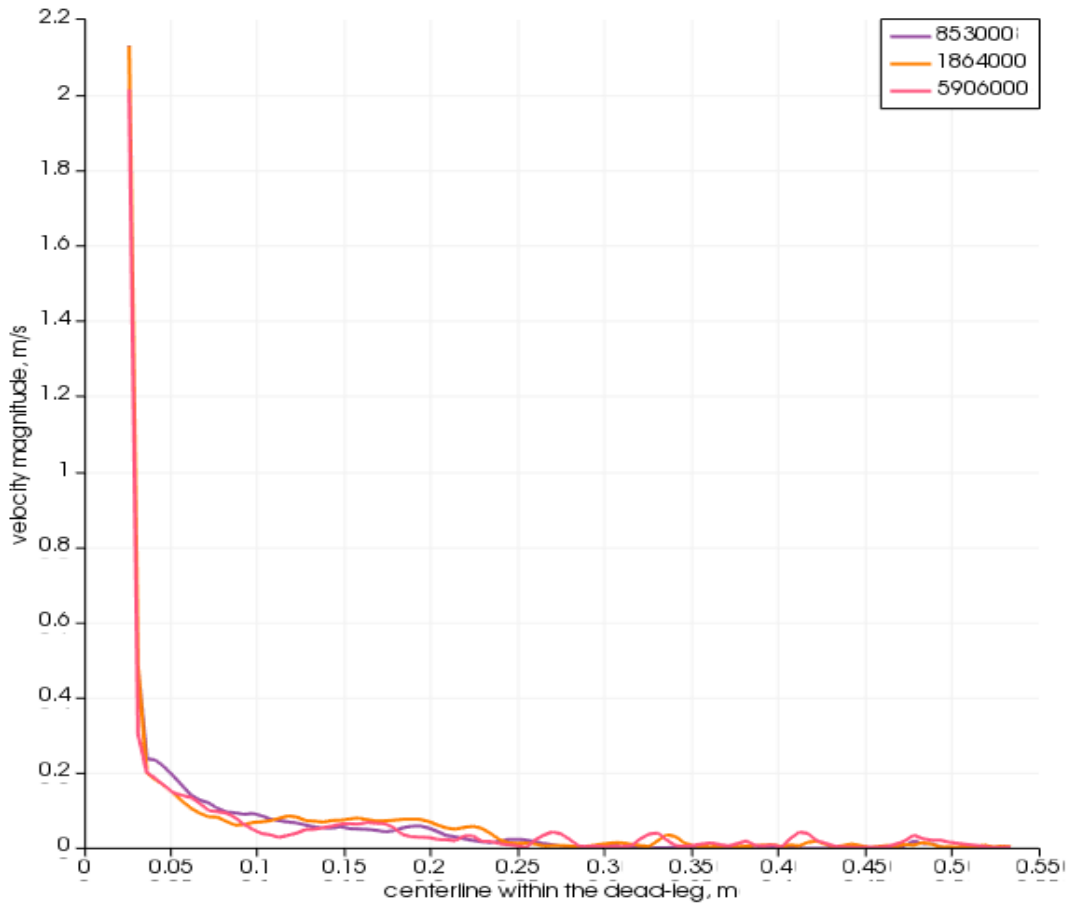


Figure 4.38. Velocity variations along the centerline ( $y$ -direction) within the vertical 3-D dead-leg for the 853,000, 1,864,000 and 5,906,000 grid densities

#### 4.2.2. Results for Three-Dimensional Pipe and the Vertical Dead-Leg System

The instantaneous volume fraction fields on the vertical symmetry plane ( $z = 0$ ) are shown in Figure 4.39 at time instants of 0, 5, 20, 40 and 60 seconds. Based on the results of 3-D computational simulations, oil fraction gradually increased within the vertical dead-leg branch. The lighter oil penetrated inside the vertical dead-leg that is dominated by a slow fluid velocity field compared to the throughflow in the main horizontal pipe. Concurrently, it was observed that the water volume fraction gradually grew at the intersection of the vertical branch and downstream of it within the horizontal pipe. Recirculating vortices within the separated zones of the vertical dead-leg were observed at regions where higher water fractions were forming. The general trends of the 3-D results are very similar to those observed earlier for the 2-D model.

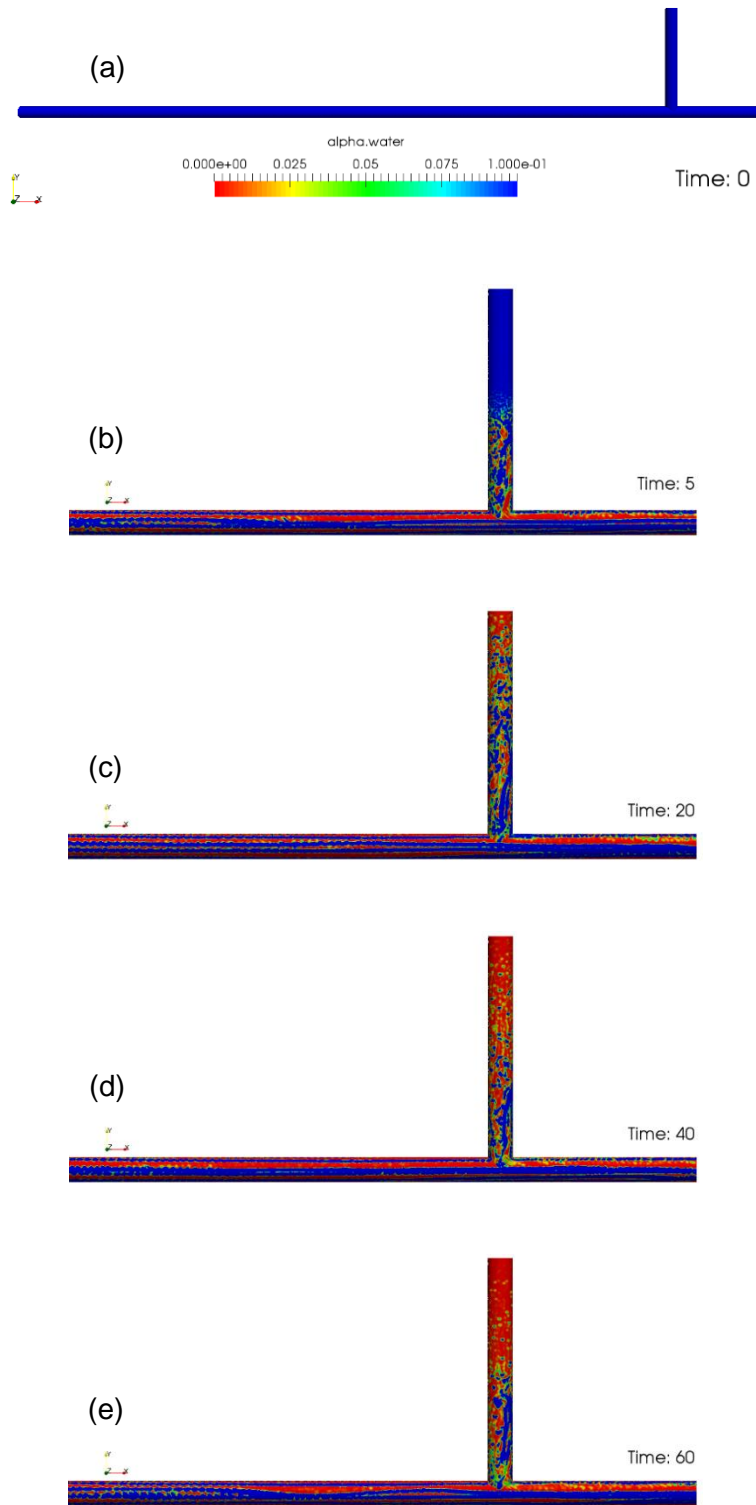


Figure 4.39. Instantaneous phase fields within the branching 3-D dead-leg on the vertical symmetry plane ( $z = 0$ ) at time instants of (a) 0, (b) 5, (c) 20, (d) 40 and (e) 60 s

It was also found that the size of the recirculating zones and the amount of the mixture which goes through the T-junction depended on the inlet velocity upstream of the dead-leg. At the time instant of 60 s, an isometric view of the phase fraction field on the inner walls of the main pipe and the branching capped vertical dead-leg is shown in Figure 4.40. Moreover, the instantaneous phase fraction field on a double-sliced dead-leg segment (slice planes of  $z=0$  and  $x=80.5D$ ) is shown to the right of the Figure 4.40. One can observe that noticeable striation patterns are visible along the horizontal feed pipe to be discussed below. With the wall surface contours providing limited information about the behavior of the complex 3-D recirculating zone on the pipe walls, the double-sliced contours exhibit a deeper understanding of the existence of complicated phase field inside the dead-leg.

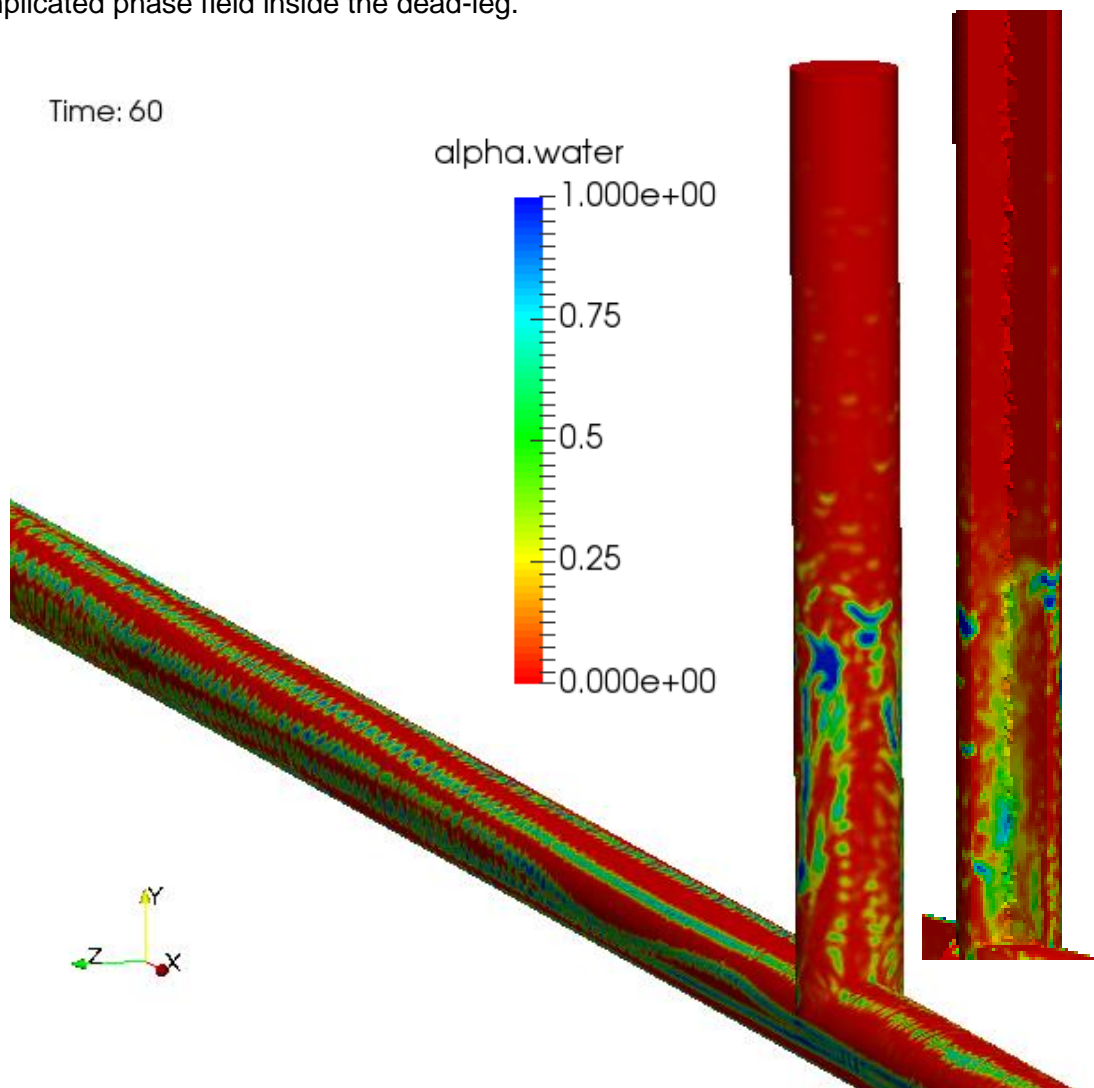


Figure 4.40. Isometric views of phase fraction contours on the pipe and dead-leg surface, and cut-view of the double-sliced dead-leg segment at the 60 s time instant, in addition to marked striation patterns on the surface of the horizontal pipe



Instantaneous phase fraction contours on 4 horizontal circular sliced cross-sections ( $y/D=0.5$ ,  $0.83$ ,  $2.5$  and  $4.17$ ) along the vertical direction are also shown in Figure 4.41 exhibiting marked non-uniformity of the oil and water volume fractions at various vertical stations. Comparing the oil fractions on the top 2 cross-sections to the 2 lower cross-sections monitored, greater accumulation of oil at higher elevation is clearly observed.

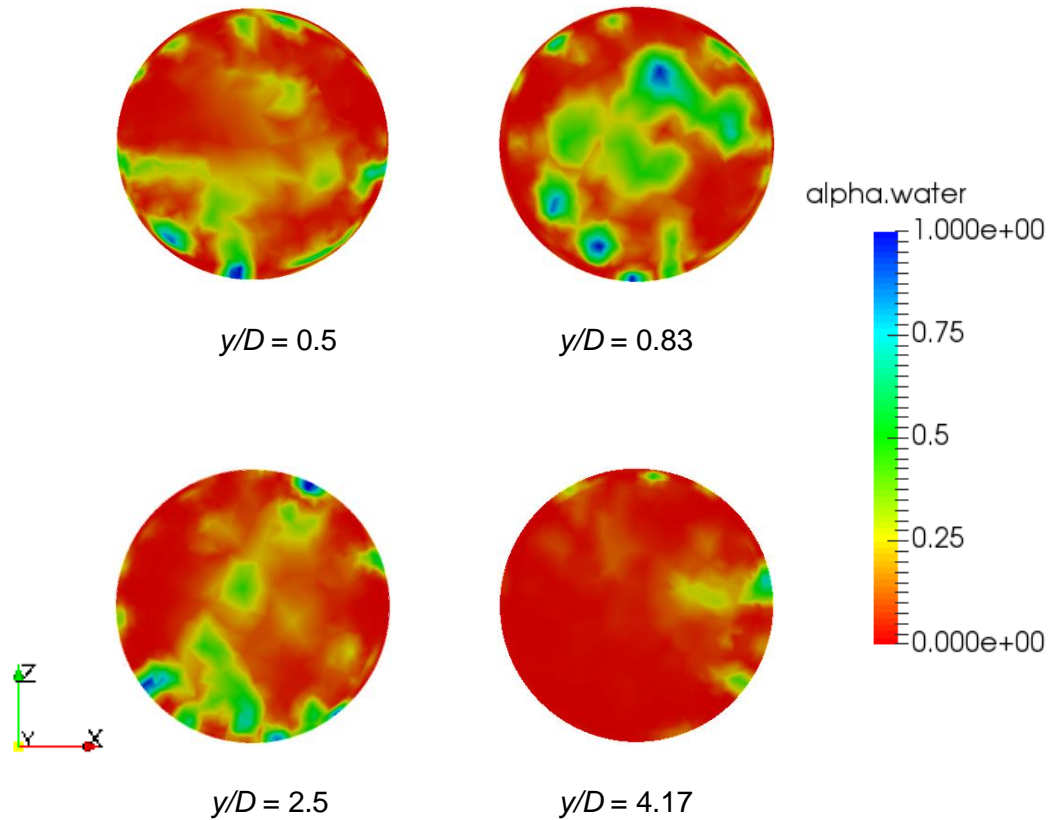


Figure 4.41. Phase fraction contours on 4 horizontal circular sliced cross-sections ( $y/D= 0.5$ ,  $0.83$ ,  $2.5$  and  $4.17$ ) along the vertical direction at the 60 s time instant

Instantaneous phase fraction contours on many vertical circular sliced cross-sections ( $x/D=\text{constant}$ ) normal to the horizontal feed pipe are shown in Figure 4.42. An enlarged view of the slice closest to the dead-leg exhibits the formation of striation patterns discussed above, along with marked fast-moving water flow in the center core of the horizontal feed pipe.

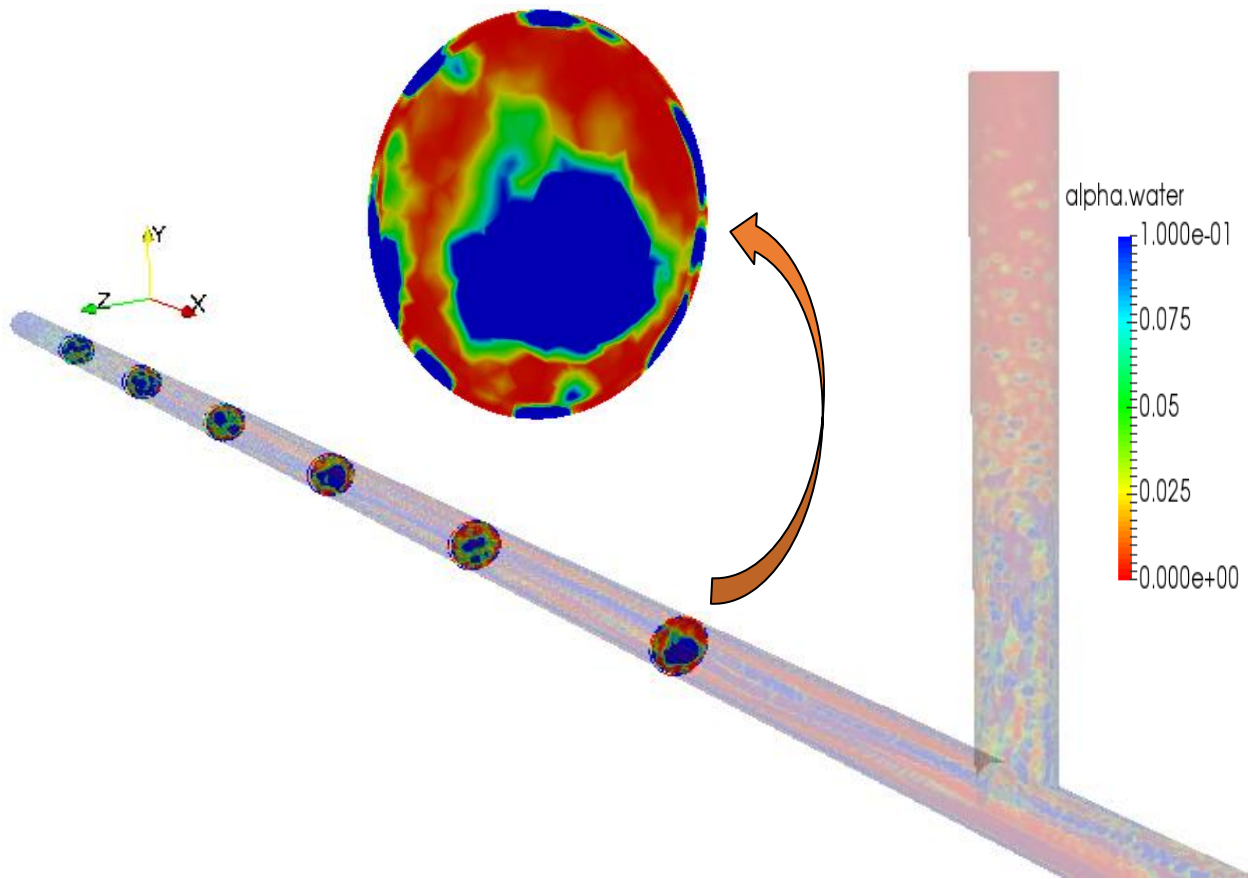


Figure 4.42. Phase fraction contours on vertical circular sliced cross-sections ( $x=\text{constant}$ ) along the horizontal feed pipe at the 60 s time instant

#### 4.3. Closure

Results of computational simulations of unsteady turbulent two-phase flow of a 90-10% oil-water mixture in both 2-D channel and realistic 3-D pipe systems with vertical capped dead-legs were presented above. For the 2-D channel unsteady simulations that covered a time duration of 1 min, a parametric study of the effects of the average inlet velocity, length of the dead-leg, width of the dead-leg, position of the dead-leg relative to the inlet of the feed channel, viscosity of crude oil and density of crude oil on the evolving flow field, extent of the recirculating vortices, oil separation and oil accumulation within the vertical dead-leg were elucidated. Due to excessive computational cost associated with 3-D unsteady turbulent simulations, a limited attempt was made to solve the associated 3-D problem for the case of a vertical capped dead-leg for a time duration of 1 min for a single set of operating conditions.

## 5. Experimental Study of Phase Separation and Oil Accumulation in a Dead-Leg

Computational 2-D and 3-D analyses of transient turbulent two-phase flows and oil accumulation within a capped vertical dead-leg were discussed in previous Chapters. Validation of simulation results and their comparison against measurements play a key role in effective design and modifications of processes/equipment. Details of an experimental investigation that was conducted in the course of this research accommodating dead-legs at various inclination angles are reported in this Chapter. Moreover, experimental findings will be compared to 3-D computational results.

### 5.1. Details of the Experimental Investigation

For validation of the CFD simulations, an experimental flow loop was conceptualized, designed and set up. An isometric view of the conceptualized flow loop system is shown in Figure 5.1. The experimental set-up is a horizontal recirculating flow loop powered by a pump, whereas a flowmeter is used to determine the instantaneous flowrate in the loop. Details of the model dead-leg shown here in its vertical orientation and the need for a curved piping section are discussed below.

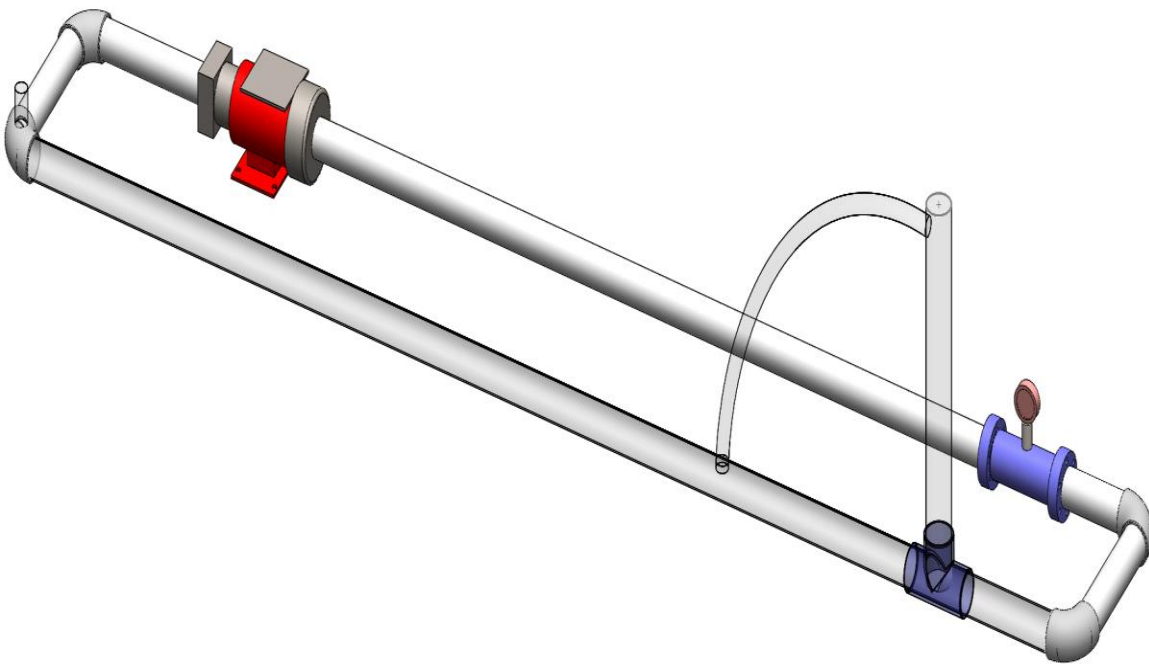


Figure 5.1. Schematic view of the proposed original experimental set-up

The experimental set-up was placed onto a sheet metal pan that served to collect any liquid leakages from the pipes, fittings, etc. A 3 HP power centrifugal pump (TEEL 2P392, Chicago, USA) was chosen as the driver for the system based on system performance calculations (Appendix C). The pump was placed on rubber spacers that served to absorb vibrations and then mounted on wood blocks (2 by 4) (Figure 5.2).



Figure 5.2. Pump resting on rubber spacers and mounted on wood blocks

Starting at the discharge side of the pump, white PVC (Schedule 40) and CPVC (Clear PVC Schedule 40) fittings/pipes were assembled. Pipes had a nominal diameter of 2" (50.8 mm). Threaded fittings were attached with aid of Teflon tape (3 mils thick, 0.4 grams/cubic centimeter density), whereas the remaining PVC pipes and fitting components were glued together with PVC cement (Oatey, Cleveland, Ohio, USA) after each component was cleaned with a primer (Oatey, Cleveland, Ohio, USA). Photographs of the system after consecutive assembly of the components in the early stages of the experiments are shown in Figure 5.3.



Figure 5.3. Post-pump discharge assembling of the PVC pipe sections/fittings

Guaranteeing that all components were positioned in horizontal position was achieved by monitoring the position of the bubble levels that were used (Figure 5.4).



Figure 5.4. Bubble levels utilized to assure that the pipes/components were placed properly

Allowing an adequate hydrodynamic development length (2.184 m) for establishment of a fully-developed flow within the 2" diameter pipe, the model dead-leg being a vertical clear pipe (length of 0.558 m) was attached to the clear PVC horizontal pipe (nominal inner diameter of

0.0508 m, Grainger, Chicago) through utilization of a clear PVC tee (diameter of 50 mm, Step-Tools Store, AliExpress, CHINA). The tee was placed between two horizontal clear PVC horizontal pipes with the aid of flexible rubber couplings (Figure 5.5) in order to gain the ability to tilt and position the dead-leg at different inclination angles. A layer of Vaseline was applied on the outer periphery of the transparent tee before it was inserted into the flexible rubber couplings and held in place by metal fasteners. It was later proven that even when the system was full of motionless fluid, upon loosening the two inner fasteners the transparent tee/dead-leg can easily be swiveled with little leakage.



Figure 5.5. Clear PVC tee connected with two flexible rubber couplings using metal fasteners

In order to initiate individual oil accumulation experiments within the clear model dead-leg with a well-mixed homogeneous oil-water fluid, the top of the dead-leg and the upstream side of the horizontal main pipe were connected with a reinforced vinyl flexible tubing of outer diameter of 0.0254 m (Figure 5.6).

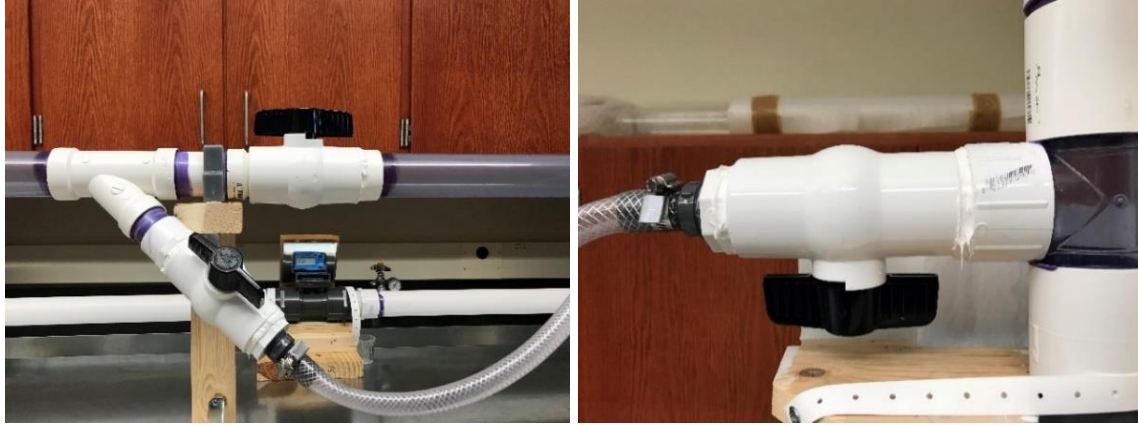


Figure 5.6. Reinforced vinyl tubing utilized for achieving a well-mixed fluid in the system before initiating oil accumulation tests

Two ball valves were placed at both ends of the elastic tube to activate this line while the mixing process was underway and deactivate it once oil accumulation was initiated (Figure 5.7-a). The upstream ball valve was positioned on the lower part of main horizontal pipe so as to minimize possible oil accumulation in the Y-branch. Another 2-inch ball valve was also placed to control flow through the horizontal pipe (Figure 5.7-b). At the beginning of each run during a time period of no more than 5 minutes, the horizontal ball valve on the clear pipe was closed and opened at regular intervals while the other two valves were left open in order to achieve a homogeneous oil and water mixture throughout the system. Contrary of actual petroleum fields, volumetric fraction of oil throughout our experiments was kept lower than water to reduce the required power of the pump by decreasing the fluid viscosity. After running the system under the specified condition for a maximum of five minutes, fluid was allowed to flow only through the horizontal pipe sections by closing the two ball valves at the ends of the vinyl tubing. Further details of the procedure will be discussed later.



(a)



(b)

(c)

Figure 5.7. (a) Reinforced vinyl tubing with two ball valves used to re-direct fluid from the main pipe to top of the dead-leg section, (b) valves used to control flows in vinyl tubing and horizontal main pipe and (c) valve used to control flow downstream of the vinyl tubing

A 0.75-inch gate valve was attached at the top of the dead-leg pipe in order to release the collected air and provide needed access at that point (Figure 5.8).



Figure 5.8. Gate valve at the top of the model dead-leg shown in its vertical position



Considering the inevitable expansion of the oil-water fluid due to expected temperature rise during the experiments, a J-shaped expansion assembly with two 3/4" gate valves was built to create an extra volume of air (Figure 5.9). The air expansion tank set-up served to absorb the expansion of the liquid system. The gate valve attached at the top of the unit was used to release the air and the other valve at the bottom of the unit served for draining the liquid when it is needed.



Figure 5.9. Two views of the J-shaped expansion assembly designed to accommodate expansion of oil-water into an air column

Another 3/4" gate valve with its discharge directed into the laboratory sink was utilized with the purpose of providing as access for drainage of the system (Figure 5.10) and accurate fluid removal steps to be discussed below. At the conclusion of the experiments, the entire fluid of the system was completely drained by collecting all of the working fluid into containers instead of draining it into the sink to avoid fire danger in sewers. The collected oil-water mixture was properly handled following established rules of Auburn University's Risk Management and Safety Department.

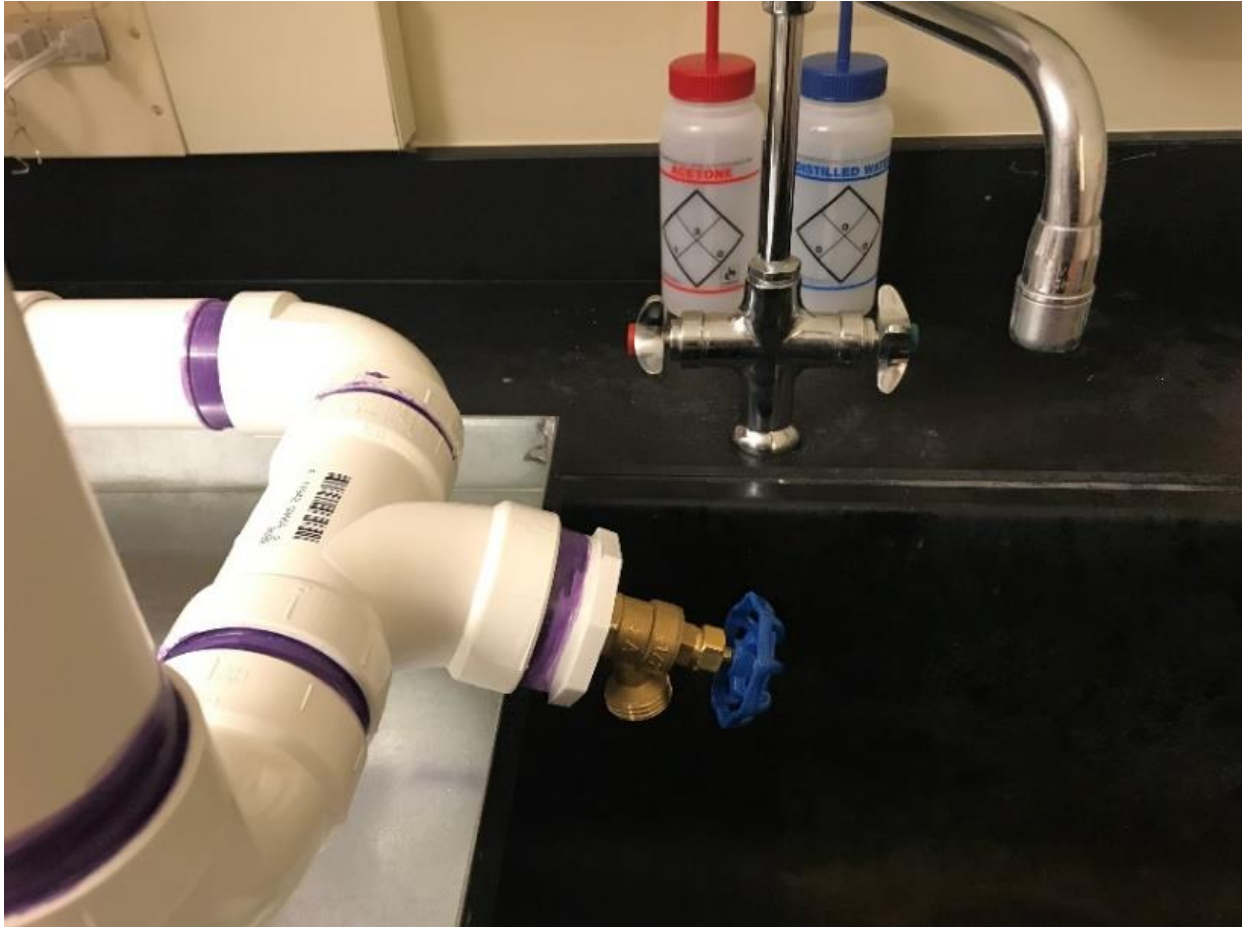


Figure 5.10. Gate valve used for drainage of the system and accurate fluid removal

#### 5.1.1. Flow Rate Measurements

Flow rate of the oil-water system was measured by means of an electronic flow meter (FLOMEC – TM200, Wichita, Kansas, USA) (Figure 5.11-b) which was installed 0.66 meters upstream of the suction side of the pump and 1.64 meters downstream of the last 90 degree bend by taking into consideration the minimum required lengths recommended in the flow meter manual (Figure 5.11). Minimum straight pipe length is suggested to be 10 times the internal diameter of the turbine for the upstream side and 5 times the internal diameter of the turbine for the downstream side in the manual of the flow meter.



(a)



(b)

Figure 5.11. (a) the location of the Flomec flow meter and (b) the flow meter

Flow range for the TM200 flow meter which is suitable for 2-inch pipes is 20–200 GPM [Flomec, 2015]. This flow rate corresponded to average fluid speed range 0.625–6.25 m/s (water) through the flow loop. It was significant to be aware of needed velocity for maintaining turbulent flow based on the percentage of each liquid component (Table 5.1). In our experiment, the average fluid velocity was maintained at the value of ~4 m/s.

Table 5.1. Operating  $Re$  numbers of the flow loop based on the concentrations of the liquid components; (a) 10 vol% and (b) 5 vol% olive oil

Room temperature : 68-70 °F	water	olive oil	$\rho_{mixture}$ (kg/m <sup>3</sup> )	990			
Density (kg/m <sup>3</sup> )	1000	900	$\mu_{mixture}$ (Ns/m <sup>2</sup> )	7.40E-03			(a)
Kinematic viscosity (m <sup>2</sup> /s)	9.53E-07	7.27E-05					
Dynamic viscosity (Ns/m <sup>2</sup> )	0.000953	6.54E-02	Average velocity (m/s)	0.25	0.5	3.988757	
Fluid fraction	0.9	0.1	The $Re$ number	1.70E+03	3.40E+03	2.71E+04	
Room temperature : 68-70 °F	water	olive oil	$\rho_{mixture}$ (kg/m <sup>3</sup> )	995			
Density (kg/m <sup>3</sup> )	1000	900	$\mu_{mixture}$ (Ns/m <sup>2</sup> )	4.18E-03			(b)
Kinematic viscosity (m <sup>2</sup> /s)	9.53E-07	7.27E-05					
Dynamic viscosity (Ns/m <sup>2</sup> )	0.000953	6.54E-02	Average velocity (m/s)	0.25	0.5	3.988757	
Fluid fraction	0.95	0.05	The $Re$ number	3.03E+03	6.05E+03	4.83E+04	

### 5.1.2. Density and Viscosity Measurements of Oil and Water

The densities of the olive oil and deionized salty water at the room temperature were measured by means of an electronic scale (Cole-Parmer, Chicago, Figure 5.12) and a measuring cup. The calibration test was conducted by measuring of water density. The density values are summarized in Table 5.2. The dynamic viscosity of the olive oil and deionized salty water were measured with a Brookfield viscosity meter (Figure 5.13) to be 0.0654 and 0.000953 Ns/m<sup>2</sup>, respectively.



Figure 5.12. Electronic scale used to measure the mass of the liquids

Table 5.2. Density measurement of the liquids

	interval		average
mass of empty container (g)	53	54	53.5
mass of container with 60 ml tap water (g)	113	114	113.5
mass of container with 50 ml salty water (g)	103	104	103.5
mass of container with 50 ml olive oil (g)	97	100	98.5
mass of 60 ml tap water (g)			60
mass of 50 ml salty water (g)			50
mass of 50 ml olive oil (g)			45
volume of tap water (ml)			60
volume of salty water (ml)			50
volume of olive oil (ml)			50
density of tap water (g/ml)			1
density of salty water (g/ml)			1
density of olive oil (g/ml)			0.9



Figure 5.13. Viscometer used to measure the dynamic viscosities of the liquids

### 5.1.3. Support of the Flow Loop

The whole system composed of the drainage pan and above-mentioned subsystems was supported by wood pieces (Figure 5.14-a) connected with double-wide corner braces (Figure 5.14-b). While the horizontal pipes were seated on these wood supports, two elevated corners of the system were placed on the corner braces (Figure 5.14-c) and fixed to the wood supports with a plastic hanger strap (Figure 5.14-d).



(a)



(b)



(c)



(d)

Figure 5.14. (a) Wood supports to bear the elevated part of the system, (b) double-wide corner brace and (c) corner brace and (d) plastic hanger strap

## 5.2. Emulsification Tests

After all components were assembled and the system was ready to run, emulsification tests were practiced with three different cooking oils which were: canola, vegetable and olive oil; and three different types of water, namely tap, deionized and distilled water.

Emulsification is a process by which a liquid is dispersed into a second immiscible liquid through formation of small droplets. In effect, the dispersed phase is found throughout the continuous phase. Since the purpose of this study is to observe the separation of the oil and water phases, a 10% oil and 90% water system was investigated to observe the possibility of formation of emulsions. To accommodate the clearest visualization of the oil-water system, commercial-grade canola oil, vegetable oil and olive oil were mixed with tap, deionized and distilled water.

### 5.2.1. Distilled and Deionized Water

Deionized water and distilled water can be obtained from tap water which has organic materials and inorganic minerals.

In order to obtain distilled water, filtered water is heated until it has evaporated. Steam is collected in a sterile container, where it condenses and turns into liquid water. Since water has a lower boiling point than most contaminants, they are left behind when the water turns into steam. Water distillation can remove many impurities such as nearly all minerals, many chemicals, and most bacteria besides ions. In order to increase the purification level, this process can be repeated two or three times (US Water Systems, no date). Distilled water for the test runs was purchased at a local supermarket.

Deionized water is water which is purified from all ions, typically all of the dissolved mineral salts. Only ions which are charged non-organic particles are removed from the water by applying the deionization process. The organics can typically be removed via physical filters, carbon filters, and reverse osmosis membranes. After this pre-treatment, the water can be sent through a deionization system, which contains two types of resin called cation and anion. Cation and anion resins attract positive and negative ions, respectively, replacing them with  $H^+$  and  $OH^-$ .  $H^+$  combined with  $OH^-$  becomes  $H_2O$ . The combination of filters and deionization resins can eliminate nearly all contaminants (US Water Systems, no date). Deionized water was provided from the water deionization system in operation in the Department of Chemistry and Biochemistry at Auburn University (Figure 5.15).



Figure 5.15. Deionized water processing unit in the Department of Chemistry and Biochemistry at Auburn University featuring a reservoir feed water purification system



### 5.2.2. Magnetic Stirring

A magnetic stirrer (Thermo Scientific, Dubuque, Iowa) in combination with a suitable magnetic stir bar was used in order to mix oil and water phases inside a 50 ml jar continuously for a period of an hour (Figure 5.16). The corresponding photos at different time instants can be observed in Appendix D. After the stirring process was completed, separation of the two phases was observed, and it was concluded that emulsification in none of the combinations of oil and water was observed. However, some oil-water systems were “cloudier” during the agitations which means there were tiny droplets of oil in water. More viscous oil exhibits a greater tendency to form an emulsion depending on having a relatively low oil-water interfacial tension. Figures 5.17-5.22 show each combination of water-oil mixing processes and separated cases. Based on the consequences of this test, olive oil and deionized water were chosen for use in the experiments due to the observed improved separation characteristics.



Figure 5.16. Stirring hot plate used to stir oil-water liquid systems



(a)

(b)

(c)

Figure 5.17. Appearance of the mixture of canola oil with (a) tap water, (b) deionized water and (c) distilled water near completion of stirring after 60 min; outlines of the distorted column of canola oil in the core of the system can be observed.

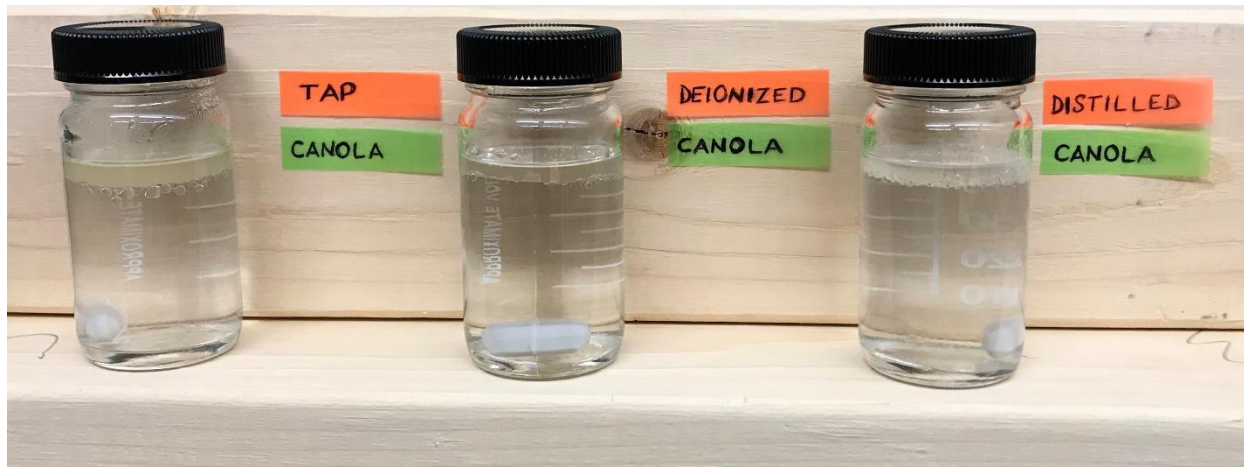


Figure 5.18. Comparison of the separation of canola oil from tap, deionized and distilled water upon conclusion of 60 minutes of magnetic stirring showing the oil layer sitting on top of the respective water layer



(a)

(b)

(c)

Figure 5.19. Appearance of the mixture of vegetable oil with (a) tap water, (b) deionized water and (c) distilled water near completion of stirring after 60 min; outlines of the distorted column of vegetable oil in the core of the system can be observed.



Figure 5.20. Comparison of the separation of vegetable oil from tap, deionized and distilled water upon conclusion of 60 minutes of magnetic stirring showing the oil layer sitting on top of the respective water layer



(a)

(b)

(c)

Figure 5.21. Appearance of the mixture of olive oil with (a) tap water, (b) deionized water and (c) distilled water at time 60 min; outline of the distorted column of olive oil in the core of the system can be observed.



Figure 5.22. Comparison of the separation of olive oil from tap, deionized and distilled water upon conclusion of 60 minutes of magnetic stirring showing the oil layer sitting on top of the respective water layer

### 5.3. Degassing of the Water-Air System and Addition of Oil

Once the desired oil-water combination was decided, the system was filled with deionized water without adding any oil with the aim of checking for any leakage. The leaking points were sealed with silicon. Afterwards, the pump was turned on in order to release air which was visible within the system as much as possible. Flow patterns of air-water two-phase flows which occur within a vertical pipe are demonstrated schematically in Figure 5.23. Experimental observation of these flow patterns in the course of this study are illustrated in Figure 5.24. Slug flow was observed within the vertical dead-leg at the beginning of a typical run (Figure 5.24-a). A big air pocket rose upward and collected in the top part of the dead-leg. The air pockets sizes were becoming smaller in time and slug flow turned to bubble flow (Figure 5.24-b). Consequently, the water level at the top of the vertical dead-leg reduced with disappearance in gas phase within the system (Figure 5.25).

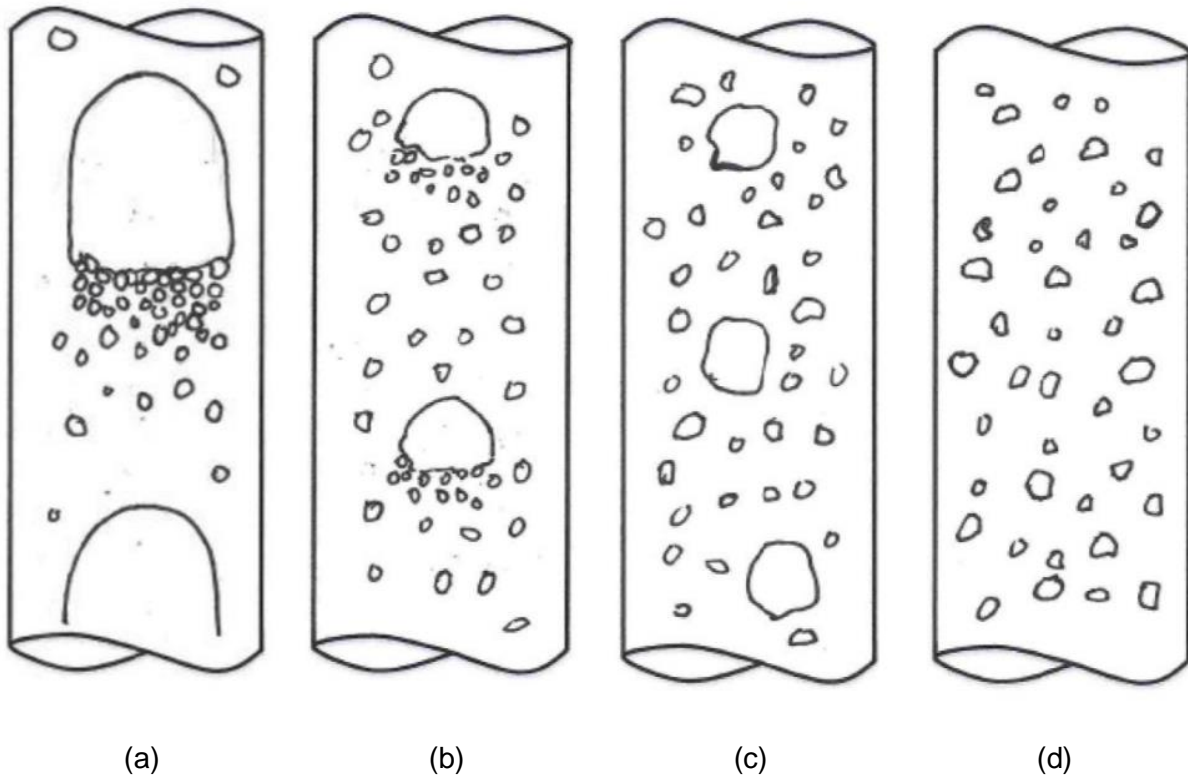


Figure 5.23. Variety of two-phase (e.g. air-water) flow patterns, i.e. (a) slug, (b) slug-bubble, (c) bubble-slug and (d) bubble flow



(a)



(b)

Figure 5.24. Observed (a) slug flow followed by a wake region and (b) slug flow turning into bubble flow within the vertical dead-leg system during degassing

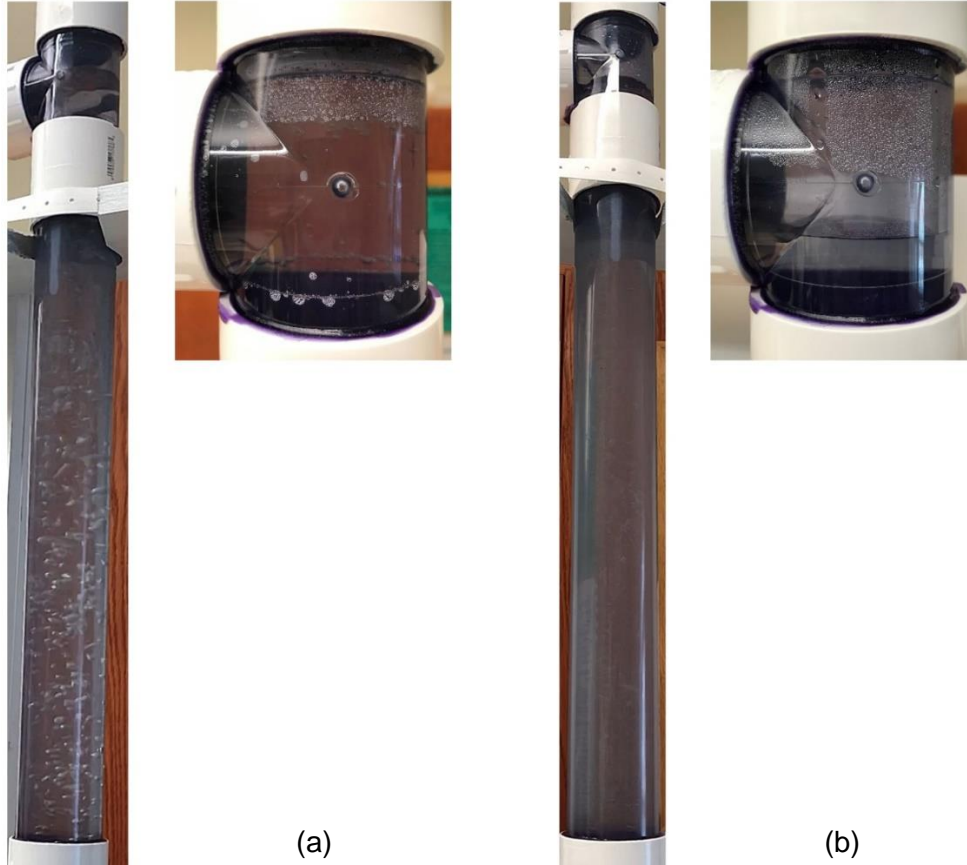


Figure 5.25. Observed water levels within the vertical dead-leg (a) with air pockets during degassing and (b) without air pockets far into degassing

### 5.3.1 Addition of Oil

Separation of phases in oil-water mixtures and oil accumulation in the dead-leg was studied by considering two different oil-water volume ratios which were 5-95 and 10-90 approximately. After degassing process, 10% water was discharged from the system and replaced with the same volume of oil. In effect, the 90% deionized water and 10% olive oil system was ready for testing with the purpose of gaining an idea on how the system worked and checking whether oil and water phases formed an emulsion. In order to have a clear view of the transparent dead-leg section and tee, fluorescent lights were located behind these parts.

Even though tests were conducted by using a magnetic stirrer to observe whether the oil and water components emulsified and deduced that there was not a risk of emulsion occurrence, after a few minutes the pump turned on, oil and water formed emulsions with a cloudy appearance (Figure 5.26).

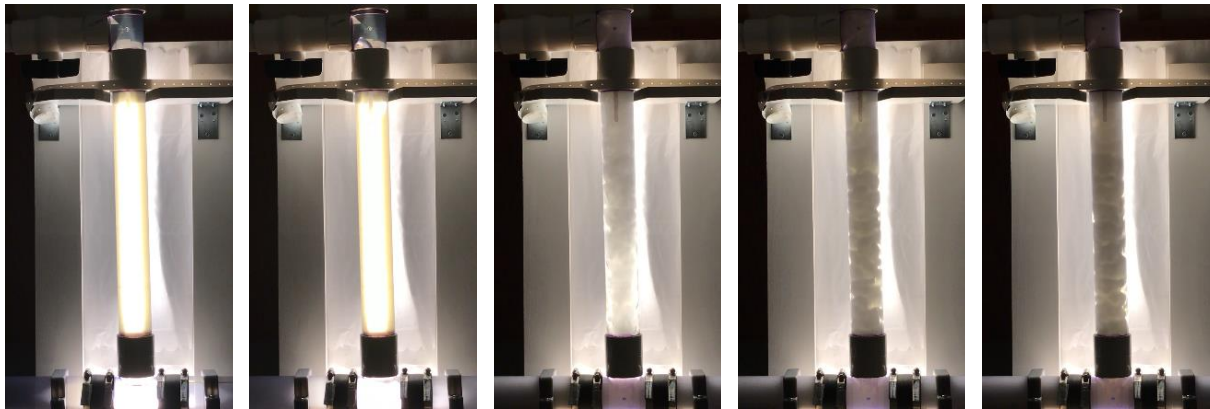


Figure 5.26. Gradual emulsion formation for the 10%-90% olive oil- water system at different time instants (left to right)

It was postulated that the high-pressure pump formed very small droplets at the interface of the two phases by imparting high shear to the dispersed phase which was oil in this case. High shear led to extreme mixing of oil and water phases and caused very small size droplet formations. Decrease in droplet size and so surface area cause lower interfacial tension. Lower surface tension exhibits a greater tendency to form emulsion. Since the system had a higher volume fraction of water than oil, the resultant emulsion is called an oil-in-water emulsion which is shown in Figure 5.27.



Figure 5.27. System with oil-water emulsion (10%-90% olive oil-water system)



### 5.3.2. Break-up of Emulsions

In order to break up an emulsion, a variety of electrolytic, physical and chemical methods are adopted based on the properties of the emulsion. Although demulsification has potential to cause corrosion within pipelines and components of the system, forming of foam, increase the fluid viscosity, and rise of power and energy consumption, emulsion breaks are applied to separate phases in many different areas. Among several emulsion breaking techniques, adding sodium chloride (NaCl), sodium sulfate ( $\text{Na}_2\text{SO}_4$ ) and alcohols which were methanol ( $\text{CH}_3\text{OH}$ ), ethylene glycol ( $\text{C}_2\text{H}_6\text{O}_2$ ) and isopropyl alcohol ( $\text{CH}_3\text{CHOHCH}_3$ ) were adopted with the intention of deciding which demulsifier was effective on separation of olive oil-deionized water emulsion at hand. The samples of emulsion were taken from the system. Sodium chloride was preferred in order to break emulsion since the best separation was observed in that case (Figure 5.28-a).

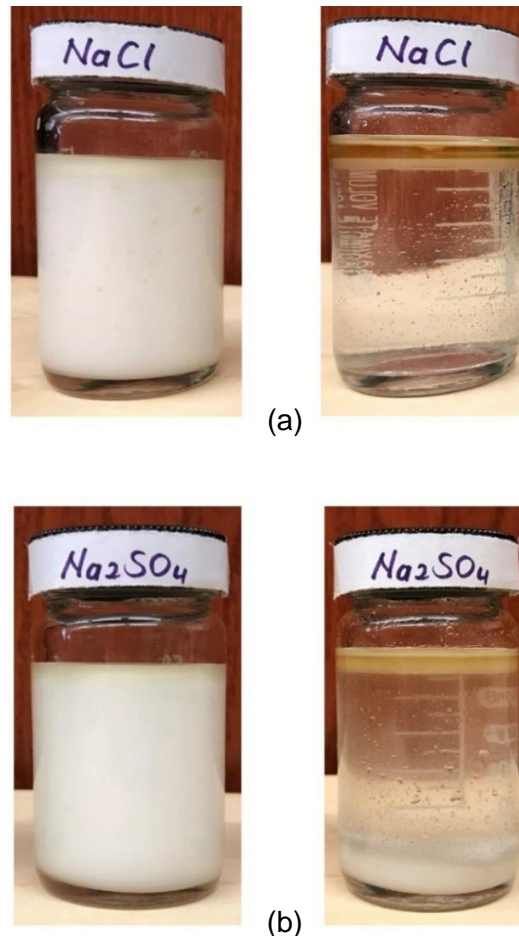


Figure 5.28. Effectiveness of sodium chloride (NaCl), sodium sulfate ( $\text{Na}_2\text{SO}_4$ ) on breaking oil-water emulsion with the combination of 10%-90% oil-water, respectively



(a)



(b)



(c)

Figure 5.29. Effectiveness of (a) methanol ( $\text{CH}_3\text{OH}$ ), (b) ethylene glycol ( $\text{C}_2\text{H}_6\text{O}_2$ ) and (c) isopropyl alcohol ( $\text{CH}_3\text{CHOHCH}_3$ ) of breaking 10%-90% oil-water emulsion

The amount of sodium chloride addition was limited by considering the maximum solubility of sodium chloride in water. Based on the saturation limit of sodium chloride in water, which is 36% at 25 °C [Tro et al., 2008], the maximum amount of sodium chloride was calculated subject to the total mass of the liquid in the system. Thus, 737 g sodium chloride which was well less than the calculated maximum amount (6,970.886 g) was added to the system, since just as the other emulsifiers, salt damages the system components such as a pump and flowmeter. It was observed that separated oil started gathering at the upper part of the vertical dead-leg (Figure 5.30). Salt helped the small droplets coalesce by increasing the ionic strength of the aqueous layer which is a measure of the concentration of ions, and the emulsion disappeared into cleanly-partitioned layers of olive oil and deionized water.



Figure 5.30. Observation of accumulated olive oil in the vertical dead-leg separated from the 90%-10% water-oil as a result of salt addition

#### 5.4. Procedure for Oil Accumulation Tests

After it was confirmed that salt could serve to break the emulsion, the system was completely drained and refilled with 5.115 gallon (0.02 m<sup>3</sup>) deionized water. After the degassing process was repeated, 5% of volume of water was replaced with the same amount of oil. Based on the calculation of the maximum solubility limit of salt in water, 737 g of table salt was added to the system. From this point forward, the flow loop was subjected to the following procedure in order to perform oil accumulation tests for a given mixture and a given inclination angle of the dead-leg.

##### 5.4.1. Homogenization of the System

As a first step, the pump was turned on and the system was allowed to mix homogeneously for 5 minutes. During this period, the ball valve connected on the horizontal pipe was opened and closed regularly by keeping open the other valves on the mixing line with the aim of achieving a homogeneous system. Visual and sound evidence of cavitation of the fluid was observed during the period that the entire fluid in the system was forced through the elastic tube. The fluid emerging horizontally at that point impinged on the downstream side of the dead-leg and cavitation resulted at that stagnation point.

##### 5.4.2. Pump Shutdown and Oil Column Initialization

After 5 min, the pump was shut down, mixing line was excluded and some amount of liquid was drained immediately from the gate valve which was inserted in the pipeline system close to the sink (Figure 5.31). This procedure was aimed at decreasing the top level of the liquid to appear within the transparent part of the vertical dead-leg.



(a)

(b)

Figure 5.31. Observed oil column within the dead-leg (a) before and (b) after careful drainage aimed at lowering the top column of oil to be visible in the transparent dead-leg; in this experiment, the top and bottom positions of the oil layer before start of the oil accumulation test are at 21” and 19.25” positions, respectively

#### 5.4.3. Transient Oil Accumulation Test

After enough amount of liquid was discharged in order to have the oil column in the dead-leg to be fully visible, the pump was turned on in order to observe the dynamic oil accumulation within the vertical dead-leg for a time period of 15 min. During this period the top and bottom positions of the oil column were recorded using a ruler placed parallel to the dead-leg. This step was recorded during the 15 min duration of the experiment to be able to measure the growth rate of the oil column within the dead-leg (Figure 5.32). Even though all 5% oil experiments were conducted for a duration of 15 min, their results were plotted for 10 min. The above steps were repeated four times for check repeatability of the experiments (Figures 5.32-5.35).

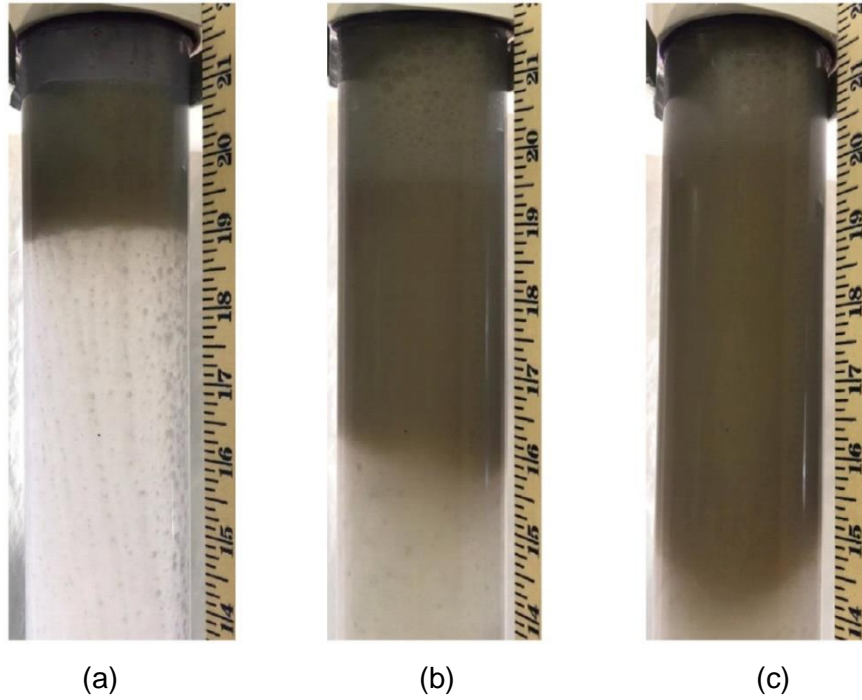


Figure 5.32. Dynamic views of oil accumulation within the 90° (vertical) dead-leg for run 1 at time instants: (a) initial time, (b) 5 min and (c) 10 min (5 vol% oil)

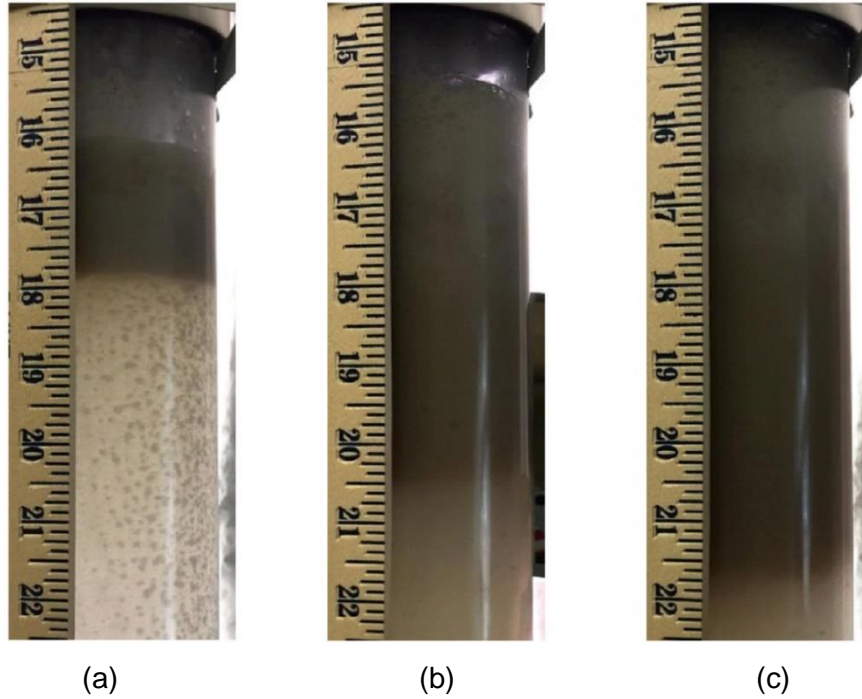


Figure 5.33. Dynamic views of oil accumulation within the 90° (vertical) dead-leg for run 2 at time instants: (a) initial time, (b) 5 min and (c) 10 min (5 vol% oil)

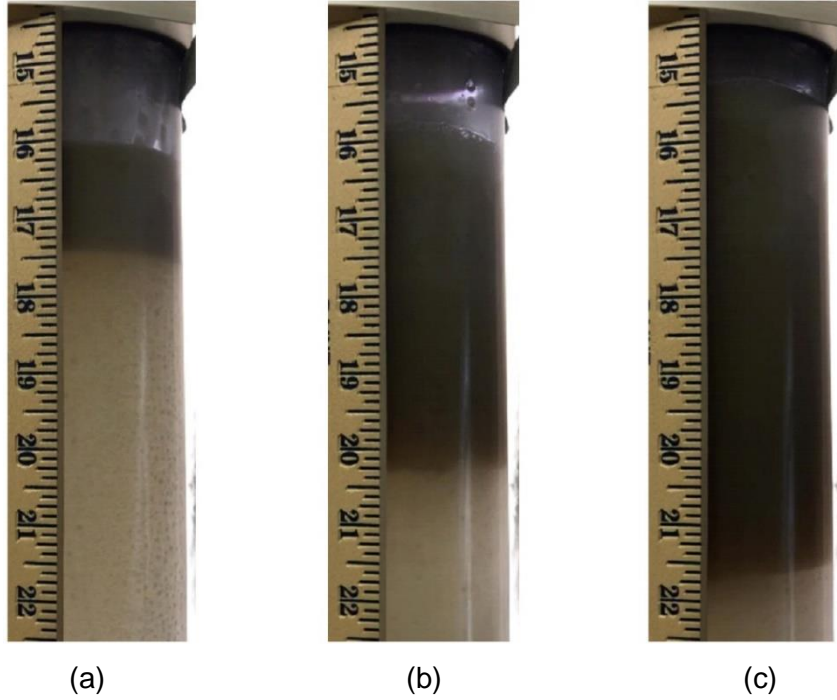


Figure 5.34. Dynamic views of oil accumulation within the 90° (vertical) dead-leg for run 3 at time instants: (a) initial time, (b) 5 min and (c) 10 min (5 vol% oil)

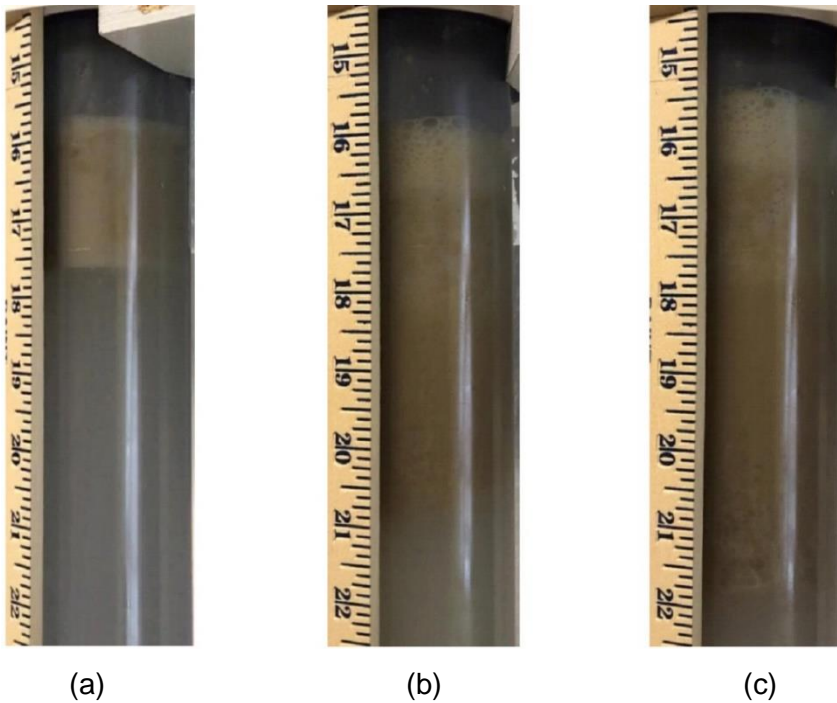


Figure 5.35. Dynamics views of oil accumulation within the 90° (vertical) dead-leg for run 4 at time instants: (a) initial time, (b) 5 min and (c) 10 min (5 vol% oil)

The raw data for these four experiments (top and bottom heights as functions of elapsed time) are provided in Appendix E (Tables E.1-E.4). The positions of top height and bottom height of the oil columns at the beginning of the oil accumulation tests are summarized in Table 5.2.

Table 5.3. Dimensionless initial heights of the top and bottom positions of the oil column with the 5%-95% oil-water mixture at the start of the oil accumulation tests

	initial top level				initial bottom level			
	D				D			
	1	2	3	4	1	2	3	4
90°	10.25	9	8.75	8.953125	9.515625	8.1875	8	8
60°	10.25	8.3125	8.0625	8.171875	9.8125	7.5625	7.375	7.59375
45°	8.28125	8.375	8.71875	8.3125	7.59375	7.6875	8.03125	7.5625
30°	9.75	9.375	9.625	9.34375	8.8125	8.53125	8.71875	8.4375

It is noted that the initial heights of the oil column at the start of the oil accumulation tests were at times greater than the diameter of the dead-leg ( $D$ ). This distance should be kept to a minimum, but this is not avoidable due to time-consuming execution of the steps that were discussed earlier. One should also make sure that the bottom positions of the initial oil columns are nearly identical.

The cumulative data for the height of the oil column obtained from the top and bottom height raw data were then plotted on the same graph (Figure 5.36). The averages of the four values of the instantaneous height of the oil column are exhibited in Figure 5.37. Individual graphs and details can be found in Appendix E. This Figure and similar graphs obtained for different inclination angles will be discussed further below.

During the experiments, volumetric flow rates were recorded by reading the digital display of the flow meter and the average value was calculated. The average volumetric flow rates within the horizontal pipe and the elastic tube (inner diameter of 0.0254 m) were recorded to be 0.008 m<sup>3</sup>/s and 0.002 m<sup>3</sup>/s, respectively. The  $Re$  numbers were calculated as 24,900 and 12,700 within the horizontal main pipe and the elastic tube section, respectively.



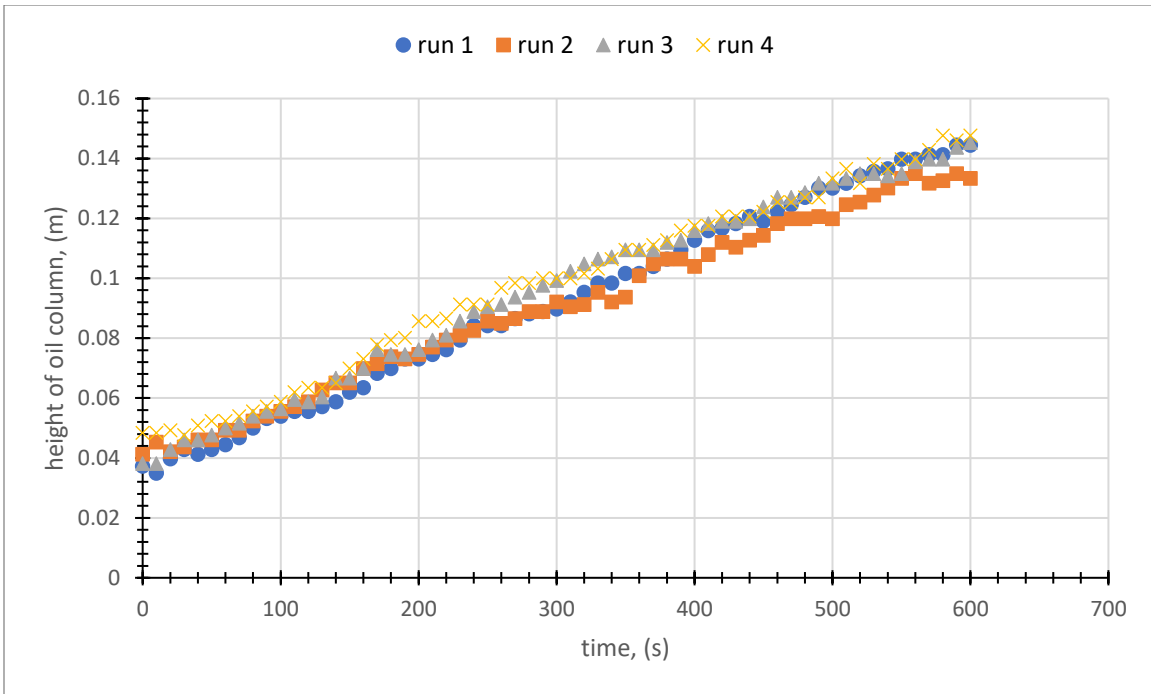


Figure 5.36. Instantaneous height of the oil column vs. time within the 90° (vertical) dead-leg for each run (5 vol% oil)

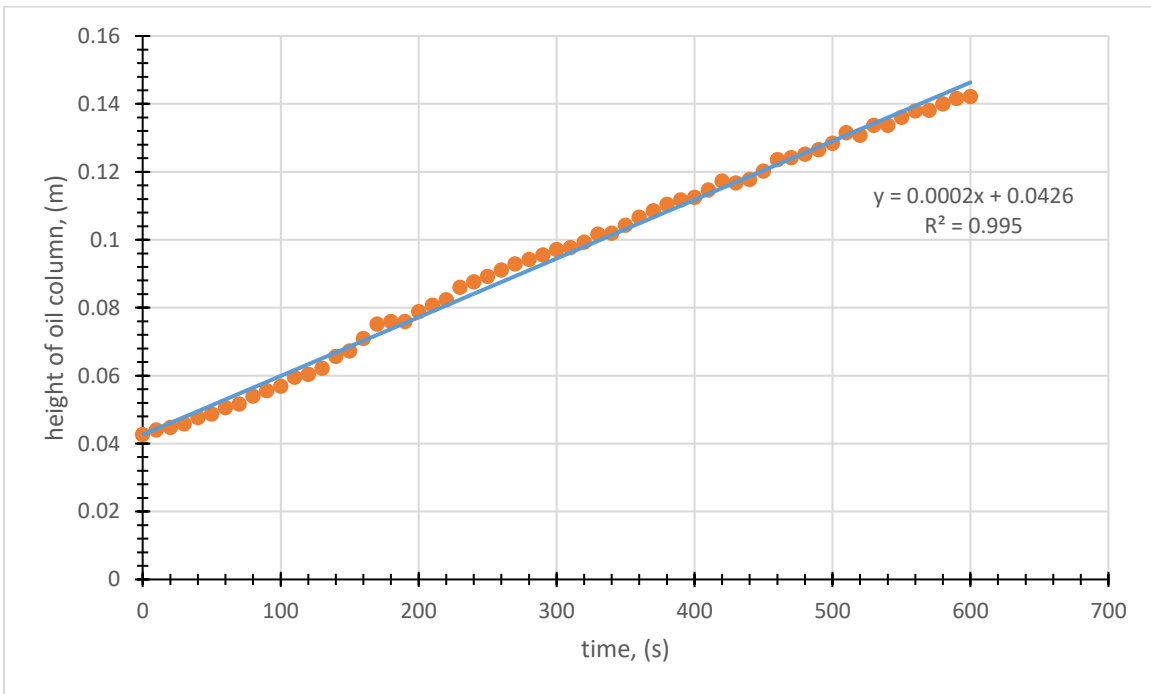


Figure 5.37. Average instantaneous height of the oil column vs. time within the 90° (vertical) dead-leg (5 vol% oil) along with the least-squares linear curve fit

At the conclusion of the 15 min time period, the pump was shut down and the accumulated oil within the J-shaped expansion section of the system was collected in order to re-introduce it back into the system to keep the oil percentage the same for the following runs (Figure 5.38). The corresponding dates of the experiments, volume of oil collected from the expansion section and the recorded temperatures are summarized in the Appendix E (Table E.9).



Figure 5.38. Example of segregated oil collected within the J-shaped expansion section

### 5.5. Recorded System Temperature Rise

The system temperature increased during the experiments due to imparted power of the pump and frictional effects. Increase in temperature was measured from the collected oil (mostly) by using an Ashcroft's industrial bimetal thermometer which is hermetically sealed. The thermometer has  $\pm 1\%$  (ASME B40.200 (B40.3) Grade A ( $\pm 1\%$  of span) accuracy. As might be expected, the temperature measured from the inactive J-shape expansion section was lower than the system temperature; however, since the liquid was taken from the same place to measure the temperature after every run, it did not affect the comparison of the results. The recorded temperatures of each run can be found in Appendix E (Table E.9). Due to the temperature rise issue with this system, only two consecutive oil accumulation tests were attempted at each session. Generally, the system was allowed to cool down for a minimum of 2 hours before new tests were performed. In response to cool-down of the system, expansion of fluid volume within the system was observed (Figure 5.39).

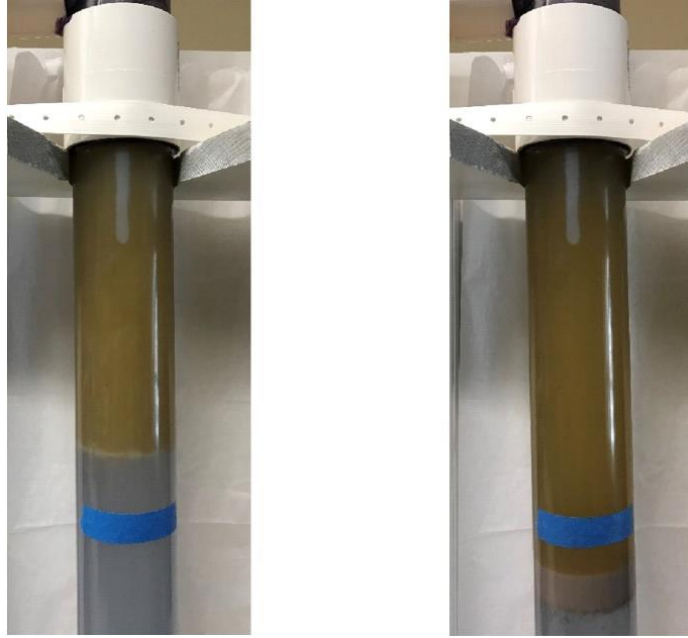


Figure 5.39. Observed change in volume after cooling down of the system (left column corresponds to the hot fluid at the end of oil accumulation test, whereas the right column shows the same system after cool-down for minimum of 1 hour)

#### 5.6. Oil Accumulation within Non-Vertically Positioned Dead-Legs

Due to gravitational force, the pipe inclination angle (horizontal, inclined and vertical positions) affects the transition mechanics. Even though a dead-leg in the system is not an active component meaning there is no dominant fluid flow within the dead-leg except the fluid coming from the main pipe, it might be useful to change the inclination angle of the dead-leg to have an idea whether the inclination of dead-leg has an effect on separation of the oil phase. Accordingly, the experimental procedures (section 5.4) were repeated with the same steps by changing the inclination angle of the vertical dead-leg to be  $60^\circ$ ,  $45^\circ$  and  $30^\circ$ . Each experiment was run for a minimum time duration of 10 min (maximum of 15 min) and the results were plotted for 10 min and shown in Figures 5.40-5.45, 5.46-5.51 and 5.52-5.57 for  $60^\circ$ ,  $45^\circ$  and  $30^\circ$  inclined dead-legs, respectively. The details and individual graphs can be found in Appendix E.

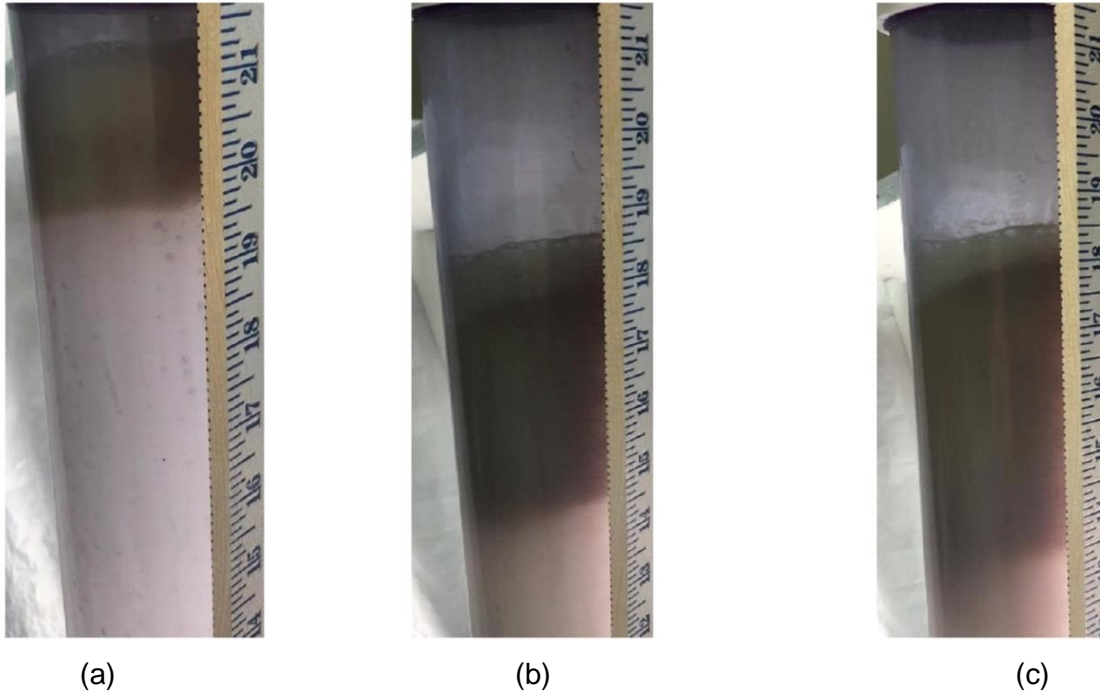


Figure 5.40. Oil accumulation within the 60° dead-leg for run 1 at time instants: (a) initial time, (b) 5 min and (c) 10 min (5 vol% oil)

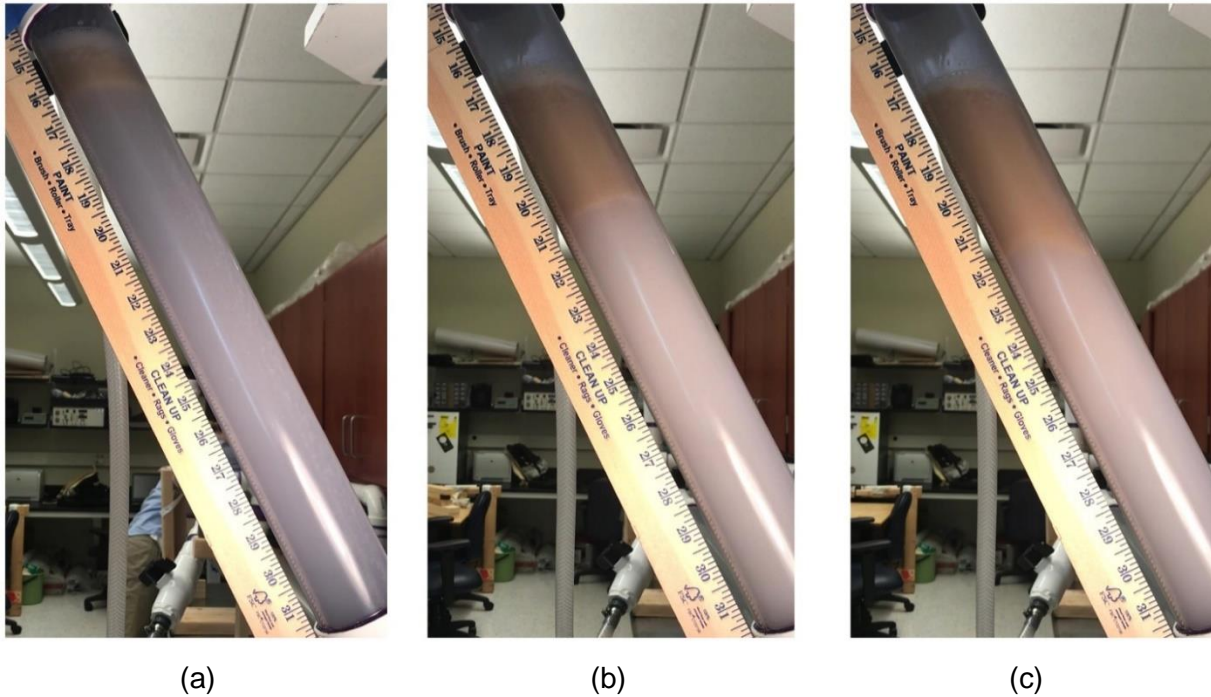


Figure 5.41. Oil accumulation within the 60° dead-leg for run 2 at time instants: (a) initial time, (b) 5 min and (c) 10 min (5 vol% oil)

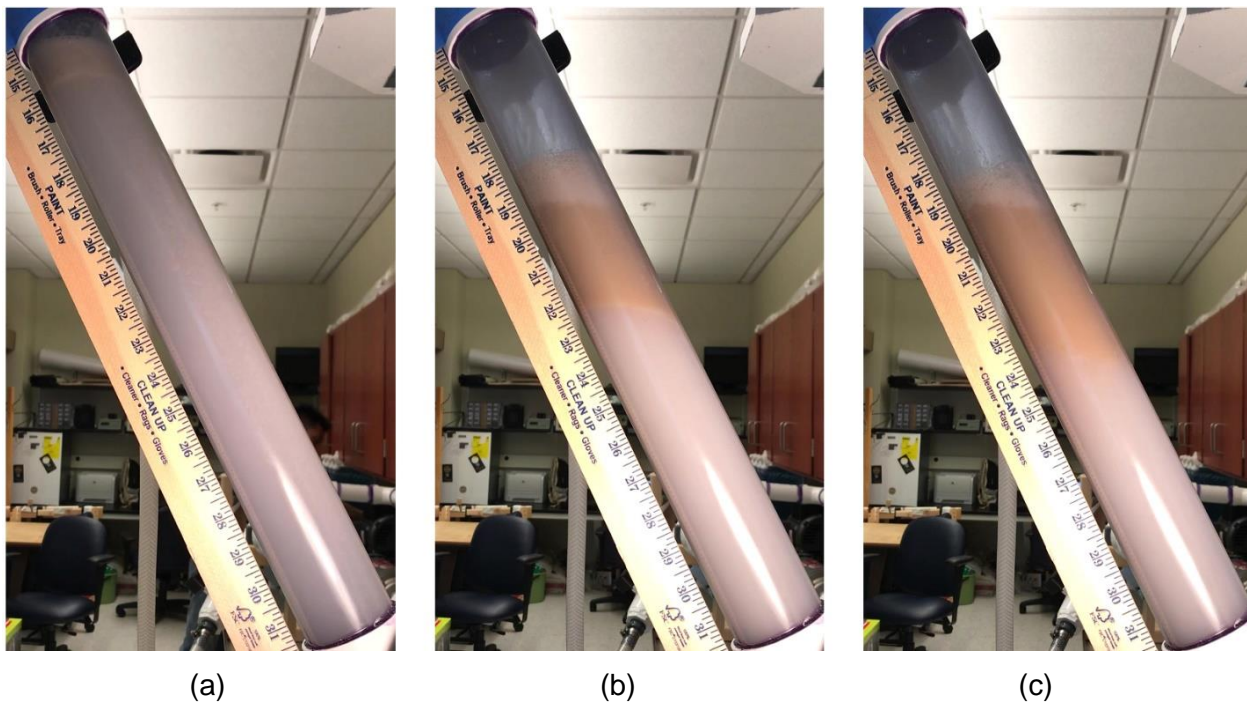


Figure 5.42. Oil accumulation within the 60° dead-leg for run 3 at time instants: (a) initial time, (b) 5 min and (c) 10 min (5 vol% oil)

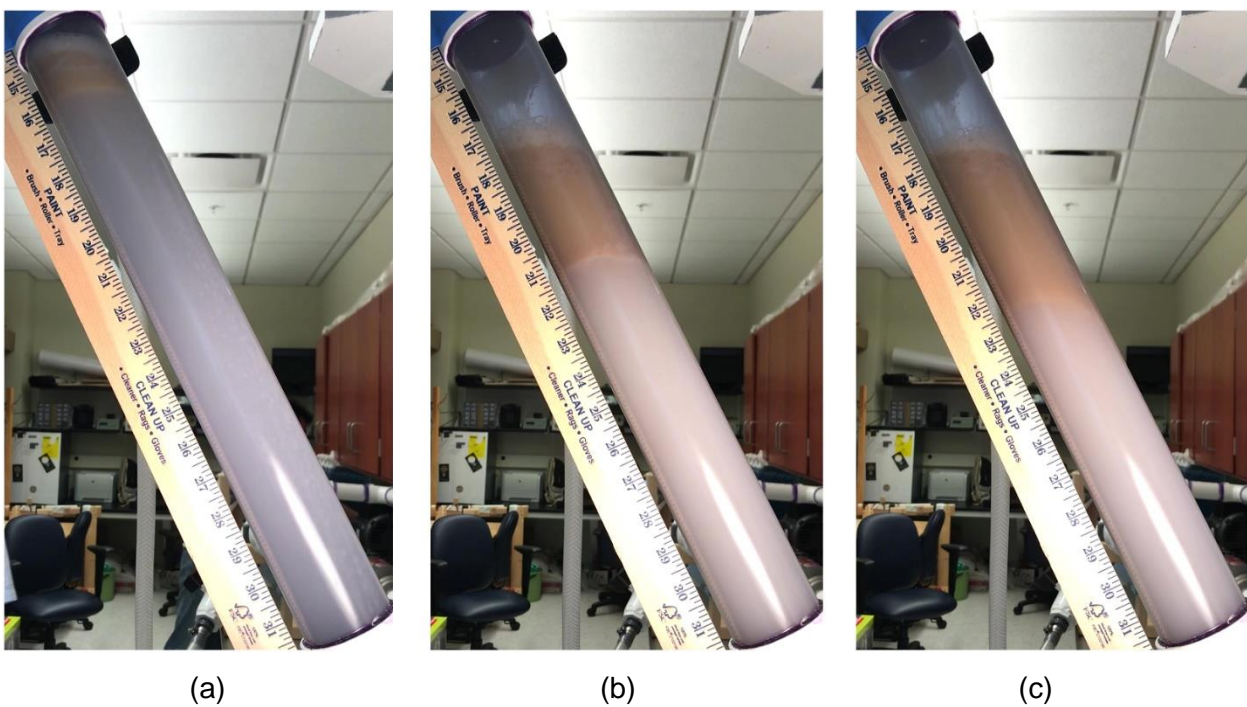


Figure 5.43. Oil accumulation within the 60° dead-leg for run 4 at time instants: (a) initial time, (b) 5 min and (c) 10 min (5 vol% oil)

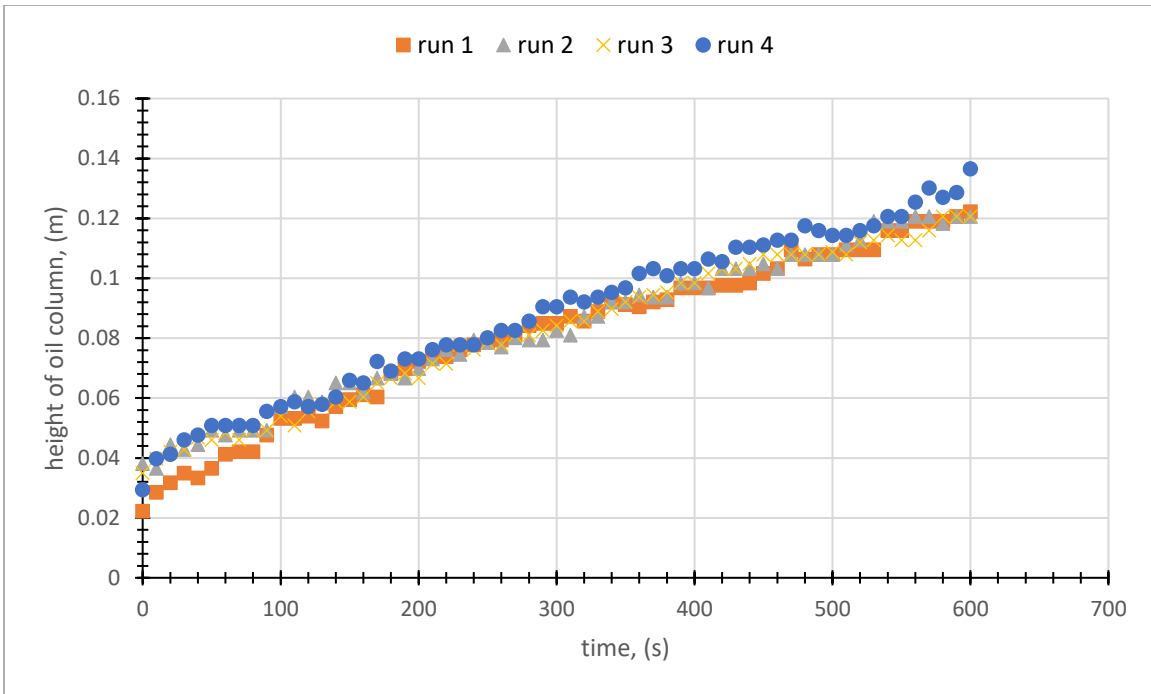


Figure 5.44. Instantaneous height of the oil column vs. time within the 60° dead-leg for each run (5 vol% oil)

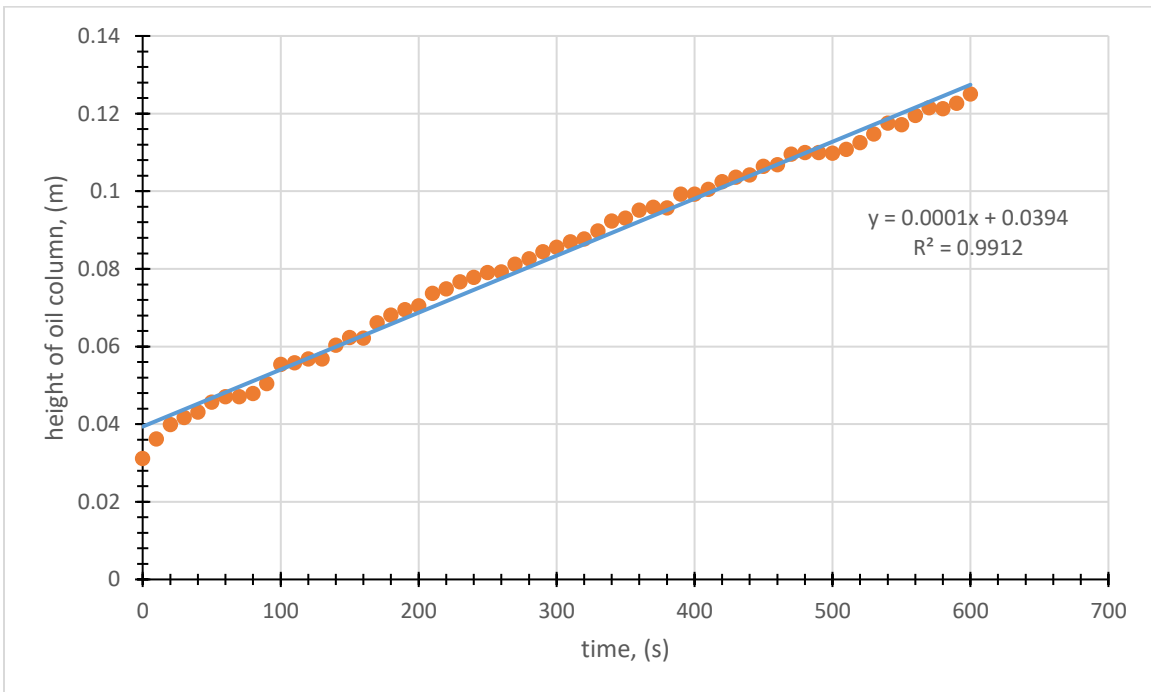


Figure 5.45. Average instantaneous height of the oil column vs. time within the 60° dead-leg along with the least-squares linear curve fit (5 vol% oil)



(a)

(b)

(c)

Figure 5.46. Oil accumulation within the 45° dead-leg for run 1 at time instants: (a) initial time, (b) 5 min and (c) 10 min (5 vol% oil)



(a)

(b)

(c)

Figure 5.47. Oil accumulation within the 45° dead-leg for run 2 at time instants: (a) initial time, (b) 5 min and (c) 10 min (5 vol% oil)



(a)

(b)

(c)

Figure 5.48. Oil accumulation within the 45° dead-leg for run 3 at time instants: (a) initial time, (b) 5 min and (c) 10 min (5 vol% oil)



(a)

(b)

(c)

Figure 5.49. Oil accumulation within the 45° dead-leg for run 4 at time instants: (a) initial time, (b) 5 min and (c) 10 min (5 vol% oil)



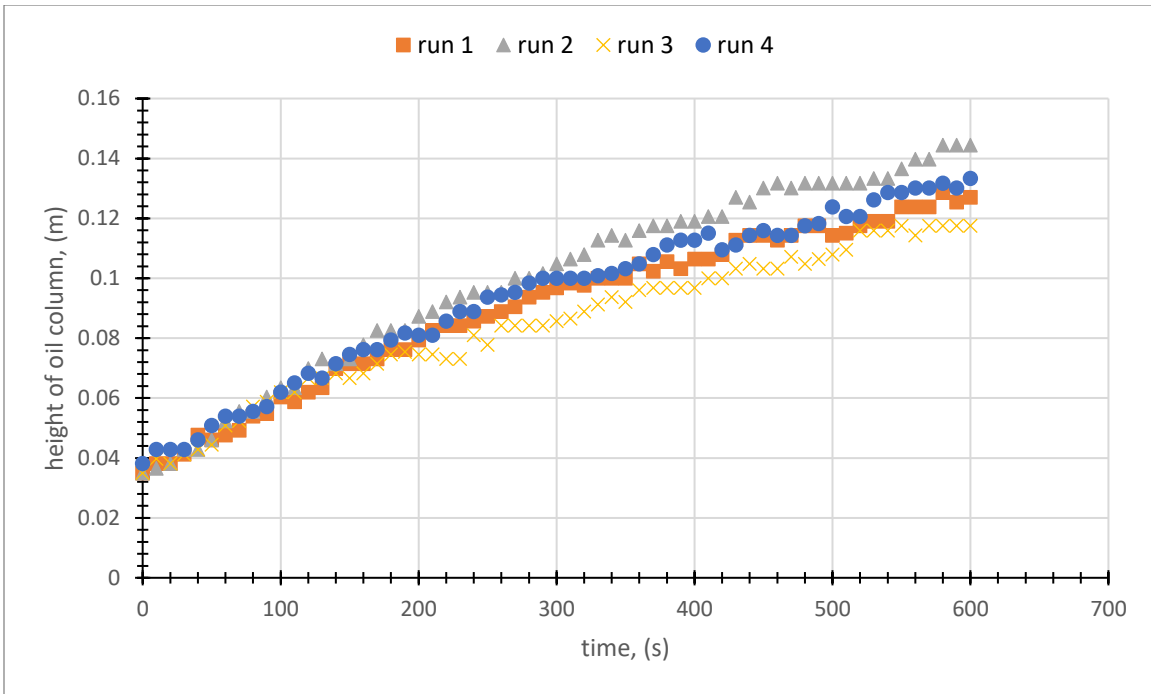


Figure 5.50. Instantaneous height of the oil column vs. time within the 45° dead-leg for each run (5 vol% oil)

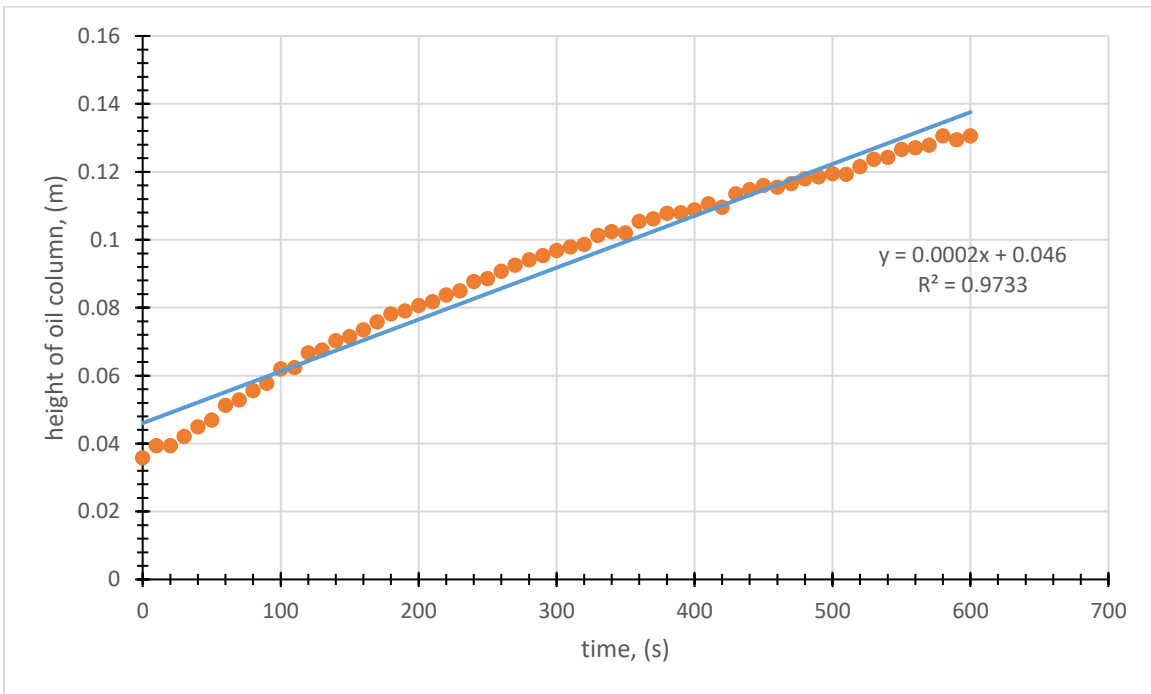


Figure 5.51. Average instantaneous height of the oil column vs. time within the 45° dead-leg along with the least-squares linear curve fit (5 vol% oil)



Figure 5.52. Oil accumulation within the 30° dead-leg for run 1 at time instants: (a) initial time, (b) 5 min and (c) 10 min (5 vol% oil)



Figure 5.53. Oil accumulation within the 30° dead-leg for run 2 at time instants: (a) initial time, (b) 5 min and (c) 10 min (5 vol% oil)



Figure 5.54. Oil accumulation within the 30° dead-leg for run 3 at time instants: (a) initial time, (b) 5 min and (c) 10 min (5 vol% oil)



Figure 5.55. Oil accumulation within the 30° dead-leg for run 4 at time instants: (a) initial time, (b) 5 min and (c) 10 min (5 vol% oil)

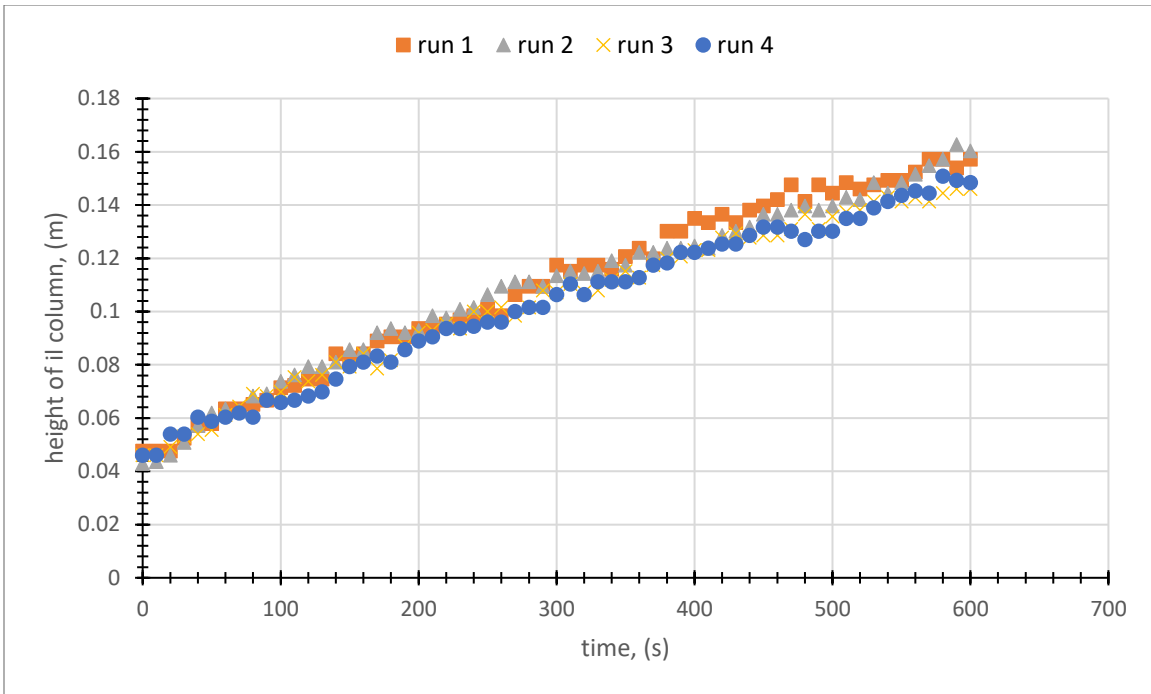


Figure 5.56. Instantaneous height of the oil column vs. time within the 30° dead-leg for each run (5 vol% oil)

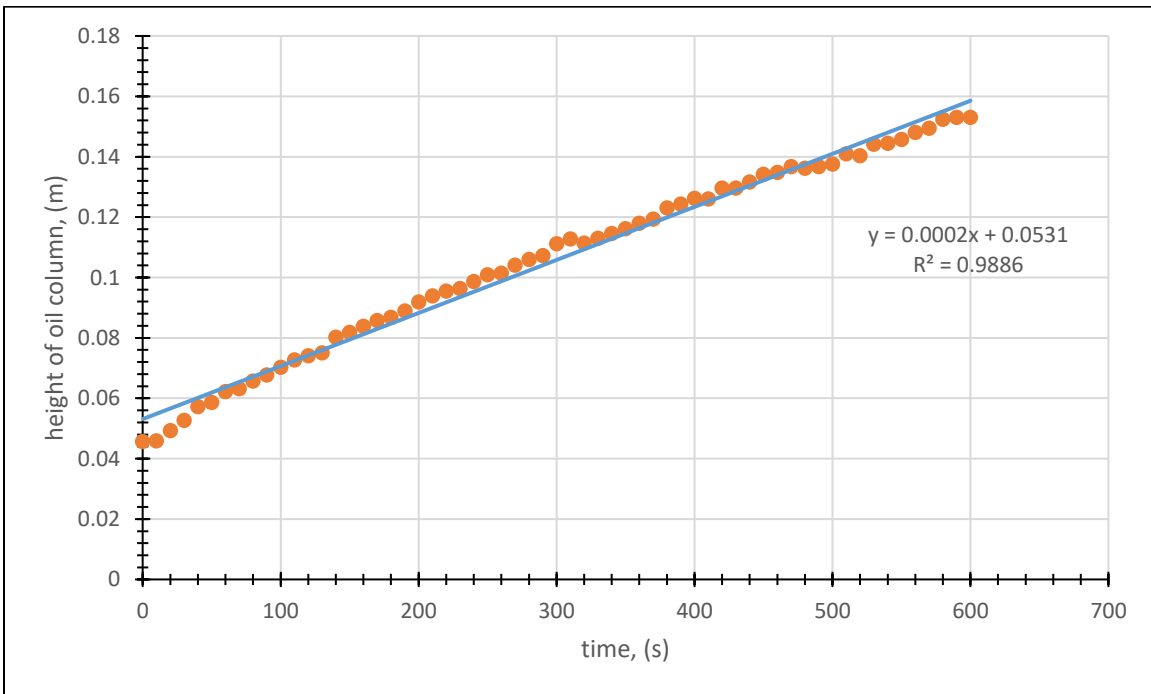


Figure 5.57. Average instantaneous height of the oil column vs. time within the 30° dead-leg along with the least-squares linear curve fit (5 vol% oil)

The average values of the instantaneous heights of the oil column as a function of time are plotted in Figure 5.58. Notice that the average values of the initial heights of the oil column are subtracted. It is observed that for each dead-leg inclination angle, a linear growth rate in oil accumulation emerges (5 vol% oil). The corresponding slopes of the height vs. time linear fits of Figure 5.58 are summarized in Table 5.3. The values of  $R^2$  being nearly 1 suggest the high quality of linear fits for this set of experiment.

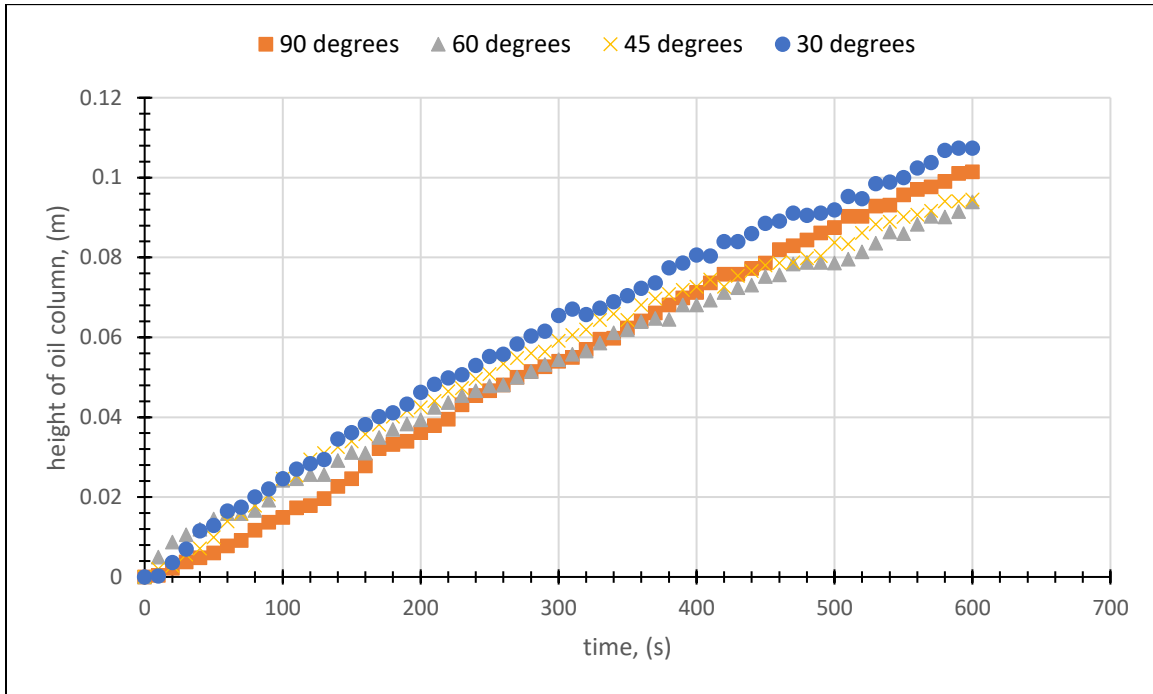


Figure 5.58. Comparison of average instantaneous height of the oil column vs. time for each dead-leg inclination angle (5 vol% oil)

Table 5.4. Oil accumulation rates (m/s) obtained using the least-squares fit method and the associated R-squared ( $R^2$ ) values (5 vol% oil)

	Oil accumulation rate x $10^{-4}$ (m/s)	$R^2$
<b>90° (vertical)</b>	1.73	0.995
<b>60°</b>	1.47	0.9912
<b>45°</b>	1.53	0.9733
<b>30°</b>	1.76	0.9886

The nominal value of the water fraction reported to this point (95%) is high compared to those encountered during the production and transportation of crude oil in oil and gas fields. However, as discussed earlier, a small value of oil fraction was used in this experiment in order to avoid very viscous fluid flow and increased pump power. Nevertheless, the experiments were repeated by following the same process but increasing the oil fraction to 10%. In this way, the effect of the oil fraction on the growth rate of oil accumulation was investigated. As before, each experiment with four different inclination angles which were 90° (vertical), 60°, 45° and 30° was repeated four times.

The raw data for these four sets of experiments (top and bottom heights as functions of elapsed time) are provided in Appendix E (Table E.5-E-8). The positions of top height and bottom height of the oil columns at the beginning of the oil accumulation tests are summarized in Table 5.4.

Table 5.5. Dimensionless initial heights of the top and bottom positions of the oil column with the 10%-90% oil-water mixture at the start of the oil accumulation tests

	initial top level				initial bottom level			
	D				D			
	1	2	3	4	1	2	3	4
90°	9.59375	10.03125	9.625	10.140625	7.6875	8.03125	8.125	8.0625
60°	10	9.671875	9.34375	11.21875	7.90625	7.75	7.390625	8.3125
45°	9.4375	10.453125	10.71875	10.84375	7	7.25	7.25	7.28125
30°	10.09375	10.375	10.4375	11.46875	8.03125	8.203125	8.109375	8

Compared to a similar table discussed above (Table 5.2), the initial heights of the oil column at the start of the oil accumulation tests were at times greater than 2 diameters of the dead-leg ( $2D$ ). This distance should be kept to a minimum, but it is not avoidable due to time-consuming execution of the steps that were discussed earlier and higher volume fraction of the oil component.

Instantaneous photographs of the oil column during the accumulation process of the 10%-90% oil-water are shown in Figures 5.59-5.66 and 5.69-5.75, respectively. The individual graphs for each run and the details recorded based on each run can be found in Appendix E.

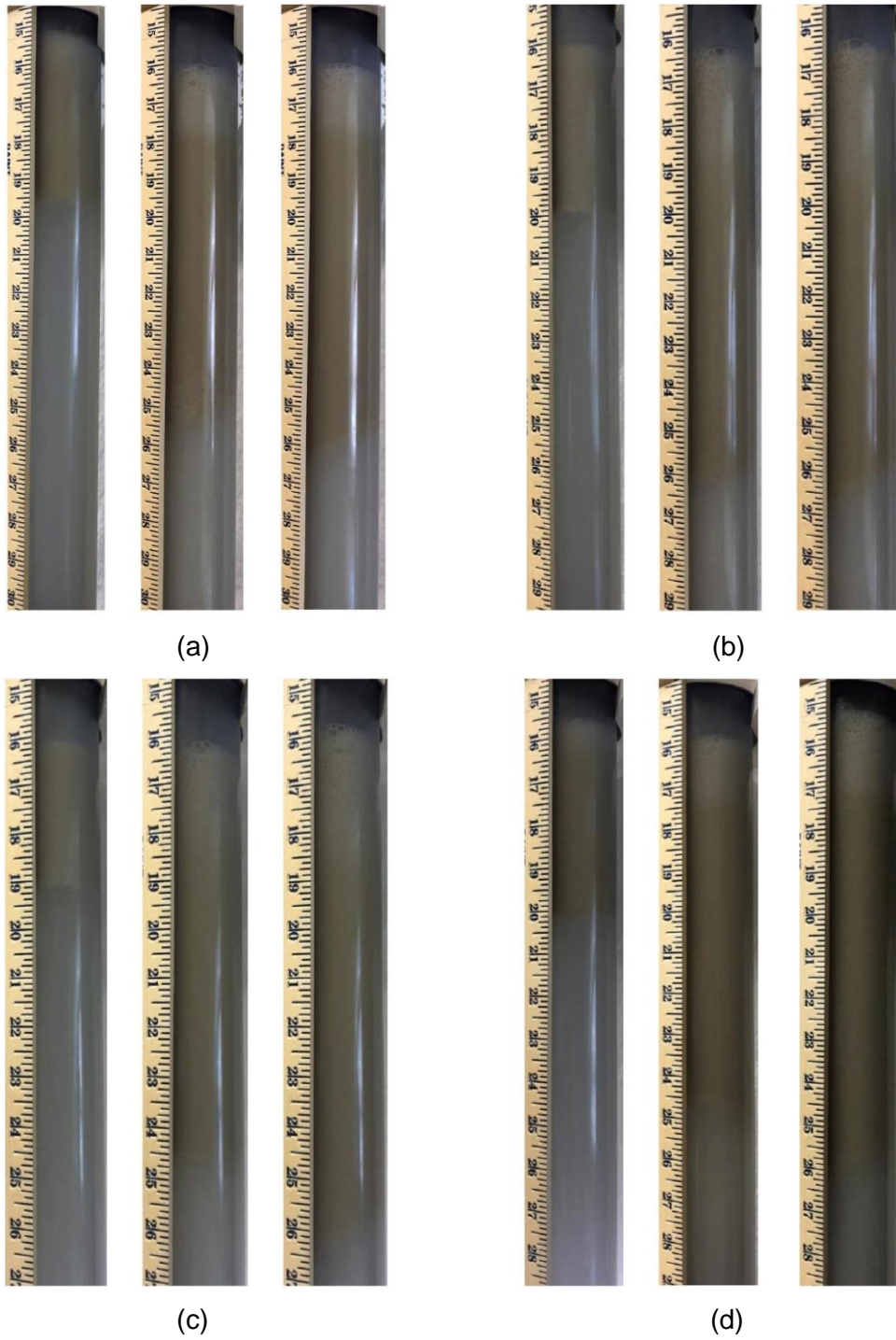


Figure 5.59. Oil accumulation within the 90° (vertical) dead-leg at initial time, 5 min and 10 min for (a) run 1, (b) run 2, (c) run 3 and (d) run 4 (10 vol% oil)

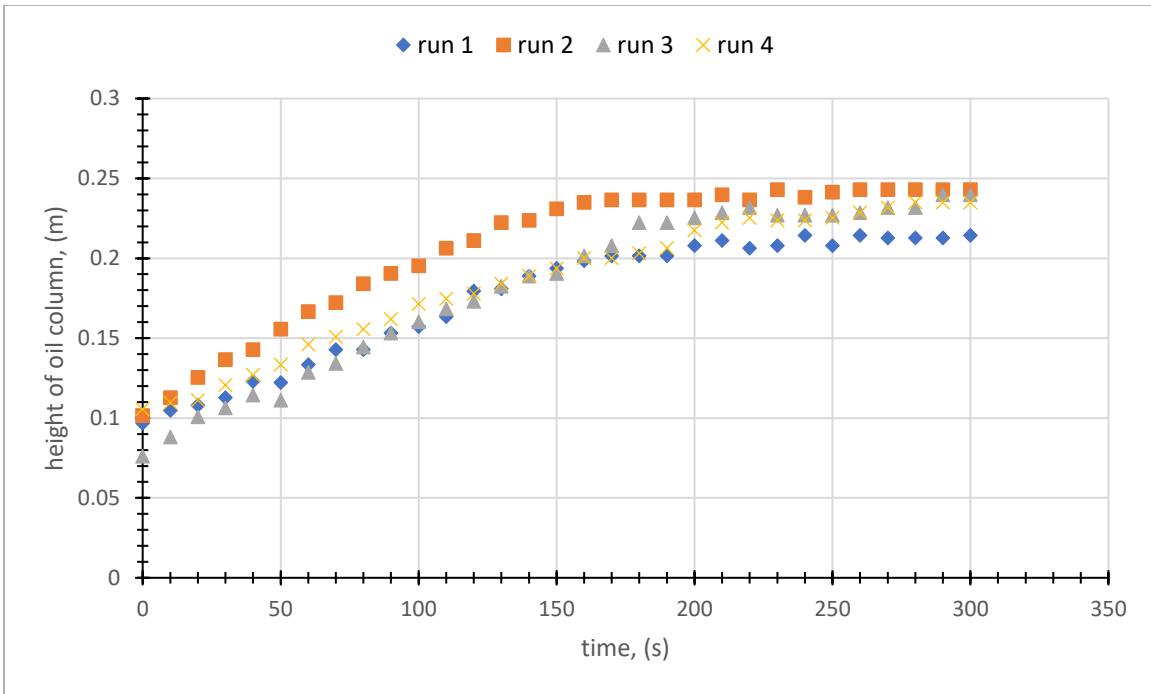


Figure 5.60. Instantaneous height of the oil column vs. time within the 90° (vertical) dead-leg for each run (10 vol% oil)

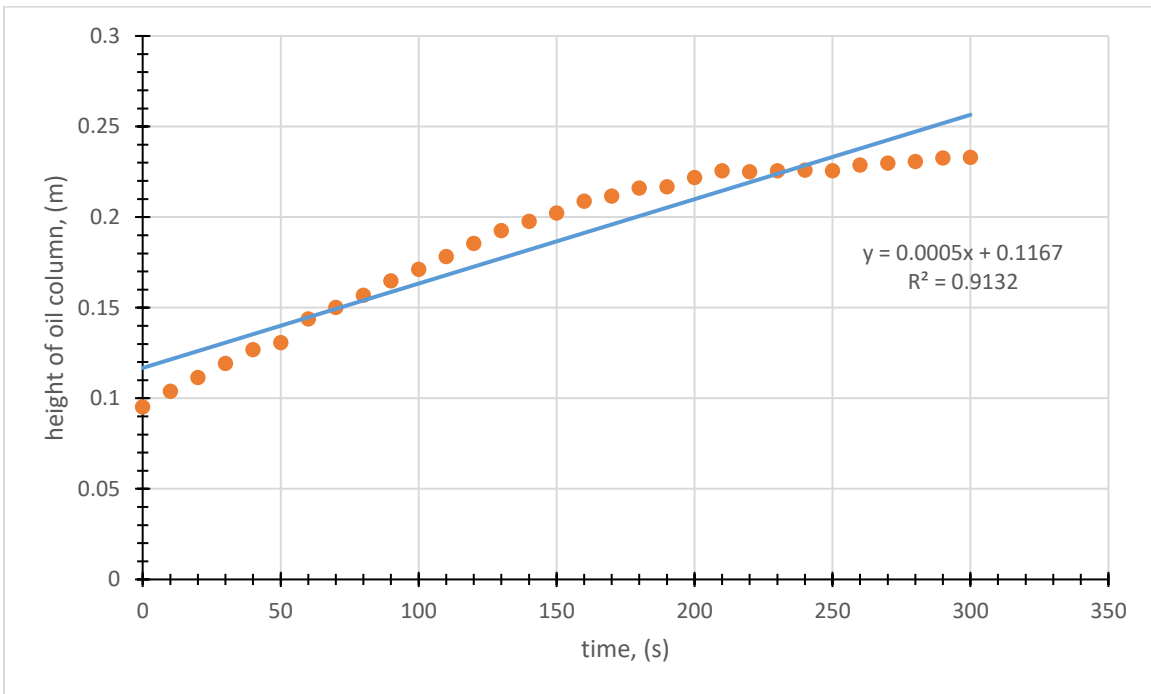


Figure 5.61. Average instantaneous height of the oil column vs. time within the 90° (vertical) dead-leg along with the least-squares linear curve fit (10 vol% oil)



(a)

(b)

(c)

Figure 5.62. Oil accumulation within the 60° dead-leg for run 1 at time instants: (a) initial time, (b) 5 min and (c) 10 min (10 vol% oil)



(a)

(b)

(c)

Figure 5.63. Oil accumulation within the 60° dead-leg for run 2 at time instants: (a) initial time, (b) 5 min and (c) 10 min (10 vol% oil)



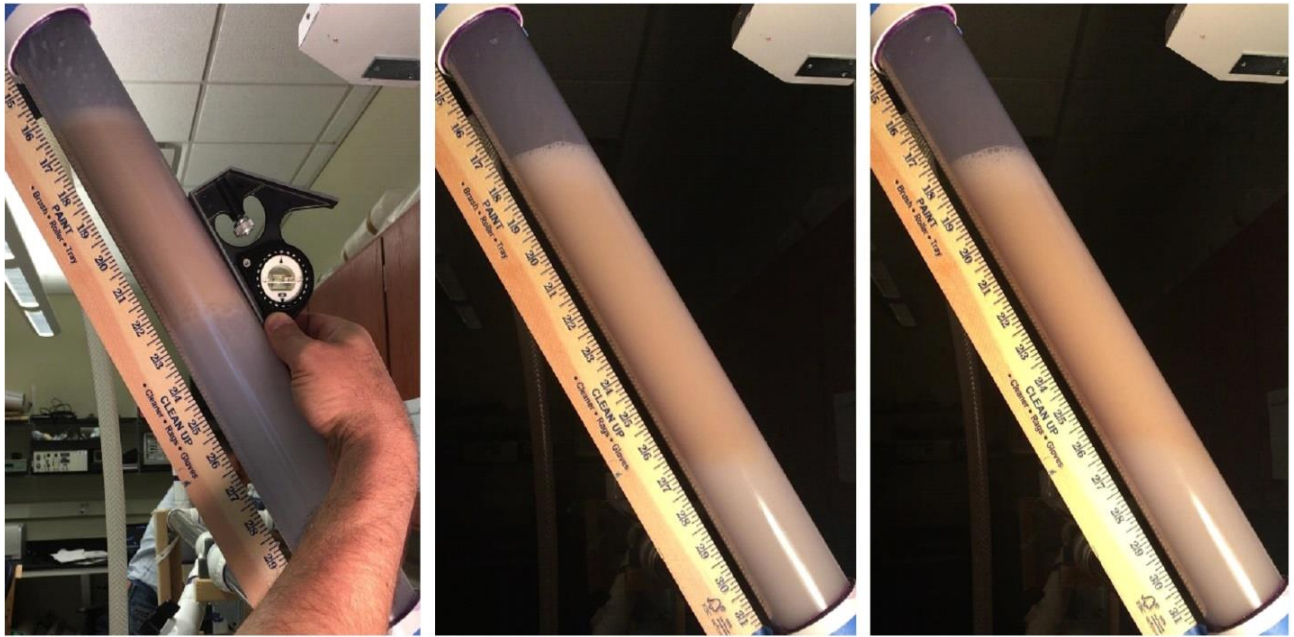


(a)

(b)

(c)

Figure 5.64. Oil accumulation within the 60° dead-leg for run 3 at time instants: (a) initial time, (b) 5 min and (c) 10 min (10 vol% oil)



(a)

(b)

(c)

Figure 5.65. Oil accumulation within the 60° dead-leg for run 4 at time instants: (a) initial time, (b) 5 min and (c) 10 min (10 vol% oil)

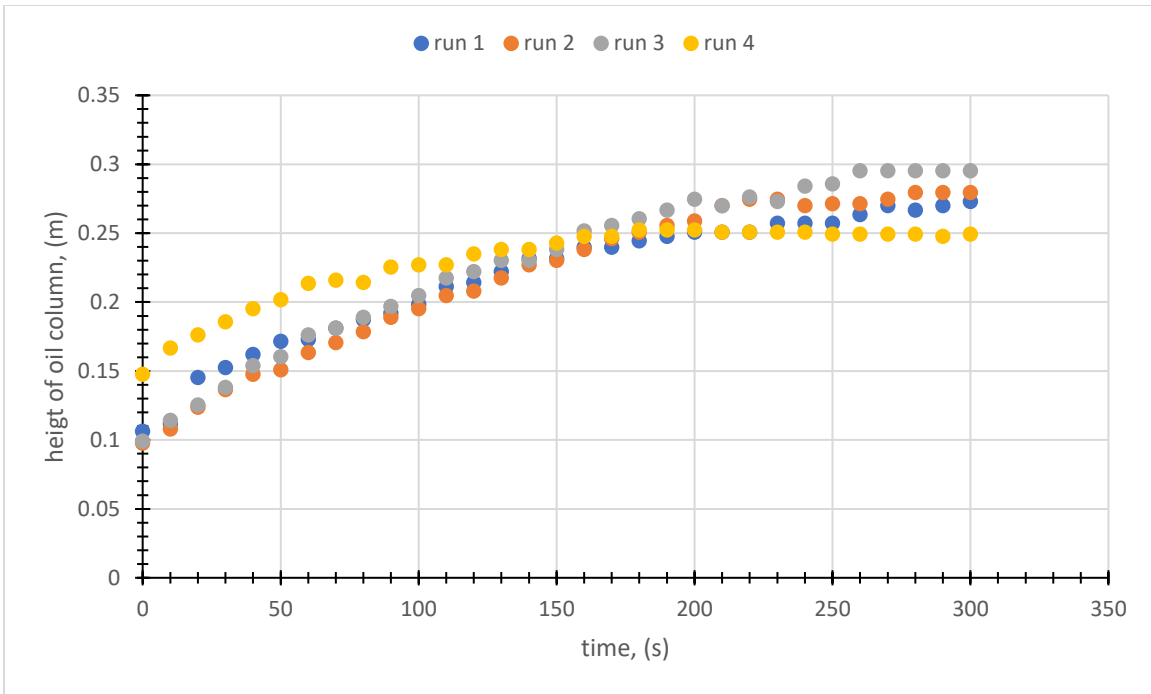


Figure 5.66. Instantaneous height of the oil column vs. time within the 60° dead-leg for each run (10 vol% oil)

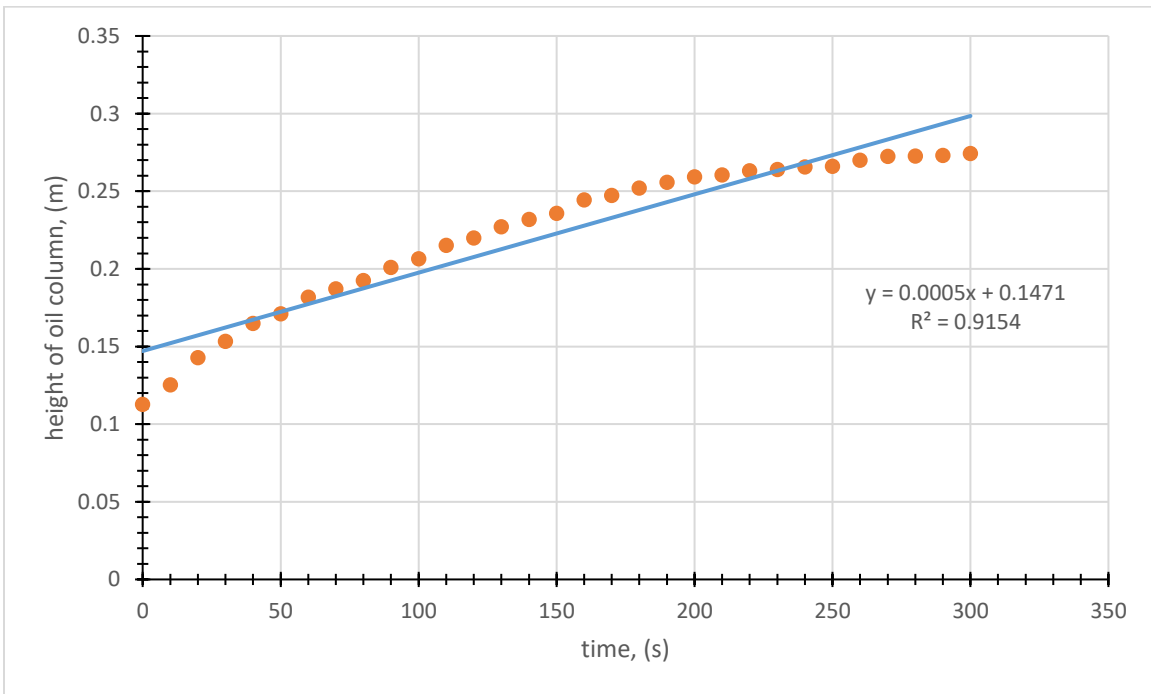
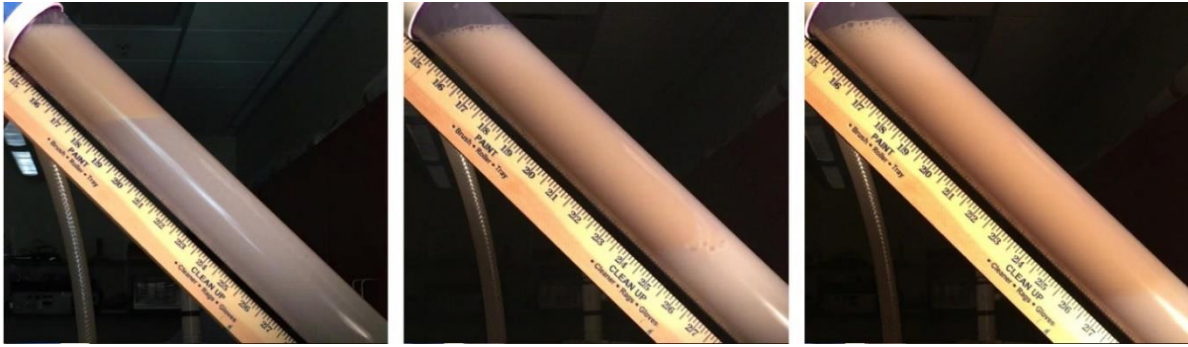
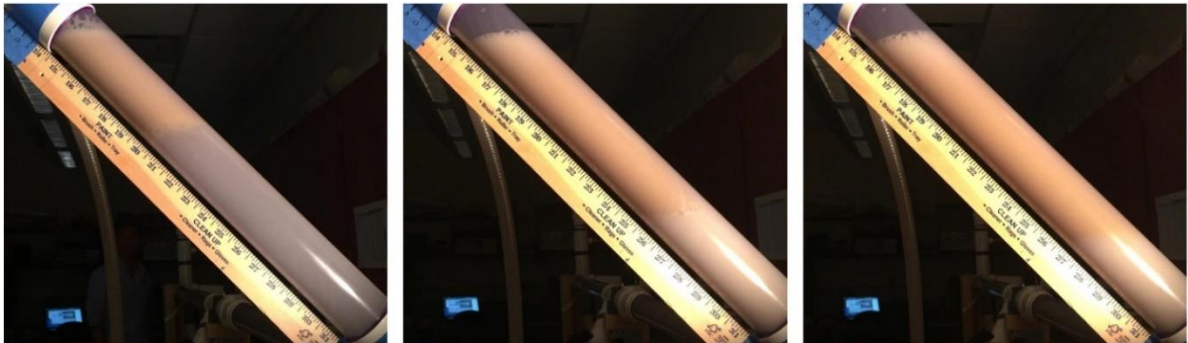


Figure 5.67. Average instantaneous height of the oil column vs. time within the 60° dead-leg along with the least-squares linear curve fit (10 vol% oil)



(a)



(b)



(c)



(d)

Figure 5.68. Oil accumulation within the 45° dead-leg at initial time, 5 min and 10 min for (a) run 1, (b) run 2, (c) run 3 and (d) run 4 (10 vol% oil)

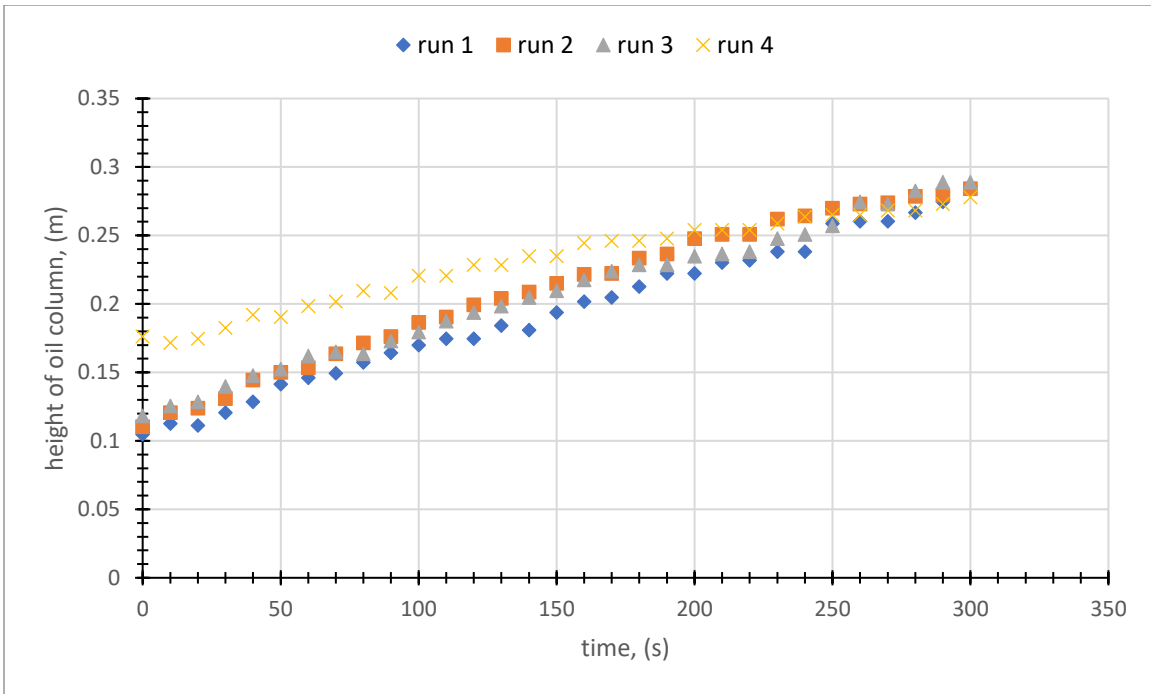


Figure 5.69. Instantaneous height of the oil column vs. time within the 45° dead-leg for each run (10 vol% oil)

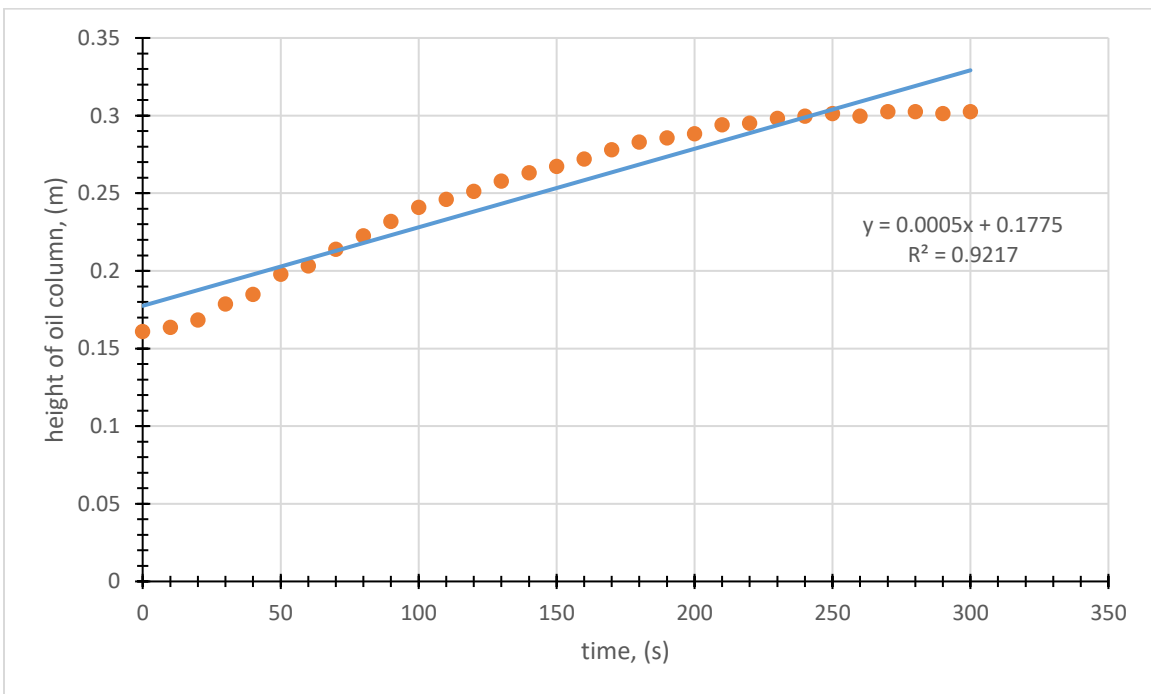


Figure 5.70. Average instantaneous height of the oil column vs. time within the 45° dead-leg along with the least-squares linear curve fit (10 vol% oil)



Figure 5.71. Oil accumulation within the 30° dead-leg for run 1 at (a) initial time, (b) 5 min and (c) 10 min (10 vol% oil)



Figure 5.72. Oil accumulation within the 30° dead-leg for run 2 at time instants (a) initial time, (b) 5 min and (c) 10 min (10 vol% oil)



Figure 5.73. Oil accumulation within the 30° dead-leg for run 3 at time instants (a) initial time, (b) 5 min and (c) 10 min (10 vol% oil)



Figure 5.74. Oil accumulation within the 30° dead-leg for run 4 at time instants (a) initial time, (b) 5 min and (c) 10 min (10 vol% oil)

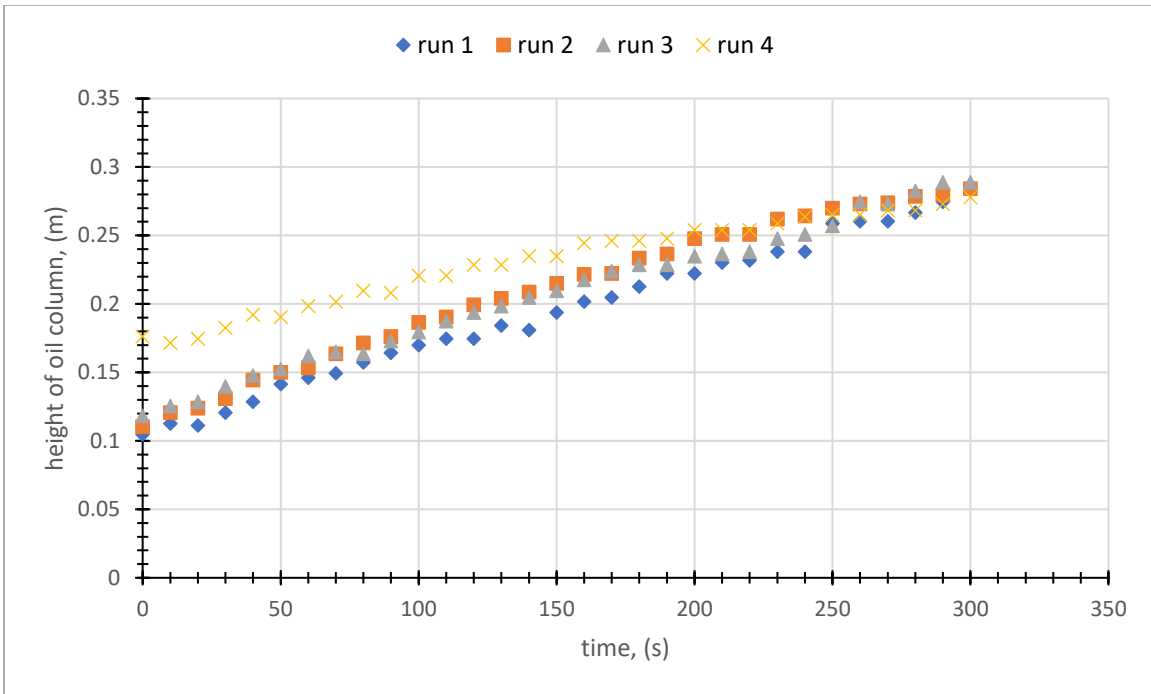


Figure 5.75. Instantaneous height of the oil column vs. within the 30° dead-leg for each run (10 vol% oil)

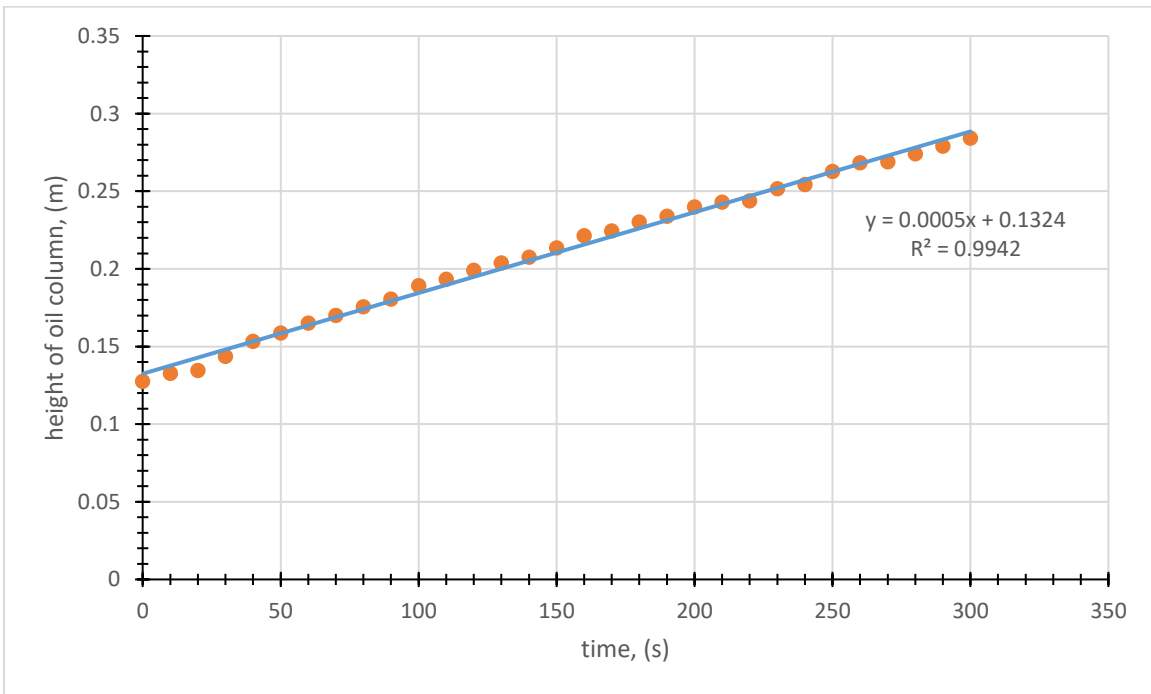


Figure 5.76. Average instantaneous height of the oil column vs. time within the 30° dead-leg along with the least-squares linear curve fit (10 vol% oil)

The average values of the instantaneous heights of the oil column as a function of time are plotted for the case of 10 vol% oil mixture in Figure 5.77. Notice that the average values of the initial heights of the oil column are already subtracted in this figure. It was observed that the initial linear growth of the oil column was generally flattened later on during the oil accumulation tests. The corresponding slopes of the height vs. time linear fits of Figure 5.77 are summarized in Table 5.5. The oil accumulation rates reported in Table 5.5 are generally greater than those in Table 5.3 by a factor about 2.6-3.43.

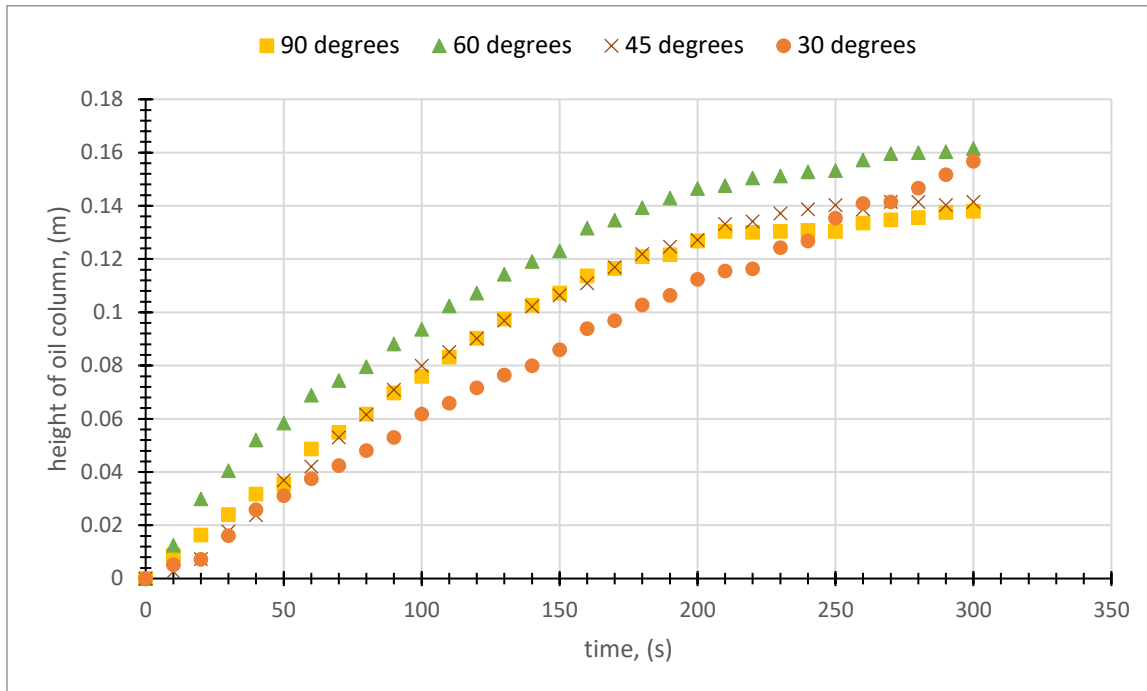


Figure 5.77. Comparison of average oil accumulation rates of each dead-leg position (10 vol% oil)

Table 5.6. Oil accumulation rates obtained using the least-squares fit method and the coefficient of determination ( $R^2$ ) values (10 vol% oil)

	Oil accumulation rate $\times 10^{-4}$ (m/s)	$R^2$
<b>90° (vertical)</b>	4.46	0.9132
<b>60°</b>	5.05	0.9154
<b>45°</b>	5.06	0.9217
<b>30°</b>	5.2	0.9942

### 5.7. Comparison of Oil Accumulation Data for 5% and 10% Oil

The average height of accumulated oil column vs. time data for all the experiments of the present study are shown in Figure 5.78 for 5% and 10% oil concentrations at different inclination angles. Naturally, the higher oil concentration data exhibit a faster accumulation rate due to availability of higher fractions of oil in the main horizontal pipe. Collectively, the height of the accumulated oil rose linearly in our experiments during the observation time period for the 5% oil samples. Besides, it was deduced that higher oil volumetric fraction gave rise to higher rate of oil accumulation (Figure 5.78).



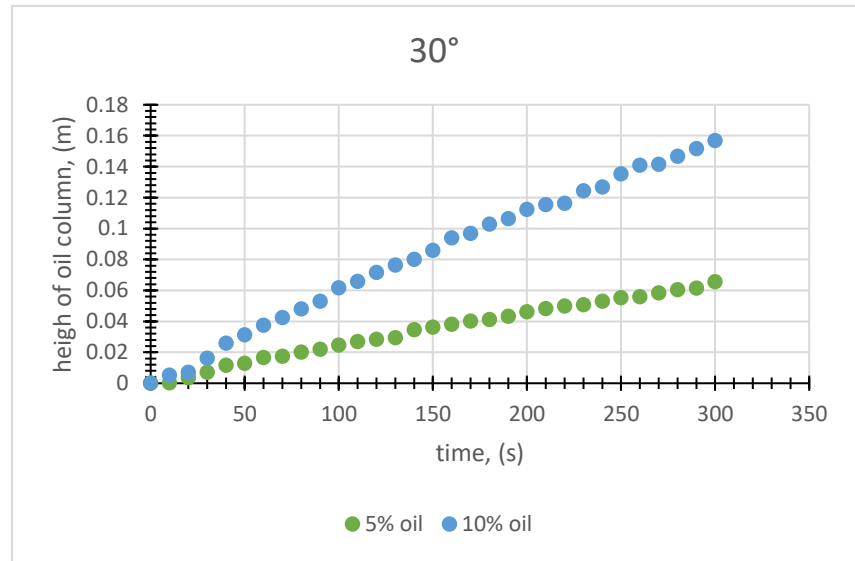
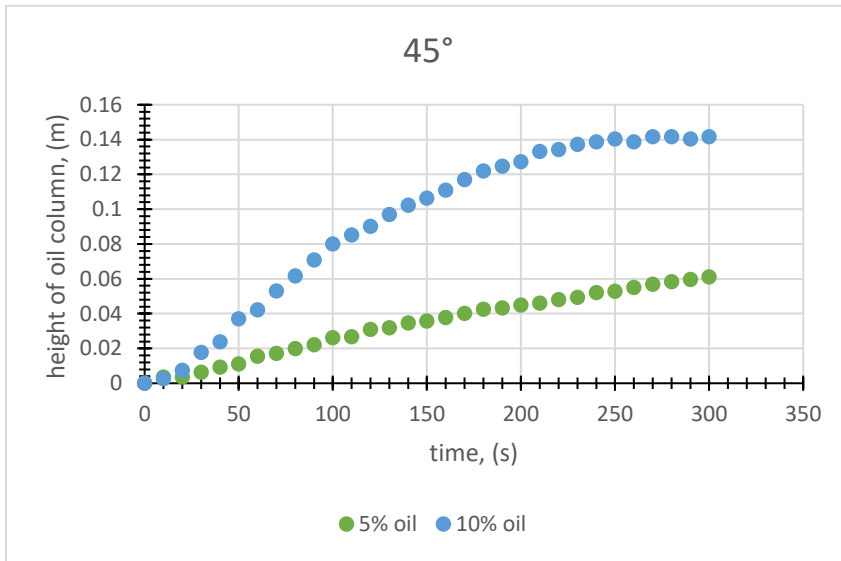
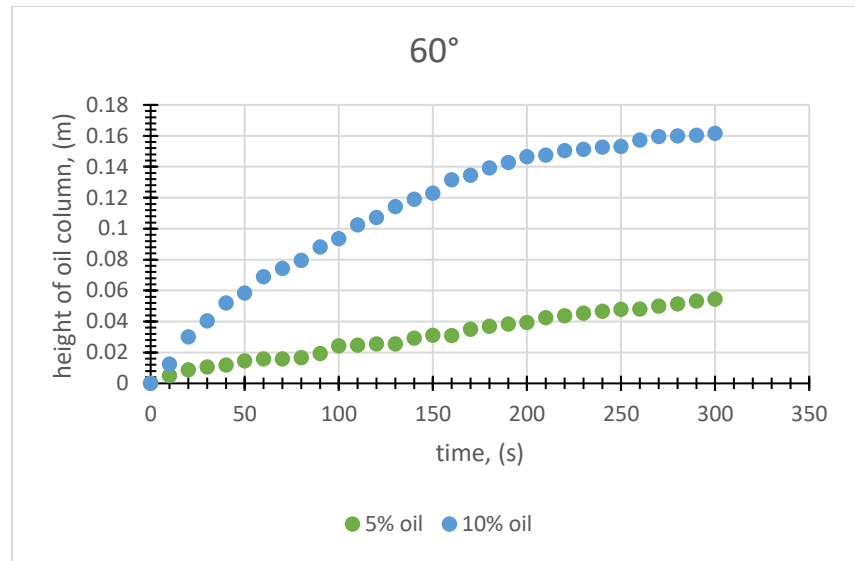
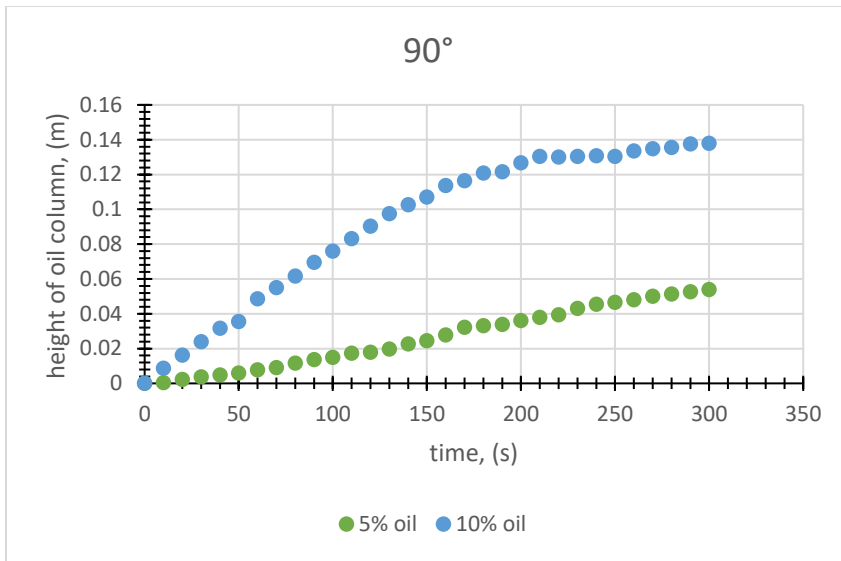


Figure 5.78. Comparison of the heights of accumulated oil columns within the dead-leg with inclination angles of 90° (vertical), 60°, 45° and 30° for 5% and 10% oil system

### 5.8. Closer Inspection of the Instantaneous Behavior of Phases

Since the system generally contained air pockets despite the degassing process, upon changing the orientation of the dead-leg pipe away from its vertical position, air bubbles were clearly observed climbing up within the inclined dead-legs leading to formation of a layer of air bubbles at the top as a consequence of salt addition. These cumulative air bubbles are called “bulk foam” which refers to an agglomeration of gas bubbles separated from each other by thin liquid films [Hirasaki, 1989]. The thickness of this layer was varied for each run. Figure 5.79 represents one of the runs to visualize the movement of an air bubble, indicating how the air bubble moved up joining an air bubble layer.

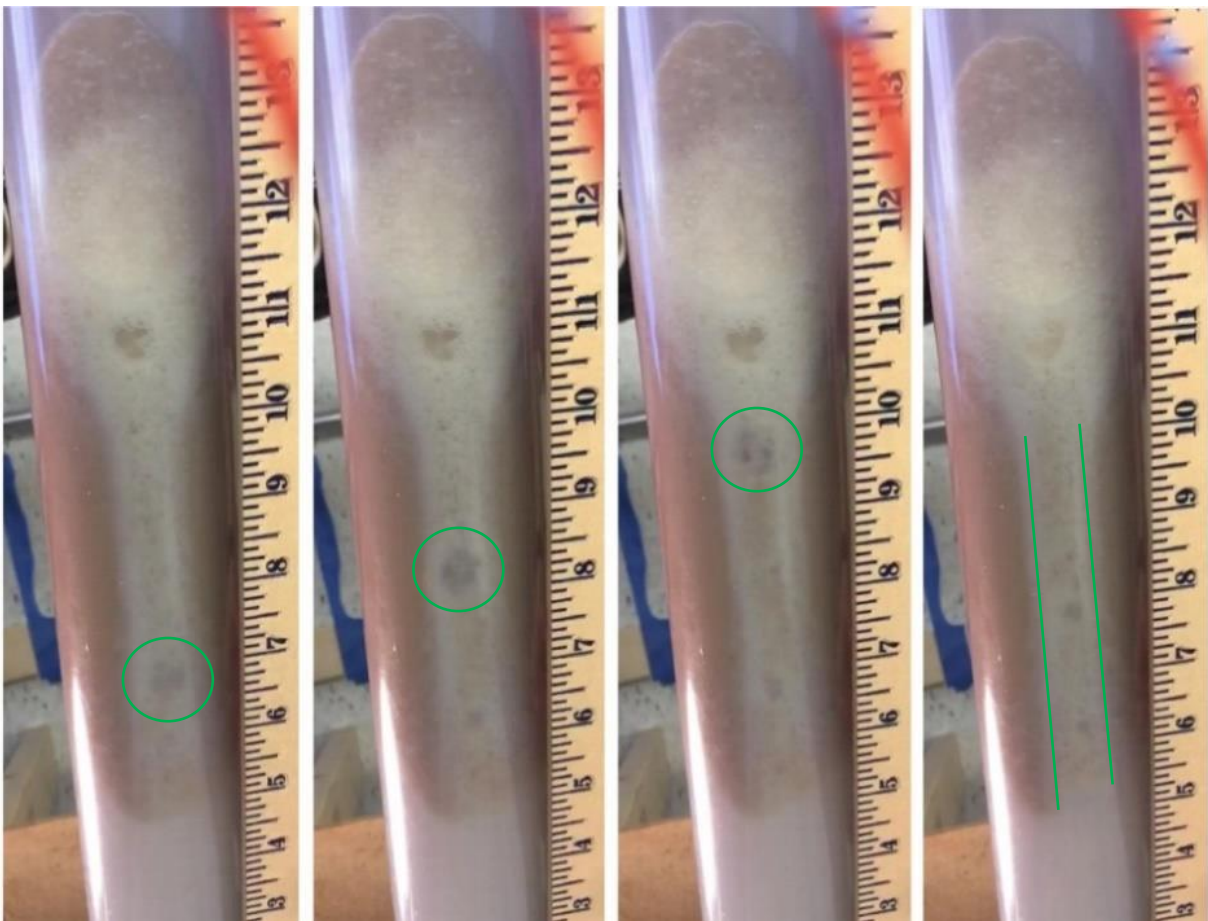


Figure 5.79. Air bubbles collected at the top of the dead-leg and consecutive images (left to right) of air bubbles moving up in the 30° inclined dead-leg (5 vol% oil)

Sometime after the system shutdown, a foamy structure was observed between the segregated oil and water phases (Figure 5.80). This phenomenon is already reported in the literature, i.e. “When pressure is reduced on certain types of oil, tiny bubbles of gas are encased in a thin film

of oil when the gas comes out of solution. This may result in foam, or froth, being dispersed in the oil and creates what is known as “foaming” oil. In other types of oil, the viscosity and surface tension of the oil may mechanically lock gas in the oil and can cause an effect similar to foam.” [Smith, 2018].



Figure 5.80. Observed foamy structure located between oil and water phases after system shutdown

### 5.9. Comparison of Experimental Observations and 3-D Simulations

Having discussed the experimental findings of the study, results of 3-D transient CFD simulations corresponding to the actual physical setup are presented next. Matching the general features of the experimental set-up in the vicinity of the main pipe and the dead-leg pipe, a 3-D geometry was created by using SOLIDWORKS which is a solid modeling computer-aided design program. The diameters of horizontal main pipe and the vertical dead-leg were the same and equal to 2” (0.0508 m). The upstream edge of the dead-leg was located at a distance of 41.5 times the diameter from the vertical inlet section. Average inlet velocity of 4 m/s was

chosen as the inlet flow boundary condition to match the same  $Re$  number of the experimental runs. The length of the dead-leg measured from the top of the horizontal pipe to the end-capped surface of the dead-leg was 10 times the diameter. This quantity matched exactly the distance from the top of the horizontal pipe to the valve in the experimental set-up. The medium grid mesh density of Chapter 4 (1,864,000) was used and a close-up view of the grid distribution in the vicinity of the dead-leg was already shown in Figure 4.37. The measured densities and dynamic viscosities of olive oil and water ( $\rho_{\text{olive oil}}=900 \text{ kg/m}^3$ ,  $\rho_{\text{water}}=1000 \text{ kg/m}^3$ ,  $\mu_{\text{olive oil}}=0.0654 \text{ Ns/m}^2$  and  $\mu_{\text{water}}=0.000953 \text{ Ns/m}^2$ ) were used for this part of the computational study. Only the case of an oil-water mixture being 10%-90% was considered. The turbulence quantities at the inlet plane were assigned  $k = 3.74 \times 10^{-2} \text{ m}^2/\text{s}^2$  and  $\varepsilon = 2.85 \times 10^{-1} \text{ m}^2/\text{s}^3$ , matching the practice outlined in Section 4.1.2. The time step used for integration of the governing equations was kept constant at  $10^{-5} \text{ s}$ . Due to high cost of computing associated with transient turbulent 3-D simulations, transient runs were performed for time duration of 1 min. In contrast to the 2-D simulations where only vertical dead-legs are meaningful, for 3-D simulations the inclination angle of the dead-leg can be varied freely. In the present study, dead-leg inclination angles of  $90^\circ$  (vertical),  $60^\circ$ ,  $45^\circ$ ,  $30^\circ$  and  $0^\circ$  (horizontal) were investigated. It must be noted that for the computational results presented below, the  $+y$  direction for each inclination angle points along the centerline of the dead-leg away from the T-junction.

#### 5.9.1. Inclined Dead-Leg 3-D CFD Results

Instantaneous color contours of the two phases on the inner surface of the 10%-90% oil-water flow system for the inclination angles of  $90^\circ$ ,  $60^\circ$ ,  $45^\circ$  and  $30^\circ$  are shown in Figures 5.81-5.84, respectively. In Figure 5.81, the instantaneous color contours of phases on the curved sheet ( $x^2+z^2=D^2$  and  $z>0$ ) of the vertical dead-leg at 10 s time intervals are presented for a computational duration of 2 mins. The linear rise of the height of the accumulated oil column in the top portion of the vertical dead-leg is clearly observed and matches the experimental findings presented earlier. One can clearly observe that pockets of separated oil originate randomly from the 3-D recirculating zone and rise up toward the evolving/increasing accumulating oil column.

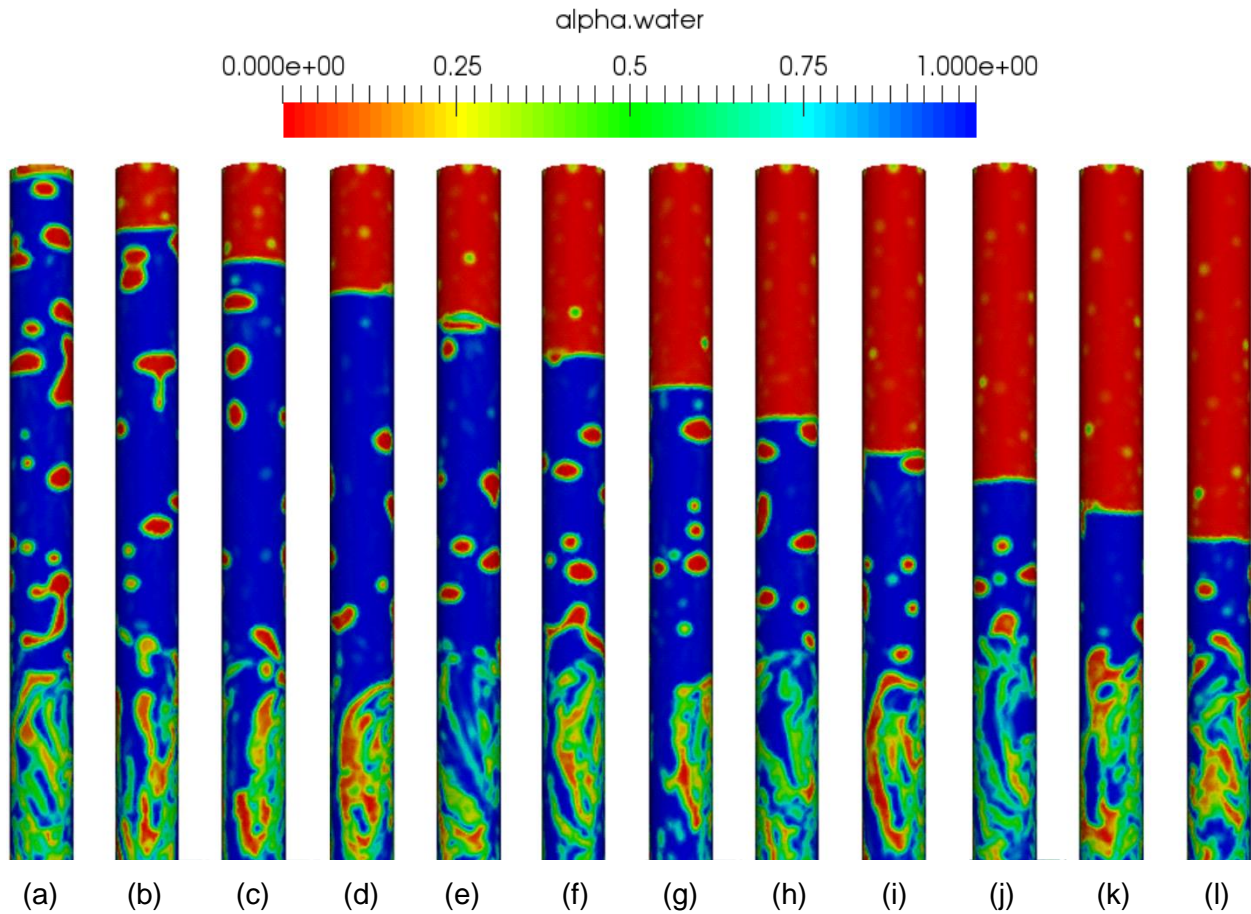


Figure 5.81. Instantaneous color contours of phases on the curved sheet ( $x^2+z^2=D^2$  and  $z>0$ ) of the dead-leg for the 10%-90% oil-water flow system for inclination angle of  $90^\circ$  (vertical) at time instants of (a) 10 s, (b) 20 s, (c) 30 s, (d) 40 s, (e) 50 s, (f) 60 s, (g) 70 s, (h) 80 s, (i) 90 s, (j) 100 s, (k) 110 s and (l) 120 s

Instantaneous color contours of phases for inclination angles of  $60^\circ$ ,  $45^\circ$  and  $30^\circ$  are now discussed in Figures 5.82-5.84. It should be noted that these images are viewed from the standpoint of an observer looking at the main pipe fluid coming toward him/her. In effect, the contours shown are on the downstream half-surface of the respective dead-legs.

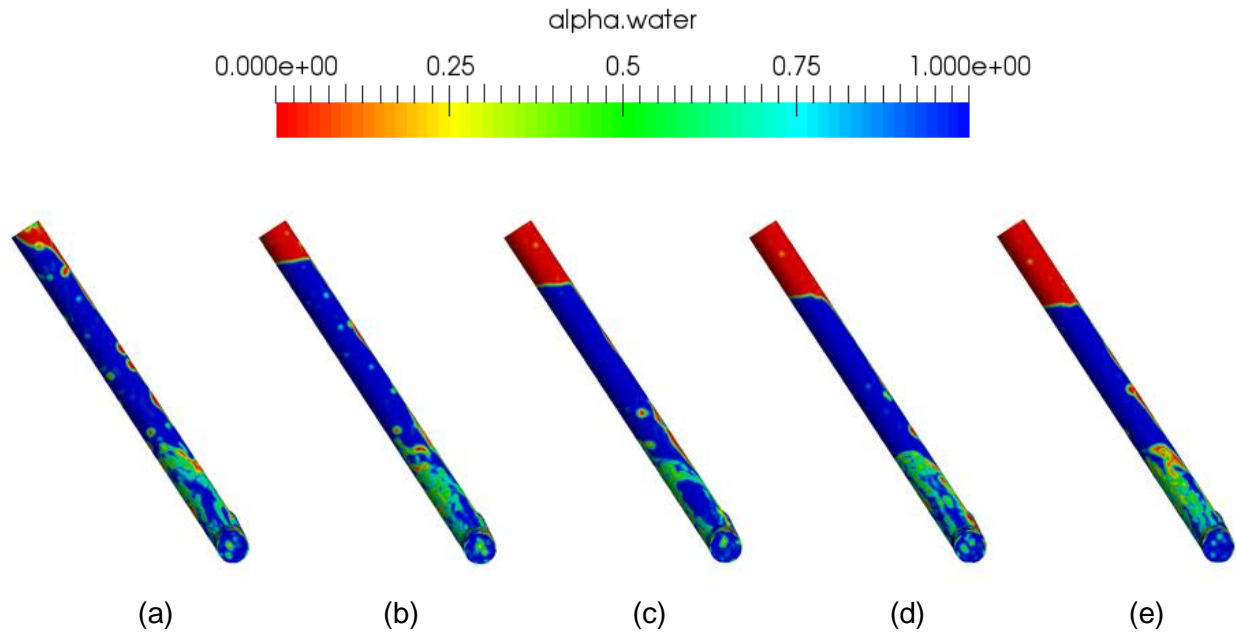


Figure 5.82. Instantaneous color contours of phases on the downstream half-surface of the dead-leg for the 10%-90% oil-water flow system for inclination angle of  $60^\circ$  at time instants of (a) 5 s, (b) 10 s, (c) 20 s, (d) 40 s and (e) 60 s

These instantaneous images correspond to the instantaneous photographs that were reproduced from the videos of the experimental runs presented earlier in Figures 5.62-5.65. Video animations of the evolving phase field for the duration of the simulations were also obtained. Upon examining these videos, one can elucidate the complicated phase separation at the T-junction and the lifting of the lighter oil phase into the inclined dead-leg. Due to lower density of the oil phase, the greater portion of oil was lifting up on the right side of images of Figure 5.82 as the recirculating fluid zone was spinning in the CCW direction according to the observer. A second route for lifting of lighter oil was also observed when the oil on the left side of images of Figure 5.82 was in a slow-moving region and its net lifting weight overcame the inertia force. Inspection of the videos clearly showed that oil droplets undergoing this route coalesced and lifted into the dead-leg. The column of accumulated oil in the end-capped dead-leg is clearly observed to rise markedly during the 1 min observation period. Similar findings were observed for inclinations angle of  $45^\circ$  and  $30^\circ$  as illustrated in Figures 5.83 and 5.84, respectively.

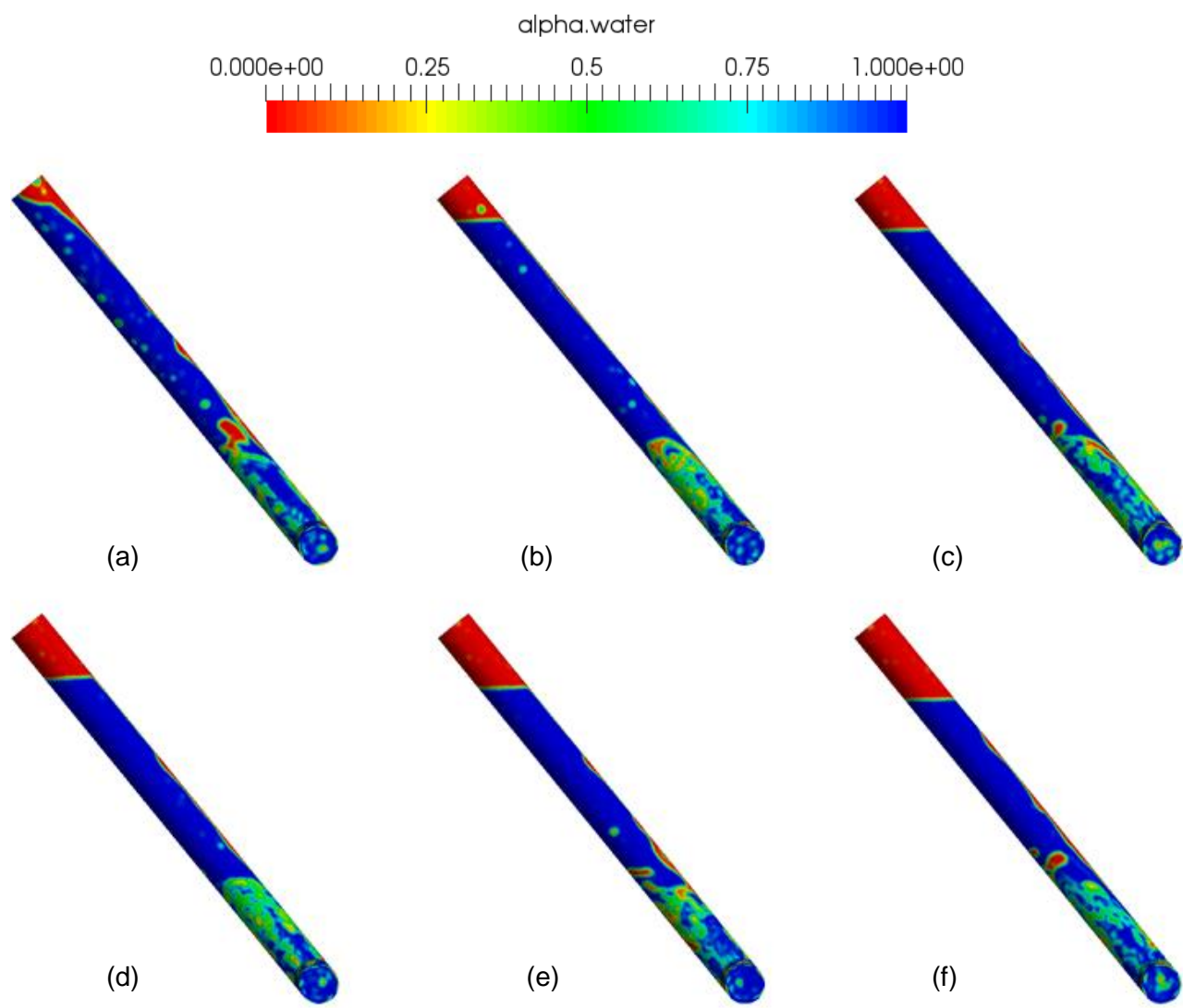


Figure 5.83. Instantaneous color contours of phases on the downstream half-surface of the dead-leg for the 10%-90% oil-water flow system for inclination angle of 45° at time instants of (a) 10 s, (b) 20 s, (c) 30 s, (d) 40 s, (e) 50 s and (f) 60 s

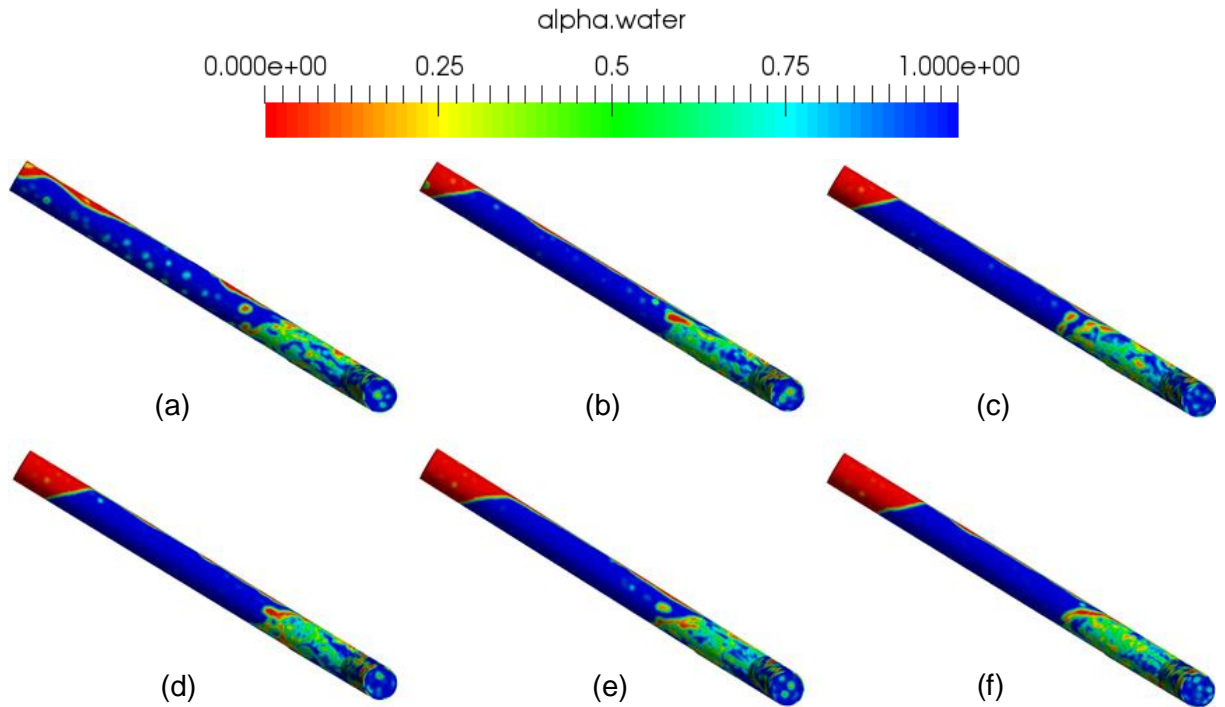


Figure 5.84. Instantaneous color contours of phases on the downstream half-surface of the dead-leg for the 10%-90% oil-water flow system for inclination angle of 30° at time instants of (a) 10 s, (b) 20 s, (c) 30 s, (d) 40 s, (e) 50 s and (f) 60 s

### 5.9.2. Horizontal Dead-Leg 3-D CFD Results

An experiment was performed with the 90%-10% oil-water mixture such that the dead-leg was positioned horizontally so that the inclination angle was equal to zero (Figure 5.85). Such a dead-leg systems are widely observed in oil processing plants.

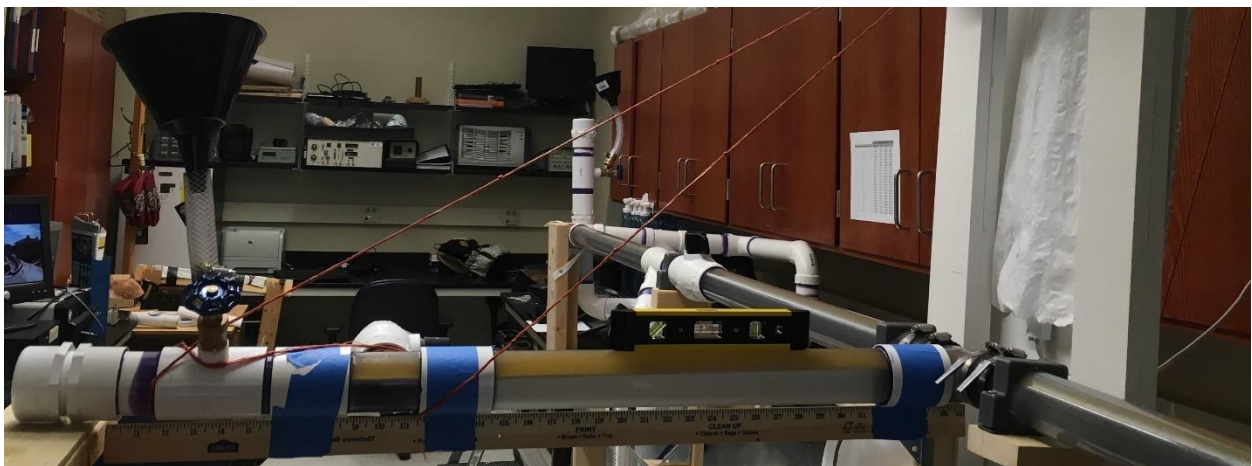


Figure 5.85 Photograph of the experimental set-up with the dead-leg in its horizontal position





from Figure 5.87, lighter oil component accumulated at the top of the horizontal dead-leg. Under the influence of the cohesive forces between the oil molecules, the surface area contacted with oil molecules was reduced by pulling the molecules on the pipe surface inward. As a result of this surface tension phenomenon, accumulated oil turned into the shape which was cambered at the bottom of the cumulative oil zone. Formation of this pattern cannot be confirmed from the experimental observations due to the absence of a clear access port to observe the cross section of the dead-leg.

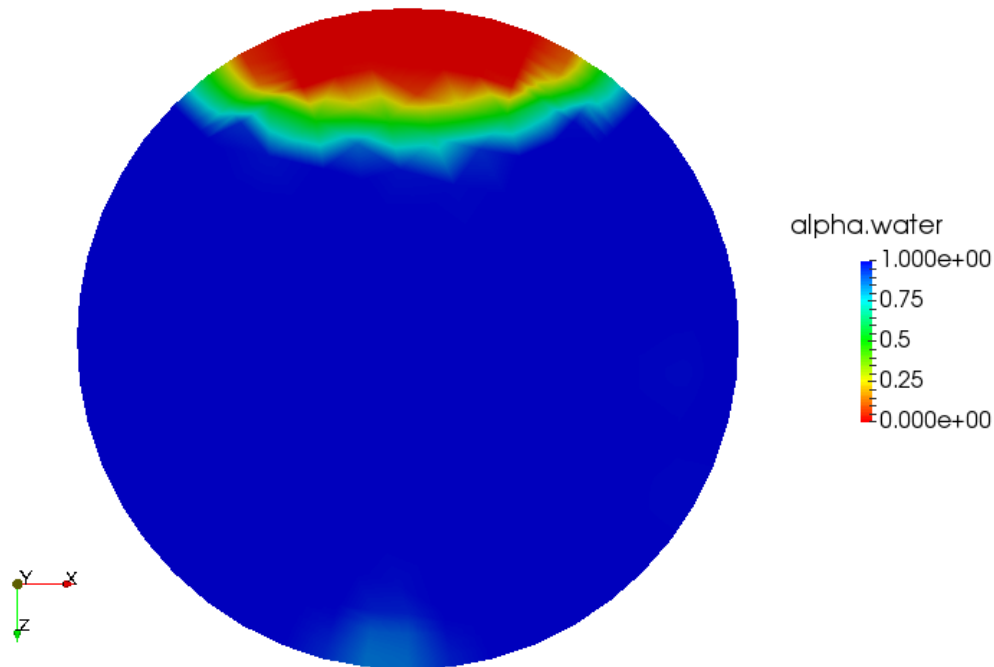


Figure 5.87. Vertical cross-sectional view ( $y/D=11$ ) of accumulation of oil at the top of the horizontal dead-leg at the time instant of 60 s for the 10%-90% oil-water mixture

#### 5.10. Closure

Results of experimental studies conducted using an in-house designed/constructed two-phase flow loop including a dead-leg that can be oriented at a desired inclination angles of  $90^\circ$  (vertical),  $60^\circ$ ,  $45^\circ$ ,  $30^\circ$  and  $0^\circ$  (horizontal) were presented. Oil-water mixtures (5%-95% and 10%-90%) were prepared by testing combinations of water (tap, deionized, distilled) and oil (olive, canola, vegetable). Based on agitation tests, combination of the deionized water and olive oil were selected as a test fluid. Upon testing this fluid, emulsification was encountered in the system. This problem was removed by adding table salt. Following a 5-min long loop homogenization procedure, oil separation/accumulation tests were performed for a minimum of

10 min. Videos of oil accumulation process within the dead-leg were obtained and the instantaneous accumulated height of the oil layer was tabulated. Through applying the least-squares linear fit method, empirical oil accumulation rates were derived. Oil accumulation rate was found to be constant for the 5% oil mixture, whereas for the 10% oil mixture the initial linear behavior was generally degraded, regardless of the inclination angle. Finally, limited 3-D simulation results were compared to experimental observations. Two different routes for oil separation, coalescence and lifting of oil pockets toward the capped end of the dead-leg were observed upon inspection of video animations of the computational results.

## 6. Conclusions

Results of both 2-D and 3-D time-dependent simulations of the two-phase turbulent flow of an oil/water mixture in a subsea vertical dead-leg model were presented. Moreover, experimental findings in terms of oil separation and accumulation within a model dead-leg for various inclination angles were discussed. Experimental data on oil accumulation in dead-legs at various inclination angles were compared to results of numerical predictions analogous to the laboratory-scale 3-D counterpart. The main conclusions follow:

(1) Baseline transient 2-D turbulent simulations were performed to elucidate the extent of evolving recirculating vortices and penetration of the lighter density oil phase into the vertical dead-leg for a realistic 90%-10% oil-water mixture.

(2) A parametric study directed at understanding the influences of the average inlet velocity, length of the vertical dead-leg, width of the vertical dead-leg, position of the vertical dead-leg relative to the inlet of the feed channel, viscosity of crude oil and density of crude oil on the development of the transient turbulent flow, pressure, concentration fields and extent of oil separation and its accumulation in the vertical 2-D dead-leg was conducted.

(3) Computationally-intensive realistic 3-D unsteady turbulent simulations of flow and volume fraction fields within a vertical dead-leg for a 90%-10% oil-water mixture were also performed. The general trends of oil separating from the mixture and lifting in the vertical dead-leg as time progressed was captured by both 2-D and 3-D models. However, the 3-D model exhibits greater refinement of the complex three-dimensional vortical effects and re-distribution of phases.

(4) Based on magnetic stirring tests and visual observations, olive oil-deionized water mixtures (5%-95% and 10%-90%) were selected for the experimental studies. This mixture had to be treated with table salt that served as a demulsifier.

(5) Following a 5 min long system homogenization procedure, oil separation/accumulation tests were performed for a minimum of 10 min. Videos of oil accumulation process within the dead-legs were obtained for various inclination angles of the dead-leg and the instantaneous accumulated heights of the oil column versus time were tabulated. Through applying the least-squares linear fit method, empirical accumulation rates were derived.

(6) The variation of the instantaneous height of the oil column within the dead-legs were observed to rise linearly for the 5% oil mixture, regardless of the inclination angle of the dead-leg.

(7) For the 10% oil mixture, the instantaneous height of the accumulated oil column was rising linearly but faster than the 5% oil mixture at the early instants, however for some inclination angles the accumulation rate flattened after a time period.

(8) For the 10% oil mixture, limited 3-D simulation results for a period of 1-2 min were compared to experimental findings matching the operating conditions in the laboratory. The complex recirculating flow zone in the vicinity of the T-junction was identified to be the major source of oil separation and its rise toward the capped end of the dead-legs. For non-vertical orientations, another route was also identified where oil droplets were separated at the bottom of the complex recirculating zone and while coalescing rose toward the expanding accumulating oil column.

(9) Limited oil accumulation experiments were performed for the case of a horizontal dead-leg. Experimentally-obtained oil accumulation data suggest that oil accumulation was limited to the top of the horizontal dead-leg and the zone of accumulated oil reached an asymptotic value early on.

## References

Akiya, T., Shimazaki, T., Oowa, M., Nakaiwa, M., Nakane, T., Hakuta, T., Matsuo, M. and Yoshida, Y., 1997. Phase equilibria of some alternative refrigerants hydrates and their mixtures using for cool storage materials. In Energy Conversion Engineering Conference, IECEC-97, IEEE, *Proceedings of the 32nd Intersociety* (Vol. 3, pp. 1652-1655).

Andersen, H., 2007. Computational study of heat transfer in subsea deadlegs for evaluation of possible hydrate formation. Master's Thesis, Faculty of Technology, Telemark University College, Porsgrunn, NORWAY.

Anderson, G.K., 2004. Enthalpy of dissociation and hydration number of methane hydrate from the Clapeyron equation. *The Journal of Chemical Thermodynamics*, 36(12), pp. 1119-1127.

Balakin, B.V., Hoffmann, A.C. and Kosinski, P., 2011. Experimental study and computational fluid dynamics modeling of deposition of hydrate particles in a pipeline with turbulent water flow. *Chemical Engineering Science*, 66(4), pp. 755-765.

Balakin, B.V., Lo, S., Kosinski, P. and Hoffmann, A.C., 2016. Modelling agglomeration and deposition of gas hydrates in industrial pipelines with combined CFD-PBM technique. *Chemical Engineering Science*, 153, pp. 45-57.

Bauck, I.J.T., 2013. Flow Assurance—A System Perspective, MEK4450-FMC Subsea technologies.

Benson, S.M. and Orr, F.M., 2008. Carbon dioxide capture and storage. *MRS Bulletin*, 33(4), pp. 303-305.

Brackbill, J.U., Kothe, D.B. and Zemach, C., 1992. A continuum method for modeling surface tension. *Journal of Computational Physics*, 100(2), pp. 335-354.

Castellani, B., Rossetti, G., Tupsakhare, S., Rossi, F., Nicolini, A. and Castaldi, M.J., 2016. Simulation of CO<sub>2</sub> storage and methane gas production from gas hydrates in a large scale laboratory reactor. *Journal of Petroleum Science and Engineering*, 147, pp. 515-527.

Çengel, Y.A. and Cimbala, J.M., 2006. *Fluid mechanics: fundamentals and applications*. Boston, McGraw-Hill Higher Education.

Chatti, I., Delahaye, A., Fournaison, L. and Petitet, J.P., 2005. Benefits and drawbacks of clathrate hydrates: a review of their areas of interest. *Energy Conversion and Management*, 46(9-10), pp. 1333-1343.

Chen, J.L., He, L.M., Luo, X.M., Bai, H.T. and Wei, Y.H., 2012. Simulation of oil-water two phase flow and separation behaviors in combined T junctions. *Journal of Hydrodynamics*, Ser. B, 24(6), pp. 848-857.

Claypool, G.E. and Kvenvolden, K.A., 1983. Methane and other hydrocarbon gases in marine sediment. *Annual Review of Earth and Planetary Sciences*, 11(1), pp. 299-327.

Currie, I.G., 2016. *Fundamental Mechanics of Fluids*. CRC press.

Darbandi, M. and Schneider, G.E., 1998. Numerical study of the flow behavior in the uniform velocity entry flow problem. *Numerical Heat Transfer, Part A Applications*, 34(5), pp. 479-494.

Demirbas, A., 2010. *Methane Gas Hydrates*. Springer Science & Business Media.

Desa, E., 2001. Submarine methane hydrates-potential fuel resource of the 21st century.

Donev, J., 2019. Energy Education - Geothermal gradient [Online]. Available: [https://energyeducation.ca/encyclopedia/Geothermal\\_gradient](https://energyeducation.ca/encyclopedia/Geothermal_gradient). [Accessed: July 7, 2019].

Drive, C. and Carroll, J., 2009. *Natural gas hydrates: A guide for engineers*. Industrial and Engineering Elsevier Science and Technology Books, p. 277.

Durham, W.B., Kirby, S.H., Stern, L.A. and Zhang, W., 2003. The strength and rheology of methane clathrate hydrate. *Journal of Geophysical Research: Solid Earth*, 108(B4).

Edmonds, B., Moorwood, R. A. S., and Szczepanski, R. 1998. Hydrate update, GPA Europe Spring Meeting, Darlington, County Durham, UK.

Ellison, B.T., Gallagher, C.T., Frostman, L.M. and Lorimer, S.E., 2000. The physical chemistry of wax, hydrates, and asphaltene. In Offshore Technology Conference. Offshore Technology Conference.

Englezos, P., 1993. Clathrate hydrates. *Industrial & Engineering Chemistry Research*, 32(7), pp. 1251-1274.

Eslamimanesh, A., Mohammadi, A.H., Richon, D., Naidoo, P. and Ramjugernath, D., 2012. Application of gas hydrate formation in separation processes: A review of experimental studies. *The Journal of Chemical Thermodynamics*, 46, pp. 62-71.

Esteban, A., Hernandez, V. and Lunsford, K., 2000. Exploit the benefits of methanol. In Proceedings of the 79th Gas Processors Association Annual Convention (GPA'00).

Fatnes, E.D., 2010. Numerical simulations of the flow and plugging behaviour of hydrate particles. Master's Thesis, Department of Physics and Technology, The University of Bergen, NORWAY).

Flomec, 2015. TM Series Electronic Water Meters [Online]. Available: <http://gpi.net/downloads/manuals/92078603-.pdf/>. [Accessed: December 26, 2018].

Frostman, L.M. and Crosby, D.L., 2003. Low dosage hydrate inhibitor (LDHI) experience in deepwater. In the Deep Offshore Technology Conference, Marseille, FRANCE (pp. 19-21).

Frostman, L.M., 2000. Anti-agglomerant hydrate inhibitors for prevention of hydrate plugs in deepwater systems. In SPE Annual Technical Conference and Exhibition. Society of Petroleum Engineers.

Gas Processors Association, 1998. GPSA Engineering Data Book. Gas Processors Suppliers Association, Tulsa, OK.

Gbaruko, B.C., Igwe, J.C., Gbaruko, P.N. and Nwokeoma, R.C., 2007. Gas hydrates and clathrates: Flow assurance, environmental and economic perspectives and the Nigerian liquified natural gas project. *Journal of Petroleum Science and Engineering*, 56(1-3), pp. 192-198.

Giavarini, C. and Hester, K., 2011. Gas Hydrates: Immense Energy Potential and Environmental Challenges. Springer Science & Business Media.

Gidaspow, D., 1994. Multiphase Flow and Fluidization: Continuum and Kinetic Theory Descriptions. Academic press.

Goodman, M.A., Giussani, A.P. and Alger, R.P., 1982. Detection and evaluation methods for in-situ gas hydrates. In SPE Unconventional Gas Recovery Symposium. Society of Petroleum Engineers.

Gudmundsson, J.S., Mork, M. and Graff, O.F., 2002. Hydrate non-pipeline technology. In Proc. 4th Intl. Conf. Gas Hydrates, Yokohama, Japan, Tokyo: Keio University (pp. 997-1102).

Guo, Y., Sun, B., Zhao, K. and Zhang, H., 2016. A prediction method of natural gas hydrate formation in deepwater gas well and its application. *Petroleum*, 2(3), pp. 296-300.



Gupta, A., Kneafsey, T.J., Moridis, G.J., Seol, Y., Kowalsky, M.B. and Sloan, E.D., 2006. Composite thermal conductivity in a large heterogeneous porous methane hydrate sample. *The Journal of Physical Chemistry B*, 110(33), pp. 16384-16392.

Habib, M.A., Said, S.A.M., Badr, H.M., Hussaini, I. and Al-Bagawi, J.J., 2005. Effect of geometry on flow field and oil/water separation in vertical deadlegs. *International Journal of Numerical Methods for Heat & Fluid Flow*, 15(4), pp. 348-362.

Hirasaki, G.J., 1989. Supplement to SPE 19505, The Steam-Foam Process-Review of Steam-Foam Process Mechanisms. paper SPE, 19518.

Hornbach, M.J., Holbrook, W.S., Gorman, A.R., Hackwith, K.L., Lizarralde, D. and Pecher, I., 2003. Direct seismic detection of methane hydrate on the Blake Ridge. *Geophysics*, 68(1), pp. 92-100.

Hu, B., Zhu, H., Ding, K., Xu, F. and Zhang, Y., 2015. Numerical investigation of heat transfer characteristics for Subsea Xmas tree assembly. *Journal of Mechanical Science and Technology*, 29(11), pp. 4933-4942.

Hyndman, R.D. and Davis, E.E., 1992. A mechanism for the formation of methane hydrate and seafloor bottom-simulating reflectors by vertical fluid expulsion. *Journal of Geophysical Research: Solid Earth*, 97(B5), pp. 7025-7041.

Irmann-Jacobsen, T.B., 2012. Flow assurance-a system perspective. MEK4450 Offshore Technology Course, Universitet I Oslo, Matematisk Institutt.

Jassim, E., Abdi, M.A. and Muzychka, Y., 2010. A new approach to investigate hydrate deposition in gas-dominated flowlines. *Journal of Natural Gas Science and Engineering*, 2(4), pp. 163-177.

Javanmardi, J., Nasrifar, K., Najibi, S.H. and Moshfeghian, M., 2005. Economic evaluation of natural gas hydrate as an alternative for natural gas transportation. *Applied Thermal Engineering*, 25(11-12), pp. 1708-1723.

John W. Slater. (2008) Examining Spatial (Grid) Convergence [Online]. Available at: <https://www.grc.nasa.gov/WWW/wind/valid/tutorial/spatconv.html/> (Accessed: 8 July 2019)

Joshi, N.B., Muhammad, M., Creek, J.L. and McFadden, J., 2003. Flow assurance: A challenging path to well completions and productivity. In Offshore Technology Conference.

K. Ding et al., 2012. A Numerical Study of Flow Field and Oil Water Separation in Vertical Dead-legs. *Applied Mechanics and Materials*, Vols. 121-126, pp. 2465-2470.

Kroes, R.F., 2013. Crude oil-water flow in horizontal pipes.

Kutlik, R. and Allen, J., 1998. Flow Assurance Instrumentation. In *Offshore Technology Conference*. Offshore Technology Conference.

Kvamme, B., Kuznetsova, T., Bauman, J.M., Sjöblom, S. and Avinash Kulkarni, A., 2016. Hydrate formation during transport of natural gas containing water and impurities. *Journal of Chemical & Engineering Data*, 61(2), pp. 936-949.

Kvenvolden, K.A. and Lorenson, T.D., 2001. The global occurrence of natural gas hydrate (pp. 3-18). American Geophysical Union.

Kvenvolden, K.A., 1993. Gas hydrates-geological perspective and global change. *Reviews of Geophysics*, 31(2), pp. 173-187.

Kvenvolden, K.A., 1995. A review of the geochemistry of methane in natural gas hydrate. *Organic Geochemistry*, 23(11-12), pp. 997-1008.

Lauder, B.E. and Sharma, B.I., 1974. Application of the energy-dissipation model of turbulence to the calculation of flow near a spinning disc. *Letters in heat and mass transfer*, 1(2), pp.131-137.

Lauder, B.E. and Spalding, D.B., 1973. The numerical computation of turbulent flows. In *Numerical prediction of flow, heat transfer, turbulence and combustion* (pp. 96-116). Pergamon.

Lee, J., 2009. Introduction to offshore pipelines and risers. N/P.

Leontaritis, K.J., 2000. Hydrate and wax formation in subsea satellite wells and flowlines. *World Oil*, 221(8), pp. 35-37.

Li, L., Xu, H.L. and Yang, F.Q., 2015. Three-phase flow of submarine gas hydrate pipe transport. *Journal of Central South University*, 22(9), pp. 3650-3656.

Li, W., Gong, J., Lü, X., Zhao J., Feng Y. and Yu D., 2013. A study of hydrate plug formation in a subsea natural gas pipeline using a novel high-pressure flow loop. *Pet. Sci.*, 10: 97. <https://doi.org/10.1007/s12182-013-0255-8>.

Liu, X., Wang, L., Liu, Y., Wang, Z., Cui, X. and Liu, L., 2017. Numerical Investigation of Waxy Crude Oil Paste Melting on an Inner Overhead Pipe Wall. *Applied Thermal Engineering*, Volume 131, 25 February 2018, pp 779-785.

Lo, S., 2011, January. CFD modelling of hydrate formation in oil-dominated flows. In Offshore Technology Conference. Offshore Technology Conference.

Lu, Y., Agrawal, M. and Skeels, H.B., 2011. CFD thermal analysis of subsea equipment and experimental validation. In Offshore Technology Conference. Offshore Technology Conference.

Manninen, M., Taivassalo, V. and Kallio, S., 1996. On the mixture model for multiphase flow.

Marić, I., 2005. The Joule–Thomson effect in natural gas flow-rate measurements. *Flow Measurement and Instrumentation*, 16(6), pp. 387-395.

Max, M.D. and Cruickshank, M.J., 1999, January. Extraction of methane from oceanic hydrate system deposits. In Offshore Technology Conference. Offshore Technology Conference.

Meysel, P., Oellrich, L., Bishnoi, P.R. and Clarke, M.A., 2011. Experimental investigation of incipient equilibrium conditions for the formation of semi-clathrate hydrates from quaternary mixtures of (CO<sub>2</sub>+ N<sub>2</sub>+ TBAB+ H<sub>2</sub>O). *The Journal of Chemical Thermodynamics*, 43(10), pp. 1475-1479.

Mokhatab, S., Wilkens, R.J. and Leontaritis, K.J., 2007. A review of strategies for solving gas-hydrate problems in subsea pipelines. *Energy Sources, Part A*, 29(1), pp. 39-45.

Murakami, S., 1998. Overview of turbulence models applied in CWE–1997. *Journal of Wind Engineering and Industrial Aerodynamics*, 74, pp. 1-24.

Naseer, M. and Brandstätter, W., 2011. Hydrate formation in natural gas pipelines. *Computational Methods in Multiphase Flow VI*, 70, p. 261.

Nazridoust, K. and Ahmadi, G., 2007. Computational modeling of methane hydrate dissociation in a sandstone core. *Chemical Engineering Science*, 62(22), pp. 6155-6177.

Obanijesu, E.O.O., Pareek, V. and Tade, M.O., 2010. Hydrate formation and its influence on natural gas pipeline internal corrosion rate. In SPE Oil and Gas India Conference and Exhibition. Society of Petroleum Engineers.

*Offshore Magazine*, January 2002

Ohta, K., 2002. Basic study on recovery system of methane hydrate. *Proc. of 4th Int. Con. on Gas Hydrates*, Yokohama, Japan, 1, pp. 206-209.

Oil States. (2019) Oil States Systems & Technologies. Connecting the Energy Future [Online]. Available at: <https://oilstates.com/wp-content/uploads/OilStatesPoster2019.pdf/> (Accessed: 1 July 2019)

OILFIELDWIKI. (no date) Hydrate Remediation [Online]. Available: [http://www.oilfieldwiki.com/wiki/Hydrate\\_Remediation/](http://www.oilfieldwiki.com/wiki/Hydrate_Remediation/) (Accessed: July 7, 2019)

Pedersen, K.S., Christensen, P.L., Shaikh, J.A. and Christensen, P.L., 2006. Phase Behavior of Petroleum Reservoir Fluids. CRC press.

Peeters, P.T., 2016. CFD of multiphase pipe flow: A comparison of solvers. Master's Thesis, Delf University of Technology, The Netherlands.

Pope, S.B., 2010. *Turbulent Flows*, volume 1. Cambridge University Press, 1st edition. ISBN 9780511840531. doi:10.1088/0957-0233/12/11/705.

Richardson, L.F. and Gaunt, J.A., 1927. VIII. The deferred approach to the limit. *Philosophical Transactions of the Royal Society of London. Series A, Containing Papers of a Mathematical or Physical Character*, 226(636-646), pp. 299-361.

Richardson, L.F., 1911. IX. The approximate arithmetical solution by finite differences of physical problems involving differential equations, with an application to the stresses in a masonry dam. *Philosophical Transactions of the Royal Society of London. Series A, Containing Papers of a Mathematical or Physical Character*, 210(459-470), pp. 307-357.

Rukthong, W., Piumsomboon, P., Weerapakkaron, W. and Chalermssinsuwan, B., 2016. Computational Fluid Dynamics Simulation of a Crude Oil Transport Pipeline: Effect of Crude Oil Properties. *Engineering Journal (Eng. J.)*, 20(3), pp. 145-154.

Ruppel, C., 2011. Methane hydrates and the future of natural gas. *MITEI Natural Gas Report, Supplementary Paper on Methane Hydrates*, 4, p. 25.

Sallehud-Din, M.T.M., 2012. Prediction of natural convection heat transfer in a pipeline bundle. PhD Thesis, Department of Chemical Engineering and Chemical Technology, Imperial Collage, London, UK.

Sami, N.A., Sangwai, J.S. and Balasubramanian, N., 2013. Gas Hydrate Applications and Problems in Oil and Gas Industry. *International Journal of Scientific & Engineering Research*, 4(8).

Samimi, A., 2012. Preventing hydrate formation in gas transporting pipe lines with synthetic inhibitors. *International Journal of Science and Investigations*, pp. 48-50.

Scardovelli, R. and Zaleski, S., 1999. Direct numerical simulation of free-surface and interfacial flow. *Annual Reviews of Fluid Mechanics*, 31(1), pp. 567-603.

Sean, W.Y., Sato, T., Yamasaki, A. and Kiyono, F., 2007. CFD and experimental study on methane hydrate dissociation Part I. Dissociation under water flow. *AIChE Journal*, 53(1), pp. 262-274.

Shuard, A.M., Mahmud, H.B. and King, A.J., 2017. An optimization approach to reduce the risk of hydrate plugging during gas-dominated restart operations. *Journal of Petroleum Science and Engineering*, 156, pp. 220-234.

Sinquin, A., Palermo, T. and Peysson, Y., 2004. Rheological and flow properties of gas hydrate suspensions. *Oil & Gas Science and Technology*, 59(1), pp. 41-57.

Sloan Jr, E.D. and Koh, C., 2007. *Clathrate Hydrates of Natural Gases*. CRC press.

Sloan Jr, E.D., 2003. Fundamental Principles and Applications of Natural Gas Hydrates. *Nature*, 426(6964), p. 353.

Sloan, E.D. and Fleyfel, F., 1992. Hydrate dissociation enthalpy and guest size. *Fluid Phase Equilibria*, 76, pp. 123-140.

Sloan, E.D. and Koh, C.A., 2008. *Clathrate Hydrates of Natural Gases* Third Edition.

Sloan, E.D., Koh, C.A., Sum, A.K., Ballard, A.L., Shoup, G.J., McMullen, N., Creek, J.L. and Palermo, T., 2009. Hydrates: state of the art inside and outside flowlines. *Journal of Petroleum Technology*, 61(12), pp. 89-94.

Smith, Glenda. (2018) Oil and gas separators [Online]. Available at: [https://petrowiki.org/Oil\\_and\\_gas\\_separators/](https://petrowiki.org/Oil_and_gas_separators/) (Accessed: 18 June 2019)

Sørheim, R. and Gudmundsson, J.S., 2005. Transportation of Petroleum in Subsea Pipelines A Competitive Analysis. Department of Industrial Economics and Technology Management at the Norwegian University of Science and Technology (NTNU).

Sule, I.O., Adedeji, A., Obeng, C., Okosun, A., Morshed, M., Rahman, M.A. and Hawboldt, K., 2015. CFD Analysis of Hydrate Formation in Pipelines. *Petroleum Science and Technology*, 33(5), pp. 571-578.

Tarek, A., 2007. Equations of state and PVT analysis. Applications for Improved Reservoir Modeling Gulf Publishing Company Houston, Texas.

Tennekes and Lumley, 1972. *A First Course in Turbulence*, MIT Press.

Theyab, M.A., 2018. Fluid Flow Assurance Issues: Literature Review.

Tro, Nivaldo J., et al. (2008) *Chemistry: A Molecular Approach*. 1st edition. New Jersey: Pearson Education, Inc.

US Water Systems. (no date) Deionized Water vs. Distilled-How Are They Made? [Online]. Available at: <https://www.uswatersystems.com/deionized-water-vs-distilled-water/> (Accessed: 23 May 2019)

Wang, W., Fan, S., Liang, D. and Yang, X., 2008. Experimental study on flow characters of CH<sub>3</sub>CCl<sub>2</sub>F hydrate slurry. *International Journal of Refrigeration*, 31(3), pp. 371-378.

Wang, Z., Li, F., Fan, T., Xiong, W. and Yang, B., 2015. Research on the application of gas hydrate in cool storage air conditioning. *Procedia Engineering*, 121, pp. 1118-1125.

Waseda, A. and Iwano, H., 2008. Characterization of natural gases in Japan based on molecular and carbon isotope compositions. *Geofluids*, 8(4), pp. 286-292.

Wikipedia contributors. (2019, July 10) Lattice constant [Online]. Available at: [https://en.wikipedia.org/w/index.php?title=Lattice\\_constant&oldid=905670059/](https://en.wikipedia.org/w/index.php?title=Lattice_constant&oldid=905670059/) (Accessed: 27 May 2018)

Wilkins, R. J. 2002. Flow Assurance, In: Fluid Flow Handbook, J. Saleh (Ed.), New York: McGraw-Hill.

Xu, X.X., 2007. Study on oil–water two-phase flow in horizontal pipelines. *Journal of Petroleum Science and Engineering*, 59(1-2), pp. 43-58.

Yang, J. and Tohidi, B., 2011. Characterization of inhibition mechanisms of kinetic hydrate inhibitors using ultrasonic test technique. *Chemical Engineering Science*, 66(3), pp. 278-283.

Yang, L., Azzopardi, B.J., Belghazi, A. and Nakanishi, S., 2006. Phase separation of liquid-liquid two-phase flow at a T-junction. *AIChE Journal*, 52(1), pp. 141-149.

Zarinabadi, S. and Samimi, A., 2012. Problems of hydrate formation in oil and gas pipes deals. *Journal of American Science*, 8(8).

## APPENDIX A

### BENCHMARKING/VERIFICATION OF RELATED FLOW CASES UTILIZING THE OPENFOAM SOFTWARE

Benchmarking and verification of computational techniques and codes are crucial to successful design of processes and fluid-handling equipment. In this appendix, predictions of the commercial software OpenFOAM for the relevant cases of:

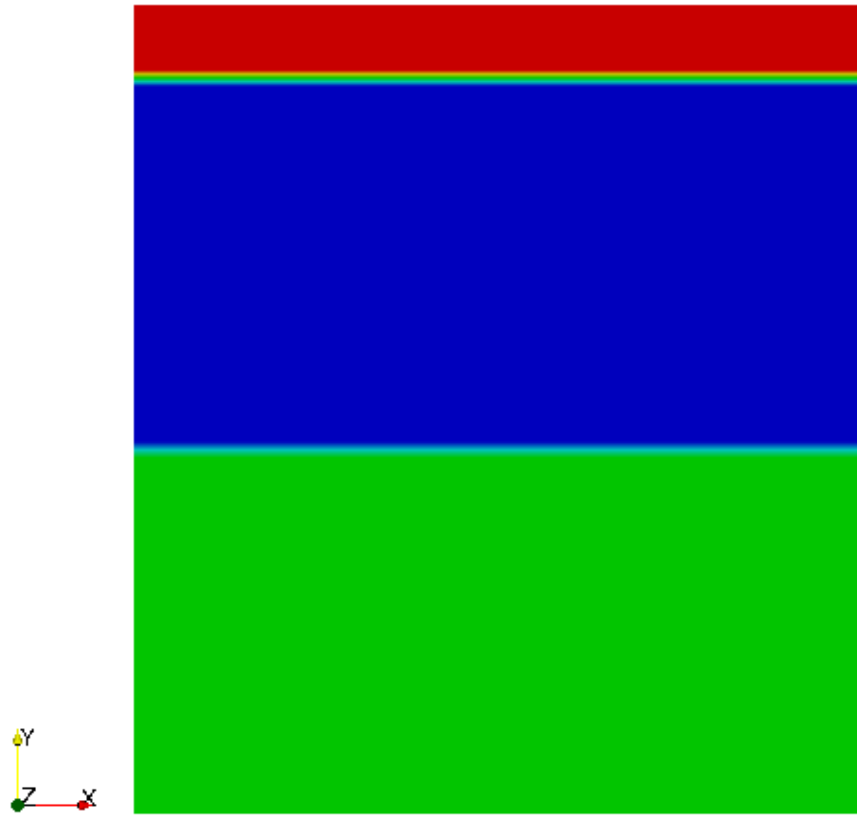
- an initially-unstable horizontal three-layer fluid system,
- an initially-unstable vertical three-fluid layer system,
- developing laminar channel flow,

are discussed.

#### A.1.1. Initially-Unstable Horizontal Three-Layer Immiscible Fluid System

Considering a two-dimensional square container, an ideally-layered three-fluid system consisting of air, water and oil immiscible fluids (Figure A.1.1.) was set up at time zero with 45% of oil at the bottom, 45% of water in the middle, and the remaining 10% air at the top of the container. The gravitational acceleration vector points in the negative y-direction. The top of the square container was open to the atmosphere. The oil-water and air-water interfaces were straight horizontal planes and various fluid velocities were set to zero at time zero.





Time: 0 s

Figure A.1.1. Configuration of the air-water-oil (top to bottom) unstable fluid system at time  $t=0$

### A.1.2. Computational Details

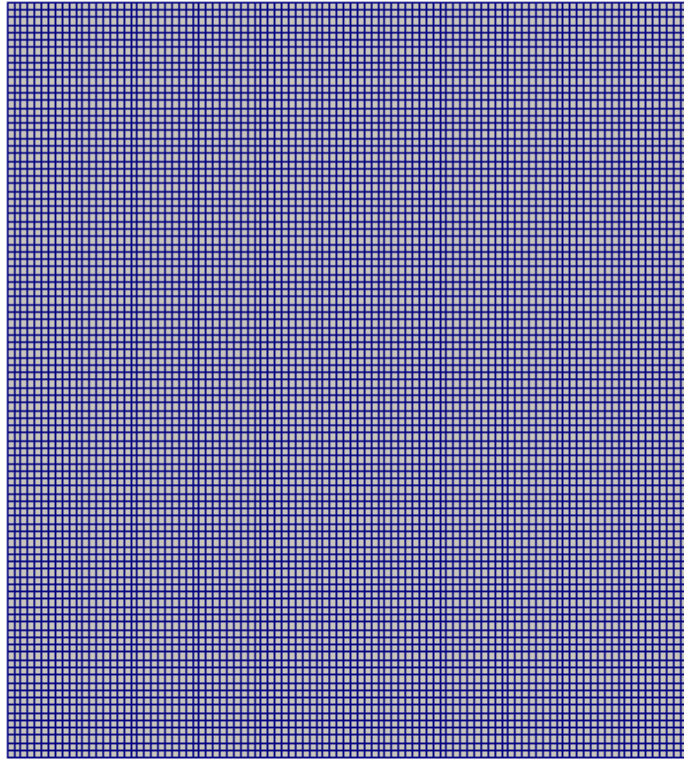


Figure A.1.2. The adopted grid system for the square container

A 2-D geometry was created in the blockMeshDict subfile under the system file with the height of 3.3 m and width of 3 m in the  $y$ - and  $x$ -directions, respectively. Even though the problem is treated as 2-D, the length in  $z$ -direction was also specified to be 0.1 m with regard to the working principle of OpenFOAM. The adopted uniform grid density covering the domain was 10,000 (Figure A.1.2.).

Pressure boundary conditions were set up as fixedFluxPressure which assigns the pressure gradient to the provided value such that the flux on the boundary is that specified by the velocity boundary condition on the left, right and bottom wall(s), and totalPressure at the top boundary.

The no-slip condition was specified at the solid walls. The velocity boundary condition at the top boundary was chosen to be pressureInletOutletVelocity which is applied to pressure boundaries where the pressure is specified as the atmospheric pressure.

Gravitational acceleration was assigned in the y-direction with the value of 9.81 m/s<sup>2</sup>.

Densities of air, water and oil were set to be 1, 1000, and 800 kg/m<sup>3</sup>, respectively. The kinematic viscosities were 1.48x10<sup>-5</sup> for air, 10<sup>-4</sup> for oil and 10<sup>-6</sup> m<sup>2</sup>/s for water, respectively.

The solver was chosen to be the multiphaseInterFoam solver which is recommended for incompressible fluids well-suited for capturing the interfaces and includes surface-tension and contact-angle effects for each phase.

Values of the surface tensions are defined the same among all three fluids to be 0.07 kg/s<sup>2</sup>.

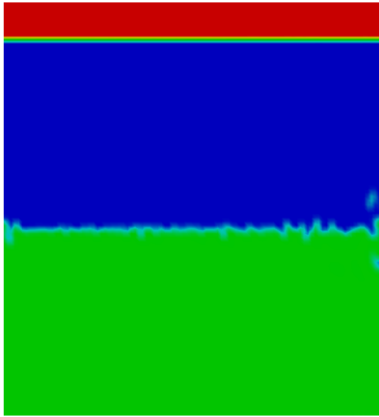
The initial time step for integrating the equations temporally was set to 10<sup>-5</sup> seconds based on the Courant number (*Co*) condition. The Courant number measures how much information traverses a grid cell in a given time step. The *Co* number for the *n*-dimensional case is;

$$Co = \Delta t \left( \sum_{i=1}^n \frac{u_{x_i}}{\Delta x_i} \right) \leq Co_{max} \quad (A.1)$$

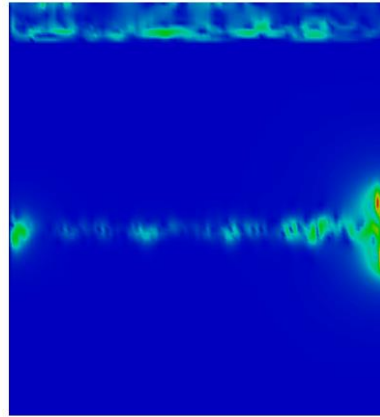
where  $\Delta t$  is the time step,  $\Delta x$  is the length interval and  $u$  is the velocity magnitude. The maximum *Co* number,  $Co_{max}$ , is preferred to be 1 for accurate solution.

### A.1.3. Results

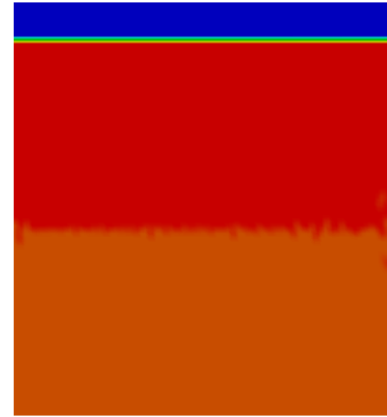
Initially at time  $t=0$ , there were two sharp idealized interfaces, one at the oil-water boundary ( $y=1.5$  m) and the other at the air-water boundary ( $y=3$  m). The multiphase fluid system was observed to exhibit unstable behavior immediately due to density difference of the two liquid components of this system. The corresponding fields of various phases,  $x$ -component of velocity, and pressure at time instants of 5, 8, 10, 15, 25, 35 and 60 seconds are shown in Figure A.1.3. The less dense oil phase is observed to move upwards replacing the heavier water medium that sinks into the lower portion of the container. Such inter-penetration of the two liquid phases is clearly observed at time instant  $t=8$  s; however, as expected both liquid layers still are located under the top air layer. Waves were formed at the emerging oil-air interface depending on the rising velocity of the oil phase. The emerging water-oil interface also exhibited an agitated wavy pattern ( $t=35$  s). After 60 seconds, the heavy water phase was located at the bottom of the container supporting the lighter oil layer above it, exhibiting a stable pattern within the domain. The pressure fields at various time instants are shown on the right column of Figure A.1.3 exhibiting transition to a hydrostatic system at the conclusion of 60 s.



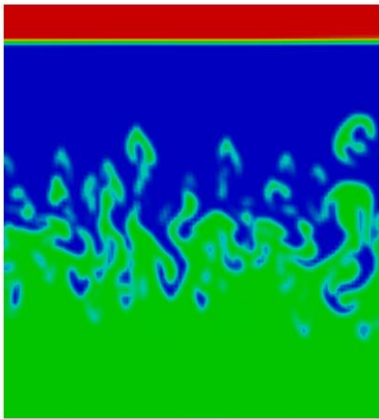
Time: 5 s



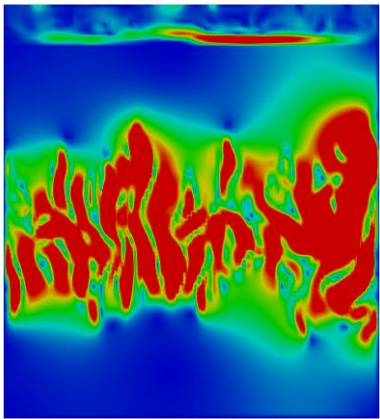
Time: 5 s



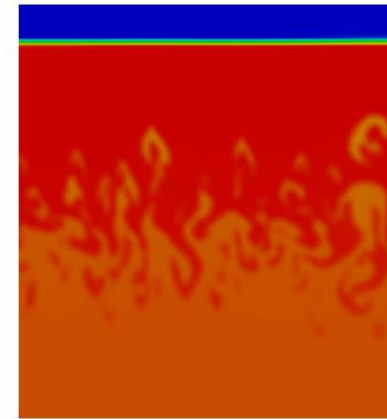
Time: 5 s



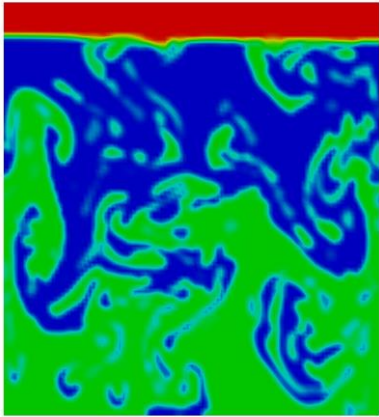
Time: 8 s



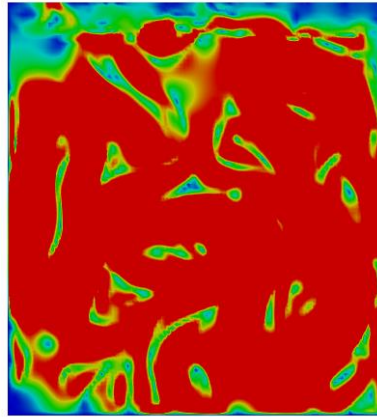
Time: 8 s



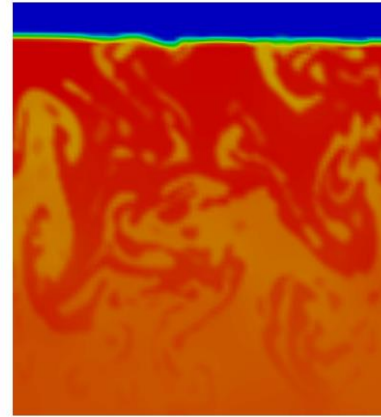
Time: 8 s



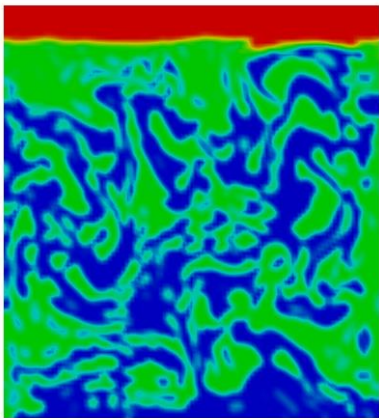
Time: 10 s



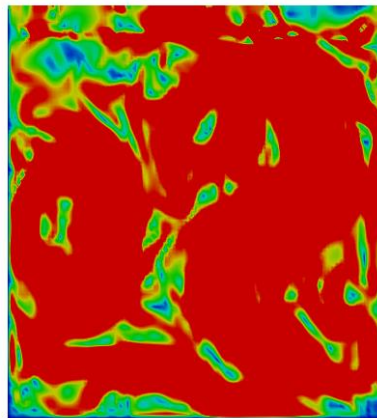
Time: 10 s



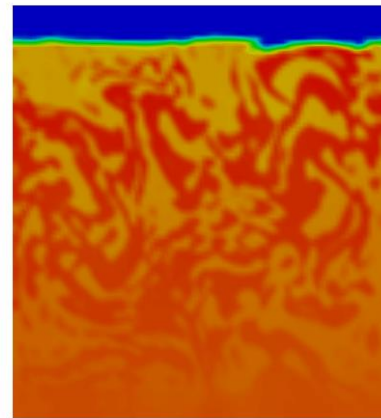
Time: 10 s



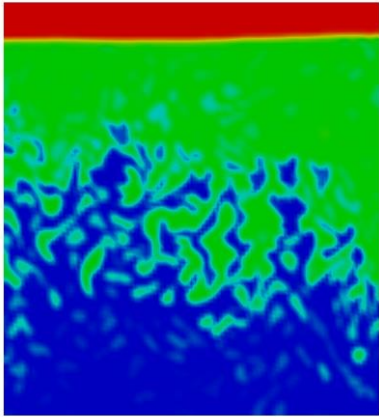
Time: 15 s



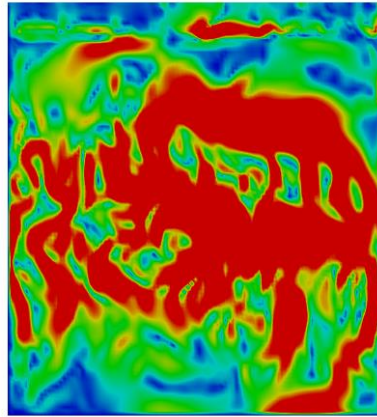
Time: 15 s



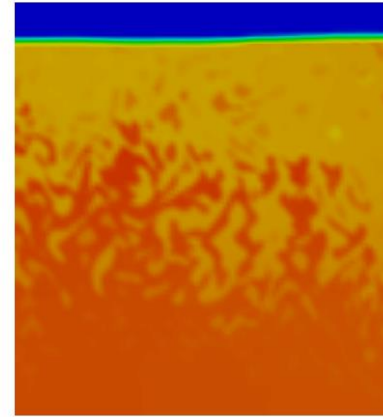
Time: 15 s



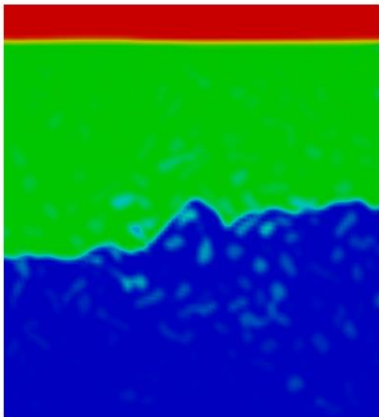
Time: 25 s



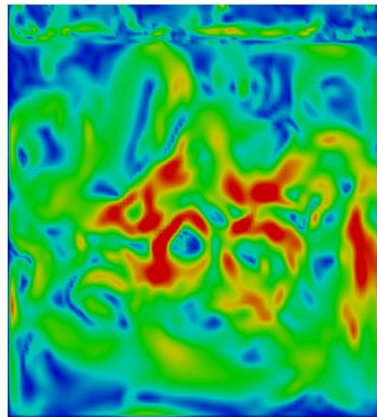
Time: 25 s



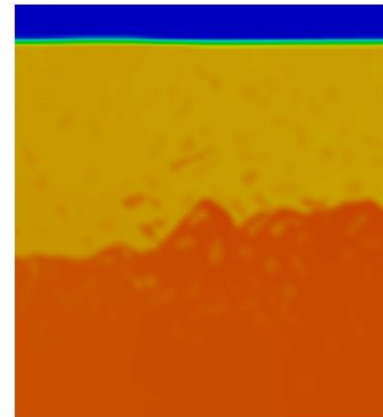
Time: 25 s



Time: 35 s



Time: 35 s



Time: 35 s

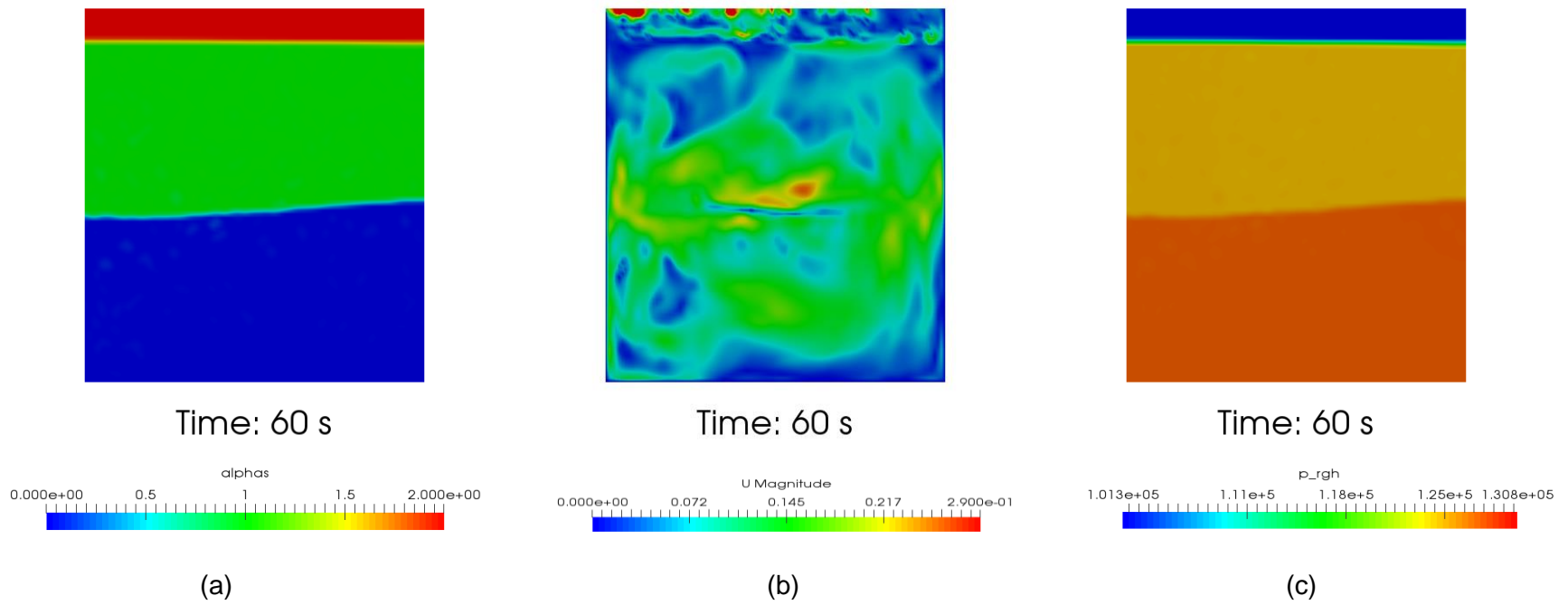


Figure A.1.3. Instantaneous fields of the three-fluid system corresponding to (a) three immiscible phases, (b) fluid velocity in the  $x$ -direction, and (c) fluid pressure at time instants of 5, 8, 10, 15, 25, 35 and 60 seconds



### A.2.1. Initially-Unstable Vertical Three-Layer Immiscible Fluid System

The multiphaseInterFoam case was set up as a 2-D-block. The square container consisted of three immiscible Newtonian fluids which were 45% oil on the left, 10% air on the right and 45% water placed in between the oil and air layers (Figure A.2.1). All phases were standing ideally as stable vertical layers at time zero. Then all fluids were relaxed simultaneously and penetrated into each other. This creates a complicated mixture of the three separate phases where the interaction among the phases need to be interpolated and the contact angles calculated. The solver algorithm is based upon the volume-of-fluid (VOF) method.



Time: 0 s

Figure A.2.1. Configuration of the oil-water-air (left to right) unstable fluid system at time  $t=0$

### A.2.2. Computational Details

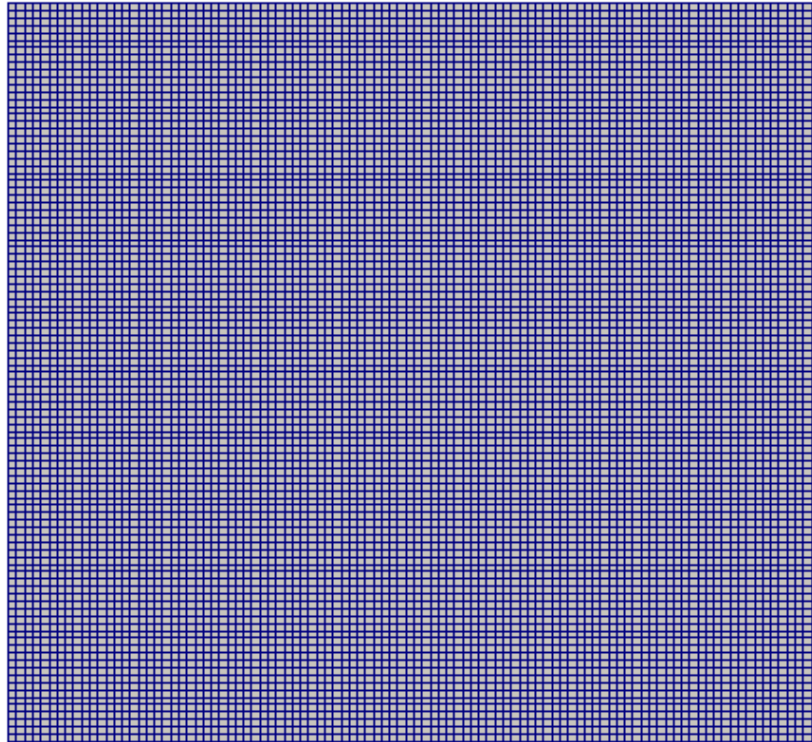


Figure A.2.2. The adopted grid system for the square container

The 2-D geometry was created in blockMeshDict subfile under the system file with a height of 3 m and width of 3.3 m. Even though it was 2-D, the depth in the z-direction was specified to be 0.1 m to satisfy the working principle of OpenFOAM. The adopted uniform grid size of the domain was 10,000 (Figure A.2.2.).

Pressure boundary conditions were set up as `fixedFluxPressure` which sets the pressure gradient to the provided value such that the flux on the boundary is that specified by the velocity boundary condition at the left, right and bottom wall(s), and `totalPressure` at the top boundary.

The no-slip condition was specified at the solid walls. Velocity boundary condition at the top boundary was chosen to be `pressureInletOutletVelocity` which is applied to pressure boundaries where the pressure is specified (atmospheric pressure).

The gravitational acceleration in the  $y$ -direction with the value of  $9.81 \text{ m/s}^2$  was applied.

Densities of air, water and oil were specified to be 1, 1000, and  $800 \text{ kg/m}^3$ , respectively. Kinematic viscosities were  $1.48 \times 10^{-5}$  for air,  $10^{-4}$  for oil and  $10^{-6}$  for water.

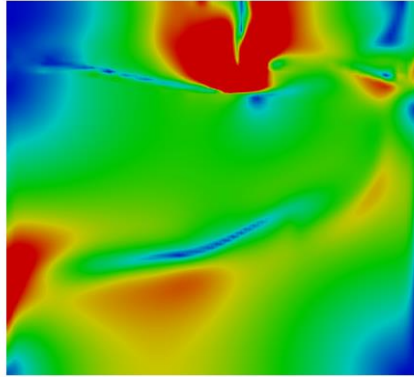
The solver was decided as `multiphaseInterFoam` which is a solver for incompressible fluids which captures the interfaces and includes the surface-tension and contact-angle effects for each phase.

### A.2.3. Results

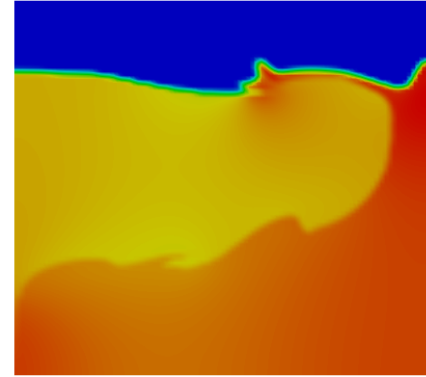
Initially, there were two sharp vertical interfaces, one at the oil-water interface ( $x=1.5 \text{ m}$ ) and the other at the air-water interface ( $x=3 \text{ m}$ ). The multiphase fluid system became unstable right after the simulation started due to density difference. The corresponding fields of various fields,  $x$ -component of velocity, and pressure at time instants of 2, 4, 6, 8, 10, 20 and 60 seconds are shown in Figure A.2.3. The water column which was the densest phase sandwiched between air and oil layers initially sank to the bottom very quickly filling the bottom of the container. At the time instant of 2 seconds, water is observed to fill the right side of the container unevenly, the general zone that was originally filled with air. With the air layer filling the top portion of the container, the greatest agitations are observed in the water and oil layers. After 20 seconds, all phases were generally separated, and the system attained a stable pattern of three fluid phases within the square container.



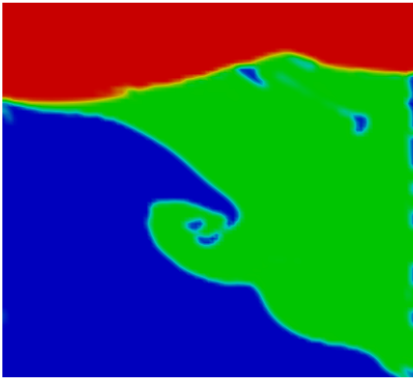
Time: 2 s



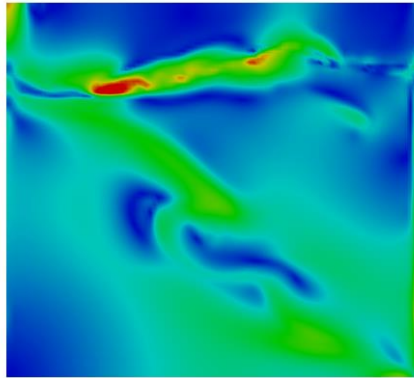
Time: 2 s



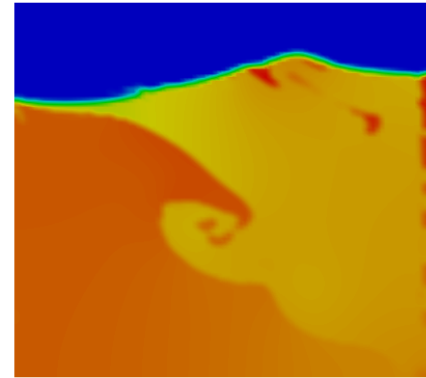
Time: 2 s



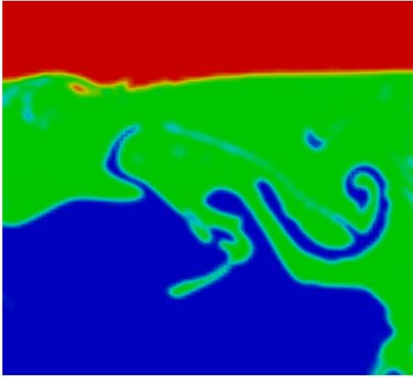
Time: 4 s



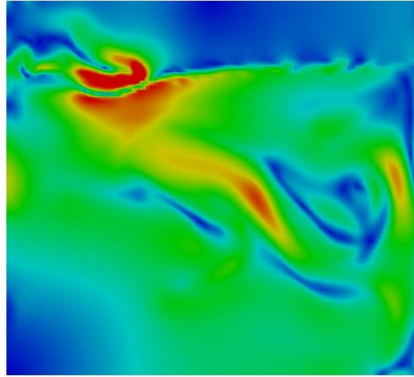
Time: 4 s



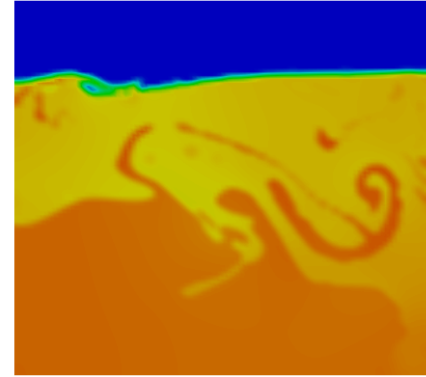
Time: 4 s



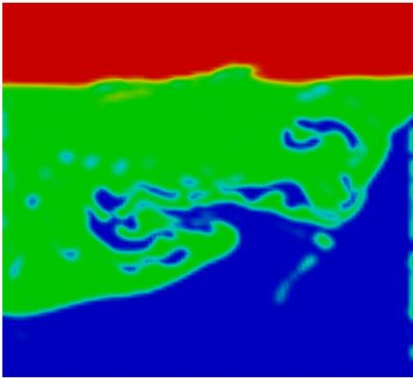
Time: 6 s



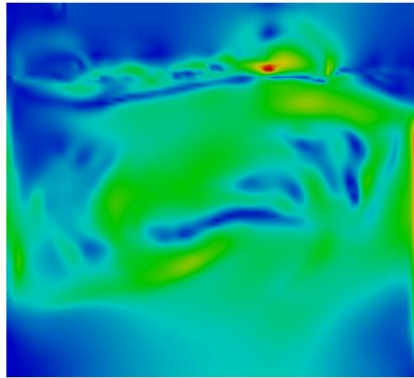
Time: 6 s



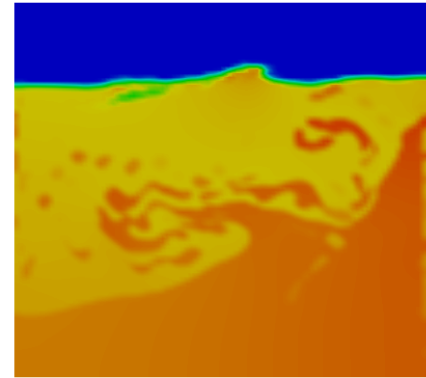
Time: 6 s



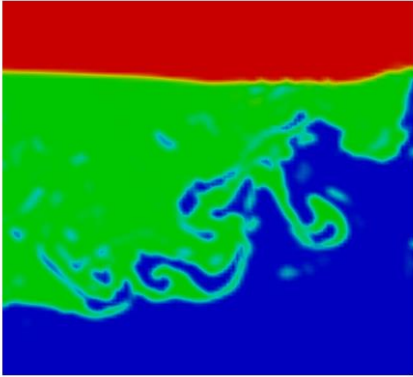
Time: 8 s



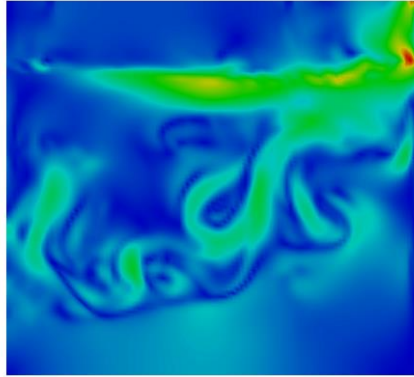
Time: 8 s



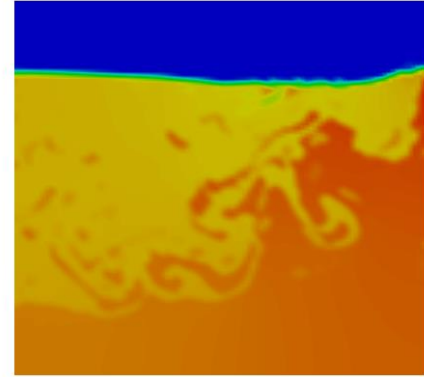
Time: 8 s



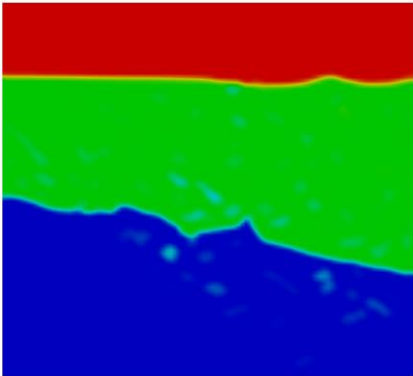
Time: 10 s



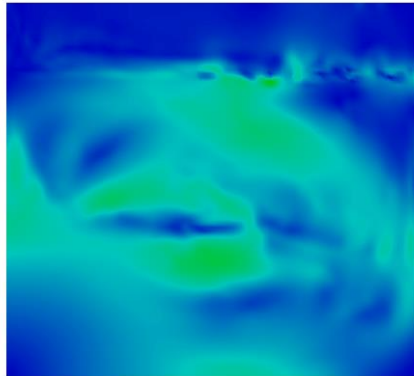
Time: 10 s



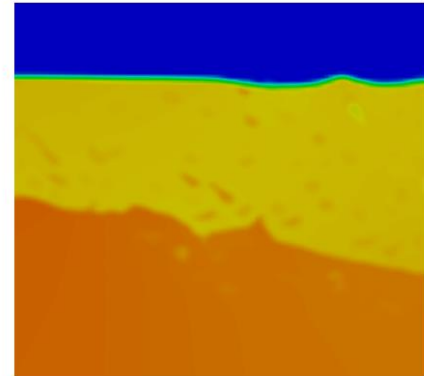
Time: 10 s



Time: 20 s



Time: 20 s



Time: 20 s

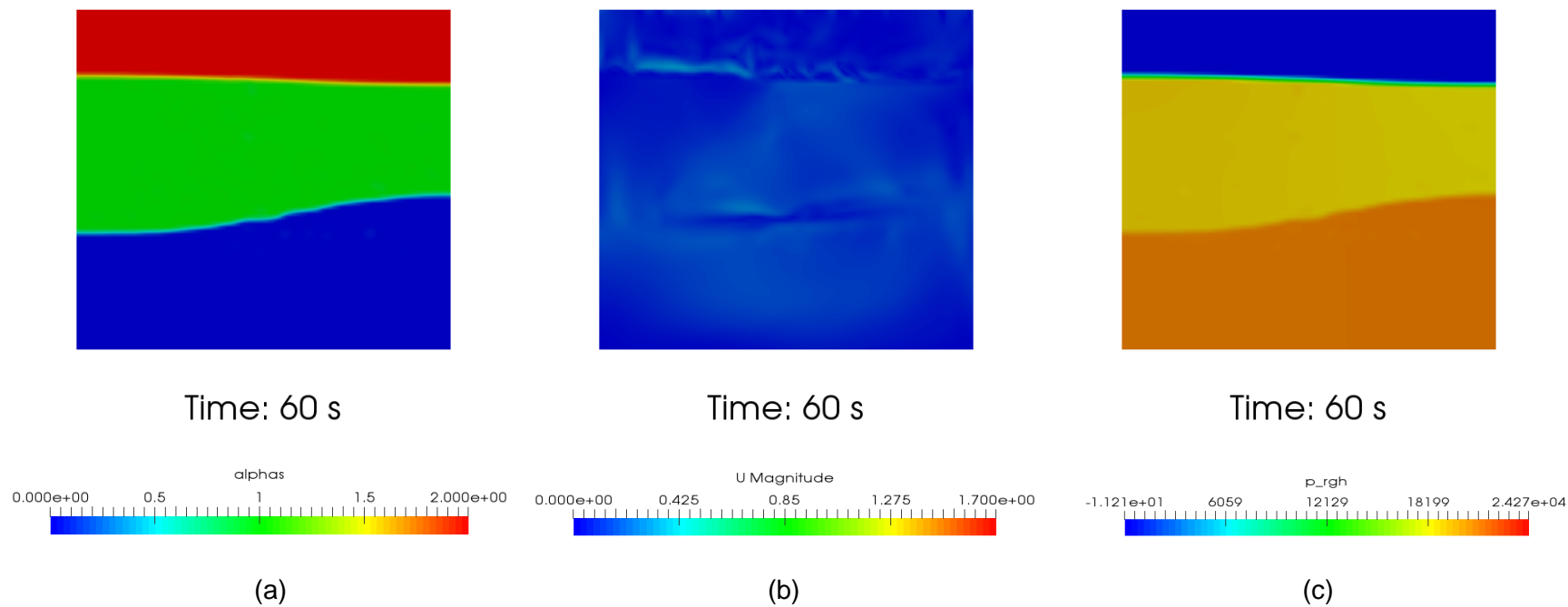


Figure A.2.3. Instantaneous fields of the three-fluid system corresponding to (a) three immiscible phases, (b) fluid velocity in the x-direction, and (c) pressure at time instants 2, 4, 6, 8, 10, 20 and 60 seconds

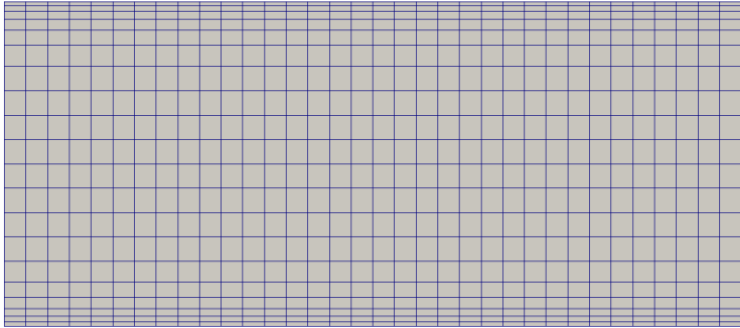
### A.3.1. Developing Laminar Channel Flow

The maximum velocity and pressure drop attained in a 2-D fully-developed laminar channel flow ( $Re$  number=1200) were investigated in order to evaluate the accuracy of CFD results in comparison to the analytical solutions. The solver was chosen as simpleFoam which is a steady-state solver for incompressible flows with turbulence modelling (if needed). Since the laminar flow was simulated in this study, turbulenceProperties subfile under constant file was re-arranged by changing simulation type as laminar. The flow-related parameters and fluid properties are summarized in Table A.3.1.

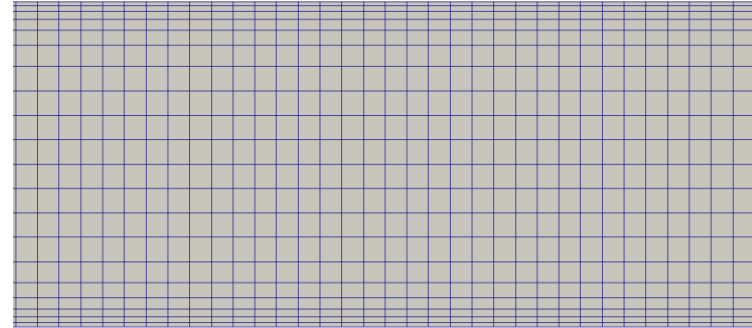
Table A.3.1. The adopted domain and properties of the fluid

Length of the channel	10 m
Width of the channel	0.12 m
Incompressible, Newtonian fluid	Water
Density	1000 kg/m <sup>3</sup>
Kinematic Viscosity	10 <sup>-6</sup> m <sup>2</sup> /s
Grid (size)	Uniform in the $x$ -direction and non-uniform in the $y$ -direction (total of 20,000)





(a)



(b)

Figure A.3.1. The adopted grid system near the (a) inlet and (b) outlet of the channel

### A.3.2. Computational Details

The adopted details related to boundary conditions imposed for solution of this problem are summarized in Table A.3.2.

Table A.3.2. Boundary conditions

Inlet velocity	fixedValue - 0.01 m/s
Outlet velocity	zeroGradient
Velocity at the walls	noSlip
Inlet pressure kinetic energy	zeroGradient
Outlet pressure kinetic energy	fixedValue - 0 m <sup>2</sup> /s <sup>2</sup>
Pressure kinetic energy at the walls	zeroGradient

### A.3.3. Results

The assigned average inlet velocity was set to 1 cm/s in order to guarantee establishment of laminar flow in the channel. The instantaneous velocity fields are shown in Figures A.3.2-A.3.2). The analytical solution for the maximum velocity at the symmetry plane of the channel ( $y=0$ ) is known to be:

$$U_{max} = 1.5U_{avg} \tag{A.2}$$

$$U_{max} = 1.5 * 0.01 = 0.015 \frac{m}{s}$$

According to the analytical solution, the maximum velocity at the center of the channel at the downstream station is supposed to be 0.015 m/s. The CFD results showed that the predicted maximum flow velocity was 0.014814 m/s. This 1.26% difference could be because of the poor mesh quality. That is why the CFD simulation was repeated with another re-arranged mesh distribution, and the outcomes were then compared with the analytical solution in the Appendix A.4.

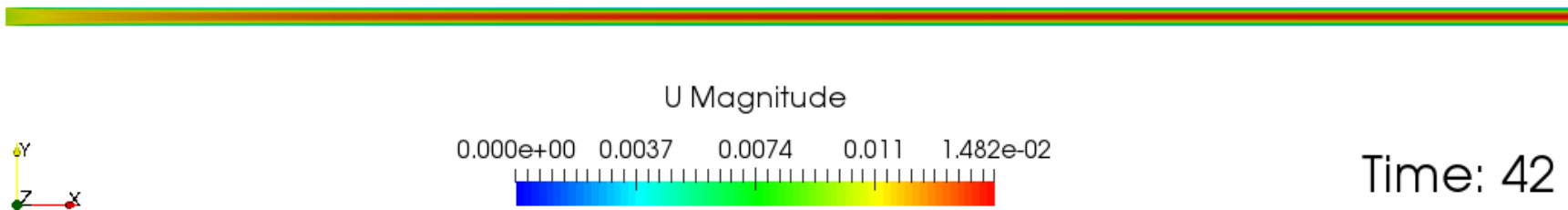


Figure A.3.2. Velocity field along the channel (m/s) with uniform mesh

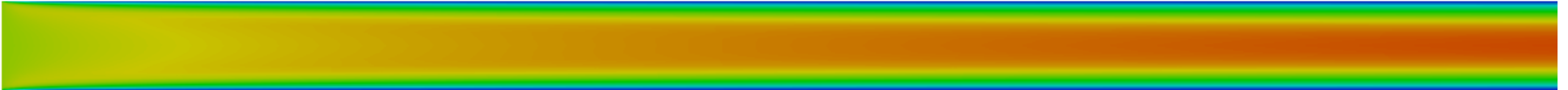


Figure A.3.3. Velocity field at the inlet of the channel (m/s) with uniform mesh

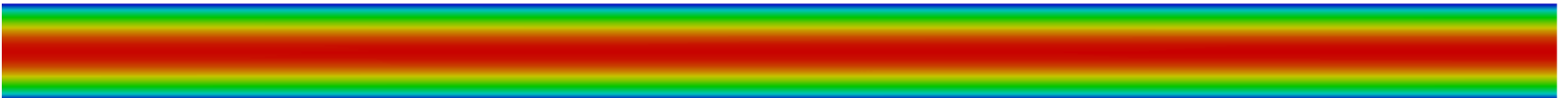


Figure A.3.4. Velocity field at the outlet of the channel (m/s) with uniform mesh

When the flow enters the channel and is subjected to frictional effects, the viscous boundary layers grow on the walls of the channel in the downstream direction, slowing the axial flow on the walls to be motionless, while the central core of the fluid is accelerated axially to satisfy the continuity requirement. Over a finite distance from the inlet (the hydrodynamic entrance length), the fluid becomes entirely affected by viscous effects and finally attains the fully-developed state (i.e.,  $u=f(y)$  and  $v=0$ ). Upon establishment of the fully-developed state, the velocity profile and the associated wall shear stress no longer vary in the axial direction, whereas the fluid pressure changes linearly in the  $x$ -direction. The wall shear stress is highest at the inlet where the thickness of the boundary layer is smallest and decreases gradually to the fully-developed value. Therefore, the pressure drop is higher in the entrance region. For laminar flow, the entrance length is given approximately as:

$$\frac{L_e}{D} \approx 0.05 Re \quad (A.3)$$

where  $D$  is width of the channel and  $Re$  is the Reynolds number (1200).

The predicted distributions of the axial velocity along the length of the channel are presented in Figure A.3.5.

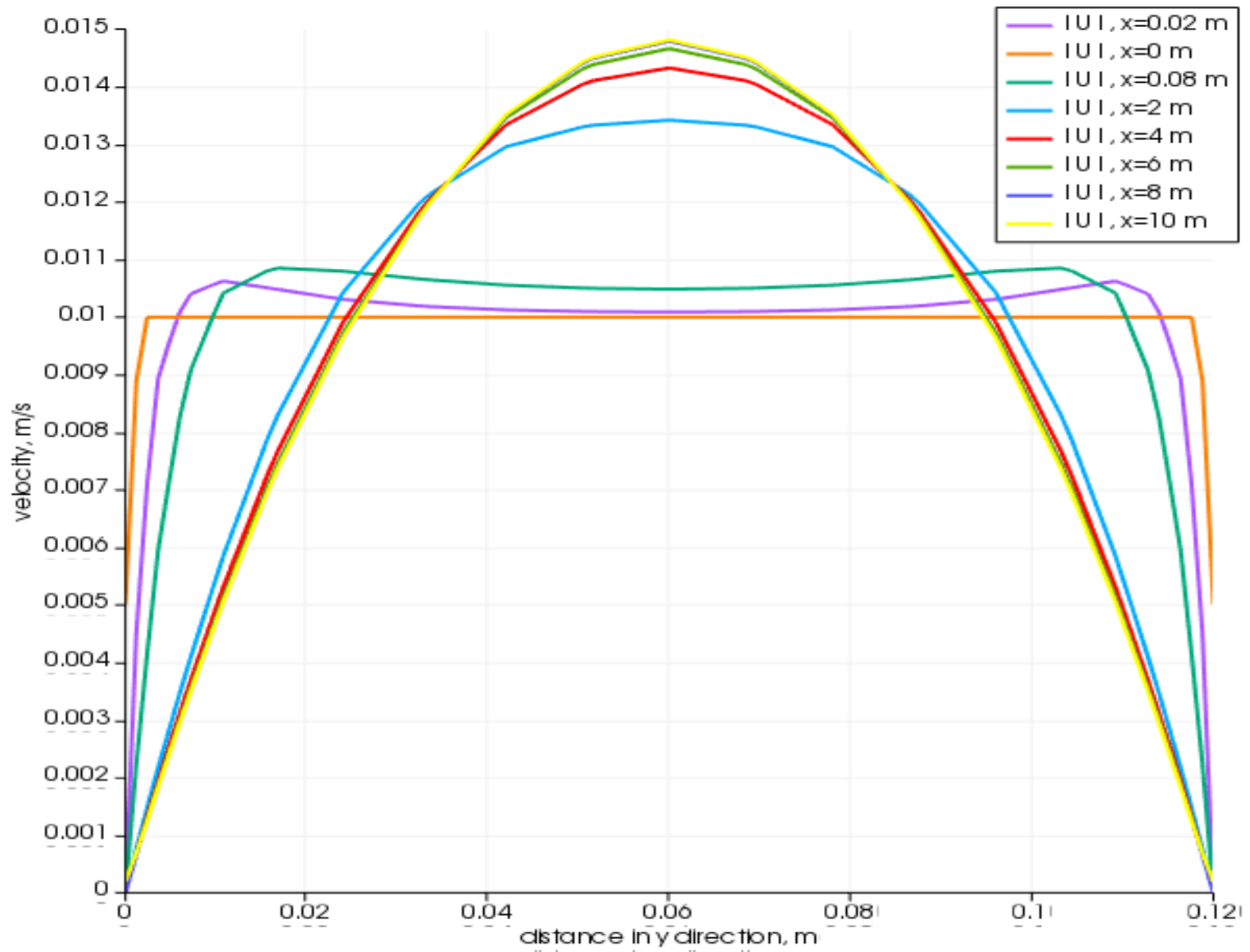


Figure A.3.5. Velocity profiles at different locations along the length of the channel (m/s) with uniform mesh

$$\frac{Q}{l} = (a^3 \Delta P) / (12 \mu L) \quad (\text{A.4})$$

$$Q = UA = Ual \quad (\text{A.5})$$

$$\Delta P = 0.01 * 0.12 * 12 * 10^{-3} * 1 / 0.12^3$$

$$\Delta P = 8.33 \times 10^{-3} \frac{\text{kg}}{\text{m} \cdot \text{s}^2}$$

$$\frac{\Delta P}{\rho} = 8.33 \times 10^{-6} \frac{\text{m}^2}{\text{s}^2}$$

Computational pressure drop divided by density was obtained to be  $8.352 \times 10^{-6} \text{ m}^2/\text{s}^2$ . The reason for this higher-pressure drop could be due to poor mesh quality.

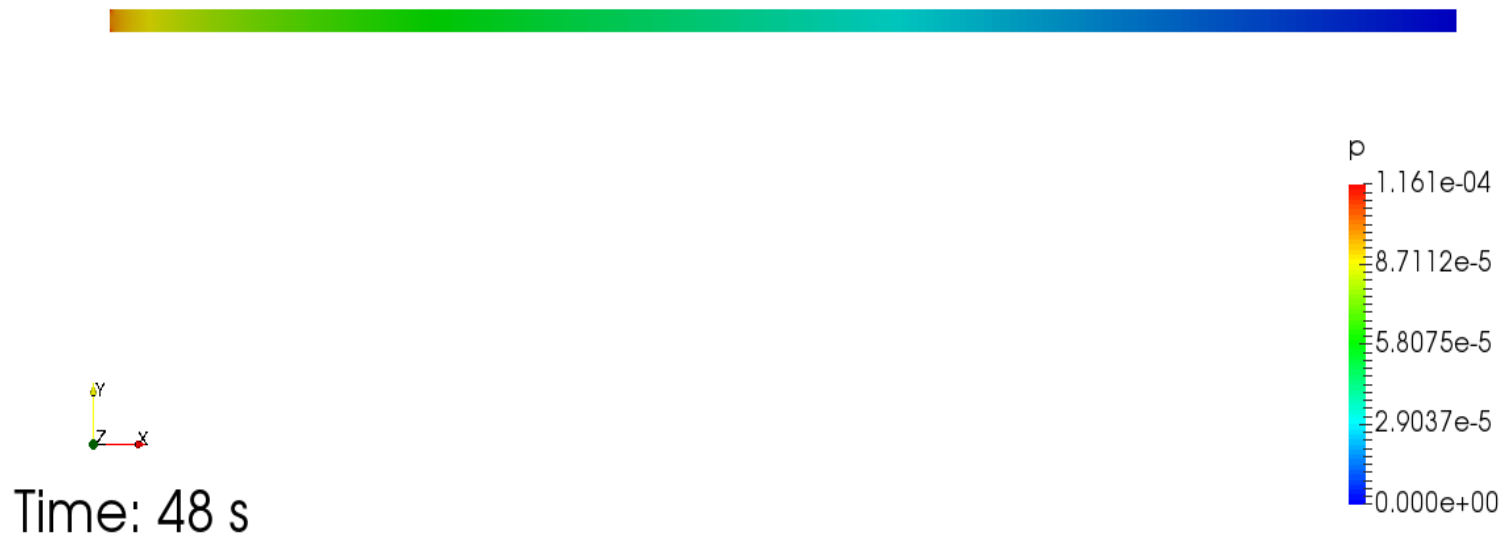


Figure A.3.6. Pressure field along the length of the channel ( $\text{m}^2/\text{s}^2$ ) with uniform mesh

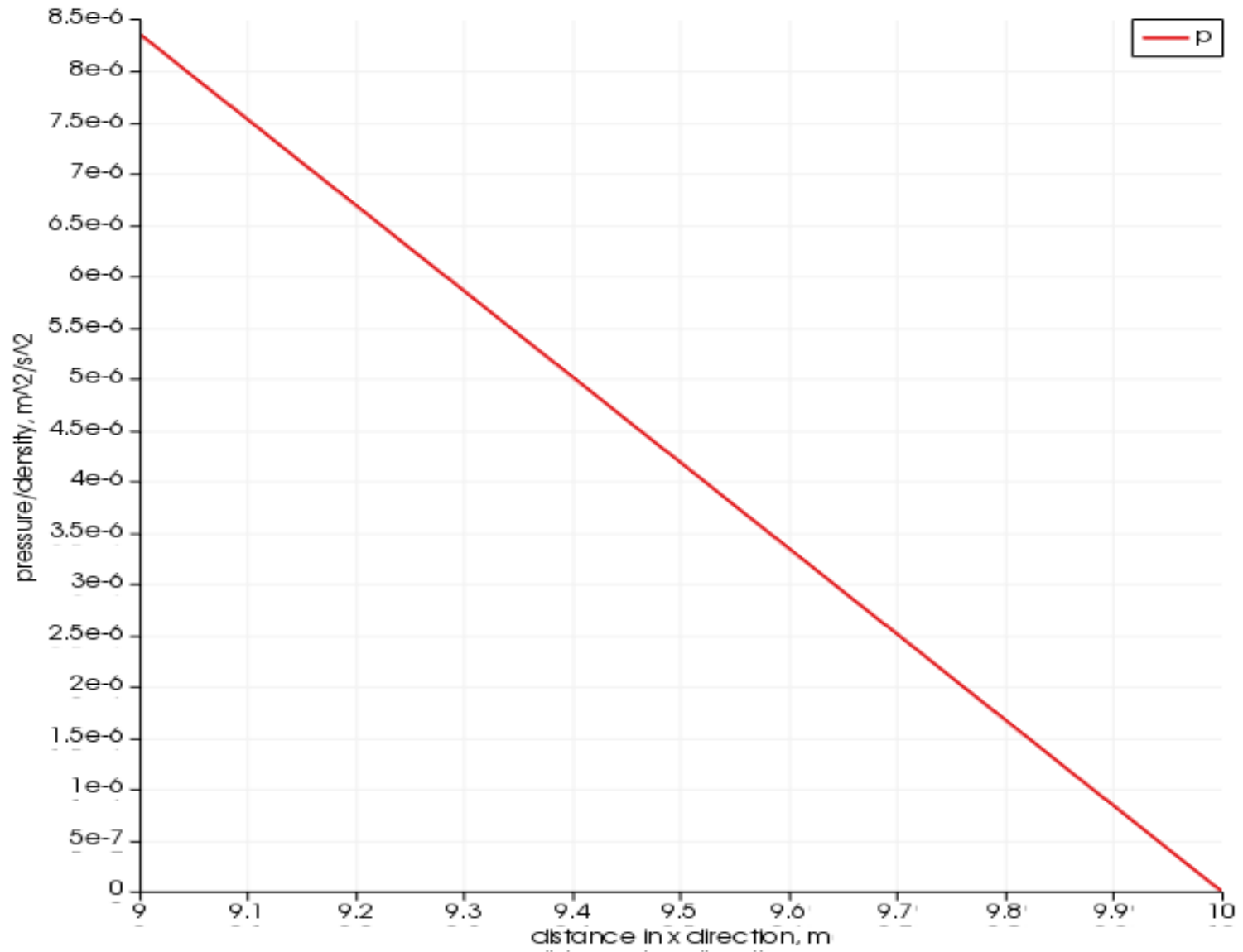


Figure A.3.7. Pressure drop divided by fluid density ( $\text{m}^2/\text{s}^2$ ) between axial positions  $x=9$ - $10$  m with uniform mesh

#### A.4.1. Developing Channel Flow Re-visited

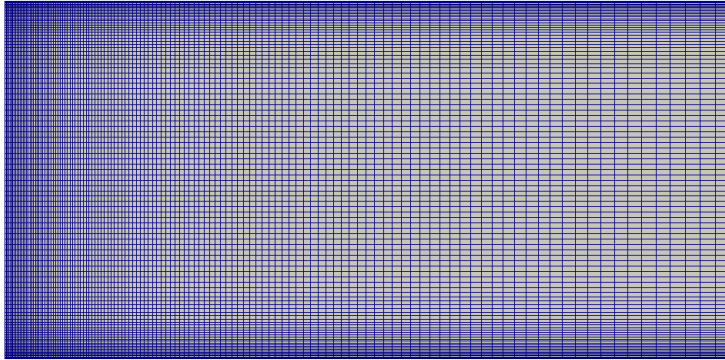
Predictions of the maximum axial velocity and pressure drop attained in a 2-D fully-developed laminar channel flow ( $Re$  number=1200) were already discussed in order to evaluate the accuracy of CFD results in comparison to the analytical solutions. The adopted computational mesh was uniformly distributed in two directions.

The computational study was repeated in order to obtain more accurate results by changing the mesh size and distribution. The same solver, simpleFoam, was used.

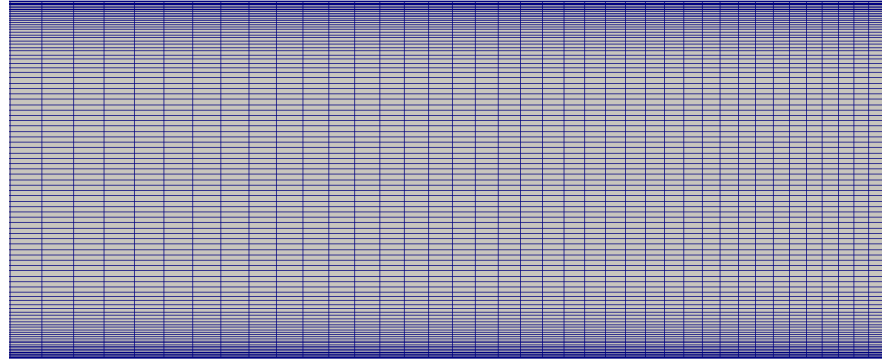
Table A.4.1. The adopted domain and properties of the fluid

Length of the channel	10 m
Width of the channel	0.12 m
Incompressible, Newtonian fluid	Water
Density	1000 kg/m <sup>3</sup>
Kinematic Viscosity	10 <sup>-6</sup> m <sup>2</sup> /s
Grid (size)	Non-uniform in both directions (50,000) with n expansion ratio of 20% in flow direction





(a)



(b)

Figure A.4.1. The adopted grid system near the (a) inlet and (b) outlet of the channel

#### A.4.2. Computational Details

Table A.4.2. Boundary conditions

Inlet velocity	fixedValue - 0.01 m/s
Outlet velocity	zeroGradient
Velocity at the walls	noSlip
Inlet pressure kinetic energy	zeroGradient
Outlet pressure kinetic energy	fixedValue - 0 m <sup>2</sup> /s <sup>2</sup>
Pressure kinetic energy at the walls	zeroGradient

### A.4.3. Results

The predicted velocity contours and axial velocity distributions are shown in Figures A.4.2, A.4.3 and A.4.4, respectively.

$$U_{max} = 1.5U_{avg} \tag{A.6}$$

$$U_{max} = 1.5 * 0.01 = 0.015 \frac{m}{s}$$

As seen on the graph, the velocity profiles became parabolic when the flow was fully-developed, and the maximum value was 0.015 m/s which was exactly the same with the analytical solution. It was proved that the exact analytical solution was obtained when the adopted mesh was fine at the entrance stations and near the two channel walls allowing for resolution of the strong gradients in these regions.

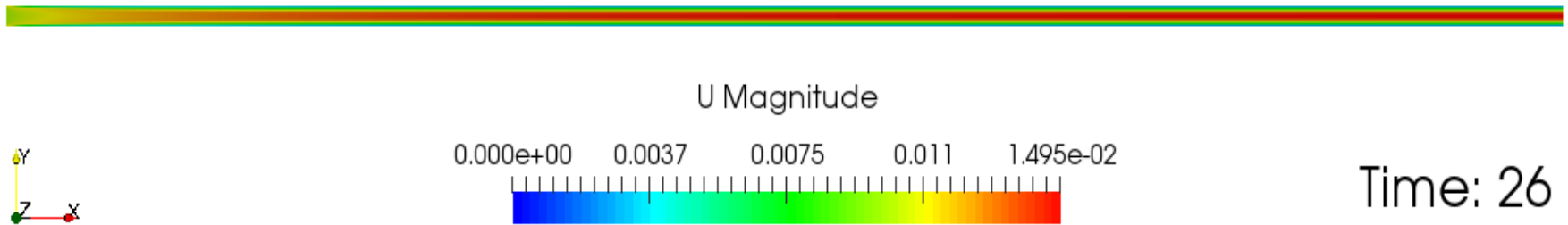
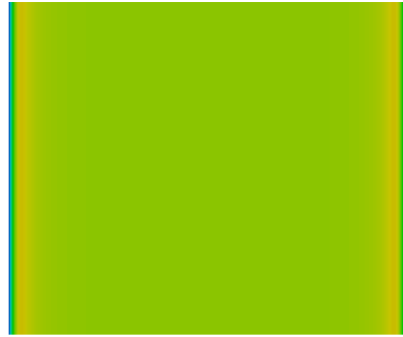


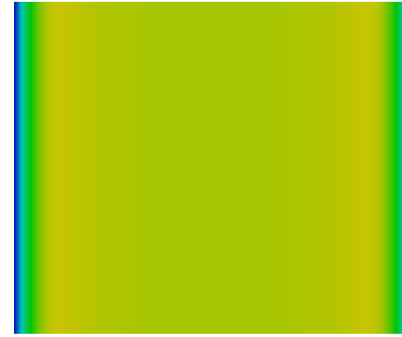
Figure A.4.2. Velocity field along the channel (m/s) with non-uniform grid



(a)



(b)



(c)



(d)



(e)



(f)

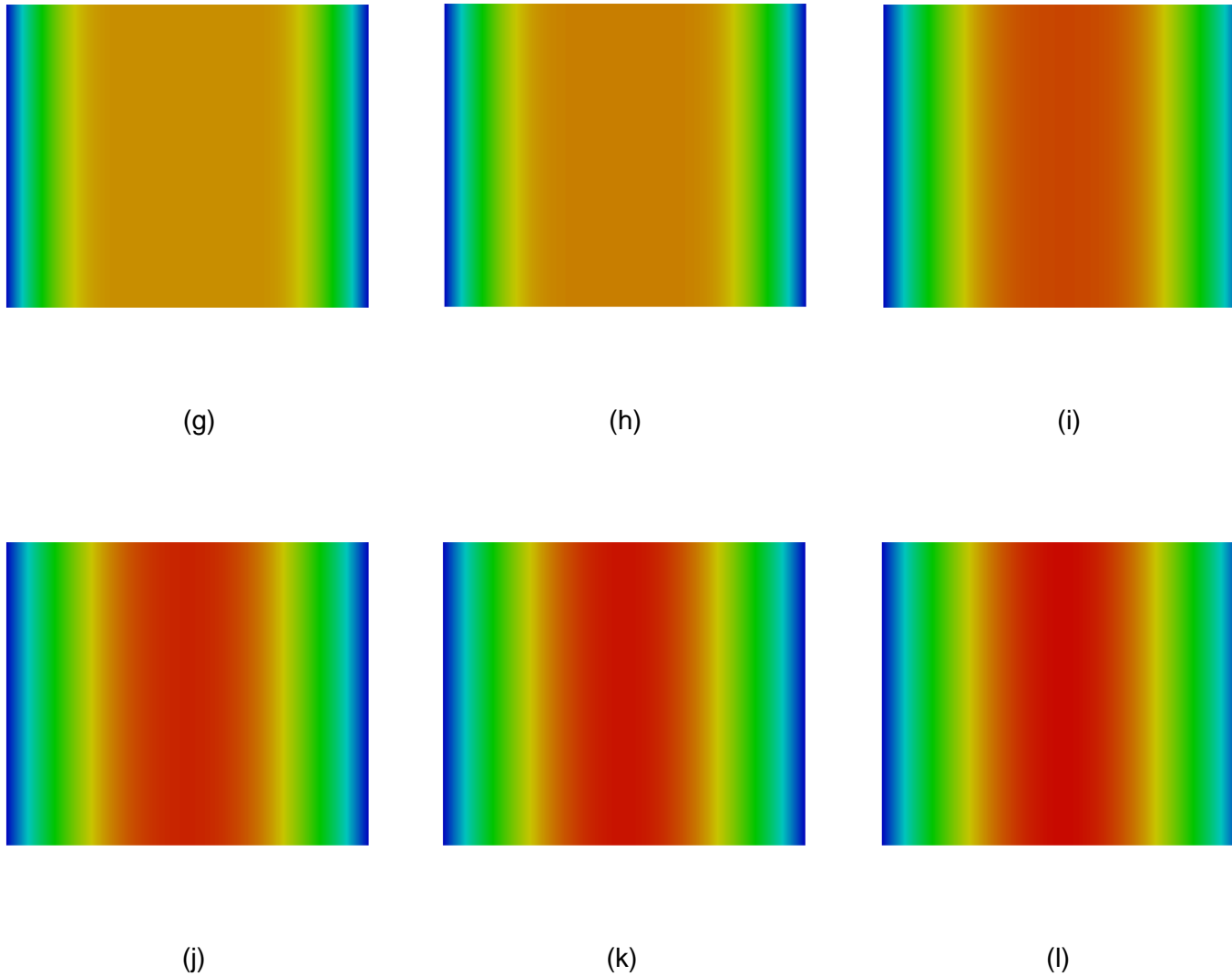


Figure A.4.3. The development of the axial velocity contours at (a)  $x=0.0001$  m, (b)  $x=0.01$  m, (c)  $x=0.1$  m, (d)  $x=0.2$  m, (e)  $x=0.4$  m, (f)  $x=0.6$  m, (g)  $x=0.8$  m, (h)  $x=1$  m, (i)  $x=2$  m, (j)  $x=7$  m, (k)  $x=9$  m and (l)  $x=10$  m, with non-uniform grid

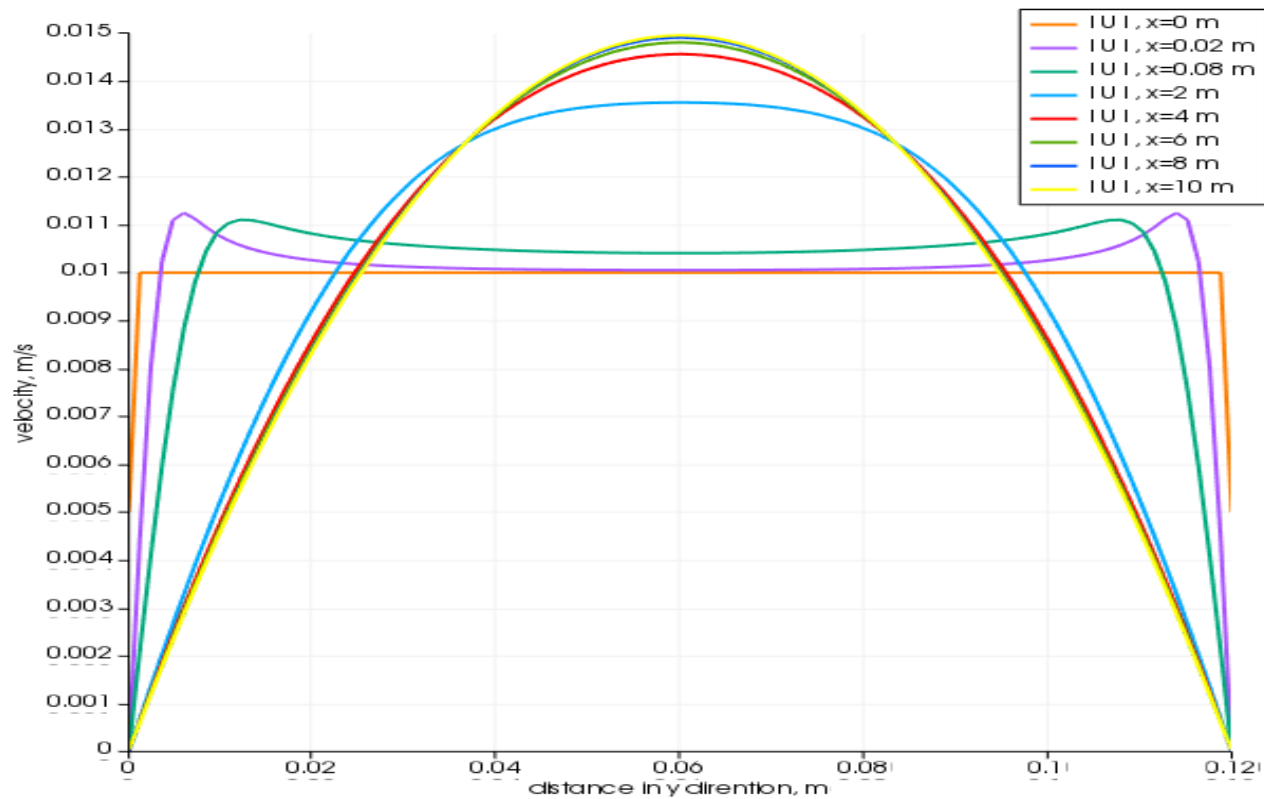


Figure A.4.4. Axial velocity profiles at different locations along the channel (m/s) with non-uniform grid

Darbandi et al. (1998) carried out a numerical study in order to capture the axial velocity profiles close to the walls at the inlet section of a developing flow in a two-dimensional channel. A non-uniform grid system was used for realizing improved resolution of the strong gradients near the inlet and close to the walls. The results revealed that the fluid particles near the walls at the inlet section are highly influenced by the shear stresses and undergo rapid deceleration and finally stay stationary meanwhile the fluid parcels near the centerline do not accelerate immediately. Velocity overshoots are generated near the inlet close to the walls in order to satisfy the continuity equation. The first 40% or less of the developing zone is where these velocity overshoots form, grow and vanish for all the  $Re$  numbers.

$$\frac{Q}{l} = (a^3 \Delta P) / (12 \mu L) \quad (\text{A.7})$$

$$Q = UA = Ual \quad (\text{A.8})$$

$$\Delta P = 0.01 * 0.12 * 12 * 10^{-3} * 1 / 0.12^3$$

$$\Delta P = 8.33 \times 10^{-3} \frac{\text{kg}}{\text{m} \cdot \text{s}^2}$$

$$\frac{\Delta P}{\rho} = 8.33 \times 10^{-6} \frac{\text{m}^2}{\text{s}^2}$$

Computed value of pressure drop divided by density was obtained to be  $8.349 \times 10^{-6} \text{ m}^2/\text{s}^2$  which was greater than what was calculated analytical with the error of 0.02%.

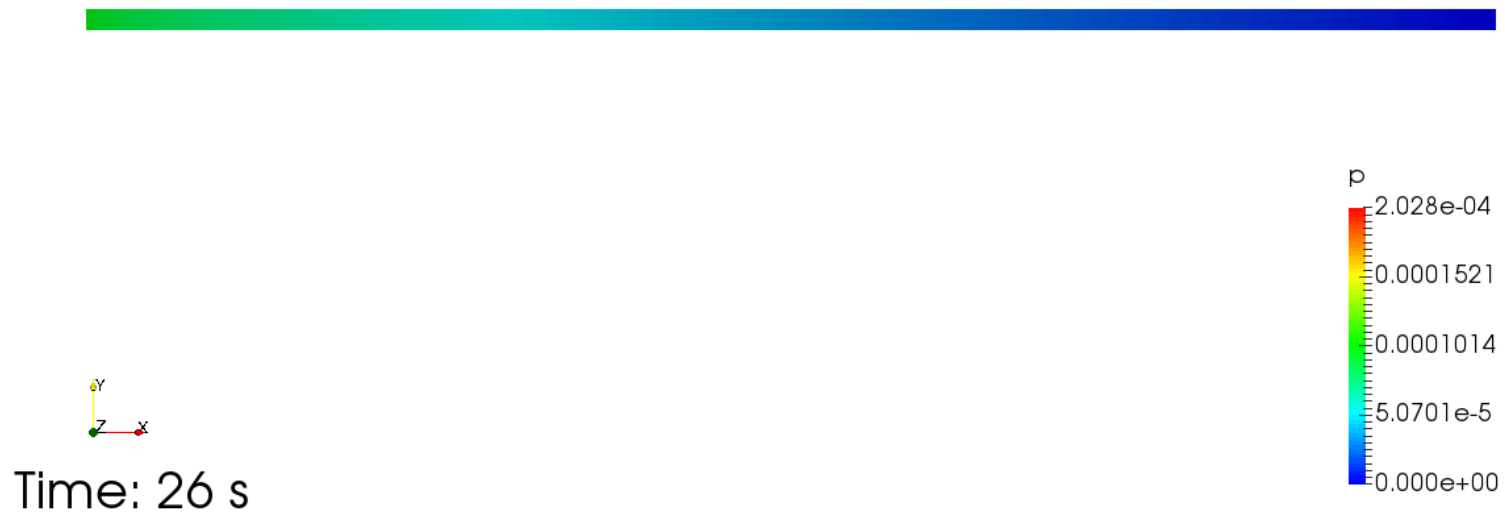


Figure A.4.5. Pressure field along the length of the channel ( $\text{m}^2/\text{s}^2$ ) with non-uniform grid

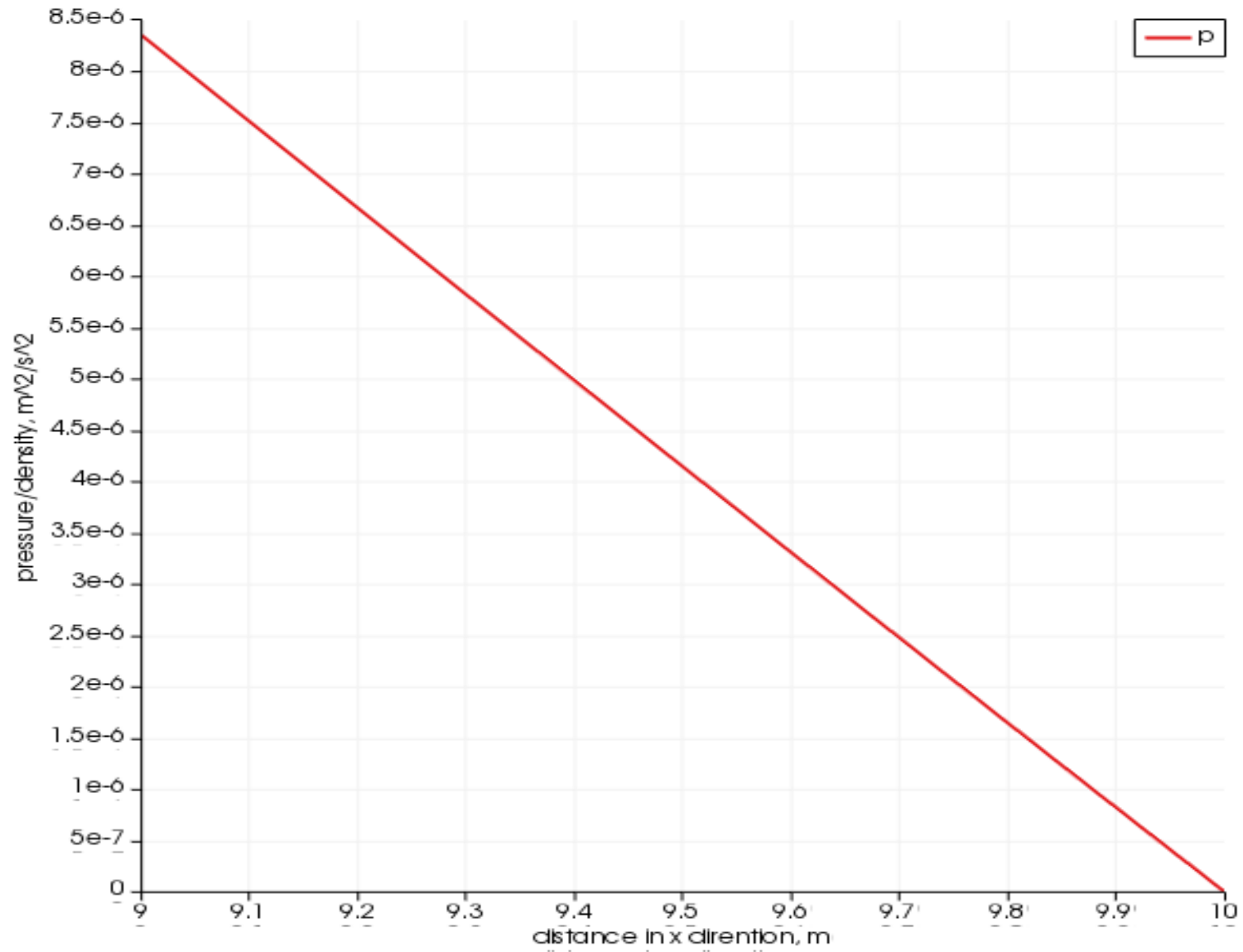
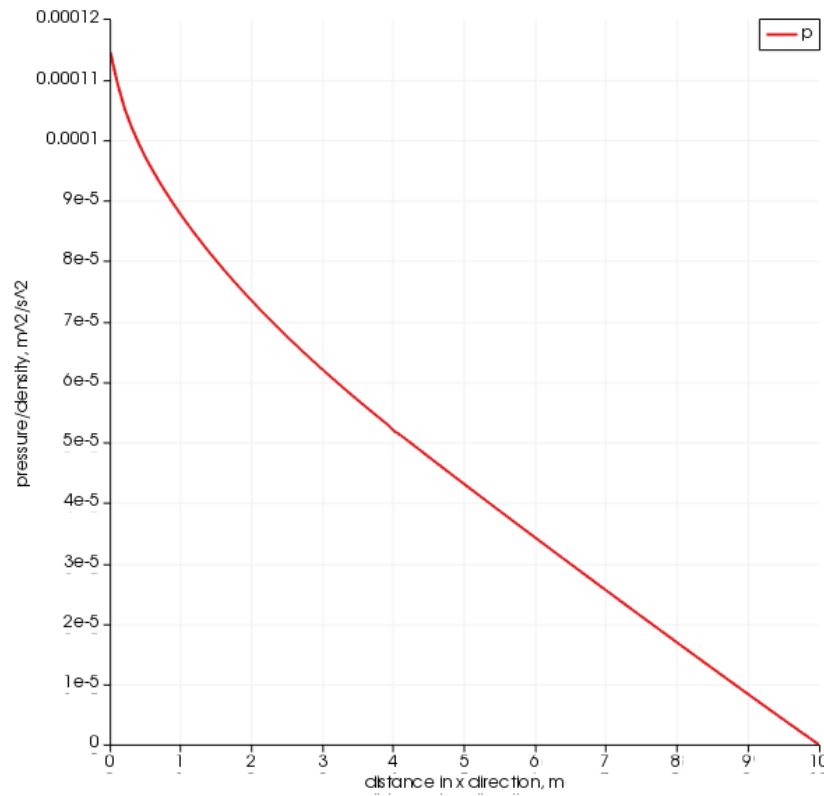
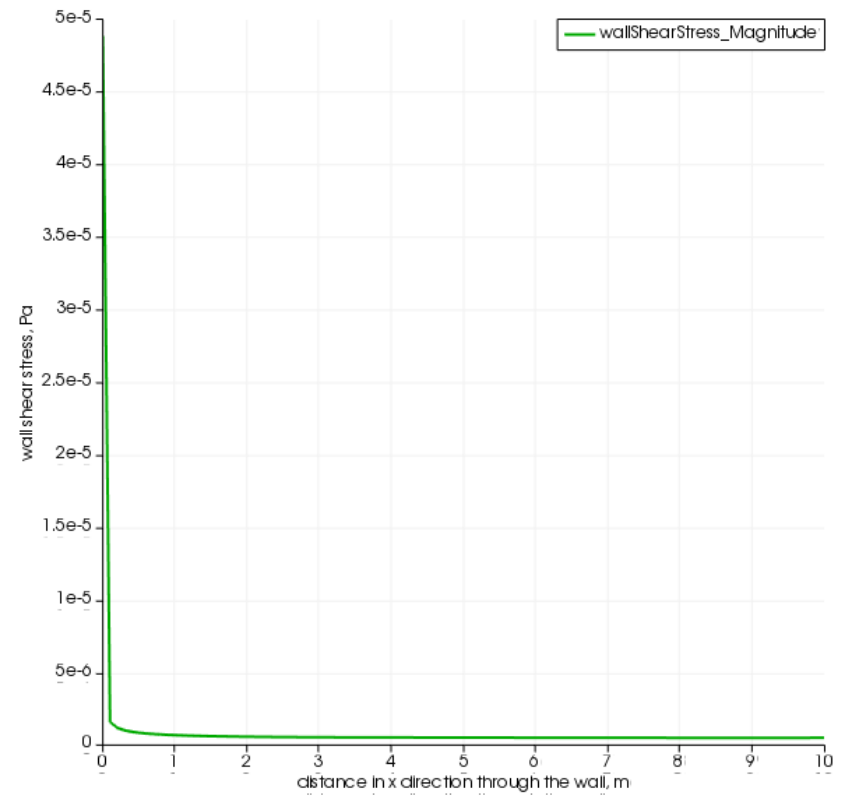


Figure A.4.6. Pressure drop divided by density ( $\text{m}^2/\text{s}^2$ ) along the channel between the axial distances  $x=9$ - $10$  m with non-uniform grid

Pressure drop cannot be computed based on the pressure differences between the inlet pressure and the outlet pressure since the pressure of the domain is non-linear in the region where flow is not fully-developed (Figure A.4.7 (a)). Pressure changes linearly after the entrance length where the velocity profile and the wall shear stress become constant (Figure A.4.7 (b)).



(a)



(b)

Figure A.4.7 (a) Pressure drop divided by density, and (b) wall shear stress between the axial distances  $x=0-10$  m with non-uniform

grid



## APPENDIX B

### GRID INDEPENDENCE TESTS FOR 2-D CHANNEL and 3-D PIPE SIMULATIONS WITH A DEAD-LEG

Following the procedure outline by Celik et al. (2008), the grid independence tests were performed. Typical sample calculations performed using an Excel file are given below for 2-D channel (left column) and 3-D pipe (right column) cases.

Table B.1. Sample calculations related to grid independence tests for 2-D channel (left column) and 3-D pipe (right column) cases

	2-Dimensional		3-Dimensional	
the length of the dead-leg (m)	1.200E+00		5.588E-01	
the length of the horizontal channel (m)	1.092E+01		3.000E+00	
the width of the channel (m)	1.200E-01		5.080E-02	
the area of the geometry (m <sup>2</sup> )	1.454E+00		7.213E-03	
the grid refinement factor	2.000E+00		2.000E+00	
		$U_1$		$U_1$
grid number - coarse	2.950E+04	2.966	8.530E+05	3.999949
grid size - coarse - (m)	9.353E-03		2.037E-03	
grid number - medium	6.650E+04	2.9526	3.864E+06	4
grid size - medium - (m)	4.677E-03		1.019E-03	
grid number - fine	1.496E+05	2.9516	5.906E+06	4.000023
grid size - fine - (m)	2.338E-03		5.093E-04	
		$\epsilon_{32} = U_3 - U_2$		$\epsilon_{32} = U_3 - U_2$
		-0.001		2.3E-05
		$\epsilon_{21} = U_2 - U_1$		$\epsilon_{21} = U_2 - U_1$
		-0.013		5.1E-05
		$\epsilon_{32}/\epsilon_{21}$		$\epsilon_{32}/\epsilon_{21}$
		0.075		0.451
		$s = 1 * \text{Sln}(\epsilon_{32}/\epsilon_{21})$		$s = 1 * \text{Sln}(\epsilon_{32}/\epsilon_{21})$
		1		1
grid refinement factor	$r_{32} = h_3/h_2$	2	grid refinement factor	$r_{32} = h_3/h_2$
grid refinement factor	$r_{21} = h_2/h_1$	2	grid refinement factor	$r_{21} = h_2/h_1$
the order of convergence	$p = \frac{1}{\ln(r_{21})} \left  \ln \left  \frac{\epsilon_{32}}{\epsilon_{21}} \right  + \ln \left( \frac{r_{21}^p - s}{r_{32}^p - s} \right) \right $	3.744	the order of convergence	$p = \frac{1}{\ln(r_{21})} \left  \ln \left  \frac{\epsilon_{32}}{\epsilon_{21}} \right  + \ln \left( \frac{r_{21}^p - s}{r_{32}^p - s} \right) \right $
extrapolated value	$U_{ext}^{32} = (r_{32}^p U_2 - U_3)/(r_{32}^p - 1)$	2.953	extrapolated value	$U_{ext}^{32} = (r_{32}^p U_2 - U_3)/(r_{32}^p - 1)$
extrapolated value	$U_{ext}^{21} = (r_{21}^p U_1 - U_2)/(r_{21}^p - 1)$	2.967	extrapolated value	$U_{ext}^{21} = (r_{21}^p U_1 - U_2)/(r_{21}^p - 1)$
approximate relative error	$e_a^{32} = \left  \frac{U_2 - U_3}{U_2} \right $	0.0003868 0.0386845 %	approximate relative error	$e_a^{32} = \left  \frac{U_2 - U_3}{U_2} \right $
approximate relative error	$e_a^{21} = \left  \frac{U_1 - U_2}{U_1} \right $	0.00451787 0.45178692 %	approximate relative error	$e_a^{21} = \left  \frac{U_1 - U_2}{U_1} \right $
extrapolated relative error	$e_{ext}^{32} = \left  \frac{U_{ext}^{32} - U_2}{U_{ext}^{32}} \right $	0.00488044 0.48804353 %	extrapolated relative error	$e_{ext}^{32} = \left  \frac{U_{ext}^{32} - U_2}{U_{ext}^{32}} \right $
extrapolated relative error	$e_{ext}^{21} = \left  \frac{U_{ext}^{21} - U_1}{U_{ext}^{21}} \right $	0.00451094 0.45109365 %	extrapolated relative error	$e_{ext}^{21} = \left  \frac{U_{ext}^{21} - U_1}{U_{ext}^{21}} \right $
grid convergence index	$GCI_{fine}^{32} = \frac{1.25 e_a^{32}}{r_{32}^p - 1}$	0.00003414 0.00341416 %	grid convergence index	$GCI_{fine}^{32} = \frac{1.25 e_a^{32}}{r_{32}^p - 1}$
1.25 - factor of safety			1.25 - factor of safety	
grid convergence index	$GCI_{fine}^{21} = \frac{1.25 e_a^{21}}{r_{21}^p - 1}$	0.00045543 0.04554304 %	grid convergence index	$GCI_{fine}^{21} = \frac{1.25 e_a^{21}}{r_{21}^p - 1}$
1.25 - factor of safety			1.25 - factor of safety	
estimated fractional error	$E_1$	0.00036434	estimated fractional error	$E_1$
estimated fractional error	$E_2$	0.00488221	estimated fractional error	$E_2$
validation if the solutions are in the asymptotic range of convergence	$GCI^{21} = r^p GCI^{32}$	0.0004575	validation if the solutions are in the asymptotic range of convergence	$GCI^{21} = r^p GCI^{32}$
	$GCI^{21}/r^p GCI^{32}$	0.99548213		$GCI^{21}/r^p GCI^{32}$
				1.0001275



## APPENDIX D

### EVALUATION OF AGITATION OF OIL (CANOLA/VEGETABLE/OLIVE) AND WATER (TAP/DISTILLED/DEIONIZED) SYSTEMS

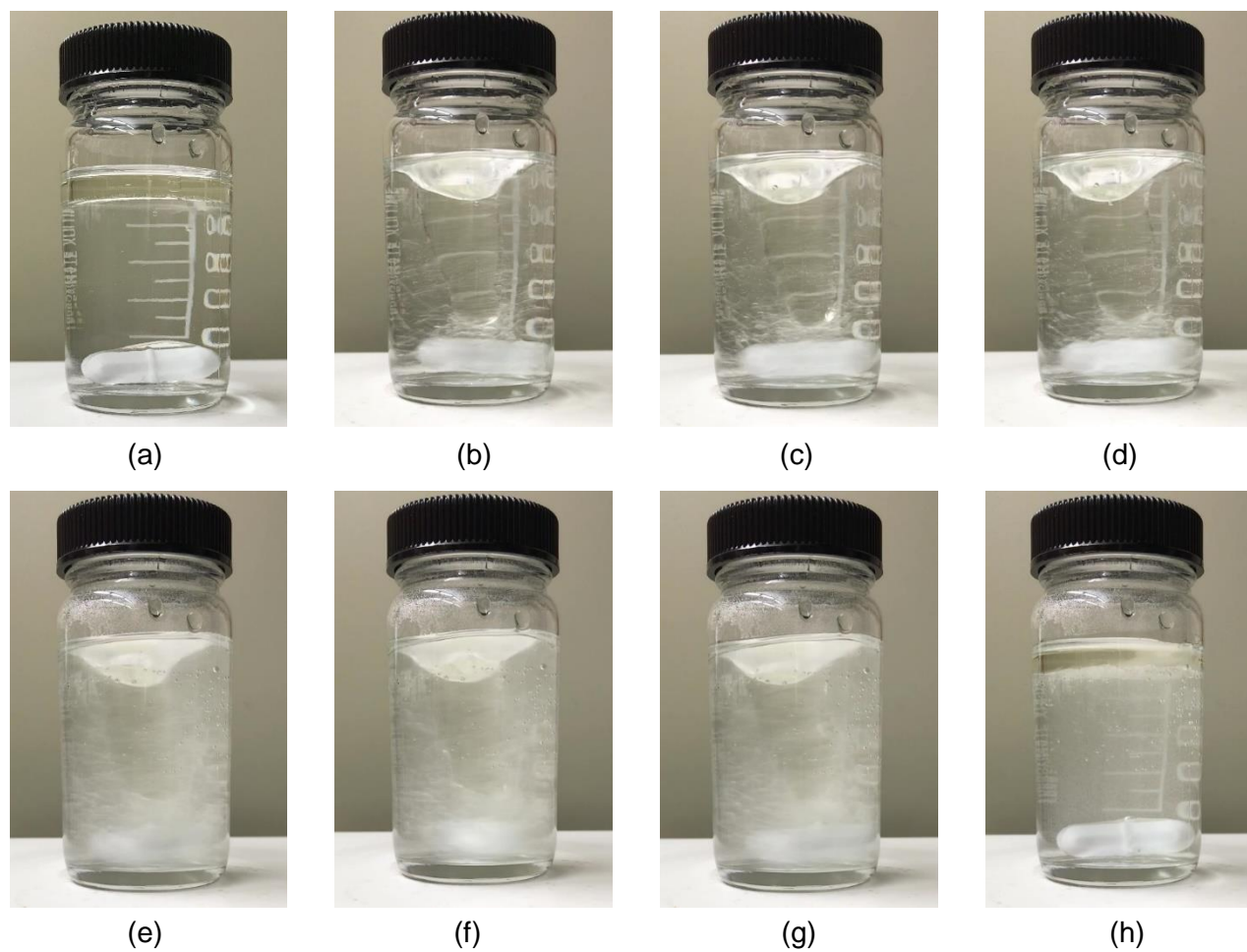


Figure D.1. Photographs of agitated 10% Canola Oil – 90% Tap Water system at various time instants (a) initial, (b) 1 min, (c) 2 min, (d) 3 min, (e) 58 min, (f) 59 min, (g) 60 min and (h) 1 min after the stirring process stops

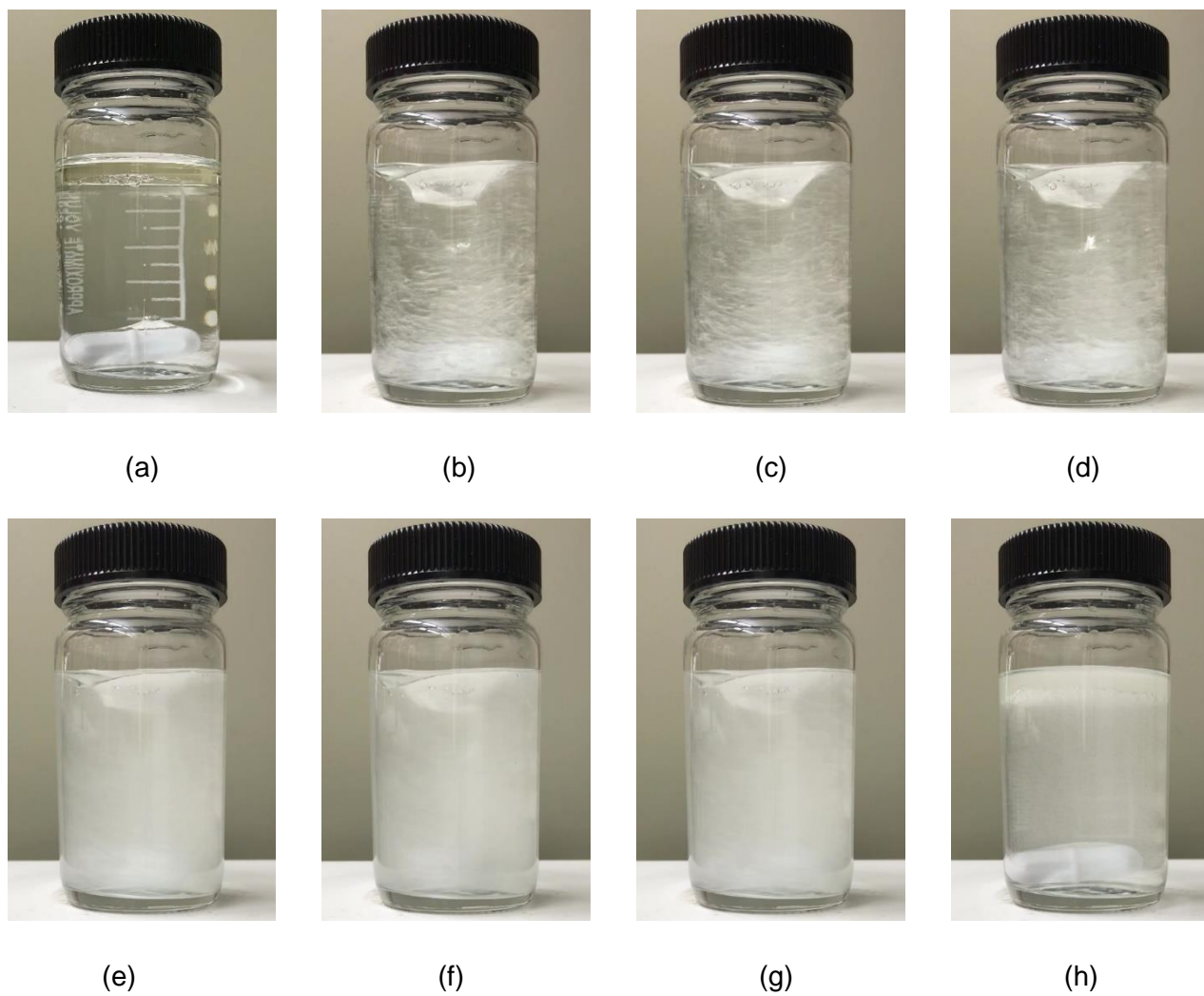


Figure D.2. Photographs of agitated 10% Canola Oil – 90% Deionized Water system at various time instants (a) initial, (b) 1 min, (c) 2 min, (d) 3 min, (e) 58 min, (f) 59 min, (g) 60 min and (h) 1 min after the stirring process stops



(a)



(b)



(c)



(d)



(e)



(f)



(g)



(h)

Figure D.3. Photographs of agitated 10% Canola Oil – 90% Distilled Water system at various time instants (a) initial, (b) 1 min, (c) 2 min, (d) 3 min, (e) 58 min, (f) 59 min, (g) 60 min and (h) 1 min after the stirring process stops



(a)



(b)



(c)



(d)



(e)



(f)



(g)



(h)

Figure D.4. Photographs of agitated 10% Vegetable Oil – 90% Tap Water system at various time instants (a) initial, (b) 1 min, (c) 2 min, (d) 3 min, (e) 58 min, (f) 59 min, (g) 60 min and (h) 1 min after the stirring process stops



(a)



(b)



(c)



(d)



(e)



(f)



(g)



(h)

Figure D.5. Photographs of agitated 10% Vegetable Oil – 90% Deionized Water system at various time instants (a) initial, (b) 1 min, (c) 2 min, (d) 3 min, (e) 58 min, (f) 59 min, (g) 60 min and (h) 1 min after the stirring process stops

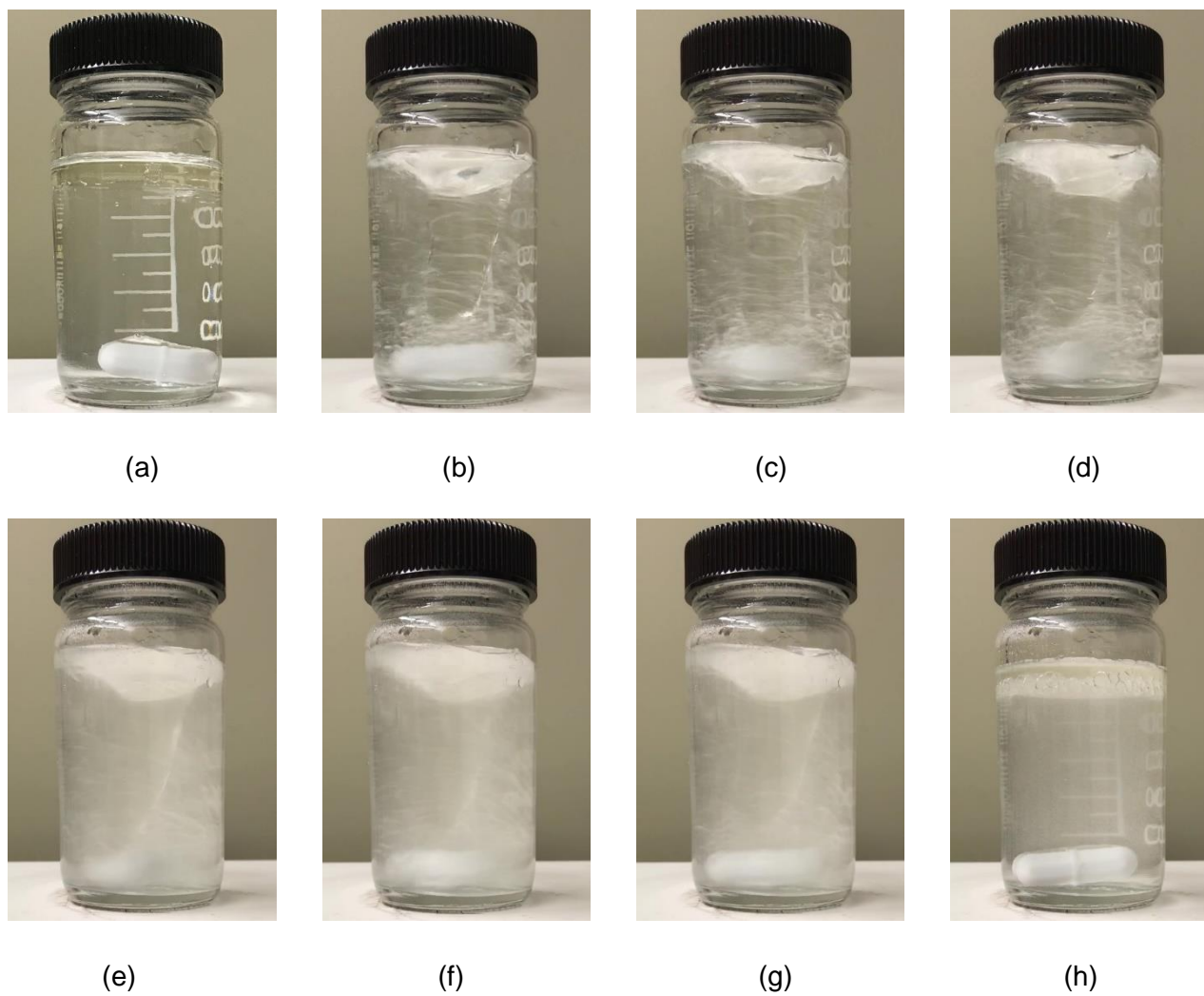


Figure D.6. Photographs of agitated 10% Vegetable Oil – 90% Distilled Water system at various time instants (a) initial, (b) 1 min, (c) 2 min, (d) 3 min, (e) 58 min, (f) 59 min, (g) 60 min and (h) 1 min after the stirring process stops



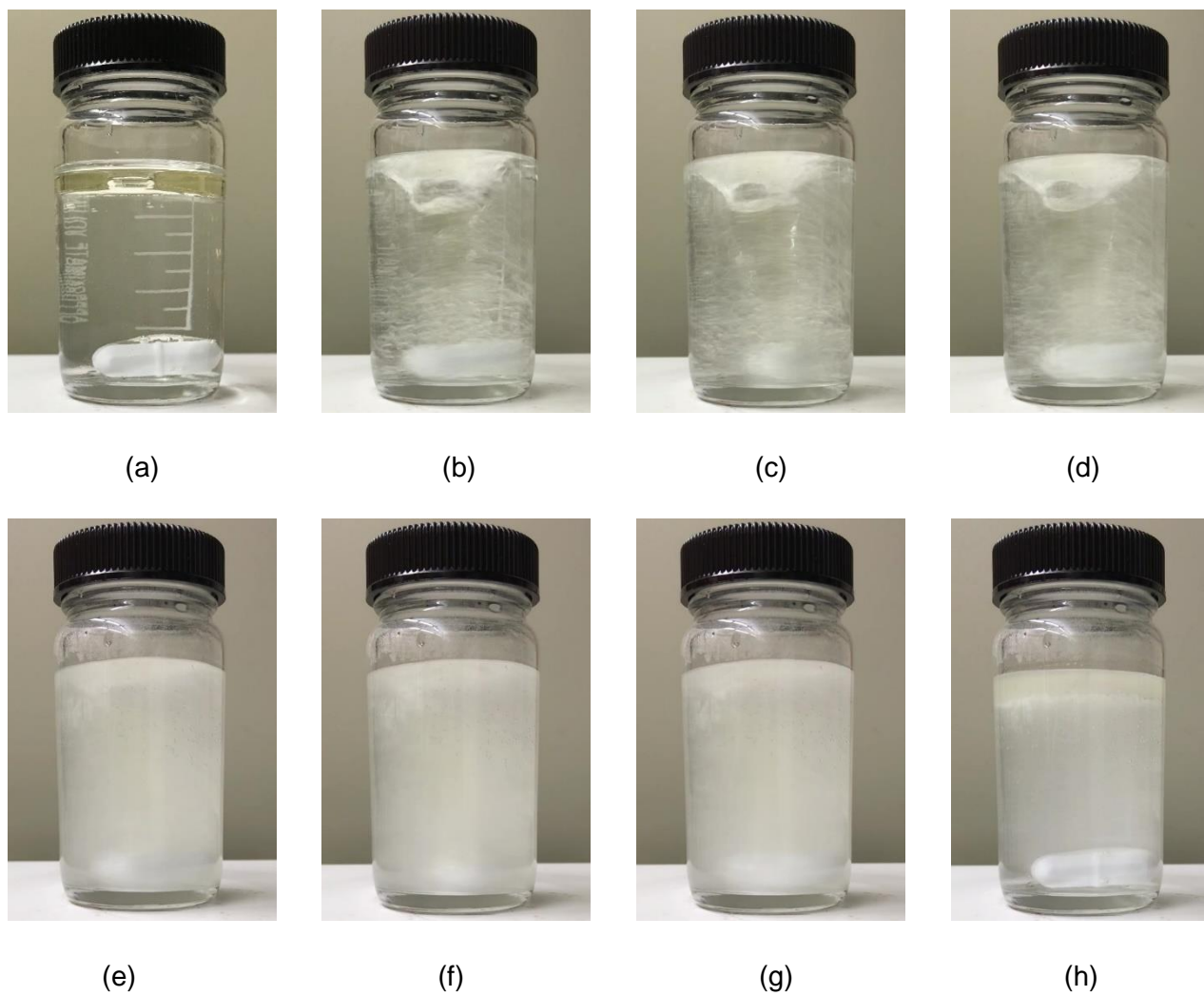


Figure D.7. Photographs of agitated 10% Olive Oil – 90% Tap Water system at various time instants (a) initial, (b) 1 min, (c) 2 min, (d) 3 min, (e) 58 min, (f) 59 min, (g) 60 min and (h) 1 min after the stirring process stops

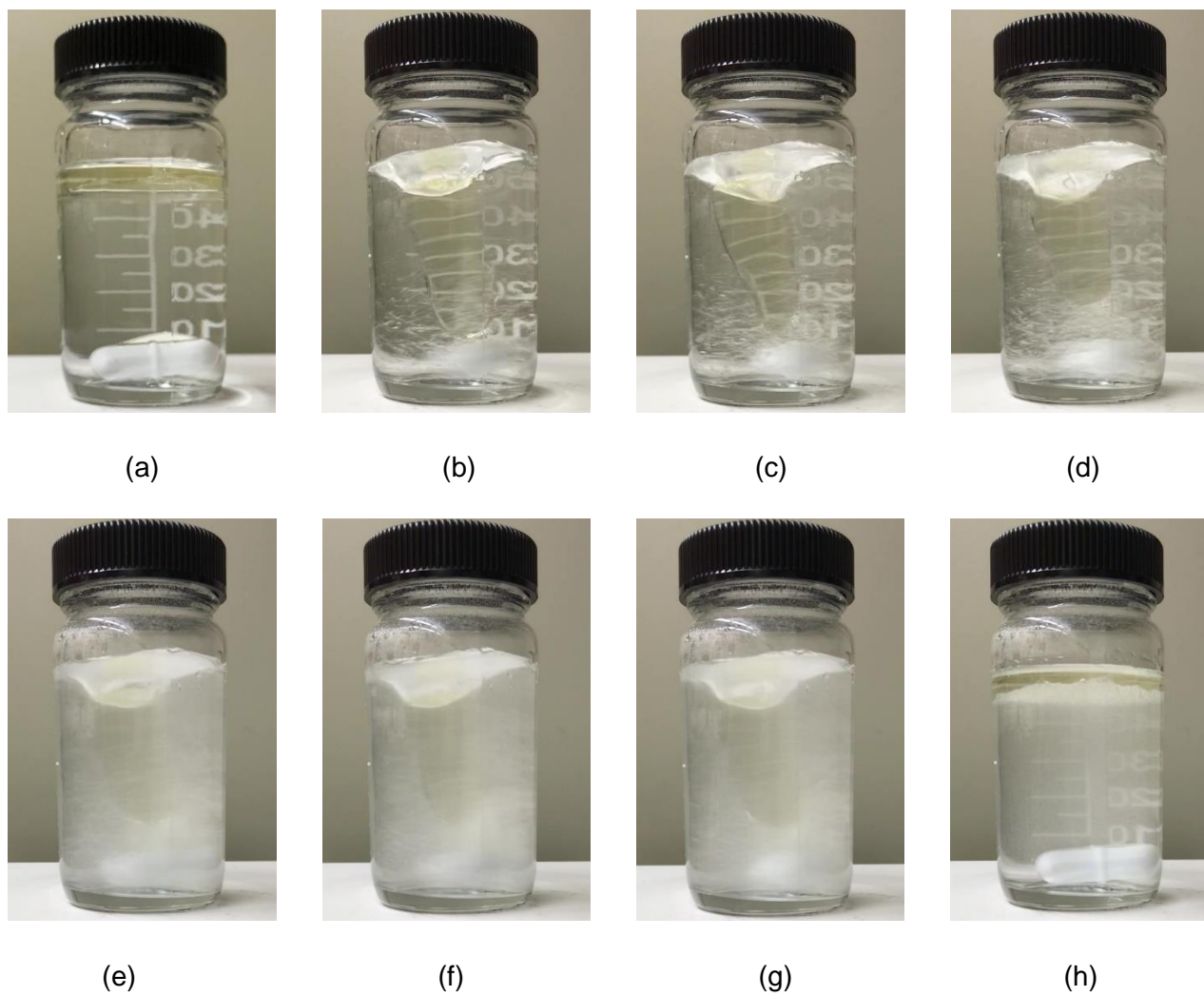


Figure D.8. Photographs of agitated 10% Olive Oil – 90% Deionized Water system at various time instants (a) initial, (b) 1 min, (c) 2 min, (d) 3 min, (e) 58 min, (f) 59 min, (g) 60 min and (h) 1 min after the stirring process stops



(a)



(b)



(c)



(d)



(e)



(f)



(g)



(h)

Figure D.9. Photographs of agitated 10% Olive Oil – 90% Distilled Water system at various time instants (a) initial, (b) 1 min, (c) 2 min, (d) 3 min, (e) 58 min, (f) 59 min, (g) 60 min and (h) 1 min after the stirring process stops

## APPENDIX E

### RAW DATA OF THE OIL ACCUMULATION IN THE DEAD-LEG EXPERIMENTS AND THE DERIVED OIL ACCUMULATION RATES

Going through videos of the experiments, values of the positions of the top and bottom levels of the oil column accumulating within the dead-leg are reported in the Tables E.1-8. For each run, the instantaneous height of the column and the average values are also listed.

Table E.1. Change in height of oil column for the system with 5% olive oil and 90° dead-leg inclination

time (s)	top level (m)				bottom level (m)				height (m)				average m
	run 1	run 2	run 3	run 4	run 1	run 2	run 3	run 4	run 1	run 2	run 3	run 4	
0	0.5207	0.4572	0.4445	0.454819	0.483394	0.415925	0.4064	0.4064	0.037306	0.041275	0.0381	0.048419	0.041275
10	0.484188	0.459581	0.46355	0.461169	0.449263	0.414338	0.42545	0.41275	0.034925	0.045244	0.0381	0.048419	0.041672
20	0.485775	0.467519	0.468313	0.466725	0.446088	0.42545	0.42545	0.417513	0.039688	0.042069	0.042863	0.049213	0.043458
30	0.485775	0.469106	0.471488	0.468313	0.442913	0.42545	0.42545	0.420688	0.042863	0.043656	0.046038	0.047625	0.045045
40	0.484188	0.471488	0.471488	0.4699	0.442913	0.42545	0.42545	0.4191	0.041275	0.046038	0.046038	0.0508	0.046038
50	0.484188	0.474663	0.473075	0.473075	0.441325	0.428625	0.42545	0.420688	0.042863	0.046038	0.047625	0.052388	0.047228
60	0.484188	0.477838	0.475456	0.47625	0.439738	0.428625	0.42545	0.423863	0.04445	0.049213	0.050006	0.052388	0.049014
70	0.485775	0.477838	0.477044	0.477838	0.438944	0.428625	0.42545	0.423863	0.046831	0.049213	0.051594	0.053975	0.050403
80	0.485775	0.481013	0.479425	0.481013	0.435769	0.428625	0.42545	0.42545	0.050006	0.052388	0.053975	0.055563	0.052983
90	0.485775	0.4826	0.481013	0.4826	0.432594	0.428625	0.42545	0.42545	0.053181	0.053975	0.055563	0.05715	0.054967
100	0.485775	0.484188	0.481806	0.485775	0.4318	0.428625	0.42545	0.427038	0.053975	0.055563	0.056356	0.058738	0.056158
110	0.485775	0.485775	0.484981	0.48895	0.430213	0.428625	0.42545	0.427038	0.055563	0.05715	0.059531	0.061913	0.058539
120	0.485775	0.487363	0.484188	0.490538	0.430213	0.428625	0.42545	0.427038	0.055563	0.058738	0.058738	0.0635	0.059134
130	0.485775	0.491331	0.485775	0.490538	0.428625	0.428625	0.42545	0.427038	0.05715	0.062706	0.060325	0.0635	0.06092
140	0.485775	0.493713	0.490538	0.492125	0.427038	0.428625	0.423863	0.427038	0.058738	0.065088	0.066675	0.065088	0.063897
150	0.487363	0.493713	0.492125	0.496888	0.42545	0.428625	0.42545	0.427038	0.061913	0.065088	0.066675	0.06985	0.065881
160	0.487363	0.498475	0.4953	0.500063	0.423863	0.428625	0.42545	0.427038	0.0635	0.06985	0.06985	0.073025	0.069056
170	0.485775	0.500063	0.500063	0.504825	0.417513	0.428625	0.423863	0.427038	0.068262	0.071438	0.0762	0.077788	0.073422
180	0.485775	0.504031	0.498475	0.506413	0.415925	0.430213	0.423863	0.427038	0.06985	0.073819	0.074613	0.079375	0.074414
190	0.48895	0.503238	0.498475	0.507206	0.415925	0.430213	0.423863	0.427038	0.073025	0.073025	0.074613	0.080169	0.075208
200	0.48895	0.504825	0.500063	0.512763	0.415925	0.430213	0.423863	0.427038	0.073025	0.074613	0.0762	0.085725	0.077391
210	0.48895	0.507206	0.503238	0.512763	0.414338	0.430213	0.423863	0.427038	0.074613	0.076994	0.079375	0.085725	0.079177
220	0.48895	0.509588	0.504825	0.513556	0.41275	0.430213	0.423863	0.427038	0.0762	0.079375	0.080963	0.086519	0.080764
230	0.492125	0.511175	0.504825	0.516731	0.41275	0.430213	0.4191	0.42545	0.079375	0.080962	0.085725	0.091281	0.084336
240	0.493713	0.512763	0.508	0.516731	0.409575	0.430213	0.4191	0.42545	0.084138	0.08255	0.0889	0.091281	0.086717
250	0.493713	0.515938	0.509588	0.516731	0.409575	0.430213	0.4191	0.42545	0.084138	0.085725	0.090488	0.091281	0.087908
260	0.4953	0.515144	0.510381	0.522288	0.411163	0.430213	0.4191	0.42545	0.084138	0.084931	0.091281	0.096838	0.089297
270	0.4953	0.516731	0.512763	0.523875	0.408781	0.430213	0.4191	0.42545	0.086519	0.086519	0.093663	0.098425	0.091281
280	0.4953	0.519113	0.512763	0.523875	0.407194	0.430213	0.417513	0.42545	0.088106	0.0889	0.09525	0.098425	0.09267
290	0.4953	0.519113	0.515144	0.525463	0.4064	0.430213	0.417513	0.42545	0.0889	0.0889	0.097631	0.100013	0.093861
300	0.4953	0.522288	0.516731	0.525463	0.405606	0.430213	0.417513	0.42545	0.089694	0.092075	0.099219	0.100013	0.09525
310	0.4953	0.5207	0.516731	0.525463	0.403225	0.430213	0.414338	0.42545	0.092075	0.090487	0.102394	0.100013	0.096242
320	0.496888	0.521494	0.519113	0.525463	0.401638	0.430213	0.414338	0.423863	0.09525	0.091281	0.104775	0.1016	0.098227
330	0.498475	0.522288	0.5207	0.52705	0.40005	0.427038	0.414338	0.423863	0.098425	0.09525	0.106363	0.103188	0.100806
340	0.498475	0.519113	0.521494	0.530225	0.40005	0.427038	0.414338	0.423863	0.098425	0.092075	0.107156	0.106363	0.101005
350	0.498475	0.5207	0.523875	0.5334	0.396875	0.427038	0.414338	0.423863	0.1016	0.093663	0.109538	0.109538	0.103584
360	0.498475	0.527844	0.523875	0.5334	0.396875	0.427038	0.414338	0.423863	0.1016	0.100806	0.109538	0.109538	0.10537
370	0.498475	0.531813	0.523875	0.534988	0.394494	0.427038	0.414338	0.423863	0.103981	0.104775	0.109538	0.111125	0.107355
380	0.500063	0.5334	0.526256	0.536575	0.3937	0.427038	0.414338	0.423863	0.106363	0.106363	0.111919	0.112713	0.109339
390	0.50165	0.531813	0.52705	0.536575	0.392113	0.42545	0.414338	0.420688	0.109538	0.106363	0.112713	0.115888	0.111125
400	0.50165	0.529431	0.52705	0.538163	0.388938	0.42545	0.411163	0.420688	0.112713	0.103981	0.115888	0.117475	0.112514
410	0.504825	0.5334	0.529431	0.538163	0.388938	0.42545	0.411163	0.420688	0.115888	0.10795	0.118269	0.117475	0.114895
420	0.504825	0.537369	0.530225	0.541338	0.388144	0.42545	0.411163	0.420688	0.116681	0.111919	0.119063	0.12065	0.117078
430	0.506413	0.535781	0.530225	0.541338	0.388144	0.42545	0.411163	0.420688	0.118269	0.110331	0.119063	0.12065	0.117078
440	0.506413	0.536575	0.531019	0.541338	0.385763	0.423863	0.411163	0.420688	0.12065	0.112713	0.119856	0.12065	0.118467
450	0.506413	0.538163	0.532606	0.542925	0.38735	0.423863	0.408781	0.420688	0.119063	0.1143	0.123825	0.122238	0.119856
460	0.508	0.542131	0.534988	0.5461	0.385763	0.423863	0.407988	0.420688	0.122238	0.118269	0.127	0.125413	0.12323
470	0.508	0.543719	0.534988	0.5461	0.383381	0.423863	0.407988	0.420688	0.124619	0.119856	0.127	0.125413	0.124222
480	0.509588	0.543719	0.535781	0.5461	0.382588	0.423863	0.407194	0.4191	0.127	0.119856	0.128588	0.127	0.125611
490	0.509588	0.544513	0.538956	0.5461	0.379413	0.423863	0.407194	0.4191	0.130175	0.12065	0.131763	0.127	0.127397
500	0.509588	0.543719	0.538956	0.55245	0.379413	0.423863	0.407194	0.4191	0.130175	0.119856	0.131763	0.13335	0.128786
510	0.509588	0.545306	0.540544	0.555625	0.377825	0.420688	0.407194	0.4191	0.131763	0.124619	0.13335	0.136525	0.131564
520	0.509588	0.5461	0.542131	0.550863	0.375444	0.420688	0.407194	0.4191	0.134144	0.125413	0.134938	0.131763	0.131564
530	0.509588	0.546894	0.542925	0.557213	0.373856	0.4191	0.407988	0.4191	0.135731	0.127794	0.134938	0.138113	0.134144
540	0.509588	0.547688	0.542131	0.555625	0.373063	0.417513	0.407988	0.4191	0.136525	0.130175	0.134144	0.136525	0.134342
550	0.509588	0.550863	0.542925	0.557213	0.369888	0.417513	0.407988	0.417513	0.1397	0.13335	0.134938	0.1397	0.136922
560	0.509588	0.55245	0.546894	0.557213	0.369888	0.417513	0.407988	0.417513	0.1397	0.134938	0.138906	0.1397	0.138311
570	0.509588	0.549275	0.547688	0.5588	0.3683	0.417513	0.407988	0.415925	0.141288	0.131763	0.1397	0.142875	0.138906
580	0.509588	0.550069	0.549275	0.563563	0.3683	0.417513	0.409575	0.415925	0.141288	0.132556	0.1397	0.147638	0.140295
590	0.512763	0.55245	0.546894	0.561975	0.3683	0.417513	0.403225	0.415925	0.144463	0.134938	0.143669	0.14605	0.14228
600	0.512763	0.550863	0.548481	0.561975	0.3683	0.417513	0.403225	0.414338	0.144463	0.13335	0.145256	0.147638	0.142677

Table E.2. Change in height of oil column for the system with 5% olive oil and 60° dead-leg inclination

time (s)	top level (m)				bottom level (m)				height (m)				average m
	run 1	run 2	run 3	run 4	run 1	run 2	run 3	run 4	run 1	run 2	run 3	run 4	
0	0.5207	0.422275	0.409575	0.415131	0.498475	0.384175	0.37465	0.385763	0.022225	0.0381	0.034925	0.029369	0.031155
10	0.50165	0.446088	0.43815	0.45085	0.473075	0.409575	0.398463	0.411163	0.028575	0.036513	0.039688	0.039688	0.036116
20	0.492125	0.454025	0.442913	0.461963	0.460375	0.409575	0.400844	0.420688	0.03175	0.04445	0.042069	0.041275	0.039886
30	0.490538	0.461963	0.449263	0.466725	0.455613	0.4191	0.4064	0.420688	0.034925	0.042863	0.042863	0.046038	0.041672
40	0.484188	0.461963	0.459581	0.473075	0.45085	0.417513	0.41275	0.42545	0.033338	0.04445	0.046831	0.047625	0.043061
50	0.477838	0.466725	0.471488	0.47625	0.441325	0.417513	0.42545	0.42545	0.036513	0.049213	0.046038	0.0508	0.045641
60	0.477838	0.4699	0.480219	0.4826	0.436563	0.422275	0.4318	0.4318	0.041275	0.047625	0.048419	0.0508	0.04703
70	0.474663	0.474663	0.48895	0.485775	0.432594	0.42545	0.442913	0.434975	0.042069	0.049213	0.046038	0.0508	0.04703
80	0.466725	0.479425	0.498475	0.48895	0.424656	0.430213	0.449263	0.43815	0.042069	0.049213	0.049213	0.0508	0.047823
90	0.466725	0.479425	0.504825	0.4953	0.4191	0.430213	0.455613	0.439738	0.047625	0.049213	0.049213	0.055563	0.050403
100	0.465138	0.487363	0.515938	0.50165	0.411956	0.430213	0.461963	0.4445	0.053181	0.05715	0.053975	0.05715	0.055364
110	0.465138	0.492125	0.519113	0.503238	0.411956	0.4318	0.468313	0.4445	0.053181	0.060325	0.0508	0.058738	0.055761
120	0.46355	0.492125	0.525463	0.50165	0.409575	0.4318	0.4699	0.4445	0.053975	0.060325	0.055663	0.05715	0.056753
130	0.460375	0.493713	0.527844	0.505619	0.407988	0.434975	0.4699	0.447675	0.052388	0.058738	0.057944	0.057944	0.056753
140	0.461963	0.500063	0.538163	0.515938	0.404813	0.434975	0.479425	0.455613	0.05715	0.065088	0.058738	0.060325	0.060325
150	0.461169	0.504825	0.541338	0.523081	0.401638	0.439738	0.4826	0.4572	0.059531	0.065088	0.058738	0.065881	0.062309
160	0.461169	0.503238	0.542925	0.523875	0.40005	0.441325	0.4826	0.458788	0.061119	0.061913	0.060325	0.065088	0.062111
170	0.455613	0.508	0.549275	0.526256	0.395288	0.441325	0.484188	0.454025	0.060325	0.066675	0.065088	0.072231	0.06608
180	0.458788	0.511175	0.55245	0.527844	0.390525	0.442913	0.485775	0.458788	0.068262	0.068262	0.066675	0.069056	0.068064
190	0.460375	0.512763	0.554831	0.531813	0.390525	0.446088	0.486569	0.458788	0.06985	0.066675	0.068263	0.073025	0.069453
200	0.460375	0.515938	0.5588	0.531813	0.388144	0.446088	0.492125	0.458788	0.072231	0.06985	0.066675	0.073025	0.070445
210	0.460375	0.519113	0.566738	0.534988	0.386556	0.446088	0.4953	0.458788	0.073819	0.073025	0.071438	0.0762	0.07362
220	0.4572	0.522288	0.56515	0.536575	0.383381	0.446088	0.493713	0.458788	0.073819	0.0762	0.071437	0.077788	0.074811
230	0.4572	0.522288	0.5715	0.536575	0.381	0.447675	0.493713	0.458788	0.0762	0.074613	0.077788	0.077788	0.076597
240	0.4572	0.528638	0.5715	0.536575	0.379413	0.449263	0.4953	0.458788	0.077788	0.079375	0.0762	0.077788	0.077788
250	0.454025	0.52705	0.578644	0.53975	0.375444	0.448469	0.500063	0.459581	0.078581	0.078581	0.078581	0.080169	0.078978
260	0.454025	0.525463	0.57785	0.541338	0.37465	0.448469	0.500063	0.458788	0.079375	0.076994	0.077788	0.08255	0.079177
270	0.454025	0.530225	0.581025	0.542925	0.373063	0.450056	0.500063	0.460375	0.080963	0.080169	0.080963	0.08255	0.081161
280	0.452438	0.530225	0.585788	0.5461	0.3683	0.45085	0.504825	0.460375	0.084138	0.079375	0.080963	0.085725	0.08255
290	0.45085	0.530225	0.587375	0.55245	0.365919	0.45085	0.504825	0.461963	0.084931	0.079375	0.08255	0.090488	0.084336
300	0.45085	0.534988	0.59055	0.55245	0.365919	0.452438	0.506413	0.461963	0.084931	0.08255	0.084138	0.090488	0.085527
310	0.45085	0.530225	0.592138	0.555625	0.363538	0.449263	0.506413	0.461963	0.087313	0.080962	0.085725	0.093662	0.086916
320	0.45085	0.536575	0.5969	0.554038	0.365125	0.449263	0.511175	0.461963	0.085725	0.087313	0.085725	0.092075	0.087709
330	0.441325	0.538163	0.5969	0.555625	0.352425	0.45085	0.508	0.461963	0.0889	0.087313	0.0889	0.093662	0.089694
340	0.4445	0.541338	0.597694	0.557213	0.352425	0.449263	0.508	0.461963	0.092075	0.092075	0.089694	0.09525	0.092273
350	0.4445	0.542925	0.601663	0.5588	0.353219	0.45085	0.509588	0.461963	0.091281	0.092075	0.092075	0.096838	0.093067
360	0.442913	0.543719	0.60325	0.563563	0.352425	0.449263	0.509588	0.461963	0.090488	0.094456	0.093663	0.1016	0.095052
370	0.4445	0.544513	0.604838	0.56515	0.352425	0.45085	0.510381	0.461963	0.092075	0.093663	0.094456	0.103188	0.095845
380	0.4445	0.544513	0.604838	0.564356	0.351631	0.45085	0.509588	0.46355	0.092869	0.093663	0.09525	0.100806	0.095647
390	0.4445	0.549275	0.606425	0.563563	0.347663	0.45085	0.508	0.460375	0.096838	0.098425	0.098425	0.103188	0.099219
400	0.4445	0.549275	0.608013	0.566738	0.347663	0.45085	0.509588	0.46355	0.096838	0.098425	0.098425	0.103188	0.099219
410	0.4445	0.549275	0.6096	0.569913	0.347663	0.452438	0.508	0.46355	0.096838	0.096838	0.1016	0.106363	0.100409
420	0.4445	0.555625	0.612775	0.569119	0.346869	0.452438	0.509588	0.46355	0.097631	0.103188	0.103188	0.105569	0.102394
430	0.4445	0.555625	0.612775	0.570706	0.346869	0.452438	0.509588	0.460375	0.097631	0.103188	0.103188	0.110331	0.103584
440	0.4445	0.555625	0.614363	0.580231	0.346075	0.452438	0.509588	0.4699	0.098425	0.103188	0.104775	0.110331	0.10418
450	0.4445	0.557213	0.61595	0.581025	0.3429	0.452438	0.508	0.4699	0.1016	0.104775	0.10795	0.111125	0.106363
460	0.4445	0.557213	0.61595	0.574675	0.341313	0.454025	0.508	0.461963	0.103188	0.103188	0.10795	0.112713	0.106759
470	0.45085	0.560388	0.61595	0.576263	0.341313	0.452438	0.508	0.46355	0.109538	0.10795	0.10795	0.112713	0.109538
480	0.446088	0.561975	0.61595	0.581025	0.339725	0.454025	0.508	0.46355	0.106363	0.10795	0.10795	0.117475	0.109934
490	0.446088	0.560388	0.617538	0.57785	0.338138	0.452438	0.509588	0.461963	0.10795	0.10795	0.10795	0.115888	0.109934
500	0.446088	0.560388	0.61595	0.57785	0.338138	0.452438	0.507206	0.46355	0.10795	0.10795	0.108744	0.1143	0.109736
510	0.446088	0.56515	0.61595	0.57785	0.33655	0.454025	0.508	0.46355	0.109538	0.111125	0.10795	0.1143	0.110728
520	0.446088	0.56515	0.618331	0.579438	0.33655	0.452438	0.506413	0.46355	0.109538	0.112713	0.111919	0.115888	0.112514
530	0.446088	0.5715	0.617538	0.581025	0.33655	0.452438	0.504825	0.46355	0.109538	0.119063	0.112713	0.117475	0.114697
540	0.449263	0.5715	0.617538	0.5842	0.333375	0.452438	0.503238	0.46355	0.115888	0.119063	0.1143	0.12065	0.117475
550	0.449263	0.5715	0.617538	0.5842	0.333375	0.452438	0.504825	0.46355	0.115888	0.119063	0.112713	0.12065	0.117078
560	0.447675	0.5715	0.617538	0.588963	0.328613	0.45085	0.504825	0.46355	0.119063	0.12065	0.112713	0.125413	0.119459
570	0.447675	0.5715	0.620713	0.593725	0.328613	0.45085	0.504825	0.46355	0.119063	0.12065	0.115888	0.130175	0.121444
580	0.447675	0.5715	0.623888	0.59055	0.328613	0.453231	0.503238	0.46355	0.119063	0.118269	0.12065	0.127	0.121245
590	0.449263	0.5715	0.623888	0.592138	0.328613	0.45085	0.503238	0.46355	0.12065	0.12065	0.12065	0.128588	0.122634
600	0.45085	0.5715	0.623888	0.600075	0.328613	0.45085	0.503238	0.46355	0.122238	0.12065	0.12065	0.136525	0.125016

Table E.3. Change in height of oil column for the system with 5% olive oil and 45° dead-leg inclination

time (s)	top level (m)				bottom level (m)				height (m)				average m
	run 1	run 2	run 3	run 4	run 1	run 2	run 3	run 4	run 1	run 2	run 3	run 4	
0	0.420688	0.42545	0.442913	0.422275	0.385763	0.390525	0.407988	0.384175	0.034925	0.034925	0.034925	0.0381	0.035719
10	0.436563	0.434975	0.466725	0.455613	0.398463	0.398463	0.427038	0.41275	0.0381	0.036513	0.039688	0.042863	0.039291
20	0.4445	0.4445	0.479425	0.466725	0.4064	0.4064	0.441325	0.423863	0.0381	0.0381	0.0381	0.042863	0.039291
30	0.455613	0.452438	0.492125	0.474663	0.414338	0.409575	0.45085	0.4318	0.041275	0.042863	0.041275	0.042863	0.042069
40	0.461963	0.458788	0.500063	0.479425	0.414338	0.415925	0.4572	0.433388	0.047625	0.042863	0.042863	0.046038	0.044847
50	0.466725	0.465138	0.508	0.48895	0.420688	0.4191	0.46355	0.43815	0.046038	0.046038	0.04445	0.0508	0.046831
60	0.466725	0.471488	0.517525	0.4953	0.4191	0.4191	0.466725	0.441325	0.047625	0.052388	0.0508	0.053975	0.051197
70	0.4699	0.47625	0.5207	0.498475	0.420688	0.420688	0.468313	0.4445	0.049213	0.055563	0.052388	0.053975	0.052784
80	0.477838	0.477838	0.528638	0.50165	0.423863	0.422275	0.471488	0.446088	0.053975	0.055563	0.05715	0.055563	0.055563
90	0.479425	0.487363	0.531813	0.503238	0.424656	0.427038	0.473075	0.446088	0.054769	0.060325	0.058738	0.05715	0.057745
100	0.48895	0.490538	0.53975	0.511175	0.428625	0.427038	0.477838	0.449263	0.060325	0.0635	0.061913	0.061912	0.061913
110	0.487363	0.492125	0.542925	0.51435	0.428625	0.428625	0.481013	0.449263	0.058738	0.0635	0.061913	0.065088	0.062309
120	0.492125	0.498475	0.550863	0.517525	0.430213	0.428625	0.484188	0.449263	0.061913	0.06985	0.066675	0.068263	0.066675
130	0.493713	0.50165	0.550863	0.519113	0.430213	0.428625	0.484188	0.452438	0.0635	0.073025	0.066675	0.066675	0.067469
140	0.50165	0.504825	0.554038	0.525463	0.4318	0.433388	0.485775	0.454025	0.06985	0.071438	0.068263	0.071438	0.070247
150	0.504825	0.506413	0.5588	0.528638	0.433388	0.433388	0.492125	0.454025	0.071438	0.073025	0.066675	0.074613	0.071438
160	0.506413	0.511175	0.560388	0.531813	0.434975	0.433388	0.492125	0.455613	0.071437	0.077788	0.068262	0.0762	0.073422
170	0.508	0.515938	0.566738	0.536575	0.434975	0.433388	0.4953	0.460375	0.073025	0.08255	0.071438	0.0762	0.075803
180	0.511175	0.519113	0.569913	0.538163	0.434975	0.436563	0.4953	0.458788	0.0762	0.08255	0.074613	0.079375	0.078184
190	0.51435	0.519113	0.573881	0.541338	0.43815	0.436563	0.498475	0.459581	0.0762	0.08255	0.075406	0.081756	0.078978
200	0.519113	0.525463	0.579438	0.542925	0.439738	0.43815	0.504825	0.461963	0.079375	0.087313	0.074613	0.080963	0.080568
210	0.522288	0.52705	0.581025	0.5461	0.439738	0.43815	0.506413	0.465138	0.08255	0.0889	0.074613	0.080963	0.081756
220	0.523875	0.530225	0.579438	0.55245	0.439738	0.43815	0.506413	0.466725	0.084138	0.092075	0.073025	0.085725	0.083741
230	0.52705	0.5334	0.5842	0.555625	0.442913	0.439738	0.511175	0.466725	0.084138	0.093663	0.073025	0.0889	0.084931
240	0.530225	0.536575	0.587375	0.557213	0.4445	0.441325	0.506413	0.468313	0.085725	0.09525	0.080963	0.0889	0.087709
250	0.531813	0.536575	0.585788	0.561975	0.4445	0.441325	0.508	0.468313	0.087313	0.09525	0.077788	0.093663	0.088503
260	0.534988	0.536575	0.593725	0.563563	0.446088	0.441325	0.509588	0.469106	0.0889	0.09525	0.084138	0.094456	0.090686
270	0.536575	0.541338	0.595313	0.56515	0.446088	0.441325	0.511175	0.4699	0.090488	0.100013	0.084138	0.09525	0.092472
280	0.541338	0.542925	0.595313	0.568325	0.447675	0.442913	0.511175	0.4699	0.093663	0.100013	0.084138	0.098425	0.094059
290	0.541338	0.544513	0.595313	0.5715	0.446088	0.442913	0.511175	0.471488	0.09525	0.1016	0.084138	0.100013	0.09525
300	0.544513	0.5461	0.5969	0.5715	0.447675	0.441325	0.511175	0.471488	0.096838	0.104775	0.085725	0.100013	0.096838
310	0.5461	0.549275	0.600075	0.5715	0.447675	0.442913	0.513556	0.471488	0.098425	0.106363	0.086519	0.100013	0.09783
320	0.546894	0.549275	0.601663	0.573088	0.449263	0.441325	0.512763	0.473075	0.097631	0.10795	0.0889	0.100013	0.098623
330	0.550863	0.555625	0.605631	0.573881	0.45085	0.442913	0.51435	0.473075	0.100013	0.112713	0.091281	0.100806	0.101203
340	0.550863	0.5588	0.608013	0.574675	0.45085	0.4445	0.51435	0.473075	0.100013	0.1143	0.093663	0.1016	0.102394
350	0.550863	0.5588	0.606425	0.576263	0.45085	0.446088	0.51435	0.473075	0.100013	0.112713	0.092075	0.103188	0.101997
360	0.555625	0.561975	0.610394	0.576263	0.45085	0.446088	0.51435	0.471488	0.104775	0.115888	0.096044	0.104775	0.10537
370	0.556419	0.563563	0.611188	0.581025	0.454025	0.446088	0.51435	0.473075	0.102394	0.117475	0.096838	0.10795	0.106164
380	0.561181	0.563563	0.608013	0.5842	0.455613	0.446088	0.511175	0.473075	0.105569	0.117475	0.096838	0.111125	0.107752
390	0.561975	0.56515	0.608013	0.5842	0.458788	0.446088	0.511175	0.471488	0.103188	0.119063	0.096838	0.112713	0.10795
400	0.56515	0.56515	0.608013	0.5842	0.458788	0.446088	0.511175	0.471488	0.106363	0.119063	0.096838	0.112713	0.108744
410	0.56515	0.566738	0.612775	0.586581	0.458788	0.446088	0.512763	0.471488	0.106363	0.12065	0.100013	0.115094	0.11053
420	0.566738	0.566738	0.611188	0.582613	0.458788	0.446088	0.511175	0.473075	0.10795	0.12065	0.100013	0.109538	0.109538
430	0.5715	0.573088	0.614363	0.5842	0.458788	0.446088	0.511175	0.473075	0.112713	0.12	0.103188	0.111125	0.113506
440	0.573088	0.5715	0.617538	0.585788	0.458788	0.446088	0.512763	0.471488	0.1143	0.125413	0.104775	0.1143	0.114697
450	0.573088	0.576263	0.619125	0.587375	0.458788	0.446088	0.515938	0.471488	0.1143	0.130175	0.103188	0.115888	0.115888
460	0.573088	0.57785	0.614363	0.585788	0.460375	0.446088	0.511175	0.471488	0.112713	0.131763	0.103188	0.1143	0.115491
470	0.574675	0.576263	0.618331	0.585788	0.460375	0.446088	0.511175	0.471488	0.1143	0.130175	0.107156	0.1143	0.116483
480	0.57785	0.57785	0.620713	0.59055	0.460375	0.446088	0.515938	0.473075	0.117475	0.131763	0.104775	0.117475	0.117872
490	0.579438	0.57785	0.6223	0.59055	0.461963	0.446088	0.515938	0.472281	0.117475	0.131763	0.106363	0.118269	0.118467
500	0.576263	0.57785	0.61595	0.593725	0.461963	0.446088	0.508	0.4699	0.1143	0.131763	0.10795	0.123825	0.119459
510	0.577056	0.57785	0.6223	0.59055	0.461963	0.446088	0.512763	0.4699	0.115094	0.131763	0.109538	0.12065	0.119261
520	0.579438	0.57785	0.62865	0.59055	0.461963	0.446088	0.512763	0.4699	0.117475	0.131763	0.115888	0.12065	0.121444
530	0.581025	0.579438	0.62865	0.597694	0.461963	0.446088	0.512763	0.471488	0.119063	0.13335	0.115888	0.126206	0.123627
540	0.581025	0.579438	0.62865	0.600075	0.461963	0.446088	0.512763	0.471488	0.119063	0.13335	0.115888	0.128588	0.124222
550	0.585788	0.582613	0.630238	0.600075	0.461963	0.446088	0.512763	0.471488	0.123825	0.136525	0.117475	0.128588	0.126603
560	0.585788	0.585788	0.625475	0.600075	0.461963	0.446088	0.511175	0.4699	0.123825	0.1397	0.1143	0.130175	0.127
570	0.585788	0.585788	0.62865	0.600075	0.461963	0.446088	0.511175	0.4699	0.123825	0.1397	0.117475	0.130175	0.127794
580	0.59055	0.59055	0.62865	0.601663	0.461963	0.446088	0.511175	0.4699	0.128588	0.144463	0.117475	0.131763	0.130572
590	0.587375	0.59055	0.62865	0.600075	0.461963	0.446088	0.511175	0.4699	0.125413	0.144463	0.117475	0.130175	0.129381
600	0.588963	0.59055	0.62865	0.60325	0.461963	0.446088	0.511175	0.4699	0.127	0.144463	0.117475	0.13335	0.130572

Table E.4. Change in height of oil column for the system with 5% olive oil and 30° dead-leg inclination

time (s)	top level (m)				bottom level (m)				height (m)				average m
	run 1	run 2	run 3	run 4	run 1	run 2	run 3	run 4	run 1	run 2	run 3	run 4	
0	0.4953	0.47625	0.48895	0.474663	0.447675	0.433388	0.442913	0.428625	0.047625	0.042863	0.046038	0.046038	0.045641
10	0.503238	0.491331	0.490538	0.477838	0.455613	0.447675	0.4445	0.4318	0.047625	0.043656	0.046038	0.046038	0.045839
20	0.508	0.500063	0.498475	0.484188	0.460375	0.454025	0.449263	0.430213	0.047625	0.046038	0.049213	0.053975	0.049213
30	0.51435	0.504825	0.504031	0.492125	0.461963	0.454025	0.45085	0.43815	0.052388	0.0508	0.053181	0.053975	0.052586
40	0.519113	0.511175	0.509588	0.498475	0.461963	0.454025	0.455613	0.43815	0.05715	0.05715	0.053975	0.060325	0.05715
50	0.521494	0.519113	0.51435	0.500063	0.46355	0.4572	0.458788	0.441325	0.057944	0.061913	0.055563	0.058738	0.058539
60	0.52705	0.5207	0.5207	0.50165	0.46355	0.4572	0.459581	0.441325	0.0635	0.0635	0.061119	0.060325	0.062111
70	0.52705	0.523081	0.525463	0.504825	0.46355	0.460375	0.461169	0.442913	0.0635	0.062706	0.064294	0.061913	0.063103
80	0.528638	0.528638	0.530225	0.504825	0.46355	0.460375	0.461169	0.4445	0.065088	0.068263	0.069056	0.060325	0.065683
90	0.530225	0.531019	0.531813	0.508	0.46355	0.461963	0.46355	0.441328	0.066675	0.069056	0.068263	0.066672	0.067667
100	0.534988	0.534988	0.5334	0.516731	0.46355	0.461169	0.46355	0.45085	0.071438	0.073819	0.06985	0.065881	0.070247
110	0.535781	0.538163	0.538956	0.517525	0.46355	0.461963	0.46355	0.45085	0.072231	0.0762	0.075406	0.066675	0.072628
120	0.538163	0.541338	0.542131	0.519113	0.46355	0.461963	0.468313	0.45085	0.074613	0.079375	0.073819	0.068263	0.074017
130	0.538163	0.542131	0.544513	0.522288	0.46355	0.462756	0.468313	0.452438	0.074613	0.079375	0.0762	0.06985	0.075009
140	0.547688	0.544513	0.547688	0.52705	0.46355	0.46355	0.466725	0.452438	0.084138	0.080963	0.080963	0.074613	0.080169
150	0.5461	0.550863	0.549275	0.529431	0.46355	0.465138	0.4699	0.450056	0.08255	0.085725	0.079375	0.079375	0.081756
160	0.547688	0.550863	0.550863	0.531813	0.46355	0.465138	0.466725	0.45085	0.084138	0.085725	0.084138	0.080963	0.083741
170	0.55245	0.557213	0.553244	0.534988	0.46355	0.465138	0.474663	0.451644	0.0889	0.092075	0.078581	0.083344	0.085725
180	0.554038	0.557213	0.5588	0.534988	0.46355	0.46355	0.477044	0.454025	0.090488	0.093663	0.081756	0.080963	0.086717
190	0.554038	0.5588	0.563563	0.538163	0.46355	0.466725	0.47625	0.452438	0.090488	0.092075	0.087313	0.085725	0.0889
200	0.557213	0.559594	0.568325	0.541338	0.46355	0.466725	0.47625	0.452438	0.093663	0.092869	0.092075	0.0889	0.091877
210	0.557213	0.563563	0.570706	0.542925	0.46355	0.465138	0.477838	0.452438	0.093663	0.098425	0.092869	0.090488	0.093861
220	0.5588	0.56515	0.573088	0.5461	0.46355	0.467519	0.477838	0.452438	0.09525	0.097631	0.09525	0.093663	0.095448
230	0.560388	0.568325	0.573088	0.5461	0.46355	0.467519	0.479425	0.452438	0.096838	0.100806	0.093663	0.093663	0.096242
240	0.561975	0.573088	0.57785	0.548481	0.46355	0.471488	0.477838	0.454025	0.098425	0.1016	0.100013	0.094456	0.098623
250	0.564356	0.576263	0.57785	0.548481	0.46355	0.4699	0.477838	0.452438	0.100806	0.106363	0.100013	0.096044	0.100806
260	0.560388	0.579438	0.582613	0.550069	0.461963	0.4699	0.481013	0.454025	0.098425	0.109538	0.1016	0.096044	0.101402
270	0.56515	0.5842	0.579438	0.55245	0.458788	0.473075	0.481013	0.452438	0.106363	0.111125	0.098425	0.100013	0.103981
280	0.566738	0.5842	0.582613	0.554038	0.4572	0.473075	0.481013	0.452438	0.109538	0.111125	0.1016	0.1016	0.105966
290	0.566738	0.5842	0.5842	0.554038	0.4572	0.474663	0.47625	0.452438	0.109538	0.109538	0.10795	0.1016	0.107156
300	0.568325	0.588963	0.5842	0.5588	0.45085	0.475456	0.477044	0.452438	0.117475	0.113506	0.107156	0.106363	0.111125
310	0.567531	0.59055	0.587375	0.564356	0.452438	0.475456	0.477044	0.454025	0.115094	0.115094	0.110331	0.110331	0.112713
320	0.569913	0.59055	0.588169	0.5588	0.452438	0.47625	0.481013	0.452438	0.117475	0.1143	0.107156	0.106363	0.111323
330	0.569913	0.594519	0.588169	0.563563	0.452438	0.479425	0.480219	0.452438	0.117475	0.115094	0.10795	0.111125	0.112911
340	0.573088	0.5969	0.591344	0.563563	0.4572	0.477838	0.479425	0.452438	0.115888	0.119063	0.111919	0.111125	0.114498
350	0.573088	0.595313	0.595313	0.56515	0.452438	0.477838	0.480219	0.454025	0.12065	0.117475	0.115094	0.111125	0.116086
360	0.57785	0.600075	0.592931	0.566738	0.454025	0.477838	0.480219	0.454025	0.123825	0.122238	0.112713	0.112713	0.117872
370	0.574675	0.600075	0.597694	0.569913	0.454819	0.477838	0.480219	0.452438	0.119856	0.122238	0.117475	0.117475	0.119261
380	0.579438	0.601663	0.600075	0.569119	0.449263	0.477838	0.480219	0.45085	0.130175	0.123825	0.119856	0.118269	0.123031
390	0.579438	0.601663	0.5969	0.5715	0.449263	0.477838	0.47625	0.449263	0.130175	0.123825	0.12065	0.122238	0.124222
400	0.581025	0.602456	0.601663	0.573088	0.446088	0.477838	0.478631	0.45085	0.134938	0.124619	0.123031	0.122238	0.126206
410	0.579438	0.60325	0.598488	0.573088	0.446088	0.479425	0.475456	0.449263	0.13335	0.123825	0.123031	0.123825	0.126008
420	0.582613	0.606425	0.60325	0.574675	0.446088	0.477838	0.475456	0.449263	0.136525	0.128588	0.127794	0.125413	0.12958
430	0.579438	0.608013	0.604838	0.574675	0.446088	0.477838	0.475456	0.449263	0.13335	0.130175	0.129381	0.125413	0.12958
440	0.582613	0.6096	0.60325	0.576263	0.4445	0.477838	0.475456	0.447675	0.138113	0.131763	0.127794	0.128588	0.131564
450	0.582613	0.612775	0.604044	0.579438	0.442913	0.47625	0.475456	0.447675	0.1397	0.136525	0.128588	0.131763	0.134144
460	0.583406	0.612775	0.60325	0.579438	0.441325	0.47625	0.474663	0.447675	0.142081	0.136525	0.128588	0.131763	0.134739
470	0.588963	0.614363	0.604838	0.57785	0.441325	0.47625	0.473869	0.447675	0.147638	0.138113	0.130969	0.130175	0.136723
480	0.587375	0.61595	0.610394	0.57785	0.446088	0.47625	0.473869	0.45085	0.141288	0.1397	0.136525	0.127	0.136128
490	0.593725	0.614363	0.604838	0.579438	0.446088	0.47625	0.473869	0.449263	0.147638	0.138113	0.130969	0.130175	0.136723
500	0.59055	0.61595	0.6096	0.579438	0.446088	0.47625	0.473869	0.449263	0.144463	0.1397	0.135731	0.130175	0.137517
510	0.59055	0.612775	0.611188	0.5842	0.442119	0.4699	0.473869	0.449263	0.148431	0.142875	0.137319	0.134938	0.140891
520	0.59055	0.616744	0.611188	0.5842	0.4445	0.474663	0.473075	0.449263	0.14605	0.142081	0.138113	0.134938	0.140295
530	0.592138	0.618331	0.612775	0.583406	0.4445	0.4699	0.471488	0.4445	0.147638	0.148431	0.141288	0.138906	0.144066
540	0.593725	0.614363	0.614363	0.585788	0.4445	0.4699	0.471488	0.4445	0.149225	0.144463	0.142875	0.141288	0.144463
550	0.592138	0.616744	0.612775	0.588963	0.442913	0.468313	0.471488	0.445294	0.149225	0.148431	0.141288	0.143669	0.145653
560	0.593725	0.618331	0.614363	0.587375	0.441325	0.466725	0.471488	0.442119	0.1524	0.151606	0.142875	0.145256	0.148034
570	0.598488	0.621506	0.6096	0.587375	0.441325	0.466725	0.468313	0.442913	0.157163	0.154781	0.141288	0.144463	0.149423
580	0.595313	0.6223	0.611188	0.592138	0.43815	0.465138	0.466725	0.441325	0.157163	0.157163	0.144463	0.150813	0.1524
590	0.595313	0.627856	0.612775	0.592138	0.441325	0.465138	0.466725	0.442913	0.153988	0.162719	0.14605	0.149225	0.152995
600	0.598488	0.625475	0.612775	0.592138	0.441325	0.465138	0.466725	0.443706	0.157163	0.160338	0.14605	0.148431	0.152995

Table E.5. Change in height of oil column for the system with 10% olive oil and 90° dead-leg inclination

time (s)	top level (m)				bottom level (m)				height (m)				average m
	run 1	run 2	run 3	run 4	run 1	run 2	run 3	run 4	run 1	run 2	run 3	run 4	
0	0.487363	0.509588	0.48895	0.515144	0.390525	0.407988	0.41275	0.409575	0.096838	0.1016	0.0762	0.105569	0.095052
10	0.5334	0.525463	0.507206	0.534988	0.428625	0.41275	0.4191	0.42545	0.104775	0.112713	0.088106	0.109538	0.103783
20	0.544513	0.541338	0.519906	0.5461	0.436563	0.415925	0.4191	0.434975	0.10795	0.125413	0.100806	0.111125	0.111323
30	0.55245	0.555625	0.530225	0.555625	0.439738	0.4191	0.423863	0.434975	0.112713	0.136525	0.106363	0.12065	0.119063
40	0.563563	0.561975	0.538163	0.561975	0.440531	0.4191	0.423863	0.434975	0.123031	0.142875	0.1143	0.127	0.126802
50	0.5715	0.57785	0.538163	0.568325	0.449263	0.422275	0.427038	0.434975	0.122238	0.155575	0.111125	0.13335	0.130572
60	0.581025	0.588963	0.5588	0.581025	0.447675	0.422275	0.430213	0.434975	0.13335	0.166688	0.128588	0.14605	0.143669
70	0.59055	0.597694	0.564356	0.585788	0.447675	0.42545	0.430213	0.434975	0.142875	0.172244	0.134144	0.150813	0.150019
80	0.593725	0.6096	0.574675	0.59055	0.45085	0.42545	0.430213	0.434975	0.142875	0.18415	0.144463	0.155575	0.156766
90	0.605631	0.619125	0.583406	0.5969	0.452438	0.428625	0.430213	0.434975	0.153194	0.1905	0.153194	0.161925	0.164703
100	0.6096	0.623888	0.59055	0.606425	0.452438	0.428625	0.430213	0.434975	0.157163	0.195263	0.160338	0.17145	0.171053
110	0.61595	0.635	0.598488	0.6096	0.452438	0.428625	0.430213	0.434975	0.163513	0.206375	0.168275	0.174625	0.178197
120	0.631825	0.639763	0.60325	0.61595	0.452438	0.428625	0.430213	0.43815	0.179388	0.211138	0.173038	0.1778	0.185341
130	0.635	0.650875	0.612775	0.6223	0.454025	0.428625	0.430213	0.43815	0.180975	0.22225	0.182563	0.18415	0.192484
140	0.64135	0.652463	0.619125	0.627063	0.452438	0.428625	0.430213	0.43815	0.188913	0.223838	0.188913	0.188913	0.197644
150	0.646113	0.659606	0.620713	0.631825	0.452438	0.428625	0.430213	0.43815	0.193675	0.230981	0.1905	0.193675	0.202208
160	0.650875	0.663575	0.631825	0.638175	0.452438	0.428625	0.430213	0.43815	0.198438	0.23495	0.201613	0.200025	0.208756
170	0.65405	0.665163	0.638175	0.638175	0.452438	0.428625	0.430213	0.43815	0.201613	0.236538	0.207963	0.200025	0.211534
180	0.65405	0.665163	0.652463	0.64135	0.452438	0.428625	0.430213	0.43815	0.201613	0.236538	0.22225	0.2032	0.2159
190	0.65405	0.665163	0.652463	0.644525	0.452438	0.428625	0.430213	0.43815	0.201613	0.236538	0.22225	0.206375	0.216694
200	0.6604	0.665163	0.655638	0.655638	0.452438	0.428625	0.430213	0.43815	0.207963	0.236538	0.225425	0.217488	0.221853
210	0.663575	0.668338	0.658813	0.6604	0.452438	0.428625	0.430213	0.43815	0.211138	0.239713	0.2286	0.22225	0.225425
220	0.658813	0.665163	0.661988	0.663575	0.452438	0.428625	0.430213	0.43815	0.206375	0.236538	0.231775	0.225425	0.225028
230	0.658813	0.671513	0.657225	0.661988	0.45085	0.428625	0.430213	0.43815	0.207963	0.242888	0.227013	0.223838	0.225425
240	0.66675	0.66675	0.657225	0.661988	0.452438	0.428625	0.430213	0.43815	0.214313	0.238125	0.227013	0.223838	0.225822
250	0.6604	0.669925	0.657225	0.663575	0.452438	0.428625	0.430213	0.43815	0.207963	0.2413	0.227013	0.225425	0.225425
260	0.663575	0.671513	0.658813	0.66675	0.449263	0.428625	0.430213	0.43815	0.214313	0.242888	0.2286	0.2286	0.2286
270	0.663575	0.671513	0.661988	0.66675	0.45085	0.428625	0.430213	0.434975	0.212725	0.242888	0.231775	0.231775	0.229791
280	0.663575	0.671513	0.661988	0.669925	0.45085	0.428625	0.430213	0.434975	0.212725	0.242888	0.231775	0.23495	0.230584
290	0.663575	0.671513	0.669925	0.669925	0.45085	0.428625	0.430213	0.434975	0.212725	0.242888	0.239713	0.23495	0.232569
300	0.663575	0.671513	0.669925	0.669925	0.449263	0.428625	0.430213	0.434975	0.214313	0.242888	0.239713	0.23495	0.232966

Table E.6. Change in height of oil column for the system with 10% olive oil and 60° dead-leg inclination

time (s)	top level (m)				bottom level (m)				height (m)				average m
	run 1	run 2	run 3	run 4	run 1	run 2	run 3	run 4	run 1	run 2	run 3	run 4	
0	0.508	0.491331	0.474663	0.569913	0.401638	0.3937	0.375444	0.422275	0.106363	0.097631	0.099219	0.147638	0.112713
10	0.521494	0.511175	0.50165	0.604838	0.409575	0.403225	0.38735	0.43815	0.111919	0.10795	0.1143	0.166688	0.125214
20	0.554831	0.5334	0.515938	0.617538	0.409575	0.409575	0.390525	0.441325	0.145256	0.123825	0.125413	0.176213	0.142677
30	0.560388	0.5461	0.531813	0.630238	0.407988	0.409575	0.3937	0.4445	0.1524	0.136525	0.138113	0.185738	0.153194
40	0.568325	0.5588	0.549275	0.64135	0.4064	0.411163	0.395288	0.446088	0.161925	0.147638	0.153988	0.195263	0.164703
50	0.57785	0.561975	0.555625	0.649288	0.4064	0.411163	0.395288	0.447675	0.17145	0.150813	0.160338	0.201613	0.171053
60	0.5842	0.576263	0.5715	0.661988	0.411163	0.41275	0.395288	0.448469	0.173038	0.163513	0.176213	0.213519	0.18157
70	0.592138	0.583406	0.581025	0.665163	0.411163	0.41275	0.40005	0.449263	0.180975	0.170656	0.180975	0.2159	0.187127
80	0.598488	0.591344	0.593725	0.665163	0.411163	0.41275	0.404813	0.45085	0.187325	0.178594	0.188913	0.214313	0.192286
90	0.604838	0.601663	0.601663	0.676275	0.41275	0.41275	0.404813	0.45085	0.192088	0.188913	0.19685	0.225425	0.200819
100	0.611188	0.608013	0.611188	0.67945	0.41275	0.41275	0.4064	0.452438	0.198438	0.195263	0.204788	0.227013	0.206375
110	0.620713	0.620713	0.623888	0.67945	0.409575	0.415925	0.4064	0.452438	0.211138	0.204788	0.217488	0.227013	0.215106
120	0.6223	0.623888	0.62865	0.688975	0.407988	0.415925	0.4064	0.454025	0.214313	0.207963	0.22225	0.23495	0.219869
130	0.630238	0.633413	0.636588	0.69215	0.407988	0.415925	0.4064	0.454025	0.22225	0.217488	0.230188	0.238125	0.227013
140	0.64135	0.642938	0.636588	0.69215	0.409575	0.415925	0.4064	0.454025	0.231775	0.227013	0.230188	0.238125	0.231775
150	0.64135	0.646113	0.644525	0.696913	0.409575	0.415925	0.4064	0.454025	0.231775	0.230188	0.238125	0.242888	0.235744
160	0.649288	0.65405	0.658019	0.701675	0.409575	0.415925	0.4064	0.454025	0.239713	0.238125	0.251619	0.24765	0.244277
170	0.649288	0.661988	0.661988	0.703263	0.409575	0.415925	0.4064	0.455613	0.239713	0.246063	0.255588	0.24765	0.247253
180	0.65405	0.66675	0.66675	0.708025	0.409575	0.415925	0.4064	0.455613	0.244475	0.250825	0.26035	0.252413	0.252016
190	0.657225	0.6731	0.6731	0.708025	0.409575	0.417513	0.4064	0.455613	0.24765	0.255588	0.2667	0.252413	0.255588
200	0.6604	0.676275	0.681038	0.708025	0.409575	0.417513	0.4064	0.455613	0.250825	0.258763	0.274638	0.252413	0.259159
210	0.6604	0.688975	0.682625	0.708025	0.409575	0.4191	0.41275	0.4572	0.250825	0.269875	0.269875	0.250825	0.26035
220	0.6604	0.693738	0.688975	0.708025	0.409575	0.4191	0.41275	0.4572	0.250825	0.274638	0.276225	0.250825	0.263128
230	0.66675	0.693738	0.6858	0.708025	0.409575	0.4191	0.41275	0.4572	0.257175	0.274638	0.27305	0.250825	0.263922
240	0.66675	0.688975	0.696913	0.708025	0.409575	0.4191	0.41275	0.4572	0.257175	0.269875	0.284163	0.250825	0.265509
250	0.66675	0.690563	0.6985	0.708025	0.409575	0.4191	0.41275	0.458788	0.257175	0.271463	0.28575	0.249238	0.265906
260	0.6731	0.690563	0.708025	0.708025	0.409575	0.4191	0.41275	0.458788	0.263525	0.271463	0.295275	0.249238	0.269875
270	0.67945	0.693738	0.708025	0.708025	0.409575	0.4191	0.41275	0.458788	0.269875	0.274638	0.295275	0.249238	0.272256
280	0.676275	0.6985	0.708025	0.708025	0.409575	0.4191	0.41275	0.458788	0.2667	0.2794	0.295275	0.249238	0.272653
290	0.67945	0.6985	0.708025	0.708025	0.409575	0.4191	0.41275	0.460375	0.269875	0.2794	0.295275	0.24765	0.27305
300	0.682625	0.6985	0.708025	0.708025	0.409575	0.4191	0.41275	0.458788	0.27305	0.2794	0.295275	0.249238	0.274241



Table E.7. Change in height of oil column for the system with 10% olive oil and 45° dead-leg inclination

time (s)	top level (m)				bottom level (m)				height (m)				average m
	run 1	run 2	run 3	run 4	run 1	run 2	run 3	run 4	run 1	run 2	run 3	run 4	
0	0.479425	0.531019	0.544513	0.550863	0.3556	0.3683	0.3683	0.369888	0.123825	0.162719	0.176213	0.180975	0.160933
10	0.508	0.550863	0.561975	0.563563	0.366713	0.388938	0.38735	0.38735	0.141288	0.161925	0.174625	0.176213	0.163513
20	0.519113	0.555625	0.576263	0.576263	0.379413	0.392113	0.392113	0.390525	0.1397	0.163513	0.18415	0.185738	0.168275
30	0.534194	0.577056	0.5842	0.579438	0.381	0.395288	0.390525	0.3937	0.153194	0.181769	0.193675	0.185738	0.178594
40	0.541338	0.585788	0.5969	0.582613	0.382588	0.396875	0.394494	0.3937	0.15875	0.188913	0.202406	0.188913	0.184745
50	0.558006	0.596106	0.606425	0.60325	0.384175	0.397669	0.395288	0.395288	0.173831	0.198438	0.211138	0.207963	0.197842
60	0.563563	0.606425	0.611188	0.611188	0.38735	0.402431	0.395288	0.395288	0.176213	0.203994	0.2159	0.2159	0.203002
70	0.581025	0.617538	0.620713	0.625475	0.388938	0.402431	0.397669	0.40005	0.192088	0.215106	0.223044	0.225425	0.213916
80	0.585788	0.623888	0.636588	0.633413	0.388938	0.402431	0.398463	0.40005	0.19685	0.221456	0.238125	0.233363	0.222448
90	0.593725	0.630238	0.6477	0.6477	0.391319	0.402431	0.398463	0.40005	0.202406	0.227806	0.249238	0.24765	0.231775
100	0.6096	0.635794	0.652463	0.665163	0.392906	0.404813	0.40005	0.401638	0.216694	0.230981	0.252413	0.263525	0.240903
110	0.617538	0.639763	0.657225	0.668338	0.392906	0.404813	0.399256	0.401638	0.224631	0.23495	0.257969	0.2667	0.246063
120	0.6223	0.652463	0.657225	0.6731	0.3937	0.4064	0.398463	0.402431	0.2286	0.246063	0.258763	0.270669	0.251023
130	0.625475	0.658813	0.663575	0.687388	0.396081	0.404813	0.398463	0.404813	0.229394	0.254	0.265113	0.282575	0.25777
140	0.64135	0.663575	0.663575	0.6858	0.3937	0.4064	0.398463	0.403225	0.24765	0.257175	0.265113	0.282575	0.263128
150	0.644525	0.66675	0.6731	0.689769	0.3937	0.4064	0.40005	0.404813	0.250825	0.26035	0.27305	0.284956	0.267295
160	0.6477	0.669925	0.681038	0.69215	0.3937	0.4064	0.40005	0.403225	0.254	0.263525	0.280988	0.288925	0.271859
170	0.663575	0.677863	0.681038	0.69215	0.3937	0.4064	0.398463	0.404813	0.269875	0.271463	0.282575	0.287338	0.277813
180	0.66675	0.682625	0.6858	0.700088	0.3937	0.404019	0.40005	0.4064	0.27305	0.278606	0.28575	0.293688	0.282773
190	0.668338	0.690563	0.6858	0.701675	0.3937	0.404019	0.40005	0.4064	0.274638	0.286544	0.28575	0.295275	0.285552
200	0.6731	0.695325	0.695325	0.6985	0.395288	0.4064	0.40005	0.407988	0.277813	0.288925	0.295275	0.290513	0.288131
210	0.6858	0.6985	0.696913	0.70485	0.395288	0.4064	0.40005	0.407988	0.290513	0.2921	0.296863	0.296863	0.294084
220	0.681831	0.700088	0.700088	0.708025	0.395288	0.4064	0.40005	0.407988	0.286544	0.293688	0.300038	0.300038	0.295077
230	0.690563	0.703263	0.695325	0.714375	0.395288	0.4064	0.40005	0.409575	0.295275	0.296863	0.295275	0.3048	0.298053
240	0.695325	0.703263	0.701675	0.708025	0.3937	0.4064	0.40005	0.409575	0.301625	0.296863	0.301625	0.29845	0.299641
250	0.700088	0.70485	0.701675	0.708025	0.3937	0.4064	0.40005	0.409575	0.306388	0.29845	0.301625	0.29845	0.301228
260	0.695325	0.706438	0.701675	0.708025	0.390525	0.409575	0.40005	0.412175	0.3048	0.296863	0.301625	0.295275	0.299641
270	0.700088	0.709613	0.701675	0.708025	0.390525	0.409575	0.40005	0.409575	0.309563	0.300038	0.301625	0.29845	0.302419
280	0.700088	0.709613	0.701675	0.708025	0.390525	0.409575	0.40005	0.409575	0.309563	0.300038	0.301625	0.29845	0.302419
290	0.696913	0.709613	0.701675	0.708025	0.388938	0.409575	0.403225	0.409575	0.307975	0.300038	0.29845	0.29845	0.301228
300	0.6985	0.709613	0.701675	0.708025	0.38735	0.409575	0.401638	0.409575	0.31115	0.300038	0.300038	0.29845	0.302419

Table E.8. Change in height of oil column for the system with 10% olive oil and 30° dead-leg inclination

time (s)	top level (m)				bottom level (m)				height (m)				average m
	run 1	run 2	run 3	run 4	run 1	run 2	run 3	run 4	run 1	run 2	run 3	run 4	
0	0.512763	0.52705	0.530225	0.582613	0.407988	0.416719	0.411956	0.4064	0.104775	0.110331	0.118269	0.176213	0.127397
10	0.534988	0.545306	0.5461	0.592138	0.422275	0.424656	0.420688	0.420688	0.112713	0.12065	0.125413	0.17145	0.132556
20	0.542925	0.555625	0.555625	0.598488	0.4318	0.4318	0.427038	0.423863	0.111125	0.123825	0.128588	0.174625	0.134541
30	0.55245	0.559594	0.56515	0.606425	0.4318	0.428625	0.42545	0.423863	0.12065	0.130969	0.1397	0.182563	0.14347
40	0.555625	0.573088	0.5715	0.61595	0.427038	0.428625	0.423863	0.423863	0.128588	0.144463	0.147638	0.192088	0.153194
50	0.56515	0.580231	0.576263	0.617538	0.423863	0.430213	0.423863	0.427038	0.141288	0.150019	0.1524	0.1905	0.158552
60	0.569913	0.581819	0.5842	0.625475	0.423863	0.428625	0.422275	0.427038	0.14605	0.153194	0.161925	0.198438	0.164902
70	0.573088	0.592138	0.59055	0.62865	0.423863	0.428625	0.42545	0.427038	0.149225	0.163513	0.1651	0.201613	0.169863
80	0.582613	0.600075	0.588963	0.633413	0.42545	0.428625	0.42545	0.423863	0.157163	0.17145	0.163513	0.20955	0.175419
90	0.589756	0.604838	0.592138	0.631825	0.42545	0.428625	0.4191	0.423863	0.164306	0.176213	0.173038	0.207963	0.18038
100	0.595313	0.613569	0.598488	0.642938	0.42545	0.427038	0.4191	0.422275	0.169863	0.186531	0.179388	0.220663	0.189111
110	0.600075	0.61595	0.601663	0.642938	0.42545	0.42545	0.414338	0.422275	0.174625	0.1905	0.187325	0.220663	0.193278
120	0.600075	0.623094	0.608013	0.650875	0.42545	0.423863	0.414338	0.422275	0.174625	0.199231	0.193675	0.2286	0.199033
130	0.606425	0.627856	0.611188	0.650875	0.422275	0.423863	0.41275	0.422275	0.18415	0.203994	0.198438	0.2286	0.203795
140	0.60325	0.629444	0.617538	0.657225	0.422275	0.420688	0.41275	0.422275	0.180975	0.208756	0.204788	0.23495	0.207367
150	0.61595	0.633413	0.6223	0.657225	0.422275	0.418306	0.41275	0.422275	0.193675	0.215106	0.20955	0.23495	0.21332
160	0.6223	0.638175	0.623888	0.663575	0.420688	0.416719	0.4064	0.4191	0.201613	0.221456	0.217488	0.244475	0.221258
170	0.619125	0.636588	0.630238	0.665163	0.414338	0.414338	0.4064	0.4191	0.204788	0.22225	0.223838	0.246063	0.224234
180	0.625475	0.6477	0.631825	0.665163	0.41275	0.414338	0.403225	0.4191	0.212725	0.233363	0.2286	0.246063	0.230188
190	0.630238	0.6477	0.631825	0.665163	0.407988	0.411163	0.403225	0.417513	0.22225	0.236538	0.2286	0.24765	0.233759
200	0.631825	0.657225	0.631825	0.668338	0.409575	0.409575	0.396875	0.414338	0.22225	0.24765	0.23495	0.254	0.239713
210	0.639763	0.6604	0.633413	0.668338	0.409575	0.409575	0.396875	0.414338	0.230188	0.250825	0.236538	0.254	0.242888
220	0.639763	0.6604	0.635	0.668338	0.407988	0.409575	0.396875	0.414338	0.231775	0.250825	0.238125	0.254	0.243681
230	0.646113	0.66675	0.644525	0.6731	0.407988	0.404813	0.396875	0.414338	0.238125	0.261938	0.24765	0.258763	0.251619
240	0.646113	0.667544	0.646113	0.676275	0.407988	0.403225	0.395288	0.412175	0.238125	0.264319	0.250825	0.263525	0.254198
250	0.6604	0.669925	0.650875	0.676275	0.401638	0.40005	0.3937	0.411163	0.258763	0.269875	0.257175	0.265113	0.262731
260	0.661988	0.671513	0.661988	0.676275	0.401638	0.398463	0.38735	0.411163	0.26035	0.27305	0.274638	0.265113	0.268288
270	0.661988	0.671513	0.658813	0.676275	0.401638	0.397669	0.385763	0.407988	0.26035	0.273844	0.27305	0.268288	0.268883
280	0.668338	0.676275	0.663575	0.676275	0.401638	0.397669	0.381	0.407988	0.2667	0.278606	0.282575	0.268288	0.274042
290	0.674688	0.677069	0.66675	0.676275	0.40005	0.397669	0.377825	0.403225	0.274638	0.2794	0.288925	0.27305	0.279003
300	0.676275	0.676275	0.66675	0.681038	0.390525	0.392113	0.377825	0.403225	0.28575	0.284163	0.288925	0.277813	0.284163

Date of the experiment, temperature and volume of oil collected within the J-bend expansion unit of the flow loop at the conclusion of the oil accumulation tests are summarized in Tables E.9. No more than 2 experiments were performed consecutively due to heat up problems associated with the current design of the flow loop. The first of the two experiments started at room temperature of the order of 294 K. The lowest and highest temperatures recorded where 295.1 and 313.7 K obtained on June 4, 2019 and May 26, 2019, respectively.

Derived values of the oil accumulation rate (m/s) are also tabulated in Table E.9.

Table E.9. Summary of the temperature and volume of oil accumulated within the J-bend expansion unit of the flow loop evaluated at the conclusion of the oil accumulation tests reported in Tables E.1-8

		5 % oil					10 % oil				
		date	T (K)	V <sub>oil-J</sub> (ml)	slopex10 <sup>-4</sup> (m/s)	R <sup>2</sup>	date	T (K)	V <sub>oil-J</sub> (ml)	slopex10 <sup>-4</sup> (m/s)	R <sup>2</sup>
90°	run1	19-May	306.4833	140	1.89	0.9976	28-May	303.7056	210	4.14	0.8968
	run2	27-May	304.8167	170	1.63	0.994	28-May	304.2611	243	4.44	0.8148
	run3	27-May	304.5389	190	1.81	0.9904	29-May	298.4278	186	5.5	0.9285
	run4	27-May	300.0944	178	1.74	0.9911	29-May	295.65	304.5	4.55	0.9572
60°	run1	19-May	305.9278	161	1.52	0.9737	29-May	304.8167	209	4.99	0.9134
	run2	20-May	310.65	162	1.4	0.99	29-May	308.15	207	6.06	0.9348
	run3	21-May	304.8167	199.5	1.41	0.9885	29-May	298.7056	219	6.4	0.9433
	run4	21-May	309.2611	194.5	1.54	0.9873	29-May	299.2611	215	2.73	0.7552
45°	run1	22-May	305.3722	184	1.49	0.9665	4-Jun	295.0944	139	6.45	0.9644
	run2	22-May	299.2611	189	1.78	0.9683	4-Jun	301.4833	158	5	0.9346
	run3	23-May	299.8167	190	1.31	0.9729	4-Jun	304.8167	160	4.41	0.8959
	run4	23-May	305.9278	166	1.52	0.9687	4-Jun	303.7056	145	4.37	0.8222
30°	run1	25-May	300.3722	196.5	1.88	0.9843	31-May	303.7056	150	5.8	0.9944
	run2	26-May	308.7056	175	1.79	0.9781	31-May	306.4833	175	5.89	0.986
	run3	26-May	307.8722	167	1.66	0.9822	31-May	305.3722	210	5.59	0.9937
	run4	26-May	313.7056	185	1.7	0.9888	31-May	305.9278	205	3.53	0.9697

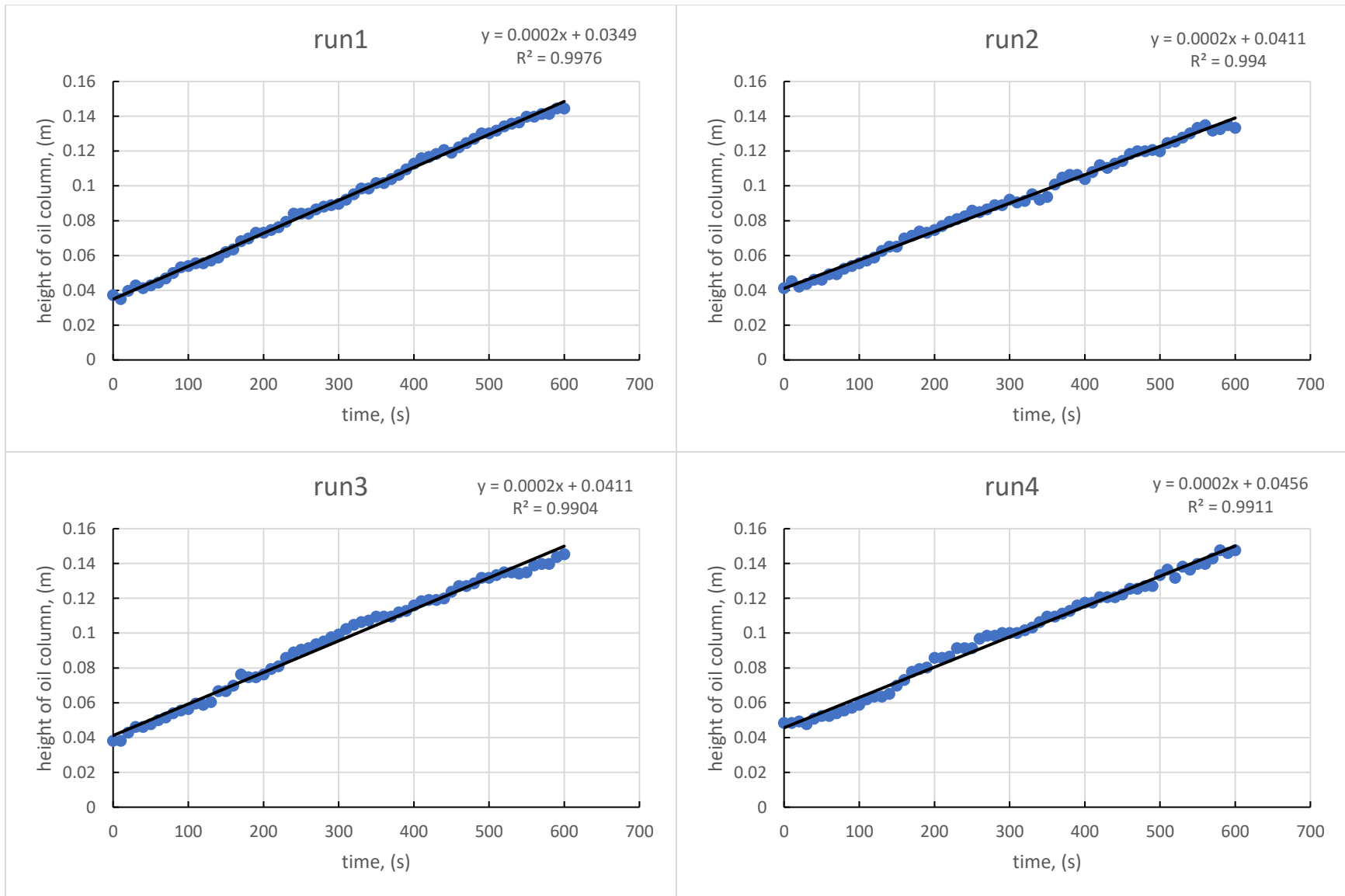


Figure E.1. Height of accumulated oil column for the case of 5%-95% oil-water for the inclination angle of 90° (vertical dead-leg)

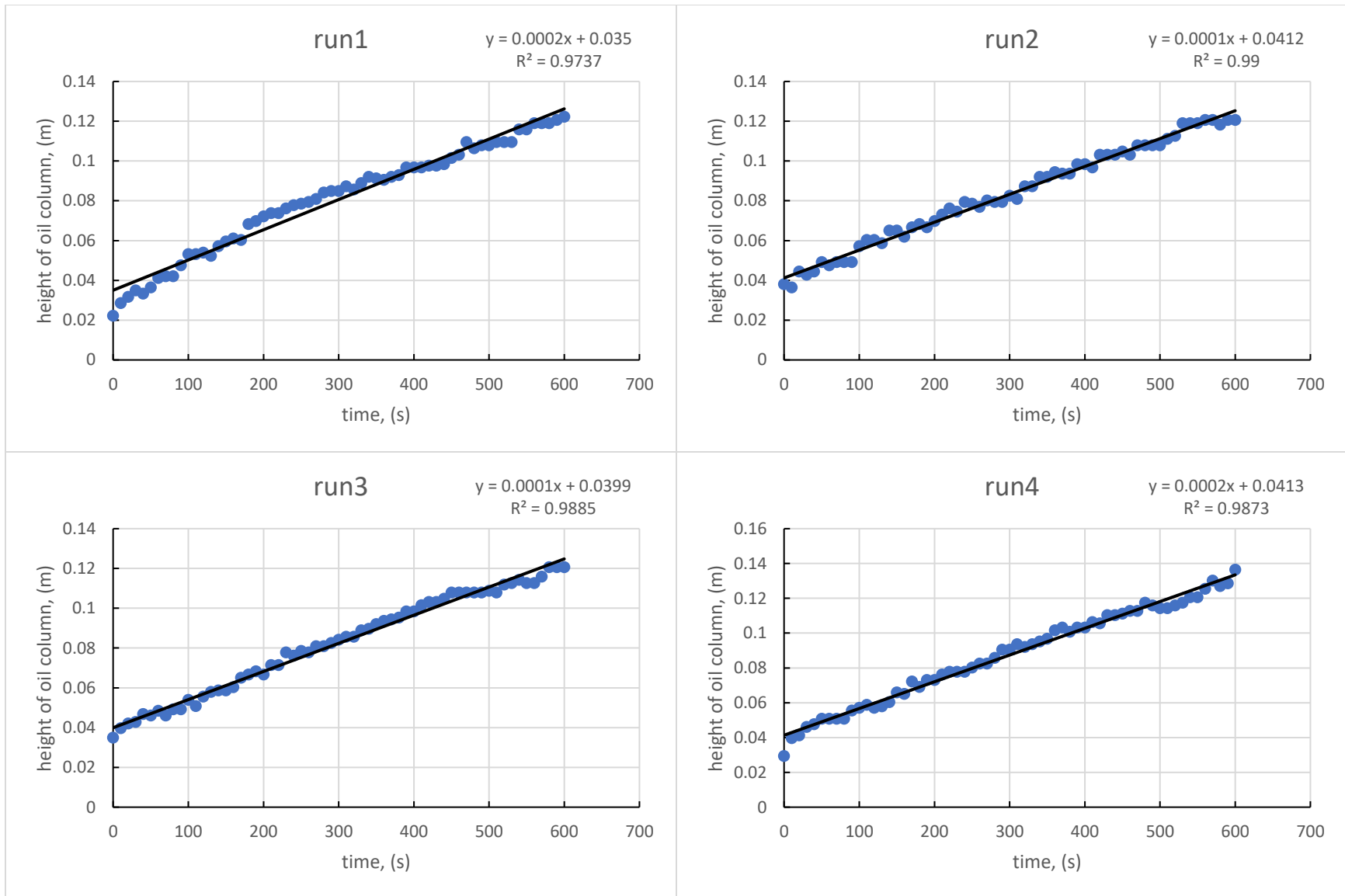


Figure E.2. Height of accumulated oil column for the case of 5%-95% oil-water mixture for the inclination angle of 60°

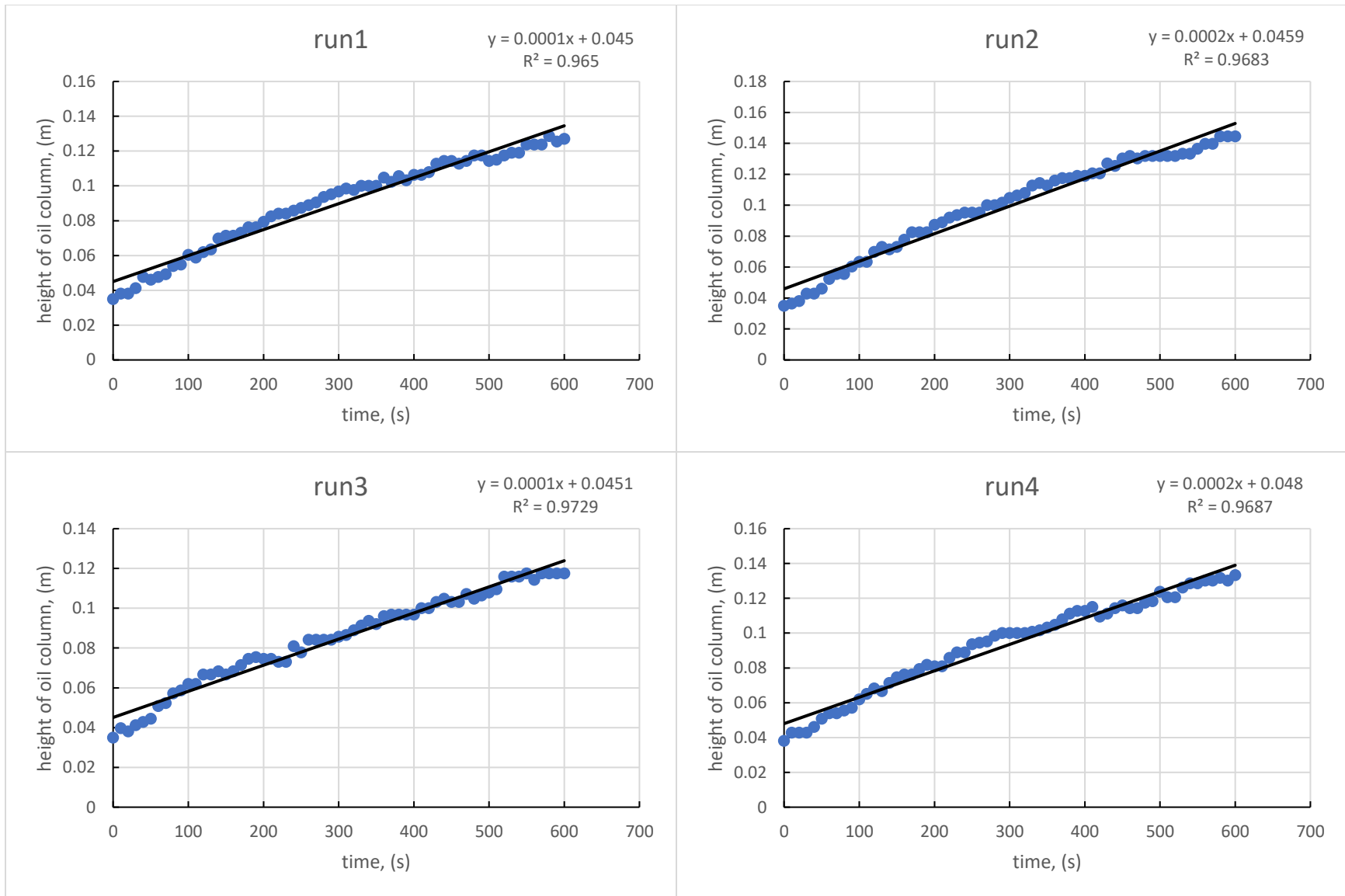


Figure E.3. Height of accumulated oil column for the case of 5%-95% oil-water mixture for the inclination angle of 45°

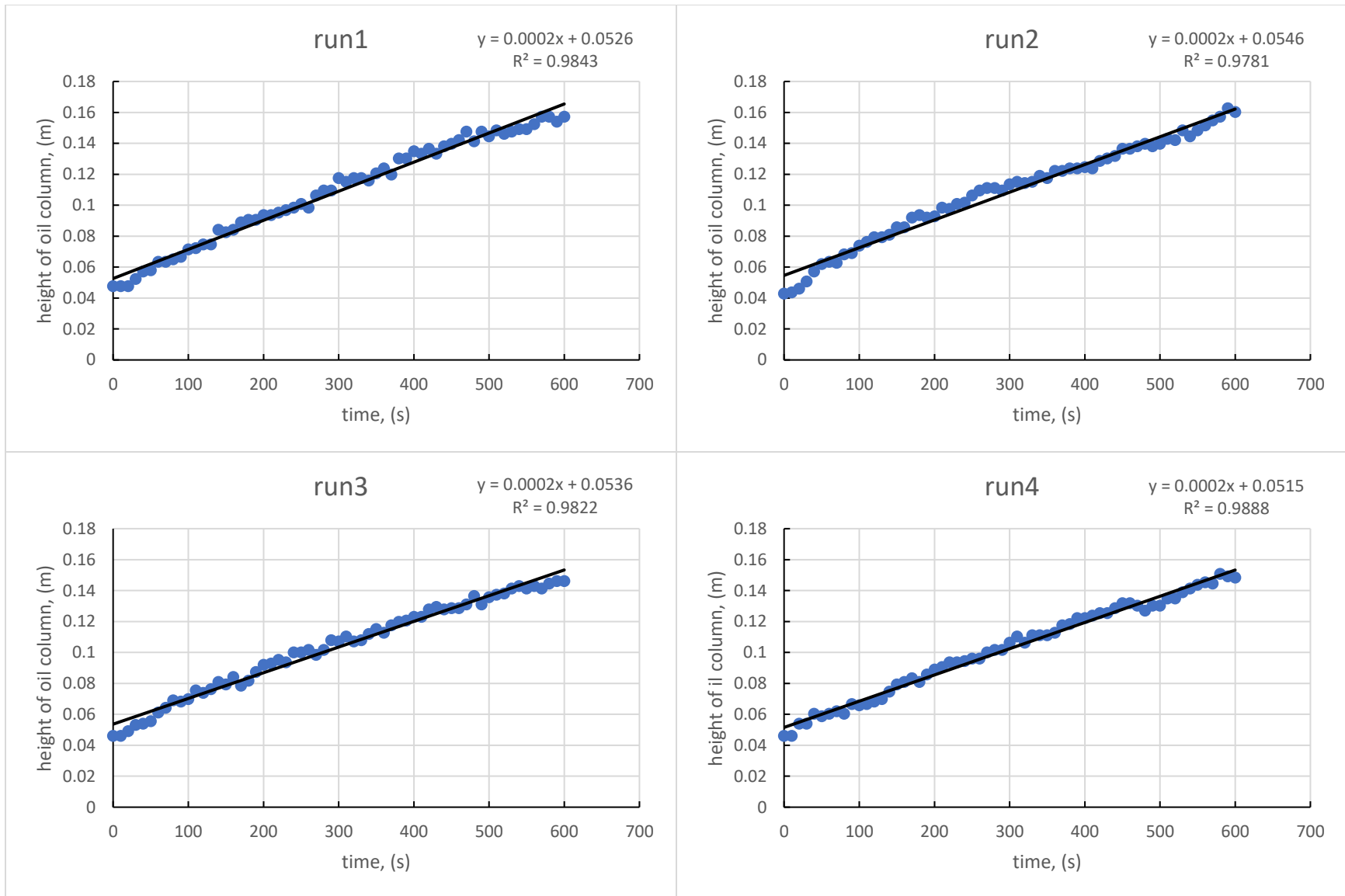


Figure E.4. Height of accumulated oil column for the case of 5%-95% oil-water mixture for the inclination angle of 30°

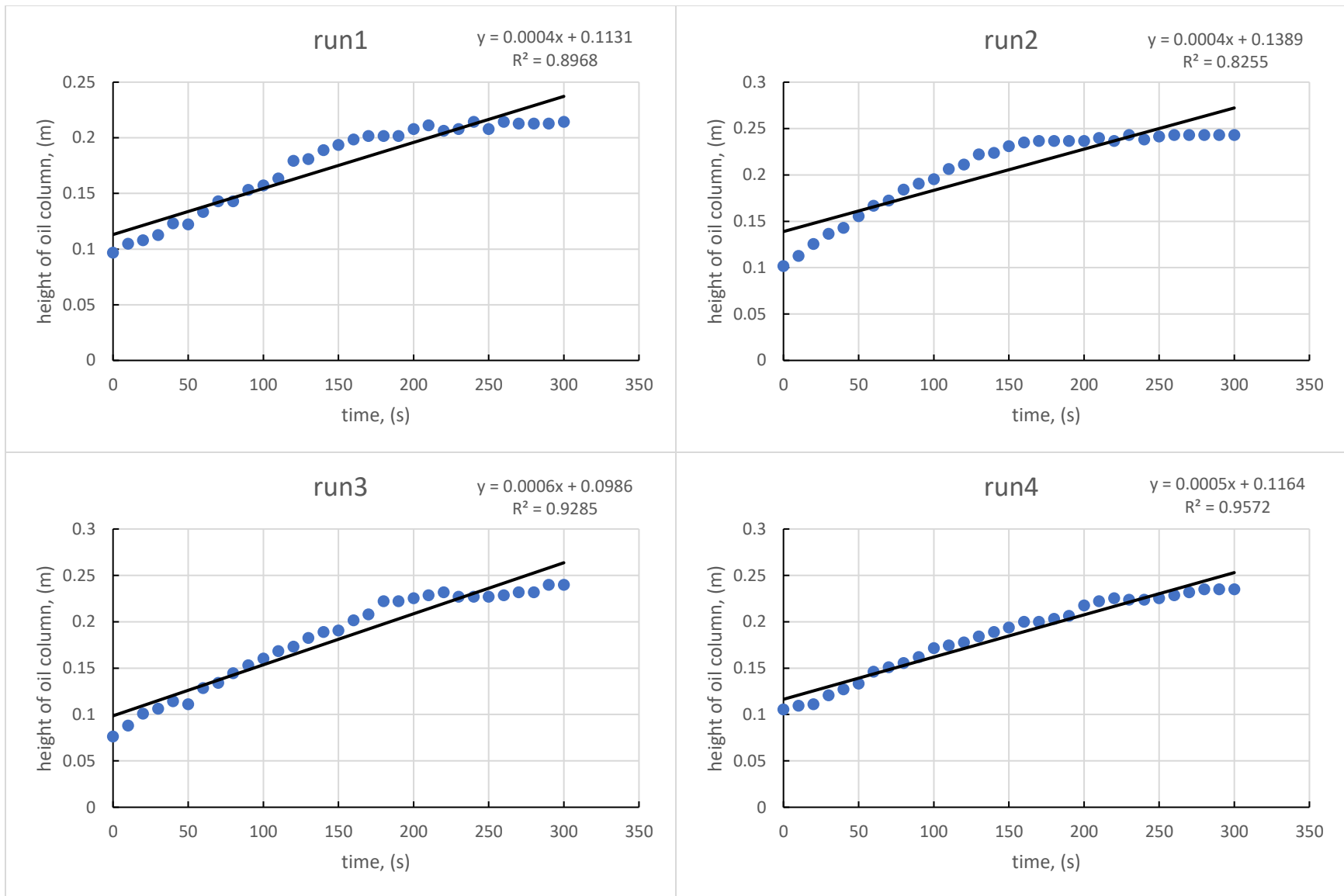


Figure E.5. Height of accumulated oil column for the case of 10%-90% oil-water for the inclination angle of 90° (vertical dead-leg)

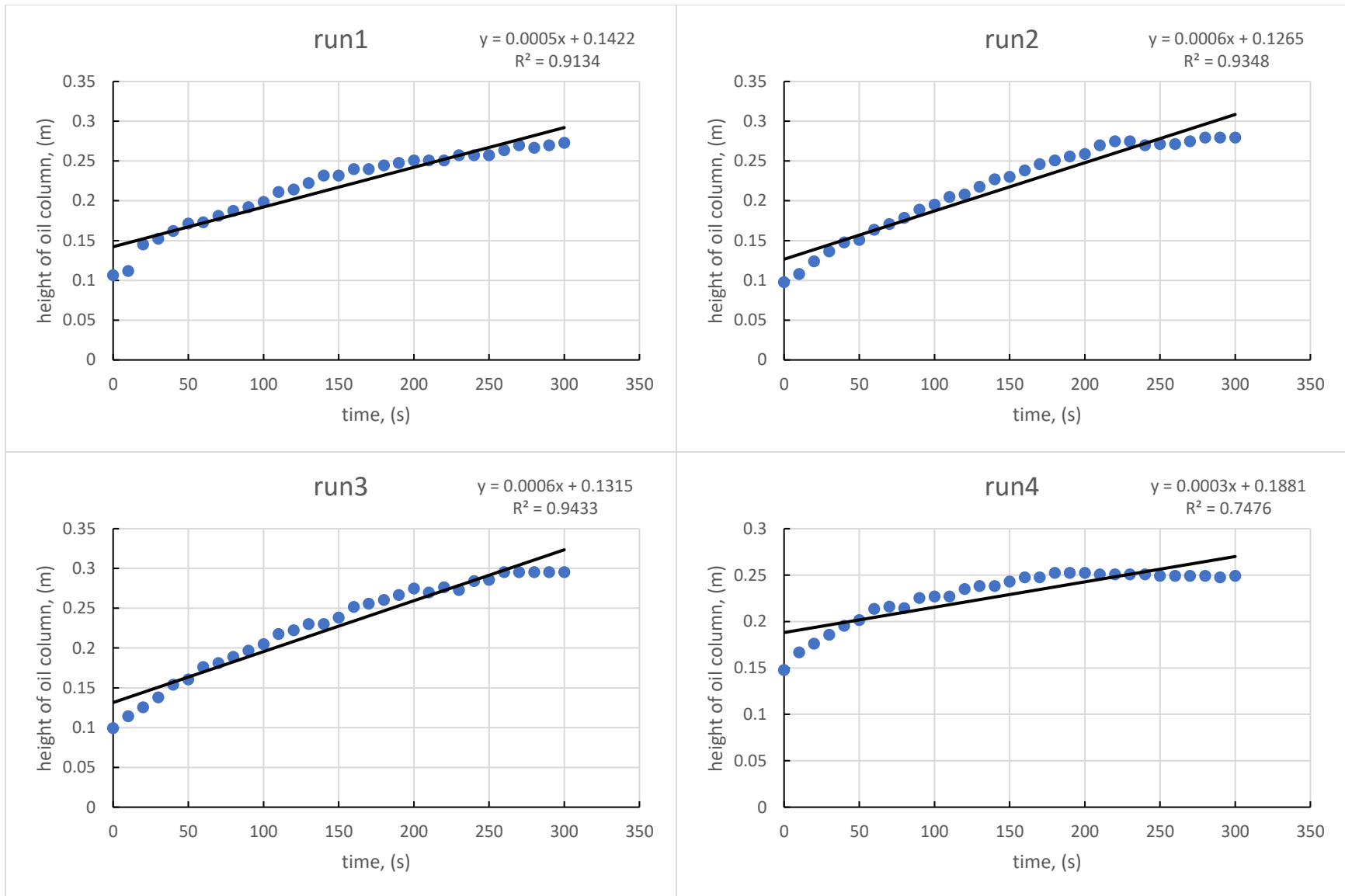


Figure E.6. Height of accumulated oil column for the case of 10%-90% oil-water mixture for the inclination angle of 60°



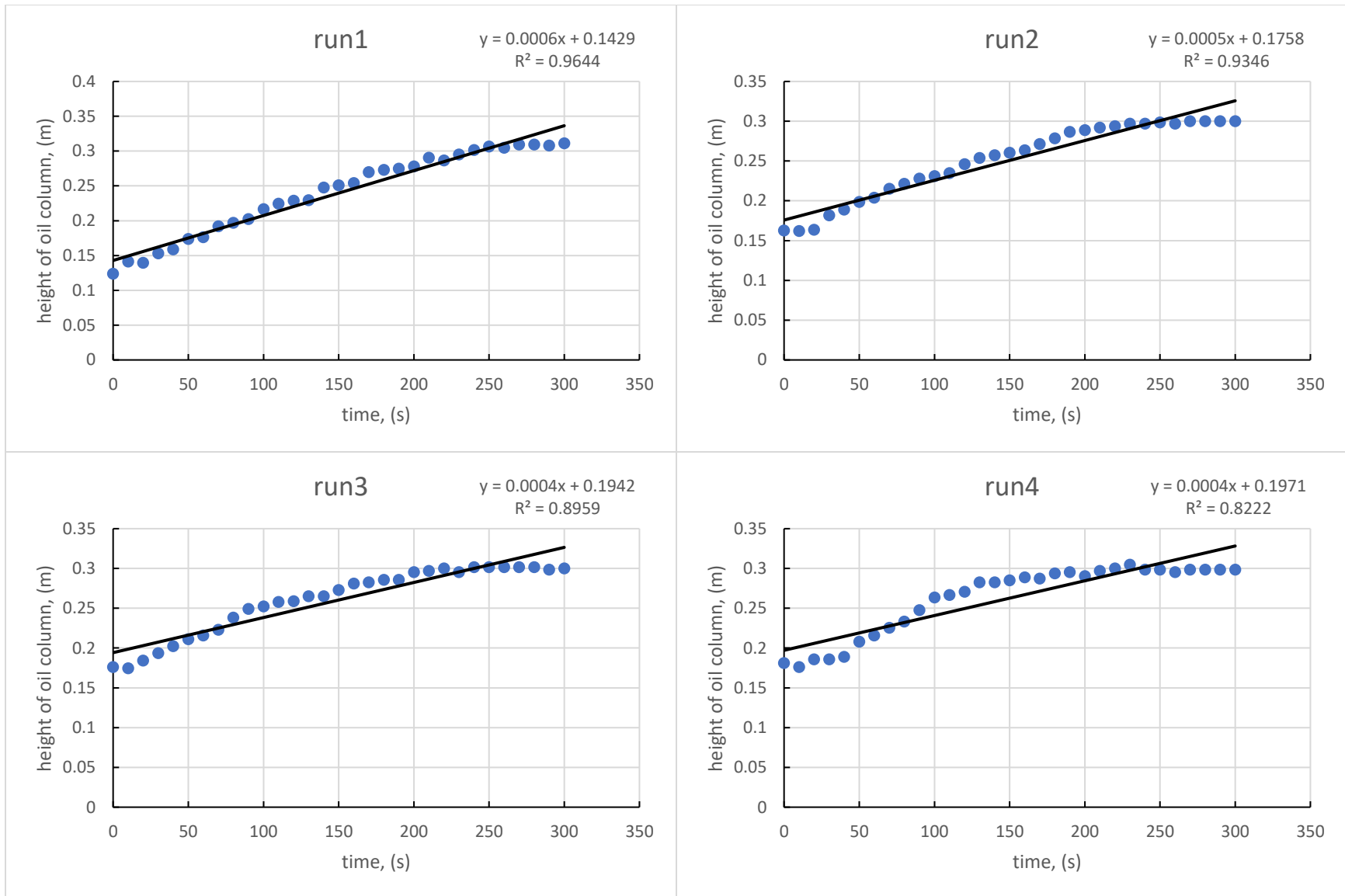


Figure E.7. Height of accumulated oil column for the case of 10%-90% oil-water mixture for the inclination angle of 45°

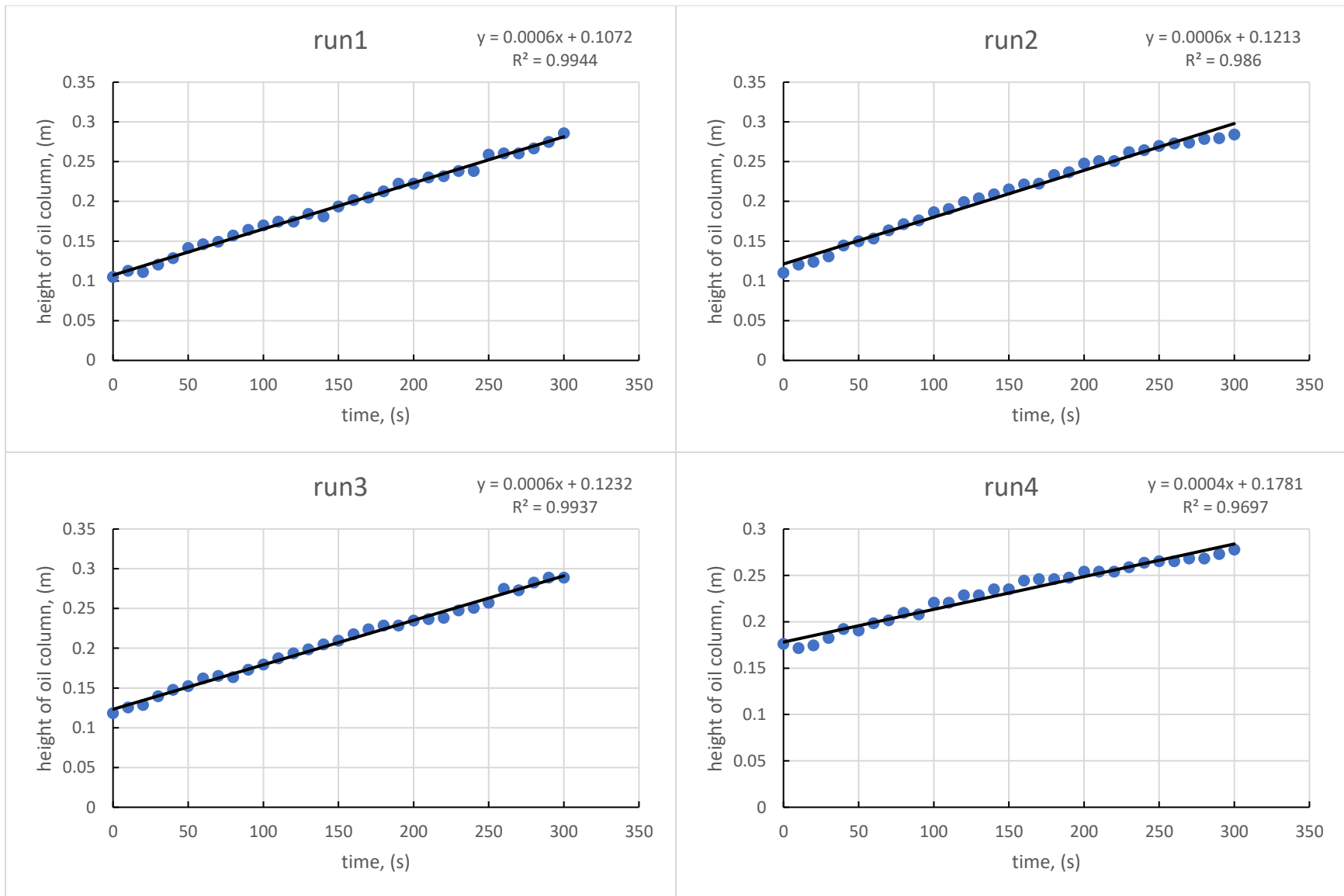


Figure E.8. Height of accumulated oil column for the case of 10%-90% oil-water mixture for the inclination angle of 30°